Technische
Universität
Braunschweig

The role of pebble fragmentation in planetesimal formation during the gravitational collapse of a pebble cloud

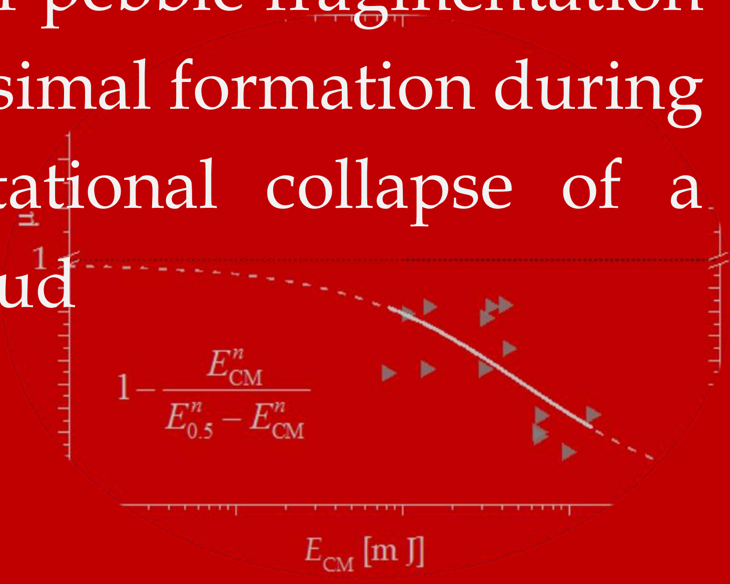

Von der Fakultät für Elektrotechnik, Informationstechnik, Physik
der Technischen Universität Carolo-Wilhelmina
zu Braunschweig
zur Erlangung des Grades eines
Doktors der Naturwissenschaften
(Dr. rer. nat.)
genehmigte
Dissertation
von
Syed Bukhari, Mohtashim Ahmad
aus
Multan, Pakistan

Referent 1
Prof. Dr. Jürgen Blum
Referent 2
Prof. Dr. Gerhard Wurm
Vorsitzender Promotionskommission
Prof. Dr. Uwe Motschmann

eingereicht am: 22. Dezember 2016
Disputation am: 6. April 2017

Publications

A large part, in the form of results, discussions and the figures presented in this thesis, have been already published in the mentioned below journals and conferences.
The published material has been reused with the permission of the Faculty of Electrical Engineering, Information Technology, Physics and the respective authors. However here some other details and aspects of the study have been provided which have not been the part of any publication.

The role of pebble fragmentation in planetesimal formation I. Experimental study
Bukhari Syed, M. A., Blum, J., Wahlberg Jansson, K., & Johansen, A. 2017, The Astronomical Journal

The role of pebble fragmentation in planetesimal formation II. Numerical study
Wahlberg Jansson, K., Johansen, A., Bukhari Syed, M., & Blum, J. 2017, The Astrophysical Journal

Laboratory Drop Towers for the Experimental Simulation of Dust-aggregate Collisions in the Early Solar System
Blum, J., et al. 2014, Journal of visualized experiments: JoVE

Some of the preliminary results have been published in the following conferences as well

The outcomes of dust-aggregate collisions during the gravitational collapse in planetesimal formation
Bukhari Syed, M. A., & Blum, J. 2016. in Planet Formation and Evolution II,
7. – 9. March 2016, Duisburg

The outcome of dust-aggregate collisions in streaming and gravitational instabilities
Bukhari Syed, M. A., & Blum, J. 2015. in The Formation of the Solar System II,
2. – 4. June 2015, Berlin

Transition between growth and fragmentation in dust-agglomerate collisions
Bukhari Syed, M. A., & Blum, J. 2014b. in Planet Formation and Evolution I, 8. – 10. September 2014, Kiel

The outcome of dust-aggregate collisions in streaming and gravitational instabilities
Bukhari Syed, M. A., & Blum, J. 2014a. in The Formation of the Solar System I,
13. – 15. May 2014, Bonn

The outcome of dust-aggregate collisions in streaming and gravitational instabilities
Bukhari Syed, M. A., & Blum, J. 2013. in Protostars and Planets VI,
15. – 20. July 2013, Heidelberg

to my father

Acknowledgment

I am proud to introduce my colleagues and friends who have been helping and supporting me till this date. I had great time and enjoyed the friendly working culture at the institute. This work would be not possible without their direct support, for this I will be always thankful to:

Karthrin Gebauer
for her support in building dust moulds, spring based cannons and maintenance.

Bernd Stoll
for building and maintaining the experimental setup and pneumatic accelerator.

Rainer Schräpler
for his supervision and discussion on scientific matters and especially for his help to improve this thesis.

Ingo von Borstal
for discussion on scientific matters and especially for his care and support during parabolic flights.

Christopher Perschke
for fruitful discussion and support at work and for his friendship.

Karl Wahlberg Jansson
for his guidance and long discussions on the model, results and support as a friend.

Stefan Kothe
for his discussion on scientific matters, assistances in lab and for the review of thesis.

Holly Capelo
for her fruitful discussion on streaming instability and for the review of the thesis.

Jürgen Blum
I am thankful to Jürgen, my Doktorvater, for trusting and giving me chance to work with him. I am thankful for his care, allowing me to test my hunches and paying attention to my stories about the results and teaching me how to do science.

I thank to Bastian Gundlach for his review. I am thankful to Tax Payers for their funding for this project through DFG and SFB 963. In addition to this my thanks also goes to the team of free software Image J (Fiji), which saved a lot of time ☺.
I do not know how to thank those special people who turned up to be my ladder, so I can reach my goals in life.

Content List

Publications ... ii
Acknowledgment ... vi
List of Figures ... xi
List of Tables ... xii
Abstract ... xiv
Zusammenfassung ... xvi

Chapter 1: Introduction

1.1 THE QUESTION FOR A MOTIVATION ... 1
1.2 STATE OF THE ART: TWO POSSIBLE SOLUTIONS ... 2
  1.2.1 Classical scenario of planetesimal formation (sweep-up) ... 2
  1.2.2 Streaming instability leading to gravitational collapse ... 4
1.3 FRAGMENTATION WITH MASS TRANSFER ... 5
1.4 HOW THIS WORK CAN CONTRIBUTE? ... 6
1.5 TIME FRAME AND THE ROAD MAP OF THE THESIS ... 7
  1.5.1 Thesis writing (2016) ... 8

Chapter 2: Protoplanetary disc and dust growth

2.1 PROTOPLANETARY DISC ... 9
  2.1.1 SED of Young stellar objects (YSOs) ... 11
  2.1.2 Observational evidence for grain growth ... 12
  2.1.3 Minimum Mass Solar Nebula ... 13
  2.1.4 Disc structure ... 14
    2.1.4.1 Radial structure ... 15
    2.1.4.2 Vertical structure ... 16
2.2 PLANETESIMALS ... 17
  2.2.1 Vertical settling ... 17
  2.2.2 Growth along vertical settling ... 19
2.3 Relative velocities ... 22
  2.3.1 Brownian motion ... 22
  2.3.2 Turbulent motion ... 23
  2.3.3 Radial drift motion ... 23
  2.3.4 Turbulent mixing and Kelvin Helmholtz instability ... 24

2.3.5 Pebbles pileup by turbulence 25
2.3.5.1 The role of eddies in pebbles pileup 25
2.4 STEAMING INSTABILITY LEADING TO GRAVITATIONAL COLLAPSE 26
2.4.1 Gravitational collapse 28
2.4.2 Modelling the gravitational collapse of a pebble cloud 29

Chapter 3: Experimental Setup

3.1 THE DROP TOWER 33
3.2 DOUBLE-WING TRAP DOOR 35
3.3 ACCELERATORS 36
3.3.1 Electromagnetic accelerators 36
3.3.2 Spring based accelerator 38
3.3.3 Pneumatic accelerator 39
3.4 DUST PROCESSING AND MOULDING 39
3.5 X-RAY TOMOGRAPHY 41

Chapter 4: Results and Analysis

4.1 COLLISION PARAMETERS AND COLLISION SERIES 45
4.1.1 Impact parameter 47
4.2 FRAGMENTATION STRENGTH μ 48
4.3 THE MODEL OF FRAGMENTATION STRENGTH μ 48
4.3.1 The onset-velocity v_1 for fragmentation 51
4.4 THE RELATIVE COLLISION STRENGTH Q* 53
4.4.1 Surface to volume ratio h 57
4.4.2 Catastrophic threshold velocity $v_{0.5}$ 58
4.5 THE PROBABILITY FUNCTION OF MASS TRANSFER 60
4.5.1 The mass-transfer efficiency 63
4.6 AREA-FREQUENCY DISTRIBUTION 66
4.6.1 The method of fragments count 66
4.6.1.1 Invariant slope (α) of area frequency distribution 67
4.7 A COMPLETE AREA- FREQUENCY DISTRIBUTION 69
4.7.1 Variation in slope α of area- frequency distribution 70
4.7.2 The critical fragment area x_i 73
4.7.3 The total fragment-frequency count C_N 74
4.8 MASS-FREQUENCY DISTRIBUTION 78

4.8.1 The correlation between critical fragment area x_i and mass μ_i 81
4.8.2 The correlation between the μ_i and actual μ largest relative fragment 82

4.9 THE MODEL OF FRAGMENT VELOCITY DISTRIBUTION 83

4.9.1 The method of velocity measurements 83
4.9.2 The result of velocity distribution 84
4.9.3 The velocity distribution in centre of mass (CM) and laboratory frame 87

4.10 THE GRAND PEBBLE FRAGMENTATION MODEL 91

4.10.1 Implementation of the pebble fragmentation model 93
4.10.2 The two size (mass) dependent regimes of planetesimals 93
4.10.3 The collapse time and the limitation of the pebble fragmentation model 96
4.10.4 The internal structure of the large size planetesimal 97
4.10.4.1 The real fragmentation models $\alpha = 0.5$ and $\alpha = 0.9$ 98
4.10.4.2 The bimodal fragmentation model 101
4.10.4.3 The 100% Mass transfer model with $\alpha = 0.9$ 102

Chapter 5: Discussion and conclusion

5.1 WHAT WAS THE ORIGINAL GOAL OF THIS STUDY? 105

5.2 WHAT DO WE LEARN FROM EXPERIMENTS? 105

5.3 WHAT DO WE LEARN FROM NUMERICAL MODELS? 107

5.4 RELEVANCE TO 67P/ CHURYUMOV-GERASIMENKO 109

5.5 THE LIMITATION OF THIS STUDY AND THE FUTURE PROSPECTS 110

5.6 CONCLUSION 110

Appendices

APPENDIX A: AREA-FREQUENCY DISTRIBUTION AFTER EQN. (4.30) 113

APPENDIX B : MASS-FREQUENCY DISTRIBUTION AFTER EQN. (4.38) 121

APPENDIX C : FRAGMENT VELOCITY DISTRIBUTION AFTER EQN. (4.47) 129

APPENDIX D : SUPPLEMENTARY IMAGES OF EXPERIMENTAL SETUP 137

BIBLIOGRAPHY 141

LEBENSLAUF 144

List of Figures

Figure 2.1. Disc formation scenerio 9
Figure 2.2. The schematic diagram of a typical SED curve 11
Figure 2.3. The schematic diagram for the packet of gas located at radius r 14
Figure 2.4. The schematic diagram of protoplanetary disc inspired by Testi et al. (2014) 21
Figure 2.5. The schematic diagram of dust-gas interaction... 27

Figure 3.1.The schematic diagram of drop tower 33
Figure 3.2. The Double-wing trap door releas mechanism. 35
Figure 3.3. The electromagnetic accelerator at home position 36
Figure 3.4. The curves of electric current and velocity on oscilloscope. 37
Figure 3.5. The spring based accelerator. 38
Figure 3.6. The pneumatic accelerator 39
Figure 3.7. The sieve of 500 μm mesh 40
Figure 3.8. The digital scale 40
Figure 3.9. The sample moulds 40
Figure 3.10. The dust aggregate of various sizes.. 41
Figure 3.11. The XRT-reconstruction of a 5 cm dust aggregate. 41
Figure 3.12. The relative cross sectional area. 42

Figure 4.1. The representative snapshots of pre-collision and post-collision scenario. 46
Figure 4.2. The normalised cumulative velocity distribution for all 8 series. 47
Figure 4.3. The modle of fragmentation strength μ as a function of E_{CM}. 49
Figure 4.4. Fragmentation strength μ as a function of projectile, target and impact velocity 52
Figure 4.5. The onset-velocity of fragmentation as a function of projectile P and target T. 52
Figure 4.6. The relative collision strength Q^* as a function of projectile P.. 55
Figure 4.7. The relative collision strength Q^* as a function of projectile T. 55
Figure 4.8. The relative collision strength Q^* as a function of projectile P and T 56
Figure 4.9. The relative collision strength Q^* as a function of surface to volume ratio 57
Figure 4.10. The catastrophic threshold velocity $v_{0.5}$ as a function of v_1 and reduced mass. 59
Figure 4.11. The $v_{0.5}$ as a function of surface to volume ratio.. 60
Figure 4.12. The probability function of mass transfer P_{MT} 61
Figure 4.13. The survival velocity v_{sur} as a function of size ratio. 62
Figure 4.14. The mas-transfer efficiency as a function of v_n, P and T 65
Figure 4.15. The time series of the single fragmentation curve 3Jun-6. 68
Figure 4.16. The model of a typical cumulative area distribution of the representative series 70
Figure 4.17. The fragmentation slope α for 141 experiments as a function of v_n and T. 71
Figure 4.18. Fragmentation slope α as a function of fragment-frequency count C_N. 72
Figure 4.19. The critical fragment size x_i for 105 events of catastrophic fragmentation. 74
Figure 4.20. The fragment-frequency count C_N as a function of v_n and P. 76
Figure 4.21. The fragment-frequency count C_N as a functino of collision energy.. 76

Figure 4.22. The x_i and C_N as a function of as a function of v_n and P. ...77
Figure 4.23. The cumulative mass-frequency distribution M_{cum}. ...79
Figure 4.24. The slope of the mass-frequency distribution β as a function of v_n and T ...79
Figure 4.25. The slope of the mass-frequency distribution for small size fragments. ...80
Figure 4.26. The slope of the mass-frequency distribution for 141 experiments ...80
Figure 4.27. A linear correlation between the size and mass of the critical fragment ...81
Figure 4.28. The correlation between the μ_i and the fragmentation strength μ ...82
Figure 4.29. The method of fragment velocity measurement. ...83
Figure 4.30. The velocity components of the fragments in the centre of mass frame. ...84
Figure 4.31. The schematic diagram of collision. ...85
Figure 4.32. The fragment count as a function of scattering angle. ...86
Figure 4.33. The velocity of fragments in centre of mass frame and in laboratory frame. ...88
Figure 4.34. The slope of fragment velocity as a function of v_n and P. ...89
Figure 4.35. The maximum fragment velocity v_{max} as a function of v_n, P and T. ...90
Figure 4.36. The mass weighted mean pebble size as a function of planetesimal R_{solid}. ...94
Figure 4.37. The collapse time t_{col} of a pebble cloud as a function of the planetesimal R_{solid}. ...96
Figure 4.38. The mean relative velocities as a function of collapse time t_{col}. ...98
Figure 4.39. The cloud contraction parameter η as a function of collapse time ...99
Figure 4.40. The mass weighted mean pebbles size as a function of collapse time. ...100
Figure 4.41. The fraction of total mass as a function of actual mean pebble size ...103

List of Tables

Table 1.1. A summary of the nine possible collision outcomes as described in Güttler et al. (2010) ...3

Table 4.1. The collision parameters taken in this study. ...45
Table 4.2. The Hill-function and its related fit parameters ...50
Table 4.3. The relative collision strength Q and the resulting values of $v_{0.5}$, and the probability of mass transfer P_{MT}.* ...62
Table 4.4. The dependence of mass-transfer on velocity v_n, projectile P and target T. ...64
Table 4.5. The fit parameters of α are derived by fitting eqn. (4.31) and eqn. (4.32) ...71
Table 4.6. The fit parameters of critical fragment size x_i obtained by fitting eqn. (4.34) ...73
Table 4.7. The fit parameters of fragment-frequency C_N derived by fitting eqn. (4.35) ...75
Table 4.8. The fit parameters x_i C_N derived by fitting eqn. (4.36) ...77
Table 4.9. The fit parameters for β derived by fitting eqn. (4.40) ...78
Table 4.10. The fit parameters for β^* derived by fitting eqn. (4.48) ...88
Table 4.11. The fit parameters of v_{max} derived by fitting eqn. (4.49) ...90
Table 4.12. The four different models of a collapse of a pebble cloud ...93

Abstract

What is a Shooting-star?

"A shooting star is a fireball thrown at Satan when he eavesdrops the conversation between God and angels". This is what I was told in my childhood. In other cultures a shooting star was considered as a divine gift. For example, Greeks kept the meteorites in the Temple of Venus. The black stone in Mecca is sacred to Muslims because it is believed to come from heavens. Our ancestors, across the cultures and history have been fascinated by the shooting stars, today better known as meteoroids. They have been trying to provide explanation and the meaning to these objects, on the basis of their imaginations. Today we are driven by the same curiosity which our ancestors had. And these objects are equally fascinating and important for us, but the difference is they kept them in temples and we keep them in laboratories and in museums. Today we are trying to answer the ages old questions, like what are the meteoroids, where do they come from, how are the formed and more importantly, how are they related to us.

Meteoroids are made of dust and ice and they are considered as the building block of planets. Today these objected can be found in Kuiper Belt and in Ort Cloud, which are actually the leftover from the cataclysmic birth of our Solar system, which took place about 4.5 billion years ago. There are convincing evidence that our Earth and other planets have born out of submicron size cosmic dust. In laboratories the growth of micron size dust has been observed as well, which is believed to continue up to millimetre to a few centimetres sized pebbles. However, what we do not understand is, how the cm-sized pebbles can grow up to the body of size which has gravity strong enough to take over the growth process, the body known as planetesimal. This is one of the missing links in the story of planet formation. Over the past ten years, several interesting ideas have been proposed which provide the missing link to this story. One of these ideas is the marriage between streaming instability (SI) and the gravitational instability (GI). Streaming instability explains how a swarm of pebbles can be generated which can have enough mass that the gravitational instability can be induced in the accumulated mass. These instabilities trigger the gravitational collapse of the swarm which ends in the formation of a planetesimal.

The motivation of this thesis is to contemplate what would happen during such a gravitational collapse. How will it be accomplished? It will be achieved with the help of experiments and numerical simulations which are the two goals of this thesis. The first goal is to conduct an experimental study to develop a grand model of pebble fragmentation. And the second goal is the execution of this model by developing a numerical code. The task of code development has been outsourced and only the results have been incorporated and discussed here. The experimental study makes use of the collision parameters (1 cm – 5 cm sized pebbles and 1 – 8 $\mathrm{ms^{-1}}$ collision velocities) which have been proposed by the studies on streaming instability. This decision, does not provide only a good starting point for the experimental parameters but also enable to validate the predictions made by SI.

By analysing 142 experiments of pebble collisions, three main models have been developed. First is the model of fragmentation strength which explains the three major collision outcomes, fragmentation, mass transfer and bouncing. Second is the model of probability function of mass transfer, which suggests that the probability of mass transfer can reach to unity if size ratio between the two pebbles is 5.8. And third is the complete model for the fragment size distribution. The combined outcome of the experimental study is the so called grand pebble fragmentation model, which consists of several constituent models, which determine the different rules of the pebbles interactions during a gravitational collapse.

The second goal of this study is the execution of this model. Since practically it is not feasible to conduct millions of collisions in a laboratory, therefore a numerical code was required to simulate the gravitational collapse, which has been accomplished by the collaborators of this study in the Lund Observatory, Sweden. The results of numerical models show: i) that the model of fragment size distribution plays a curtail role in forming the internal structure of a planetesimal. ii) There are two size regimes of planetesimal, first the regime of small size planetesimal 1 – 100 km and second is the regime large size planetesimals 100 – 1200 km. iii) Simulations show that the pebble fragmentation model is more effective in the regime of large size planetesimals and would be invalid for the planetesimal smaller than 10 km.
iv) And the longest time required to form a planetesimal in about 170 years and the shortest time is about 25 years, which is in accordance with the rapid planetesimal formation scenario, as predicted by the studies on streaming instabilities.

Zusammenfassung

Was ist eine Sternschnuppe?

„Ein Sternschnuppe ist ein Feuerball, der zu Satan geworfen wird, wenn er dem Gespräch zwischen Gott und Engeln lauscht“. Das wurde zu mir in meiner Kindheit erzählt. In anderen Kulturen wurde ein Sternschnuppe als göttliche Gabe betrachtet. Beispielsweise: Die Griechen bewahrten die heiligen Steinen im Tempel der Venus auf. Der schwarze Stein in Mekka ist für die Muslime heilig, weil es geglaubt wird, dass er vom Himmel zu kommt. Durch alle Zeiten und Kulturen haben Sternschnuppen, heute besser bekannt als Meteoroiden, unsere Vorfahren fasziniert. Sie haben versucht, Erklärungen und die Bedeutung zu dieser Gegenstände auf der Grundlage ihrer Fantasie zu liefern. Heute sind wir von der gleichen Neugier getrieben, die unsere Vorfahren hatten. Und für uns sind diese Gegenstände genau so faszinierend und wichtig. Aber der Unterschied ist, dass sie sie in Tempeln aufbewahrten und wir aufbewahren in Laboratorien und Museen. Heute versuchen wir, die alten Fragen zu beantworten, z.b, was sind die Meteoroide, woher kommen sie, wie wurden sie gebildet und noch wichtiger ist, was ist unsere Beziehung zu denen.

Meteoroide bestehen aus Staub und Eis und sie gelten als der Baustein der Planeten. Heute befinden sich diese im Kuiper-Gürtel und in der Ortschen Wolke. Die sind eigentlich den Überreste aus der kataklysmischen Geburt unseres Sonnensystems, das vor etwa 4,5 Milliarden Jahren stattfand. Es gibt überzeugende Beweise, dass unsere Erde und andere Planeten aus submikrometergroßen kosmischen Staub bestanden sind. In Laboratorien, das Wachstum von Mikrometergroßen Staub wurde auch beobachtet, das vermutlich geht weiterhin bis zu Millimeter bis zu wenige Zentimeter Kieselsteine. Doch was wir nicht verstehen, ist, wie die cm-große Kieselsteine bis zu dem Körper wachsen könnten, dass die Schwerkraft ausreicht um den weiten Wachstumsprozess, zu übernehmen, dann der Körper heißt Planetesimal. Dies ist einer der fehlenden Links in der Geschichte der Planetenentstehung. In den letzten zehn Jahren wurden einige interessante Ideen vorgeschlagen, die den fehlenden Link zu dieser Geschichte bieten. Eine dieser Ideen ist die Verbindung von Streaming Instability (SI) und Gravitational Instabiliy (GI). Die Streaming instabilität erklärt, wie aus Kieselsteinen ein Schwarm an Kieselstein gebildet weden kann, der genug Masse haben, um gravitativ instabil zu werden. Dieser gravitative Kollaps ist der letzte Schritt der Entstehung von Planetesimalen.

Die Motivation dieser Arbeit ist, zu betrachten, was während eines solchen Gravitationskollapses geschehen würde. Wie wird es geschehen? Es wird, mit der Hilfe von Experimenten und numerischen Simulationen, die zwei Ziele dieser Arbeit, erreicht werden. Das erste Ziel ist es, eine experimentelle Studie, um ein großes Modell der Kiesel-Fragmentierung zu entwickeln. Und das zweite Ziel ist die Anwendung dieses Modells durch die Entwicklung eines numerischen Codes. Die Aufgabe der Codeentwicklung wurde ausgelagert und nur die Ergebnisse der numerischen Modelle wurden eingearbeitet und diskutiert. Die experimentelle Studie nutzt die Kollisionsparameter (1 cm – 5 cm Kieselgröße

und 1 – 8 $\mathrm{ms^{-1}}$ Kollisionsgeschwindigkeiten), die von den Studien zur Streaming Instabilität vorgeschlagen wurden. Somit ist nicht nur ein anfänglicher parametersatz für die Experimente gewählt, sonder die Ergebnisse ermöglichen auch, Vorhersagen zu SI zu validieren.
Durch die Analyse von 142 Experimenten von Kieselkollisionen wurden drei Hauptmodelle entwickelt. Das erste ist das Modell der Fragmentierung Stärke, das, die drei wichtigsten Kollisionsergebnisse, die Fragmentierung, die Stoffübertragung und der Abprallen erklärt. Das zweite ist das Modell der Wahrscheinlichkeitsfunktion des Stoffübertragung, der die Wahrscheinlichkeit des Wachstums bestimmt. Es zeigt dass die Wahrscheinlichkeit des Stoffübertragung bis zur Einheit erreichen kann, wenn das Größenverhältnis zwischen den beiden Kieseln 5,8 beträgt. Das dritte ist das komplette Modell für die Fragmentgrößenverteilung. Das kombinierte Ergebnis der experimentellen Studie ist das so genannte Grand-Pebble-Fragmentierungsmodell, das aus mehreren konstitutiven Modellen besteht, was die unterschiedlichen Regeln der Kiesel-Wechselwirkungen während eines Gravitationskollapses bestimmt.

Das zweite Ziel dieser Studie ist die Durchführung dieses Modells. Da es praktisch nicht möglich ist, Millionen von Kollisionen in einem Labor durchzuführen, wurde von Kollegen im Lund-Observatorium in Schweden ein numerische Code entwickelt, um den Gravitationskollaps zu simulieren. Die Ergebnisse der numerischen Modelle zeigen: i) dass das Modell der Fragmentgrößenverteilung eine wichtige Rolle bei der Bildung der inneren Struktur eines Planetesimals spielt. ii) Es gibt zwei Größenregime der Planetesimale, zuerst das Regime der kleinen Planetesimale 1 – 100 km und zweitens das Regime großer Planetesimale 100 – 1200 km. iii) Simulationen zeigen, dass das Kieselfragmentierungsmodell im Regime von großen Planetensimalen wirksam ist und für den Planetesimale kleiner als 10 km ungültig wäre. iv) Und die längste erforderliche Zeit, um ein Planetesimal zu bilden, ist ungefähr 170 Jahren. Die kürzeste Zeit ist ungefähr 25 Jahre; die stimmt mit den schnellen Planetesimalausbildungsszenario überein, wie durch die Studien zur Streaminginstabilität vorhergesagt.

Chapter 1: Introduction

1.1 The question for a motivation
1.2 State of the art: Two Possible solutions
1.3 How this work can contribute?
1.4 Time frame and the road map
1.5 Results of this study

1.1 The question for a motivation

The process of planet formation can be seen in three distinct stages. The first stage is when a micron size interstellar dust grains grow to a few centimetres pebbles. In the second stage, centimetre-sized pebbles grow to a few hundred-kilometres sized planetesimals. In the third stage, these planetesimals have enough gravity to accrete the other planetesimals of similar size and grow into a giant planetary core. Therefore planetesimals are considered as building block of planets.

But the question is about the second stage, how do the cm-sized pebbles evolve into a planetesimal? The answer to this question is not straight forward. Different possibilities to form planetesimal are being discussed and this discussion is the context of this thesis.

As far as the first stage of pre-gravity aided growth is concerned, a broad consensus is found among the modellers and experimentalists. In this phase the micron-sized silicate grains sediment to the midplane of the protoplanetary disk. During sedimentation, the grains have Brownian motion (~10^{-4} $\mathrm{ms^{-1}}$) and as they collide with one another, they stick together by surface adhesion (due to Van der Waals force) (see e.g. Blum et al. (1996), (1999) and Kempf et al. (1999)) and they can grow up to aggregates of 100 μm, in about 1000 years (Windmark et al. 2012a) and they have been observed as well (Williams & Cieza 2011). These aggregates have fractal structure and when they collide with other fractals, they stick well and this is so called "hit and stick" regime. At this stage these aggregates are relatively porous (~ 85%) and further collisions lead to compaction (Zsom et al. 2010).

However the problem arises, when the porous aggregates collide with each other the outcome is bouncing, which leads to compaction (Dominik & Tielens 1997). Zsom et al. (2010) showed that after a few thousand years growth of the particles slows down because of bouncing collisions. The bouncing collision have been observed in experiments by Langkowski et al. (2008), Beitz et al. (2011) and Weidling et al. (2012). These studies show that the simple and straight forward mechanism of hit and stick reaches its limit when the dust grains of a few microns have been converted into pebbles of several centimetres in size. The numerical simulations, based on these experiments, e.g., by Zsom et al. (2010) and Windmark et al. (2012a), suggest that dust growth is stopped by the so called "bouncing barrier" rather by fragmentation. Since the grains get locked into cm-sized aggregates which get stuck in bouncing, the disk suffers small grain-depletion. In addition to grain-depletion, another threat surmounts, which is the radial drift velocity due to gas drag (Whipple (1972) and Weidenschilling (1977)). As the aggregates grow in size, their drift velocity increases proportionally and becomes the major contributor of the relative velocities v_{rel} (details in Sec. 2.3). The centimetre-sized pebbles are large enough to experience a significant drift velocity, (on the order 10^5 magnitude higher than the Brownian motion) which goes beyond the fragmentation threshold velocity ($\sim 1\ \mathrm{m\,s^{-1}}$) of the aggregate. If a pebble would grow to metre-sized boulder, then for such a body drift velocity reaches to $\sim 100\ \mathrm{m\,s^{-1}}$ (Weidenschilling 1977) and the collisions at these velocities obviously result in catastrophic fragmentation (Dullemond & Dominik 2005), (Blum & Wurm 2008). The pebbles which avoid the fragmentation, can easily be removed from the disk (Takeuchi & Lin 2002) and (Brauer et al. 2007) (2008).

If the velocities are low then 1) the bouncing barrier and the grain-depletion is a problem and if velocities are high then 2) the fragmentation barrier hinders the growth. If somehow both are avoided then the 3) radial drift sweeps the pebbles into the star. In this way the initial phase of growth comes to halt.

Since the formation of planets spans over 40 orders of magnitude in mass (Zsom et al. 2010), therefore for any single mechanism it is difficult to sustain the dust growth up to this scale. Hereafter growth proceeds rather on a complicated track. In order to avoid the bouncing barrier and fragmentation barrier, a mechanism is required which accounts the complex collision behaviour, i.e. direct hit and stick process, bouncing and fragmentation with mass transfer (MT). Above all it has to be fast enough to avoid the radial drift.

1.2 State of the art: Two possible solutions

In the debate of planetesimal formation, there are two leading proposals to solve these problems. One relies on the classical scenario of binary collisions resulting in coagulation and fragmentation. Whereas the second invokes the streaming instabilities (SI) to trigger the gravitational collapse of a swarm of centimetre sized pebbles.

1.2.1 Classical scenario of planetesimal formation (sweep-up)

The principal idea behind the classical scenario of planetesimal formation is binary collisions. The dust growth models based on binary collisions look for the collision parameters, such as size of the colliding binaries, their porosity and collision velocities, which are suitable for dust growth. In the pursuit of the optimum collision parameters a vast amount of experimental data has been generated over the past two decades. The details of these experiments are well discussed in Blum & Wurm (2008). Later Güttler et al. (2010) gathered the experimental data and put forward a set of collision parameters, which were implemented by Zsom et al. (2010)

in a simulation for different disc models including the MMSN (minimum mass Solar nebula, discussed in Sec. 2.1.1).

Güttler et al. (2010) showed that every binary collision has one of the 9 possible collision outcomes, see Table 1.1. They suggested that the growth as a result of binary collisions can be continued if the particles of different sizes or porosities participate in collision. It is very likely that both options (difference in sizes or porosity) can yield the same result, i.e. the fragmentation with mass transfer. Now, a mechanism is required which could counter the radial drift and locally confine the particles to grow further.

Windmark et al. (2012) proposed that the bouncing barrier can be used to generate a reservoir of particles, which would provide a wide range of size distribution. It allows the micron-sized monomers in binary collisions to grow up to few-millimetres-sized pebbles and then to fragment down to $\sim 100\ \mu$m grains.

Table 1.1. A summary of the nine possible collision outcomes as described in Güttler et al. (2010) which are observed in experiments. It is expected that the collision outcome S4 is analogous to F3, the same collision outcome could be achieved either by varying porosity or varying the size ratio, though it is neither experimental nor numerically tested. For the frequency of the events see Zsom et al. (2010).

Sticking	Bouncing	Fragmentation
Hit and Stick (S1): more likely for the grains of similar size at low velocities (on the order of Brownian motion), during the early sedimentation phase of PPD ~ 10^4 years.	**Bouncing with compaction (B1):** effective for highly porous pebbles (mm-cm-sized) at low $v_{\mathrm{rel}} \leq 1$ m s^{-1}. Starts from late sedimentation to late drift phase.	**Fragmentation (F1):** it is more likely to happen when size ratio is low, $f \sim 1$, and $v_{\mathrm{rel}} > 10$s m s^{-1}. Probably in midplane when drift velocities are dominant.
Sticking by surface effects (S2): it is effective for the aggregates of size >100 μm, which leads to fractal growth at velocity $v_{\mathrm{rel}} < 1$ m s^{-1}. It is more likely to happen in late sedimentary growth phase to early drift phase.	**Bouncing with mass transfer (B2):** it is more likely to happen when relatively a compact projectile hits a porous target and accretes mass of it and bounces back, at $v_{\mathrm{rel}} \geq 1$ m s^{-1}. Starts from late sedimentation to late drift phase.	**Erosion (F2):** it is effective when size ratio is very high $f > 100$ and velocities are high as well (e.g. ~ 100 μm projectile vs cm-m-sized target) at high $v_{\mathrm{rel}} \geq 10$s of m s^{-1}. During high radial drift and dust has wide size distribution.
Sticking by impinging (S3): it happens when relatively a compact projectile (~1 mm) penetrates a porous target (~ 1 cm), at velocity ~ 2 m s^{-1}. It is effective during the sedimentation when the size of particles and their porosities have wide range.		**Fragmentation with mass transfer (F3):** becomes effective for size ratio $f > 6$, at intermediate velocities $v_{\mathrm{rel}} < 10$ m s^{-1}.The outcome is likely to be same as S4, but it would happen in late phase, when radial drift and particle sizes are high enough, within snow line.
Partial sticking in fragmentation (S4): in this case a porous projectile collides with a compacter target, and fragments but transfers a fraction of its mass to target. Threshold velocity is ~1 m s^{-1}. It is likely to happen parallel to S3		

They artificially added cm-sized pebbles into size distribution and showed that a few lucky cm-sized pebbles can sweep-up the fine dust and can thus grow up to several hundred-metre sized boulders, the size which is enough for gravity to overtake the rest process of growth.

Later Drążkowska et al. (2013) suggested that the pressure bumps (caused by the abrupt decline of turbulent viscosity near the snow line) can be utilised for the confinement of particles. Once particles are trapped, the sweep-up process comes in action, which can convert the pebbles into planetesimals.

Although the both authors use different mechanisms for the confinement of particles, however they rely on the continuity of the binary collisions between the aggregates of high size (or mass) ratios. With this approach the required timescale for the formation of a few hundred metres boulder is 10^6 years (Windmark et al. 2012), which is rather slow if the radial drift has to be avoided.

Although it has been well proven that in the collisions that result in fragmentation with mass transfer, the target aggregates accretes a significant mass of the projectile, however by this process the formation of planetesimals of kilometre sizes faces severe problems, such as the rather large timescales required (Windmark et al. 2012) and (Johansen et al. 2014), the role of counter-acting erosion (Schräpler & Blum 2011), and fragmentation in collisions between similar-sized planetesimals (Song et al. 2005).

In this scenario Johansen & Youdin (2007) proposed a planetesimal-formation model relying on particle concentration and self-gravity. They showed that the streaming instability, first described by Youdin & Goodman (2005), is capable of concentrating pebble-sized dust aggregates such that planetesimals can directly form by gravitational instability.

In the following, a short description about streaming instability as an alternative mechanism for particle concentration which leads to the formation of planetesimals, has been given. However the topic will be thoroughly discussed in Sec. 2.4.

1.2.2 Streaming instability leading to gravitational collapse

Streaming instability is considered an effective way for the formation of planetesimals (Youdin & Goodman 2005), which exploits the aerodynamic relation between gas and dust and accumulates pebbles in a very novel way. Streaming instability relies on the idea if gas drags the dust particles, then by Newton's third law, dust particles also drag the gas in opposite direction. As a result of momentum transfer from dust to gas, gas locally moves close to Keplerian velocity (Johansen et al. 2007). This process reduces the headwind for dust particles and consequently it reduces the loss in their angular momentum which in turn reduces the radial drift. The loss of angular moment for a clump of dust is less as compared to an isolated pebble. As a result a clump moves faster than an individual pebbles, therefore a clump catches the isolated pebbles and grows in size.

Youdin & Johansen (2007) and later Johansen & Youdin (2007) showed that particle clumping reduces energy dissipation which slows down the radial drift and as a result

particles start clumping by "creating a local traffic jam" which allows the clump to grow rapidly. SI is more effective for the larger aggregates (mm-cm sized), which are marginally coupled to the surrounding gas and can be easily integrated into clumps.
Johansen et al. (2009) analysed the collision process in such a clump, which consisted of pebbles of Stokes number (details in Sec. 2.2.1) St = 0.1 to St = 0.4 (correspond to few decimetres size boulders around 1 AU (Johansen et al. 2014)). They found low collision speeds, from 0.5 m s^{-1} to 5 m s^{-1}, which can be easily tested in experiments. Afterward several studies on streaming instability e.g., Bai & Stone (2010), Johansen et al. (2012) and Carrera et al. (2015) have shown that there is a possibility of forming planetesimals of several 100 km in size from dust aggregates of Stokes numbers in the range St = 0.01 to St = 1 within the radii 1–10 AU. At 1 AU, this range of Stokes numbers corresponds to centimetre to meter-sized dust aggregates in a MMSN-model (see Sec. 2.1.1).

Later Johansen et al. (2012) showed that SI can raise the local particle density to 10^3 times above the midplane gas density at 3 AU. If the particle density goes beyond the Roche density ($\rho_R \sim 100\, \rho_g$) the self-gravity becomes relevant (Johansen et al. 2009) and gravitational collapse can be initiated. Another advantage of streaming instability is, it is very time efficient, on the timescale of a few orbits, it can convert a swarm of cm-sized pebble into a dwarf planet of the size of Ceres, as described in Johansen et al. (2007). And more recently Jansson & Johansen (2014) have analysed a collapse of a pebble cloud at 40 AU and they found that the collapse requires about 25.1 years to form a planetesimal of size of a few 100 km.

This range of pebble size and the velocities involved in above mentioned studies are quite feasible for experimentalists to test in laboratory.

1.3 Fragmentation with mass transfer

In the process of planetesimal formation by collisions, whether it takes place by the classical approach or by the streaming instability, fragmentation with mass transfer (MT) is the desired collision outcome. MT is a very probable collision outcome when the colliding binaries have either different size (or mass) ratio f or different porosities.
In this study the smaller of the two aggregates is called projectile, denoted by P and the larger aggregate is called target denoted by T. The collision which result in MT, this is the projectile which necessarily fragments and transfers a fraction of its mass to the target aggregate. The collisions in which the size ratio is high enough $f \geq 10$ the projectile can transfer 100% of its mass to target (Windmark et al. 2012a). The phenomenon is known as "sweep up".

Since 2005 growth by fragmentation with mass transfer is being studied in laboratories, e.g. first reported by Wurm et al. (2005) and then Teiser & Wurm (2009) observed growth for very different sizes (sub mm-cm) aggregates at higher velocities (~ 55 m s^{-1}). Afterwards Kothe et al. (2010) experimentally studied the MT between mm-sized pebble and infinite target. In addition to this, Beitz et al. (2011) showed that MT can occur for the same size (2 cm) aggregates as well if the velocities are low enough (~ 0.2 m s^{-1}, the range predicted in Johansen et al. (2009)).

And more recently Deckers & Teiser (2014) observed growth in the collisions between centimetre to decimetre size aggregates. The projectile aggregate can transfer up to 50% of its mass to the target aggregate (Wurm et al. 2005b), if the impact velocities are below the catastrophic threshold for the mass ratio of concern.
The same phenomenon has been observed in numerical simulation as well. For example, Garaud et al. (2013) wrote "MT in high-mass-ratio collision boosts the growth of the larger particles beyond the fragmentation barrier".

In numerical simulation the collision between high size ratios resulting in 100% MT has been studied as well. For example, Johansen et al. (2008) presents a two-species model in which they used to study the interaction between dust grains and cm-sized boulders with the inclusion of turbulence. They showed that the cm-sized pebbles by sweeping-up the small grains can grow as quickly as few mm per year. As mentioned before Windmark et al. (2012) have suggested the use the sweep-up of grains by a cm-size pebble as a solution to cross the bouncing barrier.

The fragmentation with mass transfer can be effective and efficient way to a further growth, for any mechanism which hinders the drain of the grains (radial drift), whether it is done by confining the turbulence in the mid-plane as suggested by Weidenschilling (1997), or by creating pressure bumps (Whipple 1972).

1.4 How this work can contribute?

This study has two major scientific goals.

1. The first goal is an experimental study, to develop of a pebble fragmentation model in the context of streaming instability. The overall contribution of such a model can be summarised as follow:

- Being inspired from the recent studies on gravitational collapse induced by streaming instabilities conducted by Youdin & Johansen (2007), Johansen & Youdin (2007), Johansen et al. (2007) and Johansen et al. (2009), (2012), one can experimentally simulate the collision scenario in which the particle clumping occurs and the collision parameters discussed in above mentioned studies can be tested.
- By analysing the collision experiments, a model will be developed to explain the outcomes such as fragmentation with mass transfer, catastrophic fragmentation and bouncing.
- According to the recent experimental studies by Wurm et al. (2005b), Teiser & Wurm (2009), Kothe et al. (2010) and Deckers & Teiser (2014) the target aggregate can grow significantly in the collisions of different size ratios. Here it is intended to develop an experimental model of a probability function which would predict when a given target will survive and when it will fragment.
- Developing a realistic fragment size-distribution (which has been obscure in recent collision studies) would shed light on the internal structure of the planetesimal and

answer whether the possible dust-aggregate fragmentation leads to a depletion of dust. The shape of the size-distribution affects the density of the planetesimal.

- By analysing the velocities of the fragments (produced a as result of collision) a new model for the fragment-velocity distribution can be developed, which would be useful for the future studies.

2. And the second goal of this study is the execution of the fragmentation model by developing a numerical simulation.

As described in Blum et al. (2011) the numerical studies of protoplanetary disks are global in nature and mostly the dust-rich regions can not be spatially resolved, therefore one can not make a reliable prediction about the interaction of dust aggregates. However by using the numerical simulation, which will be validated by the experimental results, can contribute in the following ways:

- The simulation will help to visualise what happens during the collapse, how the pebbles of different size ratios at the given velocities interact and what the outcome of these interactions are.
- This study is expected to reveal whether the formation of planetesimals in the frame of streaming instabilities is feasible and what would be the size of the expected planetesimal and how its internal structure will be.
- In addition, with the help of numerical simulations the limitation of the experimental model would be determined.

It is important to mention that the second goal will be accomplished by the colleagues at Lund Observatory, Sweden. Some of the unpublished results will be presented and discussed here.

1.5 Time frame and the road map of the thesis

The above mentioned goals have been successfully achieved within the time frame of 3 to 4 years in following steps.

Step 1: Building the drop tower (2012-2013)

In the first year a new experimental setup was constructed. Thanks to the already existing setup used by Beitz et al. (2011), it provided the blue prints for the new drop tower. The details will be discussed in Chapter 3.

Step 2: Calibration and data acquisition (2013-2014)

In the new drop tower, first the desired set of collision parameters were calibrated. Once the setup has been tuned, experiments were performed and the data was taken. Since the raw data was in the form of images, an algorithm had to be developed for image analysis. For the analysis of images the free software ImageJ (Fiji) has been used, where the extracted data has been analysed by Origin 9.0. All the fit values and the respective error values have been estimated by this software.

Step 3: Data analysis and modelling (2014-2015)
This is the first study in which the mass ratio of the colliding binaries has been systematically studied which varies from 1 to 126. By using the experimental data, the grand pebble fragmentation model was developed which can predict the collision outcome and can explain the fragment's size distribution. The experimental model will be used in numerical simulation to analyse the gravitational collapse which leads to the formation of planetesimal.

Step 4: Establishing collaboration with Lund Observatory (2015-2016)
For the execution of the model a collaboration with the numerical group at Lund Observatory in Sweden was established. They developed a Monte Carlo code to simulate a gravitational collapse of a pebble cloud. In which pebbles follows the rules of collision set in laboratory.
Here in Sec. 4.10.1 the results of the simulation will be presented and discussed.

Step 5: Publishing the results of experimental study and numerical simulation (2016)
Our colleagues in Lund have successfully demonstrated that the laboratory work, when implemented in the context of streaming instabilities, can provide a mechanism which can explain how the centimetre-sized pebbles can grow into a planetesimal of a few-100 km. The results of experiments and numerical simulations have been published in the two companion papers, which are mentioned in the section of Publications.

1.5.1 Thesis writing (2016)

The parallel goal of this project has been to produce a doctoral thesis, which includes not only the published results but also sheds light on the aspects which have not been the part of publications. In addition to this, a model of fragment-velocity distribution will be presented. This thesis consists of the following chapters:

Chapter 1: In this chapter the motivation, scientific goals and the context of this study will be discussed.
Chapter 2: A general overview of protoplanetary disc, the process of dust evolution and the possible scenario of planetesimal formation via gravitational collapse will be discussed.
Chapter 3: The newly build experimental setup and its details will be presented.
Chapter 4: In this chapter the result of experimental and numerical study will be presented and discussed.
Chapter 5: Discussion on the model and its astrophysical implications and the conclusion will be discussed.

Chapter 1: Introduction

1.1 THE QUESTION FOR A MOTIVATION 1

1.2 STATE OF THE ART: TWO POSSIBLE SOLUTIONS 2

1.2.1 CLASSICAL SCENARIO OF PLANETESIMAL FORMATION (SWEEP-UP) 2

1.2.2 STREAMING INSTABILITY LEADING TO GRAVITATIONAL COLLAPSE 4

1.3 FRAGMENTATION WITH MASS TRANSFER 5

1.4 HOW THIS WORK CAN CONTRIBUTE? 6

1.5 TIME FRAME AND THE ROAD MAP OF THE THESIS 7

1.5.1 THESIS WRITING (2016) 8

Bibliography

Bai, X.-N., & Stone, J. M. 2010, The Astrophysical Journal, 722, 1437

Beitz, E., Güttler, C., Blum, J., Meisner, T., Teiser, J., & Wurm, G. 2011, The Astrophysical Journal, 736, 34

Blum, J., Bodenschatz, E., Wagner, C., & Xu, H. 2011, in (TU Braunschweig, University of Goettingen: DFG/SFB 963), 24

Blum, J., & Wurm, G. 2008, Annu Rev Astron Astrophys, 46, 21

Blum, J., Wurm, G., Kempf, S., & Henning, T. 1996, Icarus, 124, 441

Blum, J., Wurm, G., Poppe, T., & Heim, L.-O. 1999, in Laboratory astrophysics and space research (Springer), 399

Brauer, F., Dullemond, C., & Henning, T. 2008, Astronomy & Astrophysics, 480, 859

Brauer, F., Dullemond, C., Johansen, A., Henning, T., Klahr, H., & Natta, A. 2007, Astronomy & Astrophysics, 469, 1169

Carrera, D., Johansen, A., & Davies, M. B. 2015, arXiv preprint arXiv:150105314

Deckers, J., & Teiser, J. 2014, The Astrophysical Journal, 796, 99

Dominik, C., & Tielens, A. 1997, The Astrophysical Journal, 480, 647

Drążkowska, J., Windmark, F., & Dullemond, C. 2013, Astronomy & Astrophysics, 556, A37

Dullemond, C., & Dominik, C. 2005, Astronomy & Astrophysics, 434, 971

Garaud, P., Meru, F., Galvagni, M., & Olczak, C. 2013, The Astrophysical Journal, 764, 146

Güttler, C., Blum, J., Zsom, A., Ormel, C. W., & Dullemond, C. P. 2010, Astronomy & Astrophysics, 513, A56

Jansson, K. W., & Johansen, A. 2014, Astronomy & Astrophysics, 570, A47

Johansen, A., Blum, J., Tanaka, H., Ormel, C., Bizzarro, M., & Rickman, H. 2014, arXiv preprint arXiv:14021344

Johansen, A., Brauer, F., Dullemond, C., Klahr, H., & Henning, T. 2008, Astronomy & Astrophysics, 486, 597

Johansen, A., Oishi, J. S., Mac Low, M. M., Klahr, H., Henning, T., & Youdin, A. 2007, Nature, 448, 1022

Johansen, A., & Youdin, A. 2007, The Astrophysical Journal, 662, 627

Johansen, A., Youdin, A., & Mac Low, M.-M. 2009, The Astrophysical Journal Letters, 704, L75

Johansen, A., Youdin, A. N., & Lithwick, Y. 2012, Astronomy & Astrophysics, 537, A125

Kempf, S., Pfalzner, S., & Henning, T. K. 1999, Icarus, 141, 388

Kothe, S., Güttler, C., & Blum, J. 2010, The Astrophysical Journal, 725, 1242

Langkowski, D., Teiser, J., & Blum, J. 2008, The Astrophysical Journal, 675, 764

Schräpler, R., & Blum, J. 2011. in EPSC-DPS Joint Meeting 2011, Erosion of large aggregates in protoplanetary disks as a source of micrometer-sized particles, 6

Song, I., Zuckerman, B., Weinberger, A. J., & Becklin, E. 2005, Nature, 436, 363

Takeuchi, T., & Lin, D. 2002, The Astrophysical Journal, 581, 1344

Teiser, J., & Wurm, G. 2009, Monthly Notices of the Royal Astronomical Society, 393, 1584

Weidenschilling, S. 1977, Monthly Notices of the Royal Astronomical Society, 180, 57

---. 1997, icarus, 127, 290

Weidling, R., Güttler, C., & Blum, J. 2012, Icarus, 218, 688

Whipple, F. L. 1972, In From Plasma to Planet (A. Elvis, ed.: Wiley, New York)

Williams, J. P., & Cieza, L. A. 2011, arXiv preprint arXiv:11030556

Windmark, F., Birnstiel, T., Güttler, C., Blum, J., Dullemond, C. P., & Henning, T. 2012, Astronomy & Astrophysics, 540, A73

Windmark, F., Birnstiel, T., Ormel, C., & Dullemond, C. 2012a, Astronomy & Astrophysics, 548, C1

Wurm, G., Paraskov, G., & Krauss, O. 2005, Physical Review E, 71, 021304

---. 2005b, Icarus, 178, 253

Youdin, A., & Johansen, A. 2007, The Astrophysical Journal, 662, 613

Youdin, A. N., & Goodman, J. 2005, The Astrophysical Journal, 620, 459

Zsom, A., Ormel, C., Güttler, C., Blum, J., & Dullemond, C. 2010, Astronomy & Astrophysics, 513, A57

Chapter 2: Protoplanetary disc and dust growth

2.1 Protoplanetary disc
2.2 Planetesimal
2.3 Relative velocities
2.4 Streaming and Gravitational instabilities

The structure of this chapter is based on the lecture notes of Armitage 2014.

2.1 Protoplanetary disc

The nebular hypotheses can be traced back to 18th century philosopher Kant 1755 (also one of the pioneers of eugenic anthropology (Kleingeld 2007) (Bernasconi 2002)) and to Laplace 1796. They argued gaseous clouds—nebulae, which slowly rotate, gradually collapse and flatten due to gravity and eventually form planets in circular and coplanar orbits around the Sun (Youdin & Kenyon 2013).

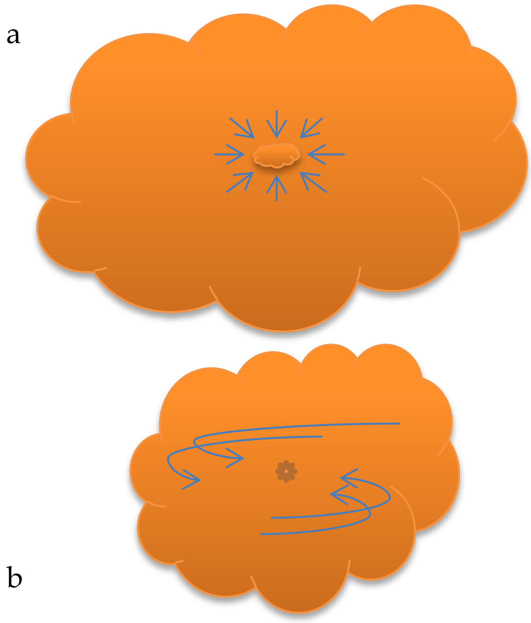

Figure 2.1 (a) The initial phase, when gas accretes directly onto the core, but this phase does not last long. **(b)** As the cloud shrinks more distant material has been brought to the core, which also brings a higher angular momentum. Hence the direct accretion is replaced with spiral accretion. The length of the arrows shows the magnitude of angular momentum and the trajectory of the in falling gas.

Since then this concept has been evolving and today there are observational evidence that planets do form around stars in a circular disc called protoplanetary disc.

The process of star formation sets in as the giant molecular cloud (GMC) meets the Jeans mass criterion and starts to fragment into the filamentary structures (due to magnetic field) of high dense regions of gas and dust.

In a molecular cloud, dense and small scale cores, spanning over 0.1 pc, have relatively higher velocity gradient up to $1\ \mathrm{km\,s^{-1}pc^{-1}}$ (Armitage 2014) as compared to that of the atomic gas (0.02 to $0.07\ \mathrm{km\,s^{-1}pc^{-1}}$) of the molecular cloud (Imara & Blitz 2011). At this stage, the angular momentum of the core $J_{\mathrm{core}} \sim 10^{54}\ \mathrm{g\,cm^{2}s^{-1}}$ is much higher than that of our present solar system $J_{\mathrm{A}} \sim 10^{48}\ \mathrm{g\,cm^{2}s^{-1}}$ (the rotational energy due to the higher angular momentum is merely a few percent of the gravitational energy; hence it can not inhibit the core-contraction).

It suggests that an efficient mechanism had been in action which has transferred a large fraction of angular moment out of the system. The problem is known as the "angular momentum problem" of star formation. In this scenario the formation of a disc structure, besides the outflows, is considered to be the effective way for the transportation of angular momentum.

Initially a molecular cloud collapses directly onto the point source as shown in Figure 2.1(a). However this process is immediately interrupted because the process of gas settling onto the core becomes slower than the gas being accreted from the cloud. As the more distant material arrives at the core, the higher angular momentum it gains (Williams & Cieza 2011). When the incoming gas of very high angular momentum encounters the slow gas near the core, it gives rise to accretion shocks at the interface, which helps to reduce the angular moment. If the incoming packet of gas is desired to be the part of the core, it must reduce its angular moment to the centrifugal radius of the core. As a result the incoming gas follows a spiral trajectory around the protostellar object, as shown in Figure 2.1(b). The advantage of spiral inflow over the straight infall is: the gas, owing to friction induced by ionic viscosity, loses angular momentum and slows down. Due to the vertical gravitational component of the protostar, all the trajectories of gas flow are pulled toward the equatorial plane of the protostar and within a few 10^{5} years a disc-form appears. Since this site is associated with the formation of planets, therefore it is called protoplanetary disc.

The size of the protoplanetary disc depends on how long the gas is accreted from the molecular cloud and the Keplerian angular frequency Ω_{K} (defined in eqn. (2.9)) of the core, as given in (Williams & Cieza 2011)

$$R(t) \propto \Omega_{\mathrm{K}}^{2} t_{\mathrm{acc}}^{3} \ , \tag{2.1}$$

where t_{acc} is the accretion time. Observations show that most young (~ 1 Myr) stars embedded within molecular clouds are surrounded by circumstellar accretion discs (Carpenter et al. 2006). Since the dusty protoplanetary discs are believed to be the birthplace of planetary systems, they have been the subject of intense observational interests in recent years (Dullemond et al. 2006).

2.1.1 SED of Young Stellar Objects

The young stellar objects (YSOs) can be identified by their typical SED (spectral energy distribution) curve. In mid 1940s T Tauri stars (TTSs) were identified as pre-main sequence stars (Joy 1945). In later observations the YSOs have been found to exhibit a strong emission at wavelength range from NIR (near-infrared) to millimetres (Rucinski 1985) (Fang 2011), which could be explained only by an extended structure close to a protostar. Therefore YSOs are usually classified by the spectral index α_{IR}, which is the slope of SED curve above 1 micron, as shown in Figure 2.2, and the slope is given as in Armitage (2014)

$$\alpha_{\mathrm{IR}} = \frac{d\log(\lambda F_\lambda)}{d\log\lambda}\ , \tag{2.2}$$

where F_λ is the emitted flux at wavelength λ. The disc has temperature radial gradient, the hotter inner disc absorbs the light from the protostar and re-emits in infrared range, which is responsible for the flattening of SED above $\lambda \sim 1\ \mu$m. On the basis of spectral index α_{IR}, Lada (1987) classified the YSOs, which are summarised in the following by Williams & Cieza (2011) and Armitage (2014):

Class 0: $\alpha_{\mathrm{IR}} \sim 0$, SED peak $\lambda \sim 100\ \mu$m, no flux at NIR, still in collapse phase
Class I: $\alpha_{\mathrm{IR}} > 0.3$, peak MIR (mid-infrared) to FIR (far-infrared), embedded PPD still in envelope
Class II: $- 1.6 < \alpha_{\mathrm{IR}} < - 0.3$, accreting disc, H$\alpha$ und UV emission, called classical TTauri
Class III: $\alpha_{\mathrm{IR}} < - 1.6$, pre-main sequence no or weak accretion

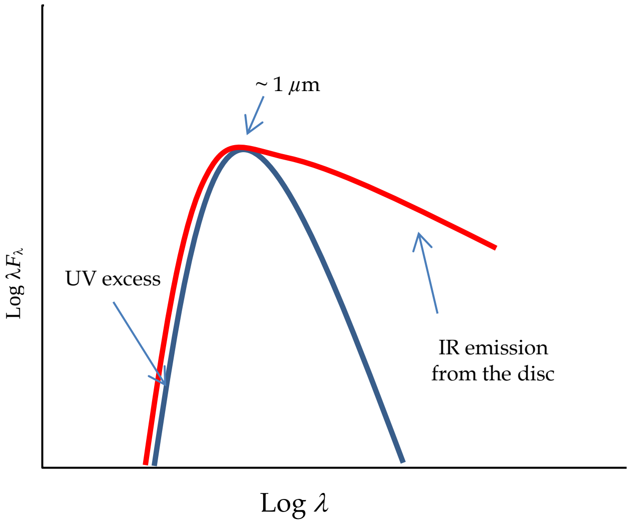

Figure 2.2 The schematic diagram of a typical SED curve of a YSO. The red curve associated with the disc, flattens above 1 μm, while the blue curve of stellar emission declines. The slope of the red curve is measured between 2.2 μm (K band) and 10 μm (N band). The slight ultra violet excess by the red curve is associated to the hot spots, the regions on stellar surfaces where gas is accreted from the disc (Armitage 2014).

Since the emission features evolve with time, so they can be correlated to different evolutionary phases. For example; the inner disc ~ 0.1 AU is associated with NIR emission. About 80% stars by the age of ~ 1 Myr show IR-excesses, which declines to 50% by the age 3 Myr. And by the age of 10 Myr the continuum infrared radiation vanishes, indicating the birth of an inner cavity. The millimetre emissions, which are associated with the outer and colder material of the disc, vanish by the age of 10-30 Myr (Klahr & Brandner 2006).

However it is important to mention that the above given classification based on SED does not provide the information about the amount and the distribution of disc material (Williams & Cieza 2011). Because it covers NIR to MIR range (IR excess), which declines with the age as gas is accreted onto the star (Carpenter et al. 2006). However the SED of sub-millimetre observations shows that protoplanetary discs have a broad distribution of dust masses (Wyatt 2008), where the column densities ρ are very high. Therefore the disc mass can be well determined by the amount of extinction in submillimetre band. At the given frequency ν, the relation between optical depth τ_ν and absorption coefficient κ_ν can be expressed as $\tau_\nu = \int \rho \kappa_\nu ds = \kappa_\nu \Sigma$, where Σ is the surface density (details in Sec. 2.1.3). A direct prescription for dust opacity at mm-wavelength is given in Williams & Cieza (2011) which reads

$$\kappa_\nu = 0.1\left(\frac{\nu}{10^{12}\ \mathrm{Hz}}\right)^{\beta} \mathrm{cm^2 g^{-1}}. \tag{2.3}$$

Here the power law index β[1] is a useful quantity which reveals information not only about grain size distribution but also about dust chemical composition, porosity and geometry. In general lower β -value ($\beta < 1$) is associated to larger grains ~ 1 mm (Testi et al. 2014).

The range of disc mass estimated, in the recent survey of sub/mm observation conducted by Ricci et al. (2011), spans over $0.003 - 0.1\ M_\odot$. These massive discs have been observed in outer region of ONC (Orion nebular cluster).

2.1.2 Observational evidence for grain growth

What do astronomical observations tell us about grain sizes? The most direct way to search for dust, is to trace the emission from stretching vibration of Si-O grains of size $a \leq 0.1\ \mu$m, the size typical to ISM (interstellar medium) (Klahr & Brandner 2006). These emissions are typically in NIR band at wavelength ~ 10 μm, which corresponds to a higher beta-index value $\beta_{\mathrm{ISM}} \sim 1.7$. Therefore when the surface of the discs are observed, one sees a wide range of thermal emission from the warm dust, ranging from NIR to mm wavelength along the radial length, which can be associated to wide range of dust grains, i.e. 1-10 μm. However IR-spectroscopy is useful only to probe dust grains of few microns (Natta et al. 2006). For example van Boekel et al. (2004) showed that as the grains grow to a few microns, e.g. 2 μm, the typical emission feature around 10 μm gets a typical flat-top and the strength declines as well, which happens within a few Myr (Dullemond & Dominik 2005).

The general trend is, as grains grow in size, the scattered light becomes more isotropic and redder (Testi et al. 2014). However the major obstacles to the characterisation of grains in

---

[1] Here the spectral index beta is non-italic, not to be confused with italic-beta used in Sec. 4.7

discs are not associated with observational constrains, such as spatial resolution or sensitivity but from the physical structure of the discs (Natta et al. 2006). Because most of the grain growth takes place in the cold midplane of the disc, the region which is beyond the IR-spectroscopy, hence the only way to measure the properties of bulk mass is to observe at longer wavelengths. Interferometric observations, at millimetre to centimetre wavelengths, show that most of the primordial pebbles have grown to cm-size by the time the central star becomes optically visible (Natta et al. 2006). And lately Ricci et al. (2011) provided evidence for the presence of mm-sized pebbles in their sub/mm survey of ONC.

As discussed in the previous section that β is directly related to grain size, therefore all the surveys of discs conducted to date have the aim of characterizing the spectral index β. Pérez et al. (2012) performed a sub/mm multi-wavelength survey of protoplanetary disc surrounding pre-main sequence star AS 209, and analysed the dependence of beta-index along the disc radius. They showed that beta increases from $\beta \sim 0.5$ within 10 AU to the level of ISM $\beta \sim 1.7$ at ~ 70 AU. Such a low β is a strong evidence for the presence of pebbles as large as few centimetres, indicating higher growth activity in the inner regions of the disc.

2.1.3 Minimum Mass Solar Nebula

Since the initial conditions of the solar system are not fully understood and the exact mass of dust and gas present at that time is not known. However by observing the masses and compositions of the planets in the current Solar system, one can calculate the minimum amount of matter that must have been present in this disc 4.56 billion years ago. This leads to the well-known "Minimum Mass Solar Nebula" (MMSN) model (Weidenschilling 1977). MMSN is not a nebula but a protoplanetary disc which gives minimum mass of solid material to build 8 planets. The key ingredients of this model are the following:

The metallicity Z i.e. dust to gas ratio and its radial distribution.
Calculating the total mass of all planets.
Dividing the Solar System into annuli, which are filled by the mass for each planet.
It yields a characteristic gas surface density, given by

$$\Sigma_{\mathrm{g}}^{\mathrm{MMSN}}(r) = 1700\left(\frac{\mathrm{g}}{\mathrm{cm}^2}\right)\left(\frac{\mathrm{r}}{1\ \mathrm{AU}}\right)^{-3/2} \tag{2.4}$$

and for dust

$$\Sigma_{\mathrm{d}}^{\mathrm{MMSN}}(r) = 7\left(\frac{\mathrm{g}}{\mathrm{cm}^2}\right)\left(\frac{\mathrm{r}}{1\ \mathrm{AU}}\right)^{-3/2} \quad (\text{for } r > 2.7\text{AU}). \tag{2.5}$$

The surface density profile of the solar nebula is considered one of basic input parameters for any protoplanetary model (Desch 2007). Integrating eqn. (2.4) up to 30 AU leads to the disc mass 0.01 $M_{\odot}$, which is relevant to the mass estimated for circumstellar discs around other stars. At 1 AU the midplane gas density reaches to $\rho_{\mathrm{gas}} \approx 1.4 \times 10^{-9}$ g cm^{-3} (Zsom et al. 2010). Here the surface density relation $\Sigma \propto r^{-3/2}$ with radius is merely the model, not an actual relation. Later the model of Minimum Mass Solar Nebula has been updated by Desch (2007). They incorporated the "Nice Model" of planetary migration and proposed that the solar system started in a much more compact configuration, which leads to a steeper slope of the surface density profile

$$\Sigma_{\text{gas}}^{\text{MMSN}} = 5.1\times10^{4}\left(\frac{\text{g}}{\text{cm}^{2}}\right)\left(\frac{\text{r}}{1\ \text{AU}}\right)^{-2.2}. \tag{2.6}$$

By assuming the Gaussian distribution of gas in the midplane at 1 AU, one gets midplane density $\rho_{\text{gas}} \approx 2.7\times10^{-8}\ \text{g}\,\text{cm}^{-3}$ (Zsom et al. 2010), which is slightly higher than the one predicted by the classical MMSN. If "α-viscosity prescription" (details in Sec. 2.1.4) is accounted for, then the radial dependence is relatively shallower, i.e. $\Sigma \propto r^{-1}$ (Armitage 2014), which has observational support as well. For example Andrews et al. (2009) reported $\Sigma \propto r^{-0.9}$ in their submillimetre survey of circumstellar discs in the ~1 Myr-old Ophiuchus star-forming region. These results can be interpreted in the favour of a viscous disc scenario.

In general the mass of the disc can be derived from millimetre radiation emitted from dust, at about ~ 100 AU from central stars. By using the dust emission, one can calculate the mass of the dust and then by using solar dust-to-gas ratio the mass of gas can be estimated (Chiang & Youdin 2010). The disc models can be more precise if viscous heating, shadowing, optical depth and external heating are taken into account.

2.1.4 Disc structure

Since all the theories of planet formation are based on the structure of protoplanetary discs, it is crucial to discuss the radial and vertical aspects of the disc. By using the resolved observation and precise modelling of SED of relatively bright and large discs, the mean radial, vertical and velocity profiles can be estimated.

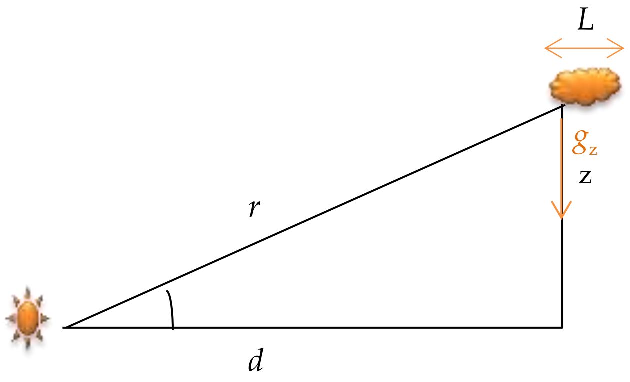

Figure 2.3 The schematic diagram for the gas packet of size L located at radius r. It has vertical distance z from midplane and g_z as vertical component of stellar gravity.

Let us assume, a packet of viscous gas of size L which is orbiting the star of mass M_* in a Keplerian fashion at radius r and has gravitational component g_z as shown in Figure 2.3.
Since the gas is viscous, due to friction within, it loses angular momentum and slides radially inward with velocity v_r such that

$$v_{\mathrm{r}} = -\frac{3\nu'}{4r}\ , \tag{2.7}$$

where ν' is the kinematic viscosity or better known as "α-viscosity prescription" introduced by Shakura & Sunyaev (1973) and as given in Armitage (2014)

$$\nu' = \alpha\frac{c_s^2}{\Omega_{\mathrm{K}}}\ , \tag{2.8}$$

here $\alpha \approx 10^{-3} \ldots 10^{-1}$ is a dimensionless parameter; it determines the strength of turbulence which transports angular momentum. And

$$c_s = \sqrt{\frac{k_{\mathrm{B}}T}{\mu m_H}} \approx 10^3 \ \mathrm{ms}^{-1} \qquad \text{and} \qquad \Omega_{\mathrm{K}} = \sqrt{\frac{GM_*}{r^3}} \approx 2\times10^{-7}\,\mathrm{s}^{-1}\ , \tag{2.9}$$

are the isothermal sound speed (k_{B} is Boltzmann constant and $\mu = 2.3$ is mean molecular weight with m_{H} as mass of hydrogen atom) and Ω_{K} is the Keplerian angular frequency respectively. By using $\alpha = 0.01$, $c_s = 10^3\,\mathrm{ms}^{-1}$ and $\Omega_{\mathrm{K}} = 2 \times 10^{-7}\,\mathrm{s}^{-1}$ in eqn. (2.8) one gets $\nu' = 5 \times 10^{10}\,\mathrm{m}^2\mathrm{s}^{-1}$.

By using $T = 300\mathrm{K}$, $r = 1$ AU, $\alpha = 0.01$ and $M_* = M_\odot$, eqn. (2.7) reads

$$v_{\mathrm{r}} = -\frac{3}{4r}\left(\alpha\frac{c_s^2}{\Omega_{\mathrm{K}}}\right) \approx -54 \ \mathrm{ms}^{-1}\ , \tag{2.10}$$

and by using Ω_{K} and $r = 1$ AU, Keplerian velocity v_{K} can be defined as

$$v_{\mathrm{K}} = \Omega_{\mathrm{K}} r \approx 2.98 \times 10^4 \ \mathrm{ms}^{-1}. \tag{2.11}$$

Now it can be shown that the disc is in steady state ($\partial\Sigma/\partial t = 0$) by showing the accretion onto the protostar and from the cloud is constant. One can define the mass accretion rate $\dot{M}$ such as

$$\dot{M} = -2\pi r\Sigma(r)v_r = 3\pi\Sigma(r)\nu' = \text{constant} \tag{2.12}$$

By using $\Sigma(\mathrm{r}) = 1000\,\mathrm{g\,cm}^{-2}$ one obtains $\dot{M} = 8 \times 10^{-8} M_\odot/\mathrm{yr}$ (Dullemond 2013).

2.1.4.1 Radial structure

By keeping the scope of this chapter in mind, here a generalised scaling relation for surface density and temperature as given in Dullemond (2013) have been introduced. The assumption made here is that surface density has power law profile, such as

$$\Sigma(r) \propto r^p\ , \tag{2.13}$$

and for temperature

$$T(r) \propto r^q\ . \tag{2.14}$$

Since viscosity is the function of temperature and Ω_{K}, so it can be written as

$$\nu' \propto \frac{T(r)}{\Omega_{\mathrm{K}}} \propto r^{q+3/2}\ , \tag{2.15}$$

and radial velocity is a function of viscosity, hence of temperature such that

$$v_{\mathrm{r}} \propto r^{q+1/2}\ . \tag{2.16}$$

By plugging eqn. (2.13) and (2.16) in eqn. (2.12) one obtains

$$\dot{M} \propto r^{p+q+3/2} = \text{constant}\,. \tag{2.17}$$

Thus it leads to

$$p + q = -\frac{3}{2}\,. \tag{2.18}$$

If it is assumed that p = - 3/2 and q = 0 and apply this to MMSN then eqn. (2.14) suggests temperature does not vary with radius ($\partial T/\partial r$ = 0), which is not the possible, q must be less than zero (e.g. q = p -3/4). Therefore, the non-turbulent models of Minimum Mass Solar Nebula, assumed by (Weidenschilling 1977) and Desch (2007) are not consistent with standard viscous accretion theory (Dullemond 2013).

2.1.4.2 Vertical structure

Now the vertical structure of a geometrically thin disc can be defined by exploiting the concept of hydrostatic equilibrium as described in Armitage (2014)

$$\frac{dP}{dr} = -\rho \frac{GM_*}{r^2} = -\rho g_z\,. \tag{2.19}$$

Since the gravity of the disc is negligible and only effective acceleration is due to the vertical component of stellar gravity g_z as shown in Figure 2.3 and it is given as

$$g_z = \frac{GM_*}{r^2}\sin\theta = \frac{GM_*}{r^3} z = \Omega_{\mathrm{K}}^2 z\,. \tag{2.20}$$

Equation (2.19) becomes

$$\frac{dP}{dr} = -\rho\,\Omega_{\mathrm{K}}^2 z\,. \tag{2.21}$$

Plugging $P = \rho c_s^2$ (c_s is constant) one obtains

$$c_s^2 \frac{d\rho}{dr} = -\rho\,\Omega_{\mathrm{K}}^2 z\,. \tag{2.22}$$

The solution to this is

$$\rho(z) = \rho_0 e^{\left(-\frac{z^2}{2H^2}\right)}, \tag{2.23}$$

where ρ_0 is the midplane density at z = 0 and H is the pressure scale height

$$H = \frac{c_s}{\Omega_{\mathrm{K}}}\,. \tag{2.24}$$

The aspect ratio can be defined by dividing with radius such as

$$\frac{H}{r} = \frac{c_s}{v_{\mathrm{K}}}\,. \tag{2.25}$$

Observations and theoretical models suggest H/r is relatively small, typically $H \leq 0.1\,r$. In other words when $c_s \leq v_{\mathrm{K}}$, discs are mainly rotationally supported, pressure gradients are only of secondary importance (Mordasini 2015).

The local orbital velocity v_0 of the gas packet, which is in balance with gravitational force, centrifugal force and pressure gradient, is given by

$$\frac{v_0^2}{r} = \frac{GM_*}{r^2} + \frac{1}{\rho}\frac{dP}{dr}. \tag{2.26}$$

Again using $P = \rho c_s^2$ and $v_\mathrm{K} = \Omega_\mathrm{K} r = \sqrt{GM_*/r}$ one gets as given in Chiang & Youdin (2010)

$$v_0 = v_\mathrm{K} - \eta' v_\mathrm{K} \approx \frac{\partial P/\partial \ln r}{2\rho v_\mathrm{K}} \approx 25\left(\frac{r}{\mathrm{AU}}\right)^{1/14} \mathrm{m/s}\,. \tag{2.27}$$

where $\eta' \sim c_s^2/v_k^2 \sim H^2/r^2 \sim 10^{-3}$ is a dimensionless measure of pressure support (Youdin & Kenyon 2013). Though the difference between the sub-Keplerian and Keplerian velocity is relatively less but it is crucial for the aerodynamics of gas and dust, as it causes the drift velocity (discussion in Sec. 2.3.3).

2.2 Planetesimals

Planetesimals, the solid bodies of kilometre in size composed of dust and ice, are the building blocks of planets. However the process of their formation is still in debate.

In 1969 Viktor Safronov, states that planets form out of cosmic dust grains that collide and stick to form larger and larger bodies. But the journey from submicron size cosmic dust to size where gravity would take over is not straight forward. It is less likely that planetesimals themselves are to form by two-body collisions alone; because objects of a few-100 metres have individually gravitational fields too weak to bind with other bodies, and the electro-static attraction of such bodies become feeble for the growth beyond few centimetres (Chiang & Youdin 2010). When the bodies reach to the size of about a kilometre, their mutual gravitational energy is higher than their kinetic energies, hence they merge and grow in size.

The dust grains go through several phases. However the aim is to confine the discussion, therefore the growth process will be analysed into two phases. In the subsequent section, the first phase of growth which takes place during the vertical settling, will be discussed. In the next section, light will be shed on the role of relative velocities and then the second phase of growing a planetesimal as a result of gravitational collapse will be discussed.

2.2.1 Vertical settling

The story of dust growth starts when the micron-sized nebular grains begin to settle onto the midplane of the disc. The dust grains are thought to be a mixture of silicates and carbons, with a size distribution from ~ 0.01 μm up to 0.3 μm (Natta et al. 2006). During the initial growth phase, dust grains are embedded in a gaseous disc and feel friction due to their velocity relative to gas (Testi et al. 2014). As a result, a particle of radius a, which has velocity v, experiences the aerodynamics drag force F_D against the surrounding gas, whose molecules have λ' as mean free path (Whipple 1972), (Weidenschilling 1977) and $\bar{c}_s$ as mean thermal velocity, then the drag force can be defined as in Armitage (2014)

$$F_D = \frac{1}{2} C_D \cdot \pi a^2 \cdot \rho_g \cdot v^2 , \tag{2.28}$$

where ρ_g is the density of gas and $C_D = 8\bar{c}_s / 3v$ is the drag coefficient and its form depends on the size of the particle and the mean free path of gas molecules. So one can write

$$F_D = \frac{4}{3} \bar{c}_s v \rho_g \pi a^2 . \tag{2.29}$$

The particle, besides drag force, also experiences gravitational force F_g at height z above the midplane and it is given by

$$F_g = m\, \Omega_\mathrm{K}^2 z . \tag{2.30}$$

As the two forces balance each other, the particle reaches settling velocity v_set (terminal velocity), such as

$$\frac{4}{3} \bar{c}_s v \rho_g \pi a^2 = m\, \Omega_\mathrm{K}^2 z , \tag{2.31}$$

$$v_\mathrm{set} = \left(\frac{\rho_d}{\rho_g} \right) \left(\frac{\Omega_\mathrm{K}^2}{\bar{v}} \right) a\ z . \tag{2.32}$$

Here $\rho_d = 3\ \mathrm{g\,cm^{-3}}$ is the density of the dust grain. Now the settling time can be defined as

$$t_\mathrm{set} = \frac{z}{v_\mathrm{set}} . \tag{2.33}$$

For a micron size dust particle at $z = h$ at 1 AU the settling velocity is $v_\mathrm{set} \approx 0.1\ \mathrm{m\,s^{-1}}$ and settling time is $t_\mathrm{set} \approx 2 \times 10^5$ years (Armitage 2014). At higher z, the vertical component of gravity g_z is stronger and gas density is lower, so the settling velocity is higher, which in turn leads to rapid settling. If the dust grains were not coupled to gas then their vertical motion would be oscillatory around the midplane (Birnstiel 2011). The friction induced by the drag force slows down this motion and thus the particle will settle towards the midplane.

In this phase, the dust particles are small i.e. $\mathrm{St} \ll 1$ and they are strongly coupled to the gas molecules. If this coupling is long enough to alter the relative motion between the particle and gas by the order of unity, this duration is called stopping time t_s (also called coupling time). The duration of this time depends on the size of grain a and the mean free path of the gas molecule λ'. In Epstein regime where $a < 9\lambda'/4$, let us assume a particle of mass m and cross-sectional area σ_0 is passing through the gas which is in Brownian motion v_Br (details in Sec. 2.3.1). If ρ_g is the density of gas then the stopping time can be defined as in Zsom et al. (2010)

$$t_\mathrm{s} = \frac{3m}{4 v_\mathrm{Br} \sigma_0 \rho_g} . \tag{2.34}$$

If the particle has grown to a larger cross sectional area or the density of gas has increased, then particle is assumed to be in the first Stokes regime and its stopping time can be defined as

$$t_s = \frac{3m}{4v_{\mathrm{BR}}\sigma_0\rho_g}\frac{4a}{9\lambda}. \tag{2.35}$$

The particles of large cross sectional area more frequently hit the gas molecules and rapidly lose energy and give rise to radial drift, another contributor of relative velocity.

Stokes number St

Here one can introduce a useful dimensionless quantity called Stokes number St. The Stokes number is defined as a product of stopping time t_s of the gas-grain and the Keplerian frequency Ω_K (Cuzzi et al. 1993) such that

$$\mathrm{St} = \Omega_K t_s. \tag{2.36}$$

The application of Stokes number becomes significant because particles of same Stokes number exhibit same aerodynamic characteristics regardless of being different in size, shape or composition or in different environment (Testi et al. 2014).

Now eqn. (2.32) can be expressed in a more generalised terms of Stokes number, as given in Drążkowska & Dullemond (2014)

$$v_{\mathrm{set}} = -z\Omega_K\left(\frac{\mathrm{St}}{1+\mathrm{St}^2}\right). \tag{2.37}$$

2.2.2 Growth along vertical settling

The important implication of drag force is the radial drift (Testi et al. 2014) and that of magnetic field is the turbulence, and both processes contribute to the random Brownian motion; which facilitates the growth process.

As shown in Figure 2.4, dust settles to the midplane and the grains upon collision "hit and stick" by the Van der Waals forces and starts to grow (Blum et al. 1996) (Kempf et al. 1999) (Blum et al. 2000). The phenomenon has been experimentally observed by Poppe et al. (2000a). They did shoot 0.5 μm and 1.2 μm silica spheres on the silica wafer and reported sticking probability ~ 80% at impact velocity ≤ 1 ms^{-1}. However the threshold velocity for sticking decreased when the size of the colliding grains was increased (Testi et al. 2014).

Heim et al. (1999) experimentally determined the force between 0.5 μm and 2.5 μm spheres of SiO_2 particles, which is on the order of 10^{-7} N (Klahr & Brandner 2006). And they found the force is proportional to surface energy and the reduced radii of spheres. If growth is desired then the collision energy must be less than the corresponding binding energy between the two monomers. Dominik & Tielens (1997) described the rolling energy E_{roll} as the minimum energy with which any contact surface of two grains is held together. If two grains each of equal radii $a = 1$ μm collide, they roll over each another over the distance πa and the rolling energy as given in Güttler et al. (2010)

$$E_{\mathrm{roll}} = \frac{\pi a}{2}F_{\mathrm{roll}}, \tag{2.38}$$

where $F_{\mathrm{roll}} \sim 8.5 \times 10^{-10}$ N is the value of the rolling force between the monomers as given in Heim et al. (1999), one gets $E_{\mathrm{roll}} \approx 1.3 \times 10^{-12}$ mJ. The particles will hit and stick if their collision energy E_{coll} satisfies the relation given in Güttler et al. (2010)

$$E_{\text{coll}} = \frac{1}{2} m' v_{\text{n}}^2 \leq 5 E_{\text{roll}}, \tag{2.39}$$

where m' is reduced mass of the dust particles and v_{n} is the normalised collision velocity[2]. The corresponding sticking velocity v_{s} can be described as in Güttler et al. (2010)

$$v_{\text{s}} \leq \sqrt{\frac{5\pi a F_{\text{roll}}}{m'}} . \tag{2.40}$$

On the timescale of few collisions, the monomers grow in chain-like fractals. First Blum et al. (2000) and later Krause & Blum (2004) have experimentally observed the Brownian-motion-driven growth of micron size grains into fractals, which have dimensions $d_{\text{f}} \sim 1.4$.
The collision time t_{coll} at a given temperature is the function of particle cross-sectional area σ_0, and particle number density n_0 and Brownian motion v_{Br} which has been described in Klahr & Brandner (2006) as

$$t_{\text{coll}} = \frac{1}{n_0 \sigma_0 v_{\text{Br}}} . \tag{2.41}$$

The experimentally observed value of the collision timescale t_{coll}, between the μm-sized particles with particle number density $n_0 = 10^{12}\ \text{m}^{-3}$ and $\sigma_0 = 3 \times 10^{-12}\ \text{m}^2$, is of the order of a few minutes (Klahr & Brandner 2006). From here the collision frequency f_{coll} can be defined as

$$f_{\text{coll}} = \frac{1}{t_{\text{coll}}} . \tag{2.42}$$

In order to estimate, the mass growth of a dust particle of radius a and mass m traversing through the gaseous medium, one can consider simple single particle growth model (Dullemond & Dominik 2005). For simplicity let us assume that every collision ends in sticking then the mass gain dm during time interval dt is proportional to the geometric cross section πa^2 of the particle and the column density as given in Armitage 2014

$$\frac{dm}{dt} = \pi a^2 \left(v_{\text{set}} \right) Z \rho_g(z), \tag{2.43}$$

where Z is the dust to gas ratio in the disc. Plugging eqn. (2.32) leads to

$$\frac{dm}{dt} = \pi a^2 \left(\left(\frac{\rho_d}{\rho_g} \right) \left(\frac{\Omega_{\text{K}}^2}{\bar{v}} \right) a \ z \right) Z \rho_g(z) . \tag{2.44}$$

Using $m = (4/3)\ \pi a^3 \rho_d$ and the rearranging leads to

$$\frac{dm}{dt} = \frac{3}{4} \left(\frac{\Omega_k^2}{\bar{v}} \right) m\ \text{Z}\ z . \tag{2.45}$$

The growth process continues, particles grow in clusters and the clusters get together to form larger aggregates. In first few hundred years the cluster-cluster aggregation (CCA) dominates and within 600 years the dust grain of different sizes grow up to millimetre in size by reaching

---

[2] It is the relative velocity of corrected for the impact parameter and will be introduced formally in Sec. 4.1.1

close to the midplane (see Figure. 19 in Armitage (2014)).

Surprisingly, the aggregates of mm in sized are also preserved from the formation of our solar system, which can be found in chondrules, mm-sized spherules, with radio-isotope dating back to the first few million years of the solar nebula (Blum 2010). If two chondrules collide, the outcome is bouncing (Güttler et al. 2010).

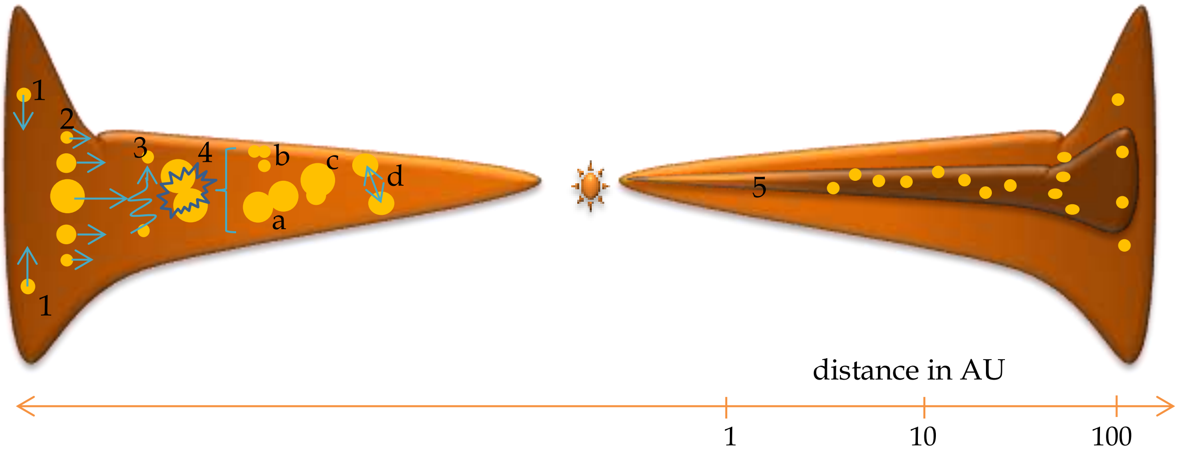

Figure 2.4 The schematic diagram of protoplanetary disc inspired by Testi et al. (2014) depicting the various evolutionary stages.

1. Vertical settling
2. Radial drift
3. Turbulent mixing
4. Collisions
a) Hit and Stick
b) Fragmentation
c) Fragmentation with mass transfer
d) Bouncing
5. Midplane

However the collision between a chondrule and μm-sized grain results in sticking. For example Ormel et al. (2008) showed that micron-sized grains stick to chondrules and form a porous dust rim. In chondrule-grains interaction, the collision energy is dissipated in compacting the rim and allowing the chondrules to stick more easily (Carrera et al. 2015).

This growth model is based on cluster-cluster aggregation. Since the process of sticking is of probabilistic nature (0.2 – 0.8 for impact velocity $\leq 100\ \mathrm{m\,s^{-1}}$), therefore not every collision ends in sticking, sometime particles are also ejected from the cluster. Hence the growth process has to account the loss of parties as well. Hence the particle gain over time is given by the coagulation equation derived by Smoluchowski, (1916), as given in (Klahr & Brandner (2006))

$$\frac{dn_i}{dt} = \underbrace{\frac{1}{2}\sum_{j=1}^{i=1} K(i-j,\, j) n_{i-j} n_j}_{\text{formation of aggregates with } i \text{ constituents}} \quad - \quad \underbrace{n_i \sum_{j=1}^{\infty} K(i,\, j) n_j}_{\text{loss of aggregates with } i \text{ constituents by number density } n_i} \quad , \tag{2.46}$$

here $K(i, j) = B(i, j)v(i, j)\sigma_0(i, j)$ is the collision kernel which depends on adhesion efficiency $B(i,j)$ between particle i and j which have velocity v_n and cross-sectional area σ_0.

As the particle size reaches to centimetre or larger, it gets separated from the gas and maintains its path on Keplerian orbit around the star. Since the gas is supported by the pressure gradient, it moves slightly slow in a Sub-Keplerian orbit, which causes friction with dust particles and results in the loss of angular momentum (Weidenschilling 1977) (Dullemond & Dominik 2005) and drift inward (details in Sec. 2.3.3).

2.3 Relative velocities

There are several contributors to the relative motion of the dust aggregates, such as Brownian motion (thermal velocities), azimuthal and vertical motion, and radial drift. Each of the velocity contributors is size dependent, as the size of the particle varies, so their velocities. Therefore the interaction between the particles of different size leads to relative velocities (Birnstiel 2011). For small dust grains St << 1, the relative velocities lead to collision resulting in efficient sticking and hence fast growth (Nakagawa et al. 1981), (Dullemond & Dominik 2005) (Brauer et al. 2008). Keeping the scope of this chapter in mind, here three main contributors of relative velocities have been discussed, namely Brownian motion, turbulent motions and radial drift.

2.3.1 Brownian motion

The random Brownian motion of the particles arises due to their different thermal velocity distribution. The relative velocity between two particles of mass m_1 and m_2 can be written as in Windmark et al. (2012a)

$$\Delta v_{\mathrm{Br}}\left(m_1+m_2\right)=\sqrt{\frac{8k_BT(m_1+m_2)}{\pi m_1 m_2}}\,. \tag{2.47}$$

In the above equation one can see that Brownian motion depends on the mass of the colliding binary. It is significant for the particles of low mass, e.g. for micron-sized grains the relative velocity is about $10^{-2}\,\mathrm{ms}^{-1}$, which drops down to $10^{-5}\,\mathrm{ms}^{-1}$ for the centimetre sized pebbles. If one simply relies on Brownian motion then growth will not only be very slow but it will have porous and fractal structure with a narrow size distribution. Therefore the role of Brownian motion is significant as long as the collision is between low mass grains. So the growth in the initial stage is driven by the Brownian motion.

2.3.2 Turbulent motion

The random motion and the shear due to friction within the gas give rise to turbulent motion in the disc (Völk et al. 1980). In general a large fraction of gravitational energy released from dust accretion, is transferred to turbulence (Takeuchi et al. 2012). The turbulent motion is required for the turbulent viscosity, which is crucial for energy dissipation and angular momentum transport. This relation can be expressed by plugging eqn. (2.24) in eqn. (2.8) such as

$$\nu' = \alpha c_s H\,. \tag{2.48}$$

Rather going into details, one can simply exploit the closed-form expressions of average relative turbulent velocities, given by Ormel & Cuzzi (2007) which reads

$$\Delta v_{tur} = c_s \sqrt{9\alpha/2}\,. \tag{2.49}$$

They showed that as the vertical settling and radial drift are proportional to Stokes number, likewise the relative turbulent velocity is proportional to the difference between the Stokes number of the colliding particles (Testi et al. 2014). In general the relative turbulent velocity increase with the Stokes number until St = 1. However for the particles St > 1, owing to the poor coupling to gas the turbulent velocity decreases. But this decrease is not as rapid as the relative velocities induced by radial drift or vertical settling decline (Testi et al. 2014).
Besides the above discussed sources of turbulent motion, MRI (magneto-rotational instability) is considered an effective source of turbulent viscosity. It is assumed that MRI induces shear as well, which further stirs the dust in sublayers and consequently more hindrances to the sedimentation process.

2.3.3 Radial drift motion

As discussed in Sec. 2.2.1 the settling dust grains experience the drag force. One of the direct consequences of the drag force is the radial drift, first realised by Whipple (1972) and Weidenschilling (1977). Since the drag force is proportional to the particle size (eqn. (2.29)) so is the radial drift. Therefore the large particles St ≥ 1 easily lose angular momentum for the above reason, hence have higher radial drift velocity v_{r} (eqn. (2.7)). On the other hand the accreting gas, which has velocity v_{g}, also drags the particle inwards with velocity v_{acc} (Lynden-Bell & Pringle 1974) which has higher impact on smaller particles St ≤ 1. The contribution of the two sources of radial drift has been expressed in Zsom et al. (2010), such as

$$v_{\mathrm{rd}} = v_{\mathrm{r}} + v_{\mathrm{acc}}\,. \tag{2.50}$$

The eqn. (2.7) can be express in terms of Stokes number

$$v_{\mathrm{r}} = -\frac{2v_{\max}}{\mathrm{St} + \dfrac{1}{\mathrm{St}}}\,, \tag{2.51}$$

and $v_{\max}$ is the maximum radial drift velocity (Whipple 1972) (Weidenschilling 1977). The second term is given as

$$v_{\mathrm{acc}} = -\frac{v_g}{1+\mathrm{St}^2}\,. \tag{2.52}$$

For a large particle St ~ 1, the contribution of radial drift and turbulent motion is higher, as a result particles experience erosion and fragmentation (Brauer et al. 2008) and (Blum & Wurm 2008). At 1 AU the relative velocities reach to the order of 100 $\mathrm{m\,s^{-1}}$ (Armitage 2014). The cm-sized pebbles colliding at this velocity necessarily fragment. The boulders which may escape collisions will be swallowed by the star. Such a body at 1 AU requires about 100 years to fall into the proto-Sun (Weidenschilling 1977). The particles rapidly lose angular momentum, in turn it increases the inward drift velocity up to ~ 50 $\mathrm{m\,s^{-1}}$ (Testi et al. 2014).

Fragmentation velocity

The combined effect of relative velocities is that pebbles reach the fragmentation threshold velocity v_1, which is ~ 1 $\mathrm{m\,s^{-1}}$ for the cm-sized pebbles. The fragmentation velocity sets the upper limit to particle size grown by coagulation method. However large pebbles are required for the onset of streaming instability. In Sec 4.3.1 it will be shown that how by increasing the size ratio f the coagulation method can still produce the pebbles large enough to trigger streaming instability.

2.3.4 Turbulent mixing and Kelvin Helmholtz instability

As the particles grow in size St ~ 1, they start to decouple from gas. Since the gas is supported by the pressure gradient, it moves with sub-Keplerian velocity v_0 (eqn. (2.27)) which is slightly less than the Keplerian velocity v_K (eqn. (2.11)) of the particles. This velocity difference can be expressed by rewriting eqn. (2.27) such as

$$v_\mathrm{K} - v_0 = \eta' v_\mathrm{K} \approx 10^{-3} v_\mathrm{K}\,. \tag{2.53}$$

Due to the relative velocities between the upper gas layer and the midplane dust layer, a vertical shear between the two layers arises. As a result of shear the dust in the midplane is stirred up, which interacts with infalling dust. This interaction gives rise to turbulent mixing and brings the sedimentation process to an end.

Sekiya (1998) explained that the velocity difference, between dust-rich region and a dust-poor region, causes vertical sheer which gives rise to Kelvin Helmholtz instability (KHI) and the dust layer becomes turbulent, which hinders the dust to settle further. The energy contributed by KHI to the turbulent motion can be expressed in terms of relative velocity between gas and dust, as given in Takeuchi et al. (2012)

$$\Delta E_\mathrm{KH} = \frac{1}{2}\Sigma_d \Delta v^2 = \frac{1}{2}\Sigma_d \eta^2 v_\mathrm{K}^2\,. \tag{2.54}$$

The higher value of η implies the dust grains experience strong headwind in azimuthal direction, which reaches up to $\eta v_\mathrm{k} \geq 25\ \mathrm{m\,s^{-1}}$ (Youdin & Kenyon 2013).

2.3.5 Pebbles pileup by turbulence

According to Youdin & Chiang (2004) in MMSN conditions, the super-solar metallicity, 5 – 20 times of its solar value of $\Sigma_\mathrm{p}/\Sigma_\mathrm{g} \sim 5 \times 10^{-3}$, is one of the main requirements for gravitational instability (set by Toomre criterion Q, see Sec. 2.4.1) which leads to planetesimal formation. Turbulence under these conditions can locally enhance the accumulation of pebbles. The radial drift piles up the pebbles of difference sizes at different radii and so locally increases dust to gas ratio (Chiang & Youdin 2010). Stepinski & Valageas (1996) proposed that in a viscous gas disc, the combination of radial drift and turbulent diffusion often increases the solids-to-gas ratio in a disc, as the gas accretes onto the star. Besides this, the enrichment can be achieved, by other mechanisms such as feedback by the bipolar outflows and removal of gas by magnetic accretion and photo-evaporation (see e.g. Youdin & Shu (2002)). Youdin & Chiang (2004) calculated the turbulent stress (turbulent particle diffusivities), derived from the vertically upward and downward flow of particles within the marginal KHI and showed that turbulent stress speeds up the pileup process. As the surface density goes beyond the saturation limit then the pileup of pebbles become sites of planetesimal formation by gravitational instability.

Ida & Lin (2008) have suggested an alternative scenario, where at the moderate rate of gas accretion $\dot{M} \sim 10^{-9} - 10^{-8}\, M_{\odot}/\text{yr}$ the "dirty snowball"(mixture of dust and ice) can be brought inside the snow line, where the sublimation of ice leaves behind abundance of dust grains (Chiang & Youdin 2010).

2.3.5.1 The role of eddies in pebbles pileup

Eddies (or vortex) are the feature of gas which appear due to the local variation in pressure and they induce turbulence in the protoplanetary disc. For a given eddy, the Kolmogorov scale defines the smallest possible length $l = (\nu'^3/\varepsilon)^{1/4}$, the turnover time $t_e = (\nu'/\varepsilon)^{1/2}$ and the rotation velocity $u = (\nu'\varepsilon)^{1/4}$ Peters (1999), where ε is the energy dissipation per unit mass and ν' (see eqn. (2.8)) is the kinematic viscosity. The lifetime of the larger eddy is limited by orbital shear, such that $t_0 \sim 1/\Omega_K$. Smaller the size of an eddy is, slower is the velocity and shorter the turnover time. The kinematic viscosity damps the energy of the largest and the fastest one by forming many smaller eddies in a cascade manner. The smaller eddies relatively decay earlier and dissipate energy efficiently.

Since the dust grains are coupled to the gas, so they are accelerated as they fall into these eddies which have different sizes and different turnover times (Zsom 2010) (Windmark et al. 2012). These eddies give rise to the local pressure gradients. Because at the vortex, pressure is lower and the higher centrifugal force expels the pebbles out of eddies and they start to pileup in the region (of high pressure) between the eddies and lead to preferential concentration of particles (Eaton & Fessler 1994). The pebbles are more likely to be expelled from an eddy if their settling velocity v_{set} and their stopping time t_s are comparable to the velocity of the eddy u and turnover time t_e of the eddy respectively. As given in Beuther et al. (2014) then eqn. (2.37) gets the form

$$v_{\text{set}} = \frac{t_s}{t_e} u \,. \tag{2.55}$$

Therefore the pebbles which have $t_s \sim t_e$ and alternatively $v_{\text{set}} \sim u$ will fling out of the eddies and get lock into their interstices and hence increase the pebbles concentration. And moreover in the case of larger eddies the reduced pressure may also draw dust from the surface of the eddy into the core (Cuzzi et al. 2001). The size-selective concentration of the chondrules and the other submillimetre particles found in the primitive asteroids, have been assumed to be formed in the interstices of eddies as a result of a turbulent disc Cuzzi et al. (2001).

Reynolds number

Here a useful quantity called Reynold number can be introduced. It is the ratio of inertial forces to viscous forces acting on the fluid, which is given as

$$\text{Re} = \frac{ul}{\nu'}\,, \tag{2.56}$$

where u and l are the Kolmogorov scales for the velocity and length of the eddy and ν' is the kinematic viscosity. It tells whether the flow is laminar or turbulent. If Re < 2300 the flow is laminar and it is dominated by viscosity. In the case Re > 2300 the flow is turbulent and is dominated by the inertial forces, which tend to produce chaotic eddies, vortices and other flow instabilities.

2.4 Steaming instability leading to gravitational collapse

The pebbles of millimetre to centimetre size can not be glued either chemically or gravitationally. On the other hand their mounting kinetic energy is self-destructive for the reasons discussed in Sec. 2.3.3. Therefore an efficient mechanism is required, which must perform two tasks; first saving the particles from spiralling into the protostar, second it enhances the local dust concentration.

The streaming instability thrives due to the relative motion of gas and particles. It is being considered as a very efficient way to overcome the drift barrier and to locally increase the particle concentration (Youdin & Goodman 2005) (Johansen & Youdin 2007) (Bai & Stone 2010). However, it has been shown that a strong clumping, which is required for planetesimal formation, is possible if the particles are as large as $\mathrm{St} \sim 1$ (Beuther et al. 2014). Drążkowska & Dullemond (2014) have suggested that the $\mathrm{St} \geq 0.01$ is the minimum size required for the onset of streaming instability. As described in Chiang & Youdin (2010) that the minimum amount of physics is required to turn on the streaming instability, namely Keplerian motion, gas pressure and drag acceleration. The principle of streaming instability is shown in Figure 2.5 and the main ideas are discussed in the following.

- **Relative velocity**: Streaming instability feeds on the velocity difference ηv_{k} between gas and dust particles (Johansen et al. 2012), which gives rise to radial drift.
- **Outward streaming of gas**: If gas drags the dust inwards, then according to Newton's Third Law, dust also drags the gas outwards (Chiang & Youdin 2010). As a result of headwind caused by the velocity difference, the particles slow down and transfer momentum to the gas, in turn gas moves outward. This backreaction of particles on gas leads to powerful drag instabilities (Chiang & Youdin 2010).
- **Higher metallicity**: It implies that the inward drifting dust would be scarce of gas, which would leads to higher metallicity Z (dust-to-gas ratio) required for streaming instability. Alternatively the higher metallicity can be achieved by photo-evaporation or by disc winds (Carrera et al. 2015).
- **Coupling time**: The coupling time t_{s} plays an important role in the outward streaming of gas. Because it is proportional to the size of the particle (see eqn. (2.35)) and large particles have higher momentum, therefore they give a stronger kick to gas outward. Hence the longer the coupling time is, the larger is the particle and the intense will be the back-reaction on the gas.

Youdin & Goodman (2005) treated gas and dust as two aerodynamically coupled fluids, and showed that inward flow of dust and outward flow of gas do not remain in equilibrium and are linearly unstable to small particle-density perturbation, which grows exponentially with

time (Beuther et al. 2014). As described in Bai & Stone (2010) the particles with $t_s \geq 0.01$ actively participate in SI and they do maintain turbulence and a sufficient height from the midplane, before KHI comes in action. And they showed that SI is more effective than KHI in setting the dynamics for the particles of size St = 0.1 (Johansen et al. 2012) .
Here the point to be noticed is the role of dust-to-gas ratio. As discussed in Beuther et al. (2014), for $Z \ll 1$ the outward streaming of gas increases more or less linearly with Z.

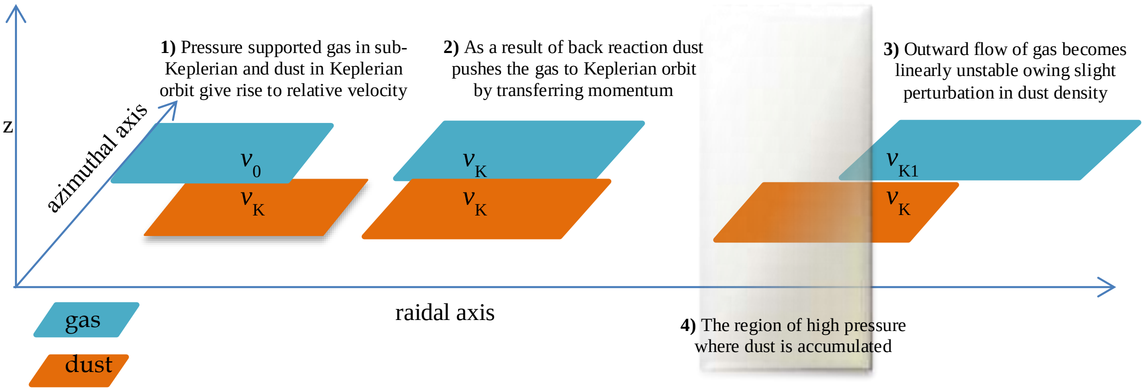

Figure 2.5. The schematic diagram of dust-gas interaction. **1)** The accreting gas shown in blue sheet has local orbital velocity v_0 which is supported by the pressure gradient. The gas is in sub-Keplerian orbit and moves slower than the fast moving dust shown in green sheet, which has Keplerian velocity v_K. As a result of relative velocity, dust experiences friction from the gas and lose angular moment (Johansen et al. 2012). **2)** The momentum is transferred to gas, in this way gas is accelerated and moves outward into Keplerian orbit. Now the dust and gas have same Keplerian velocity. However the momentum transfer is not linearly stable. The larger particles, owing to longer coupling time more effectively transfer momentum. Youdin & Goodman (2005) showed that the inward flow of the dust and outward flow of the gas do not remain in equilibrium. **3)** A slight perturbation in dust density intensifies the outflow of gas by few orders of magnitudes (Beuther et al. 2014). Therefore more gas flows outward with little increase in particle density. **4)** As a result the dust starts to get accumulated inside and the pressure of the region increases which hinders the dispersal of dust.

However in a nonstratified disc (which are already prone to particle concentration) as $Z \geq 1$, the linear increase in dust density changes into an exponential rise, which is a few orders of magnitude, even for small particles St = 0.3 (Johansen et al. 2012) (Beuther et al. 2014). For Z = 3 and St ~ 1 the particle density increases by 1000 times, while for smaller particles St = 0.1 (owing to their shorter coupling time) and Z~ 1 the rise is only 60 times of gas density.

In the case of stratified discs, Carrera et al. (2015) has thoroughly examined the increase in particle concentration and the corresponding probability of streaming instability as a function of the initial particle size. In their phase diagram (Fig. 8 in Carrera et al. (2015)) they showed that SI is very likely to occur for the particles size between St = 0.003 (mm-sized pebbles) to St = 4 (~ 5 m boulder), given that $Z \gg Z_\odot$. The reason for strong clumping observed in stratified simulation could be explained by a very thin midplane, of height ~ 0.001 H (Beuther et al. 2014).

The particle concentration produced by the streaming instability would be susceptible to gravitational instability and can collapse into planetesimals of a few 100 km. For example Johansen et al. (2007) and Johansen & Youdin (2007) showed that a swarm of cm-sized pebble becomes gravitationally unstable and can collapse into a dwarf planet of the size of Ceres, within the elapse of few orbits (Youdin & Kenyon 2013).

2.4.1 Gravitational collapse

Gravitational collapse is a top-bottom approach to form a planetesimal. It is one of the ways to overcome the growth barriers, namely the fragmentation and radial drift barrier. If any mechanism, such as streaming instability, zonal flows and pressure bumps, could pileup enough pebbles, then the mutual gravitational attraction can induce gravitation instabilities which can trigger a runaway collapse of the pile into a planetesimal — even when sticking is inefficient and radial drift is dominant (Youdin & Kenyon 2013).

The idea is not new that a prolonged sedimentation of dust onto the midplane would make the disc gravitationally unstable. As described by Safronov (1960) and Goldreich & Ward (1973) that dust particles settle to the midplane which becomes gravitationally unstable and collapses into planetesimals of about 0.1 km. Later Weidenschilling (1977) argued that such a collapse is very unlikely in the presence of turbulence caused by the shear between the dust layer and the gas (Klahr & Brandner 2006). Even a tiny amount of turbulence is enough to end the sedimentation process and prevent the midplane from reaching the critical density. However, in recent years the idea has been resurrected, Youdin & Shu (2002) have suggested that if the local solid to gas ratio is $Z > 0.01$ (2-10 times of its cosmic value) the gravitational instability can take over. However the question is how to get such a high concentration.

In this scenario, streaming instabilities seems promising owing to its prominent feature of turning the turbulence into a mechanism of increasing the dust-to-gas ratio and can raise the local dust density high enough to meet the so-called Toomre criterion, first described by Goldreich & Lynden-Bell (1965) such as

$$Q = -\frac{\Omega_{\mathrm{K}} c_s}{\pi \mathrm{G} \Sigma_d} < 1. \tag{2.57}$$

In this way the radial drift can be avoided and gravitational instability can be triggered.
The physics behind this criterion is relatively simple. It arises as a result of competition between the force which destabilize the disc, namely self-gravity and the forces which stabilize the disc, i.e. outward pressure and centrifugal force. Beuther et al. (2014) explains, that $Q < 1$ implies that the combined effect of pressure and centripetal force are higher against the self-gravity, so the disc is stable. If self-gravity dominates the pressure and centrifugal force, then $Q > 1$ and disk becomes unstable. If Σ_g is the surface density of the gas packet introduced in Figure 2.3, then according to Beuther et al. (2014) such a packet of gas will have its attractive gravitational force $F_g \sim G\Sigma_\mathrm{g}^2 L^2$, the repulsive outward pressure force would be $F_p \sim c_s^2 \Sigma_\mathrm{g} L$ and the stabilising centrifugal force would be $F_C \sim \Omega_\mathrm{K}^2 \Sigma_\mathrm{g} L^3$. If this packet of gas has to undergo a gravitational collapse then its self-gravity must overcome the opposing forces of pressure and centrifuge i.e. $F_\mathrm{g} > (F_\mathrm{p} + F_\mathrm{c})$. The win against F_p requires the gas packet to have size $L \geq c_s^2 / \Sigma_\mathrm{g} L$ and to win against F_c the size should be $L \leq G\Sigma_\mathrm{g} / \Omega_\mathrm{K}^2$. This sets the lower and upper limit to the

size of the gas packet. By using the conditions of a solar-type star, assume a packet of gas at r = 1 AU and temperature T = 300 K, one gets the surface density as given in Beuther et al. (2014)

$$\Sigma_{\rm gas} > \frac{\Omega_{\rm K} c_s}{\pi {\rm G}} \approx 10^5 \left(\frac{\rm g}{\rm cm^2}\right)\left(\frac{r}{1\ {\rm AU}}\right)^{-7/4} , \tag{2.58}$$

which is much higher than the value given in eqn. (2.4) and the slope is relatively steeper as well. Planetesimals corresponding to 100 km and 1000 km in size can be formed as a result of gravitational collapse of the overdense filaments. Youdin & Goodman (2005) were the first who predicted the formation of large planetesimals, depending on the mass available in linear modes (Beuther et al. 2014). More recently Johansen et al. (2014) showed the formation of planetesimals of size 20—200 km is possible in the overdense filamentary structure formed by streaming instability.

2.4.2 Modelling the gravitational collapse of a pebble cloud

Wahlberg Jansson & Johansen (2014) and Wahlberg Jansson et al. (2017), hereafter WJJ 2014 and WJ 2017 respectively, envision the gravitational collapse of a pebble cloud. Their model starts with the assumption that the streaming instability triggers exponential rise in the outward streaming of gas which leaves behind a swarm of pebble to collapse. The method to follow the collapse is in the following.

Method of representative particle approach

WJJ 2014 and WJ 2017 have used the method of representative particle approach in their Monte Carlo code. In this method, the mass of the cloud is divided into N ($\sim 10^{24}$) number of physical pebbles, each of size a = 1 cm and the filling-factor ϕ = 0.35. Here rather following the whole population of N particles, a sample of randomly selected n = 250 representative particles has been taken. Each representative particle n_i ($\sim 10^{21}$) can be considered as a swarm of physical particles which have their own identical properties, such as mass and velocity. The values of each property will be updated after every collision. This method was originally developed by Zsom & Dullemond (2008) and since then have been used in different models of pebble clouds.

The pebble cloud

Imagine a cloud in which n numbers of representative pebbles are uniformly distributed and the cloud has no net rotation and the effect of surrounding gas has been neglected. The cloud is located at semi-major axis of Pluto. The evolution of the collapsing cloud can be followed by using the initial conditions of the cloud such as mass M, the initial radius R_0 and the pebble size a. It is assumed that the surface density $\Sigma_{\rm d}$ of the cloud meets Toomre criterion, such that $Q > 1$ and it undergoes a gravitational collapse. If the initial radius R_0 of the cloud is the Hill-radius $R_{\rm Hill}$ then collapse will continue unless the cloud reaches the radius $R_{\rm solid}$, the radius at which the density of dust in the cloud is equal to the monomer density $\rho_{\rm SiO2}$ = 2.5 gcm^{-3}. Whereas the initial Hill radius is given by

$$R_0 = R_{\rm Hill} = \left(\frac{M_0}{3M_*}\right)^{1/3} r , \tag{2.59}$$

where r is semi-major axis of the cloud to the star. The time required to reach $R_{\rm solid}$ is defined as collapse time t_{col}, as given in WJ 2017

$$t_{\rm col} = 4.1\,{\rm kyr}\left(\frac{R_{\rm solid}}{1\,{\rm km}}\right)^{-1}\left(\frac{a}{1\,{\rm cm}}\right)\phi^{2/3}\left(1-C_R^2\right)^{-1}, \tag{2.60}$$

where C_R is the coefficient of restitution; its value varies between 0 and 1. Here the point to be noticed is the collapsing time is inversely related to $R_{\rm solid}$ (or cloud mass) and directly related to the pebble size a.

WJJ 2014 defines that the cloud is initially in the virial equilibrium such that its initial kinetic energy T_0 is equal to the minus ½ of its initial potential energy U_0 and the sum of the two defines the initial total energy E_0 such as

$$E_0 = -\left(T_0 + U_0\right),$$

$$E_0 = -\frac{1}{2}Mv_{vir,0}^2 - \frac{3}{10}\frac{GM^2}{R_0}, \tag{2.61}$$

where $v_{\rm vir}$ is the virial velocity of the pebbles, which can be defined as given in WJ 2017

$$v_{\rm vir} = \sqrt{\frac{3GM}{5R_{\rm t}}}. \tag{2.62}$$

As one can see $v_{\rm vir}$ depends on the mass of the cloud and its radius at time $R_{\rm t}$. The relative velocity is simply

$$v_{\rm rel} = \sqrt{2}\times v_{\rm vir}. \tag{2.63}$$

As the cloud contracts, R_0 reduces and the total internal energy $E(t) = -(T_t + U_t)$ increases with time t. The minus sign indicates the negative gravitational potential, which means cloud has become more tightly bound. One can define the cloud contraction parameter η as the ratio between the initial total energy E_0 and the total energy $E(t)$ at any time t, as given in WJ 2017

$$\eta = \frac{-E_0}{-E(t)}. \tag{2.64}$$

The contraction parameter η is a positive values which reaches to its minima when the cloud has reached the radius $R_{\rm solid}$, which means the cloud can not be contracted further. During the contraction the pebbles will inevitably collide with one another and dissipate the kinetic energy. How fast a cloud will dissipate its gravitational potential energy dE/dt, it depends on the energy dissipated per collision ∂E and the collision frequency $f_{\rm coll}$, which can be expressed as

$$\frac{dE}{dt} = -\partial E\times f_{\rm coll}. \tag{2.65}$$

Plugging eqn. (2.39) and (2.42) leads to

$$\frac{dE}{dt} = \left(\partial E = E_{\rm coll} = -\frac{1}{2}m'v_{\rm n}^2\left(1-C_R^2\right)\right)\times\left(f_{\rm coll} = t_{\rm coll}^{-1} = n_0\sigma_0 v_{\rm coll}\right), \tag{2.66}$$

where v_n is the collision velocity between the pebbles which depends on the mass of the cloud and it plays a crucial role in the collapse. In low mass clouds (R_{solid} < 10 km) the collision velocity is lower than the onset-velocity[3] for fragmentation v_1, such that $v_n < v_1$. In such clouds the collisions result in bouncing, in which ∂E is minimum and cloud will have time enough to get virilised. Therefore throughout the collapse, the cloud remains in virial equilibrium and takes longer time to reach R_{solid}. WJJ (2014) in Fig. 5 showed that as the mass of the cloud increases (R_{solid} ~ 50 km), most of the collapsing time the cloud remains in virial equilibrium, however very lately the virial velocity becomes higher than the fragmentation velocity i.e. $v_{vir} \geq v_1$. This difference in velocities between v_{vir} and v_1 leads the cloud to fall freely with free-fall velocity v_{ff} as given in WJ 2017

$$v_{ff} = \sqrt{\frac{2GM}{R_0}}\sqrt{\frac{R_0 - R}{R}} . \tag{2.67}$$

As the starting mass of the cloud will increase, earlier the difference between v_{vir} and v_1 will occur, so earlier the collapse will enter the free-fall regime and will take less time to reach R_{solid}. For massive clouds (R_{solid} > 100 km) the v_{vir} increases immediately after the collapse and cloud will reach R_{solid} in free-fall time t_{ff}, which can be expressed as

$$t_{ff} = \frac{\pi}{2}\sqrt{\frac{R_0^3}{GM}} . \tag{2.68}$$

WJJ (2014) estimated $t_{ff} \approx 25.1$ yrs at the present orbit of Pluto. Any gravitationally bound system will have a negative heat capacity. WJ 2017 describes that as a massive cloud (R_{solid} > 100 km) contracts, the release of gravitational potential energy immediately raises the collision velocity above the fragmentation velocity $v_n > v_1$. The outcome of such collisions is intense fragmentation, in which ∂E is maximum and the collision energy is dissipated very efficiently, so the cloud contracts more rapidly, supplies more energy for fragmenting collisions. The process eventually triggers a runaway collapse, the scenario of a *gravothermal catastrophe*. The massive clouds remain in virial equilibrium for very short time, because the rapid contraction sets a higher virial velocity v_{vir} from the beginning, so the pebbles do not have enough time to catch v_{vir} and collide with each other and further raise the v_{vir}. As a result the collapse immediately becomes free-fall.

The results and implication of this model are discussed in Sec. 4.10.

---

[3] It is the minimum velocity to set fragmentation and will be introduced formally in Sec.4.3.1

Chapter 3: Experimental Setup

3.1 Drop tower
3.2 Release mechanism
3.3 Accelerators
3.4 Dust process and moulding
3.5 X-ray tomography test

3.1 The drop tower

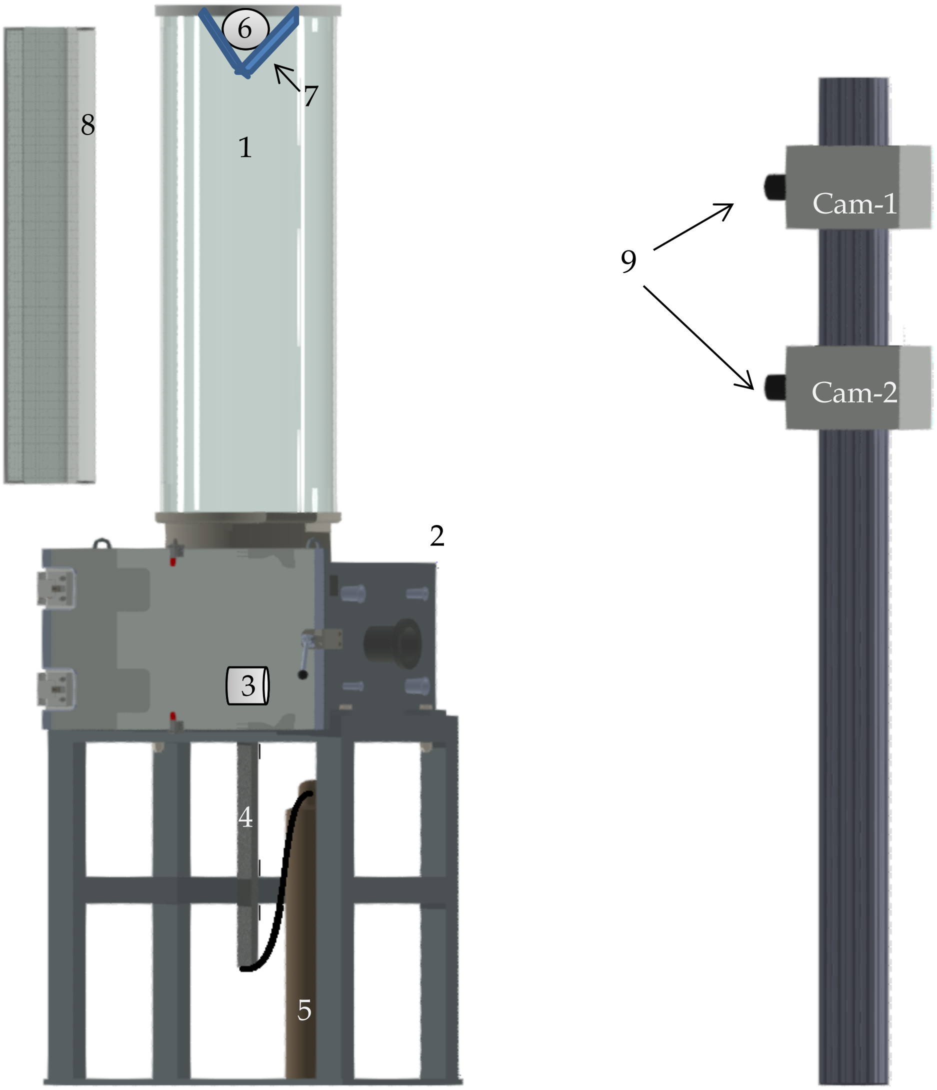

Figure 3.1. The schematic diagram of drop tower

(1) Glass cylinder
(2) Vacuum chamber
(3) Projectile dust-aggregates
(4) Pneumatic accelerator
(5) Gas cylinder
(6) Target dust-aggregates
(7) Release mechanism
(8) LED Panel
(9) High speed cameras

As discussed in Sec. 1.2 whether the growth of dust agglomerate proceeds by the so called process of sweep up (Windmark et al. 2012a) or by the mechanism of gravitational collapse (Johansen et al. 2007), studies show that the particles cm-to-dm in size within the velocity range 1 – 10 ms^{-1} play a crucial role in the evolution of dust. The suggested range of particle size and velocity is quite feasible to test experimentally. In this situation building a new experimental setup, where the collision parameters can be refined, was inevitable.

In the first phase of the project a new experimental setup was constructed. The schematic diagram of the drop tower is shown in Figure 3.1. One of the main parts of the setup is the glass cylinder (1), it has length 150 cm and diameter 50 cm which is mounted on the vacuum chamber (2). The vacuum chamber is 80 cm in length, 73 cm in width and 60 cm in height and has stainless steel body, which was delivered on order by Pfeifer Vacuum GmbH. Inside the chamber the projectile dust-aggregate (3) is placed on a sample holder which is attached to the pneumatic accelerator (4) (details in Sec. 3.3.3). The pneumatic accelerator is connected to the cylinder of nitrogen gas (5). In the next step the target dust-aggregate (6) has been loaded on the double-wing trap door release mechanism (7) (details in Sec. 3.2) which is adjusted at the top of the cylinder. Once the target and the projectile aggregates have been loaded to their respective positions, the desired collision velocity was adjusted by the time delayer and then the drop tower is evacuated in two steps. First by using the normal vacuum pump, air pressure has been decreased to a few millibar. In the second step, with the help of a turbo molecular pump the pressure has been lowered down to ~ 10^{-3} millibar.
Once the required pressure has been achieved, the whole setup is illuminated by the LED panel (8), the trigger is pressed (not shown here) and the two high speed cameras (9). Cam-1 operates as a master camera and the upper half of the drop tower is its field of view, whereas the lower half of the drop tower is in the field of view of Cam-2, which acts as slave. Both cameras record the collision at 7500 frames per second at the selected resolution 1024 × 1000 pixels.

The collision velocity can be adjusted by the time delayer (see Appendix D 3). For example; the high collision velocity was achieved by delaying the launch of the accelerator (holding projectile aggregate) by a fraction of a second after the release system has dropped the target aggregate. In this way some extra time was provided to the target aggregate to accelerate and meet the projectile in the lower half of the drop tower. For the low collision velocity the sequence of delay was reversed, the accelerator launched the projectile bit earlier. As soon as the projectile was launched, gravity starts to decelerate it. Once it has achieved the maximum height, where it was virtually suspended, the release mechanism dropped the target aggregate. In this way, low-velocity collisions took place on the upper half of the drop tower.

Once the experiment has been accomplished, it has been made sure that the debris of dust, in particular the fine dust grains inside the chamber, do not contaminate the air in laboratory. Therefore, immediately after the refilling of air the whole setup has been connected to the industrial vacuum cleaner (see Appendix D 5), which maintains the low pressure inside the chamber and enables the experimenter to clean up the setup.

The drop tower in live operation has been published in JoVE, hereafter Blum et al. (2014) and for more images see Appendix D

3.2 Double-wing trap door

In order to release of the target aggregate from top, a mechanism was required which would safely hand over the target aggregate of any size to the gravity. For this, a device called double-wing trap door, a release mechanism has been designed. In Figure 3.2(a) one can see the close view of the double-wing trap door system. The whole system consists of doors (1), a solenoid magnet (2), the lock lever (3) and the Eddy-current brakes (4). A simulant[4] (S) is laid on the closed doors, as the trigger is pressed, the solenoid magnet rotates the lock lever by 90° and the doors are opened and the target aggregate is dropped as shown in Figure 3.2 (b).

In order to avoid the bouncing of the doors the Eddy-current brakes (4) have been used at the pivot of each door. Brakes do not only avoid the bouncing but provides a wide passage to the free falling target aggregate as shown in Figure 3.2 (b) (for live view see Blum et al. (2014)). The whole system sets the target aggregate in a free fall which is free from any rotation or tilt. The release mechanism has been fixed to the flange which acts as a ceiling of the cylinder as shown in Figure 3.2 (c) holding the simulant aggregate (S).

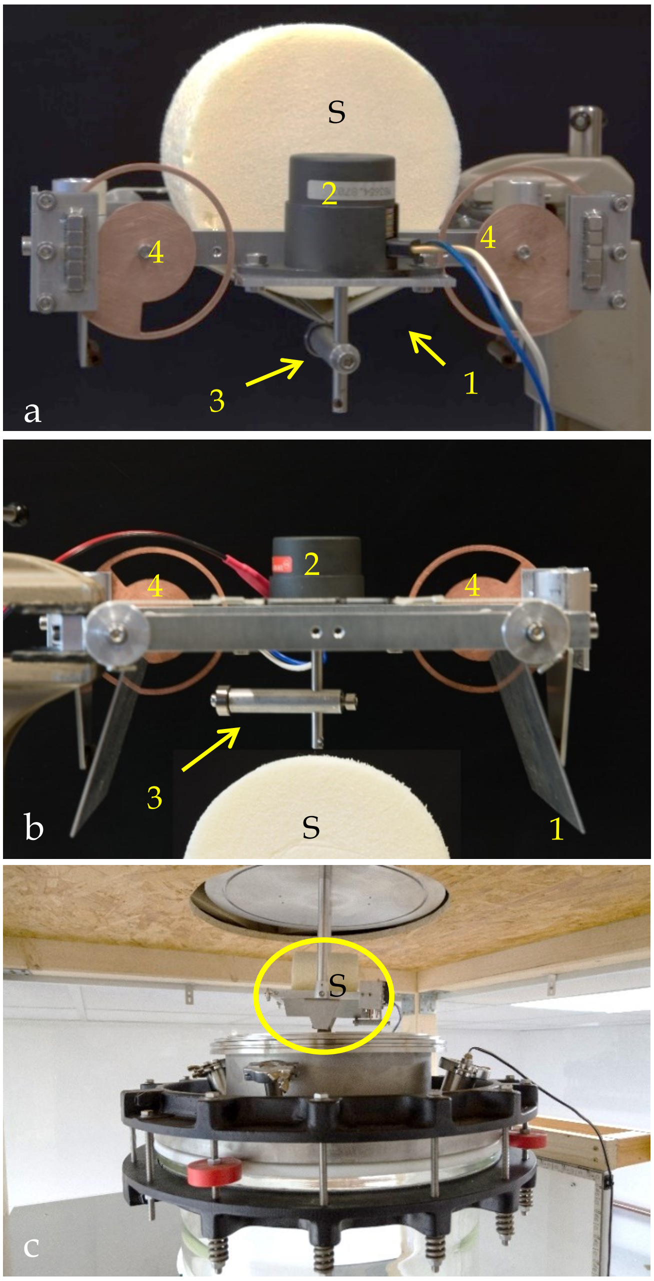

Figure 3.2. (a) The details of the device: (1) Doors, (2) Solenoid magnet, (3) 90° rotatable lock lever and (4) the Eddy current brakes (b) The door have been opened and the simulant is dropped. (c) The release mechanism fitted to the ceiling flange of the glass cylinder holding the simulant aggregate (S).

---

[4] A simulant is a styrofoam material used as an analogue to actual dust aggregate, for calibration.

3.3 Accelerators

Although the aggregates compressed to filling-factor 0.35 are considered relatively compact, but they are still fragile and vulnerable even to a slight vibration. Therefore contrary to the release of target aggregate, accelerating the projectile has not been straightforward. Therefore several accelerators have been tried as discussed in the following.

3.3.1 Electromagnetic accelerators

In the beginning, an electromagnetic accelerator shown in Figure 3.3 was used in the first run of experiments. The collision series 5 cm – 5 cm, presented in Sec. 4.2, has been accomplished by using electromagnetic accelerator.

The accelerator was purchased from Metronix Meßgerät und Elektronik GmbH. It consists of a sledge (1) which is electromagnetically guided over a track of 1040 mm (2). The shaft (3), which operates partially in air and partially in vacuum, is fitted on the hovering sledge that remains outside the vacuum chamber. With the provided software one could easily adjust the desired acceleration and reach the maximum velocity 5 m s^{-1}.

However in some cases the selected parameters (e.g., current at linear motor for the desired velocity) were not effective when the device was subjected to vacuum and air simultaneously.

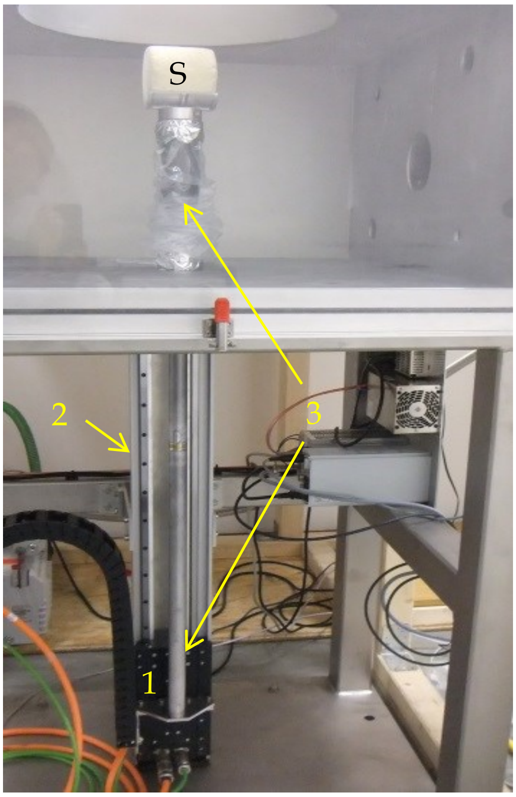

Figure 3.3. The electromagnetic accelerator at home position. (1) Sledge (2) Track (3) Shaft and (S) simulant. It has been used for the study of collision series 5 cm – 5 cm

As one can see in Figure 3.3 that a part of the shaft (3) is in air and a part inside the chamber. High vacuum inside the chamber further accelerated the shaft upward, therefore for deceleration a high current at the motor had to be applied, which induced undesirable jitter motion and resulted in pre-collision cracks in the projectile aggregate and in some cases complete fragmentation when the projectile was less massive.

Figure 3.4 (a) the red curve shows the current supplied to the linear motor as a function of time when operated in air. The encircled region (1) of the curve shows a supply of constant current to the linear motor, as a result the sledge smoothly moves upward with the desired velocity. The green curve stands for the velocity of the sledge, which reaches to its maximum value when the sledge has achieved the desired height. Once the sledge has reached the desired height, the polarity of the current to the motor is reversed and sledge again with constant current (2) recedes to the home position as shown in Figure 3.3.

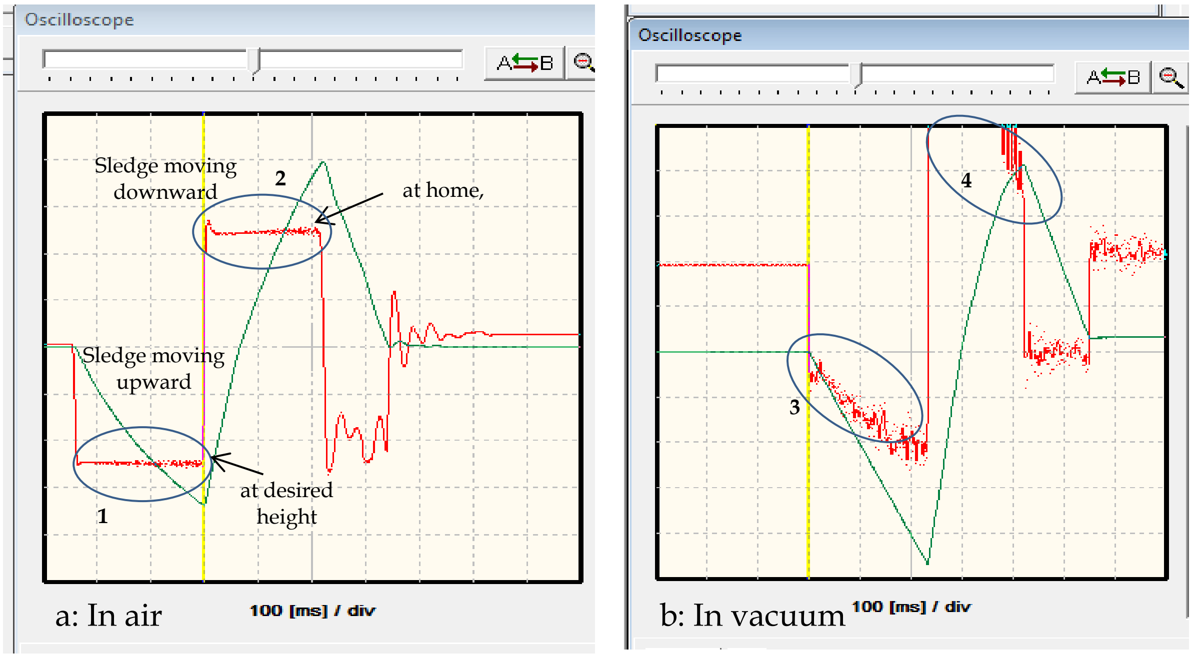

a: In air

b: In vacuum

Figure 3.4. The curves of electric current and velocity on oscilloscope. **(a)** The red curve, which has units on y-axis 2A/div, shows (1) a supply of constant current to linear motor when sledge is moving upward. Once the desired height is attained, the polarity of the current is reversed, (2) a constant current is supplied and sledge recedes downward to home position. The green curve is the velocity of the sledge and it has units on y-axis 1000 mm/s/div. **(b)** As the accelerator was operated in vacuum and air simultaneously, (3) the supply of current could not be constant, the motor drew more current to counter the extra acceleration due to the vacuum inside the chamber and the same was true when sledge was moving downward (4). The high fluctuation in the supply of electric current induced jitter motion and fragmented the projectile before the launch.

However when the device was operated in high vacuum, the current at the motor started to fluctuate, the encircled region (3) of the red curve shown in Figure 3.4(b). The vacuum inside the chamber pulled the shaft with some acceleration, therefore the motor drew more current for the deceleration of the sledge and to counter the effect of vacuum.

Although the desired velocity ~ 5 ms^{-1} was reached but the journey has not been smooth for the projectile aggregate, hence it fragmented before collision. Thus the success rate of launching an intact projectile was not so high.

3.3.2 Spring based accelerator

The electromagnetic accelerator was replaced with a spring based accelerator which is shown in Figure 3.5. It is simple in design; a spring (not shown here) which is fitted inside the cylinder, has been compressed and the projectile aggregate is placed on the sample holder. The spring is released with the help of a solenoid magnet fitted at the bottom of the cylinder.

In addition to its low cost, it was relatively easier in operation. However the setback appeared in the length and strength of the spring. For this study the projectiles of various masses had to be tested, mass range varied on the order of 10^3. Therefore within the given experimental conditions no single spring available in market could cover this range. The spring with shorter length and higher strength was suitable for massive projectiles ~ 700 g but catastrophic for the low mass ~ 0.7 g. In the case of the longer spring with lower strength, a slight twist got stored during compression. This twist, which was released with the spring, induced undesired rotation in the projectile. Hence, this was replaced with the pneumatic accelerator.

Figure 3.5. The spring based accelerator, holding a simulant projectile (S). A spring, which was compressed by hand, is released by a lever which is controlled with solenoid magnet, fitted at the bottom of the system.

3.3.3 Pneumatic accelerator

Figure 3.6. shows the pneumatic accelerator carrying a simulant aggregate (S). The pneumatic accelerator consists of a simple shaft, housed in an aluminium casing (1) which is connected to the gas cylinder (2). As the trigger is pressed the solenoid valve (3) opens and high pressure is delivered to the casing which lifts the shaft upward with high speed.

In practice the pressure 7 – 8 bar was high enough to shoot a 5 cm projectile aggregate with velocity ~9 – 10 $\mathrm{m\,s^{-1}}$. Since its commissioning more than 200 experiments have been conducted, neither pre-collision cracks nor rotation or any sort of tilt has been observed. It has successfully launched the projectiles of various sizes. The device is cheaper in cost and being simple in design it required minimum efforts for maintenance.

Figure 3.6. The pneumatic accelerator (1) Aluminum casing (2) Bottle of nitrogen gas (3) Solenoid valve (S) Simulant

3.4 Dust processing and moulding

The dust used in this study is silicon dioxide (SiO_2). According to the manufacturer Sigma-Aldrich GmbH, product ID S-5631. The dust is crystalline (SIGMA-ALDRICH 2012) and it has 99% of grain size 0.5 – 10 μm (approx. 80% between 1-5 μm) and material density 2.65 $\mathrm{g\,cm^{-3}}$. The dust powder provided by the company has lumpy structure and hence requires processing, which is explained in following three steps.

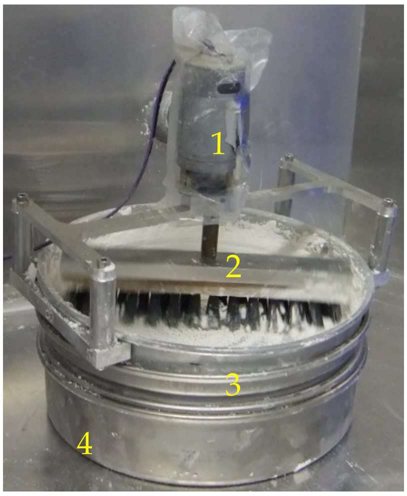

Figure 3.7. Sieve of 500 μm mesh

Step 1: Sifting

The dust aggregates must be homogenous in compression and should be free from internal structures. In order to remove the lumps the dust is required to be sifted.

For this purpose an electric sieve has been designed, which has mesh size 500 μm as shown in Figure 3.7.

It consists of four parts; a brush (2) which is fitted to an electric motor (1) and both parts are mounted on the mesh. The dust poured onto the mesh is grinded and collected in the container (4).

Figure 3.8. Digital scale

Step 2: Weighing

The sieved dust is weighted, for the mass m required for the given dust aggregate, such that

$$m = \rho \cdot V \cdot \phi \, .$$

Here $\rho = 2.65\ \mathrm{g\,cm^{-3}}$ is the material density, V is the volume of the given aggregate and ϕ = 0.35 is the volume filling-factor, which has been fixed for every sample. A digital scale shown in Figure 3.8 has been used to weigh the dust.

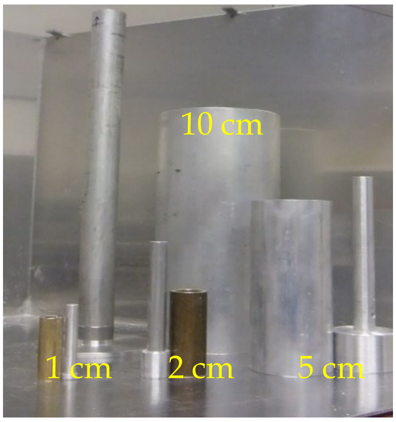

Figure 3.9. Sample moulds

Step 3: Moulding

Figure 3.9 shows the moulds of various sizes. Once the dust is sifted and weighted, it is poured into the mould of the respective size. With the help of a piston dust is slowly compressed till the required size of sample is reached. The mould is turned upside down and the compressed dust aggregate is taken out. The live view of dust processing has been shown in Blum et al. (2014)

The outcome of dust and moulding process is shown in Figure 3.10.

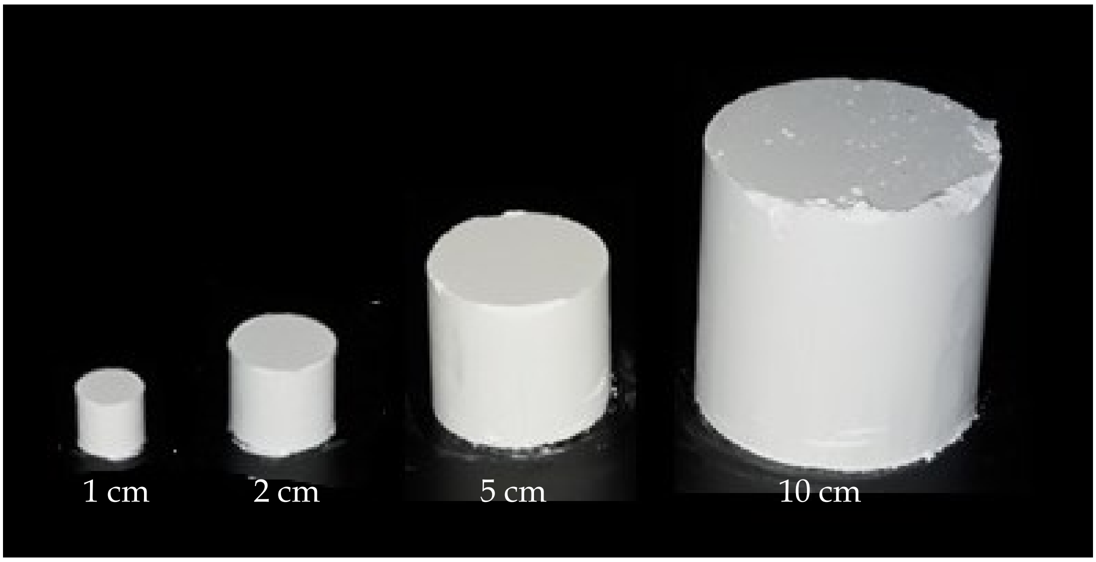

Figure 3.10. The dust aggregate of various sizes but fixed filling-factor, i.e., $\phi = 0.35$ have been produced by the procedure discussed above, which will be used as a projectile and target.

3.5 X-ray Tomography

The volume filling-factor ϕ, is defined as the ratio of the density of the dust aggregate to the density of the material (2.65 $\mathrm{g\,cm^{-3}}$). In this study the value of the filling-factor remains fixed to $\phi = 0.35$. The experimental studies, e.g. Beitz et al. (2011) as well as the numerical studies e.g. Meru et al. (2013) have shown that variation in filling-factor dramatically change the collision outcome. Therefore it has been carefully controlled throughout the dust processing.

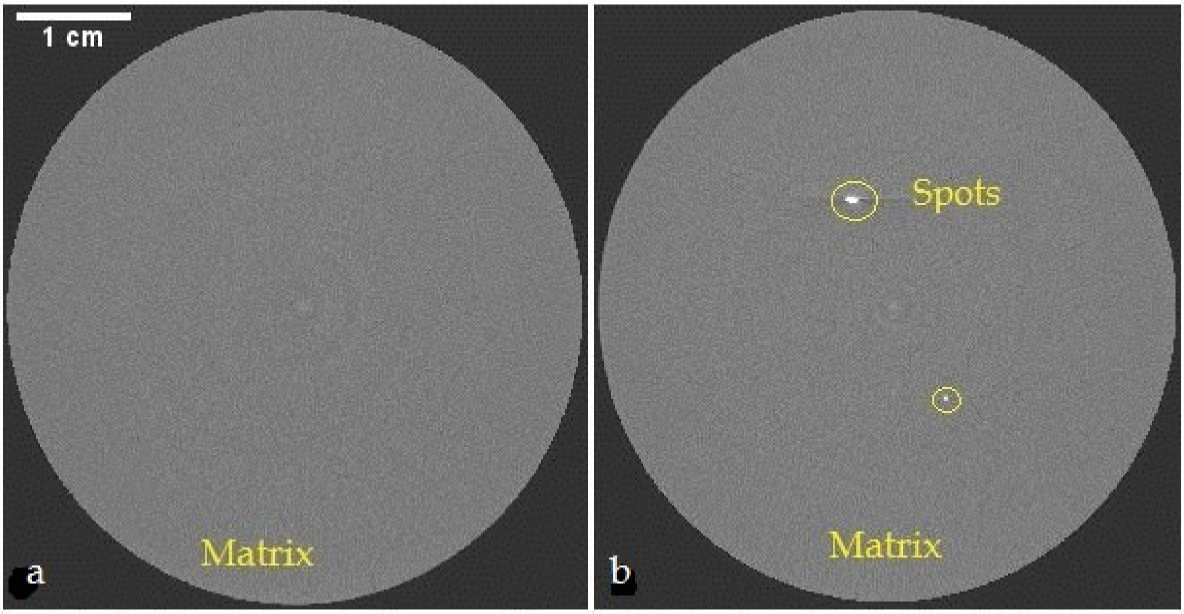

Figure 3.11. The XRT-reconstruction of a 5 cm dust aggregate. **(a)** It is the cross-sectional view of the sample. The homogenous grey matrix has mean filling-factor $\overline{\phi} = 0.35 \pm 0.02$. (b) It shows that there are some dense regions which appear as bright spots of higher filling-factor $\phi \sim 0.56$. These spots are randomly scattered over the length of 5 cm (BS 16b).

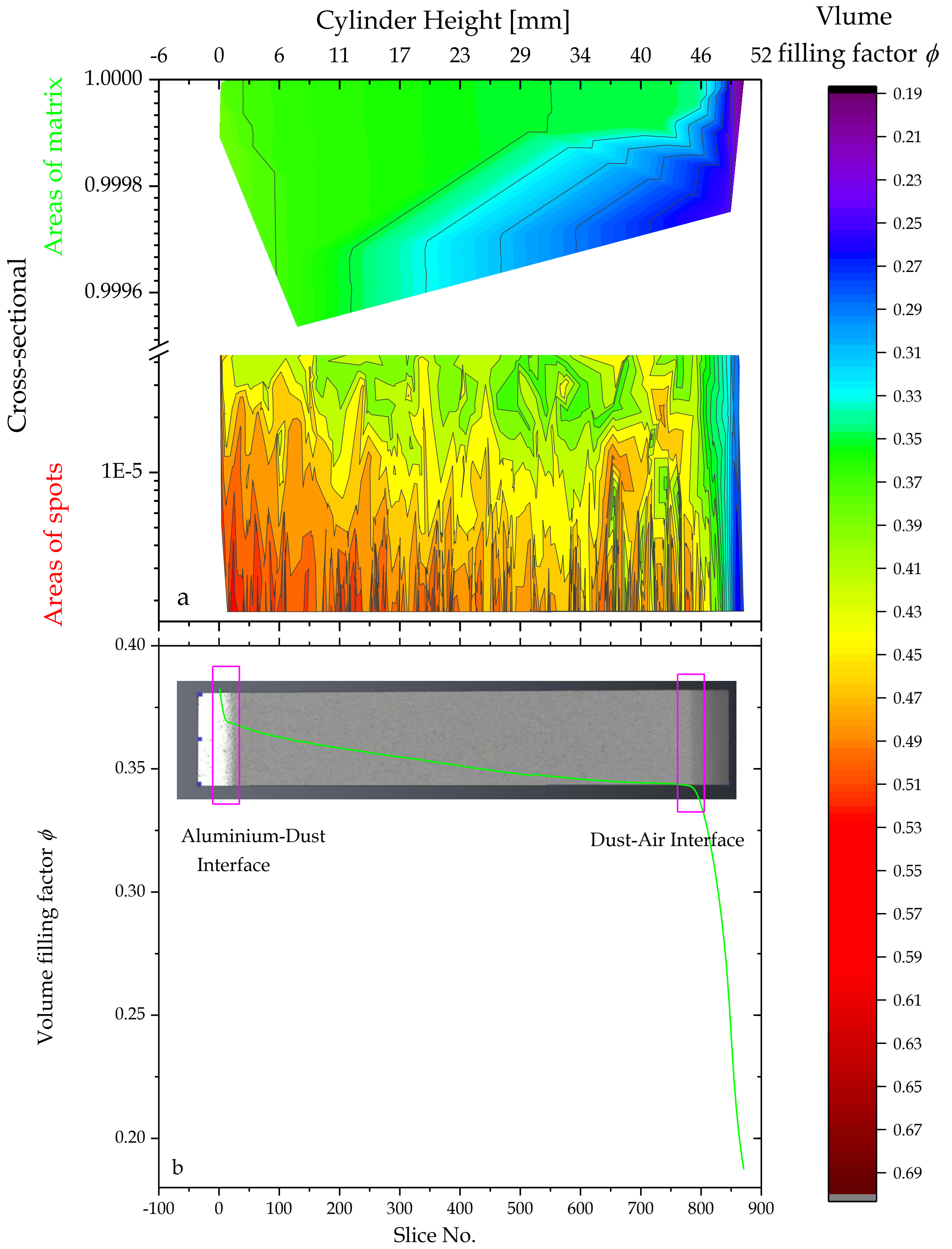

Figure 3.12. (a) The y-axis is the relative cross sectional area of the aggregate as a function of its symmetry axis of 5 cm in length (averaged over XRT–images each of length ~ 57 μm). The z-axis shown in colours is the volume filling-factor of the corresponding region. The y-axis has been split into two parts, the upper y-axis refers to the relative area of the matrix, which has mean filling-factor $\bar{\phi} = 0.35$ and largely falls in the green region of the spectrum. Whereas the lower y-axis is the relative area of the bright spots, which has mean filling-factor $\bar{\phi} = 0.56$ and largely falls in the red region of the spectrum. However the bright spots are ~ 10^{-5} smaller than that of the matrix.
In **(b)** the green line shows the volume filling-factor of the aggregate along the length of the cylinder. The inset is the global profile of XRT–image of the sample. The marked boxes in the inset are supposed to be the x-ray reflections: (left) from the interface between the aluminium sample holder and the dust sample, (right) from the interface between dust sample and air (BS 16b).

To see whether the compressed dust-cylinders have the same fill factor i.e. $\phi = 0.35$ the XRT-test were performed on the dust aggregates of 5 cm.

Figure 3.11 (a) and (b) are the reconstruction of X-ray tomography. The homogenous grey matrix is the cross sectional area of 5 cm aggregate. The standard deviation of the whole aggregate over the length of 5 cm varies only by 5 to 6%, which translates into $\Delta\phi = \pm 0.02$ relative to the mean filling-factor $\bar{\phi} = 0.35$. However there are also some dense regions of relatively high filling-factor which appear as bright spots as shown in Figure 3.11 (b). These bright spots are sporadic across the 5 cm length of aggregate. The mean filling-factor of these spots is $\bar{\phi} \sim 0.56$ and reaches up to $\bar{\phi} = 0.68$. However the impact of these highly dense regions on the collision outcome is negligible. In Figure 3.12(a) one can see the relative area of the bright spots, shown on the lower y-axis, is on the order of 10^{-5} smaller as compared to the area of the grey matrix, shown on the upper y-axis. Whereas the colour spectrum shows the filling-factor of the corresponding region.

Figure 3.12(b) shows the global profile of the entire dust aggregate of size 5 cm. Here one can see that the regions of higher filling-factor and the lower filling-factor tend to lie on the ends of the aggregate. The slightly higher filling-factor $\phi \sim 0.38$, in the first 15 images (or 0.92 mm from the bottom of the cylinder) could be an artefact due to the x-ray reflection from the interface between the aluminium sample holder (on which the aggregate was placed) and the dust sample. The declining value of filling-factor $\phi \sim 0.19$, starting from slice ~ 800 (or 46 mm from the bottom) can be associated to the x-ray reflection from the interface between dust aggregate and air. However over the effective length of the sample between slice 15 and 800, the length which has to participate in the collision, the slice-averaged filling-factor decreases from $\phi = 0.37$ to $\phi = 0.33$. The overall decline in filling-factor from left to right could be associated to the unidirectional compression (Beitz et al. 2013).

Schräpler et al. (2012) has also performed the XRT analysis of their 5 cm dust aggregate, which was produced by a procedure slightly different than the one used in this study. However the profile curve of the filling-factor, shown in their Figure 2, and its feature are very identical to the one shown in Figure 3.12(b). They found the maxima of the curve at $\phi = 0.38$ (same as here) and the minima $\phi = 0.17$ (0.19 in this study).

It confirms that the new procedure of dust processing discussed in Sec. 3.4 can produce the dust aggregate on "industrial scale" and maintains the quality of homogeneity as high as described in Schräpler et al. (2012).

Chapter 4: Results and Analysis

4.1 Collision parameters and collision series
4.2 Fragmentation strength μ
4.3 The model of fragmentation strength μ
4.4 The relative collision strength Q^*
4.5 The probablity funtion of mass transfer
4.6 Area-frequency distribution
4.7 A complete model of area-frequency distribution
4.8 Mass-frequency distribution
4.9 The model of fragment velocity distribution
4.10 The grand fragmentation model

A large part of this chapter has been published in Bukhari Syed et al. (2017) hereafter BS 17. The unpublished data presented in Sec. 4.10.1 has been provided by *Lund Observatory, Sweden*.

4.1 Collision parameters and collision series

In this section, the list of all 142 experiments, collision parameters, projectile size P, target size T and impact velocity v_n are presented. These experiments are grouped in 8 series. In the first three series, the collision between same size aggregates has been studied, where the size ratio f between target and projectile is $f = 1$, such as 1 cm – 1 cm, 2 cm – 2 cm and 5 cm – 5 cm.

Table 4.1. The collision parameters taken in this study. The target T and the projectile P both are in cylindrical form and have equal height and diameter. Here CF stands for catastrophic fragmentation, in which projectile and target aggregate both fragment, whereas MT stands for fragmentation with mass transfer. In this case only projectile fragments and a part of its mass has been transferred to target, whereas the target remains completely intact.

No.	**Series Name**	**Size ratio f**	**No. of Experiment**	**Velocity Range [m s^{-1}]**	**Outcome**
1	1.0 cm – 1.0 cm	1.0	13	2.1 – 5.3	MT+CF
2	2.0 cm – 2.0 cm	1.0	18	2.0 – 6.0	MT+CF
3	5.0 cm – 5.0 cm	1.0	21	2.0 – 6.2	CF
4	1.0 cm – 2.0 cm	2.0	10	2.2 – 7.7	CF
5	1.0 cm – 2.6 cm	2.6	19	2.5 – 5.7	MT+CF
6	1.0 cm – 5.0 cm	5.0	21	3.6 – 8.7	MT+CF
7	2.0 cm – 5.0 cm	2.5	24	1.6 – 7.1	MT+CF
8	3.5 cm – 5.0 cm	1.4	16	1.5 – 4.4	CF

Camera details

Image Res.	**Pixel Scale**	**Optic**	**Frames per second**
1020 x 1024	1cm = 24 pix	84mm Nikon	7500

In the rest of the 5 series the collisions between unequal size aggregates, i.e. $f > 1$, for example; 1 cm – 2 cm, 1 cm – 2.6 cm, 1 cm – 5 cm, 2 cm – 5cm and 3.5 cm – 5 cm have been studied. Here it should be mentioned that the series 1 cm – 2.6 cm is a test series, which was incorporated later into the analyses, because a comparison with the series 2 cm – 5 cm was desired. Since both series have similar f value, they can be useful in understanding the collision of different size aggregates but same size ratio. Figure 4.1 presents the raw images for an impression of a real collision as recorded by the camera. In the post-collision scenario, in all the 8 series, two collision outcomes have been observed; one catastrophic fragmentation (CF) shown in Figure 4.1(b) and the second outcome is the fragmentation with mass transfer (MT), see Figure 4.1(d).

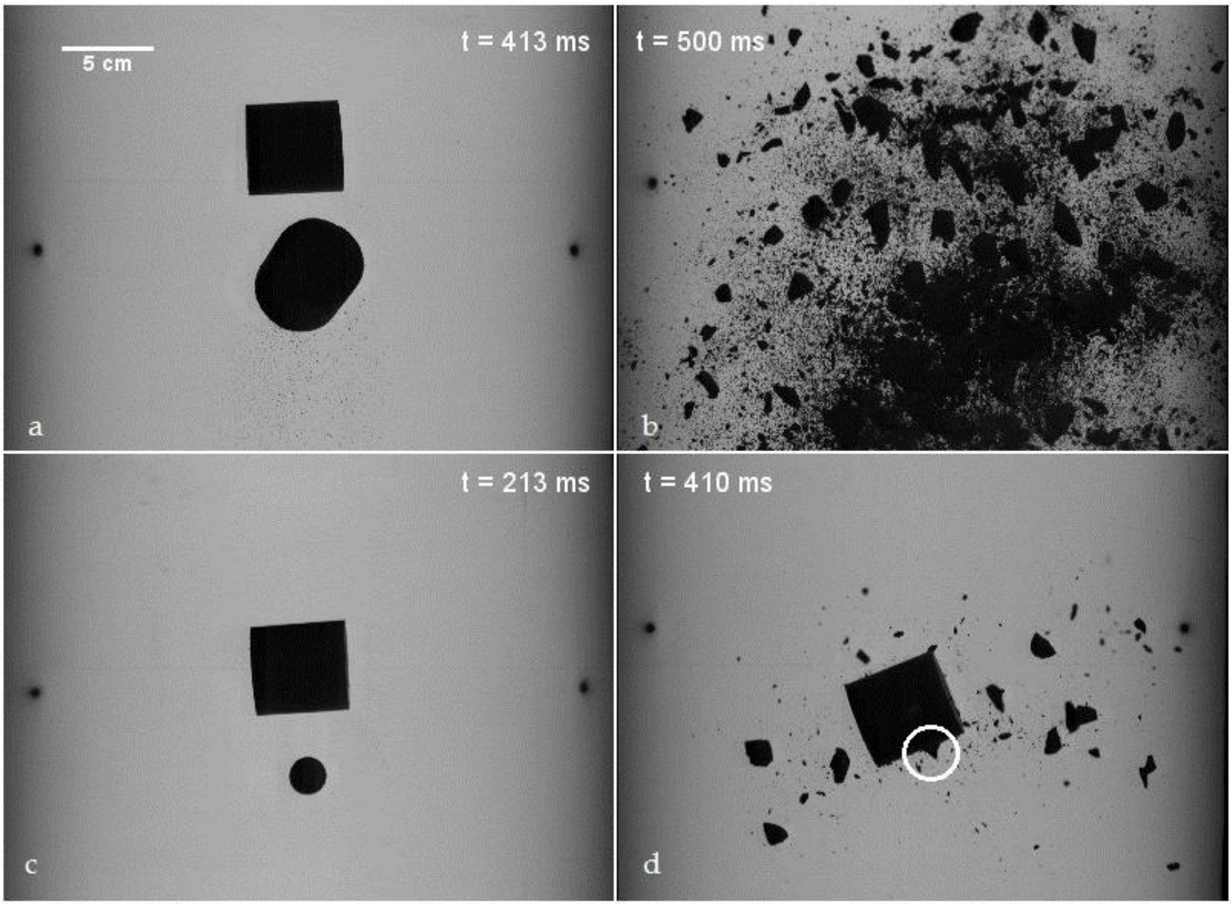

Figure 4.1. The representative snapshots of pre-collision and post-collision scenario. (a) The pre-collision scene of same size aggregates 5 cm – 5 cm colliding at 6.2 ms^{-1}, which normally ends in a catastrophic fragmentation (b). In the collisions of higher size ratio aggregates such as in (c), where 2 cm projectile collides with 5 cm target at 2.8 ms^{-1}, the probability of mass transfer is relatively high and target will survive. The cone highlighted in (d) is the typical sign of mass accreted onto the target (BS 17).

The geometry of the collision has been set in such a way that neither of the symmetry axis point in the velocity direction. The target, which is dropped from the top, projects a rectangular shape onto the camera as shown in Figure 4.1(a)(c), while the projectile shot from bottom appears as a circle, as shown in Figure 4.1(c). This setup provides minimum contact area between the aggregates at first contact and imitates the conditions as two spheres were colliding. But in practice it has been challenging to preserve these conditions, first due to the slightly inherent nonalignment along the line joining the centre of release mechanism and the accelerator. Second if the aggregates were improperly placed to their respective positions, the effect of rotation of the aggregate and nonalignment became prominent. The 5 cm projectile in Figure 4.1(a) is slightly tilted because the series 5 cm – 5 cm was completed by using the electromagnetic accelerator shown in Figure 3.3. However, these problems bring the controlled experimental conditions more close to reality. For the material properties of the dust aggregates see Sec. 3.4.

4.1.1 Impact parameter

The above mentioned complications of nonalignment gave rise to impact parameter, which has x and y components. Due to the limitation of the experimental design only the x-component (on the plane parallel to the camera) has been accessible. Hence the impact velocity has been corrected for the impact parameter b. Therefore in the analysis the normal component v_n of the relative velocity v_{rel} has been taken into account, which is given by

$$v_n = v_{rel} \cdot \sin\left(\arctan\left(\frac{b}{r_p + r_t}\right)\right), \tag{4.1}$$

where r_p and r_t are the radii of the projectile and the target respectively. Figure 4.2 shows the cumulative distribution of the velocities investigated in this study. One can see that the velocities tested in each collision series are homogenously distributed. The mean impact velocity in all series, with the exception of the series 1 cm – 5 cm, is $\bar{v}_n \sim 4.51$ ms^{-1}. The reason, that the series 1 cm – 5 cm in cyan-dashed-dotted has higher velocity, is the higher fragmentation threshold velocity $v_{0.5}$ owing to very high size ratio (details in Sec. 4.3.1 and 4.4.2). However the velocities are within the range of collision velocities in the collapsing cloud discussed in Johansen et al. (2009).

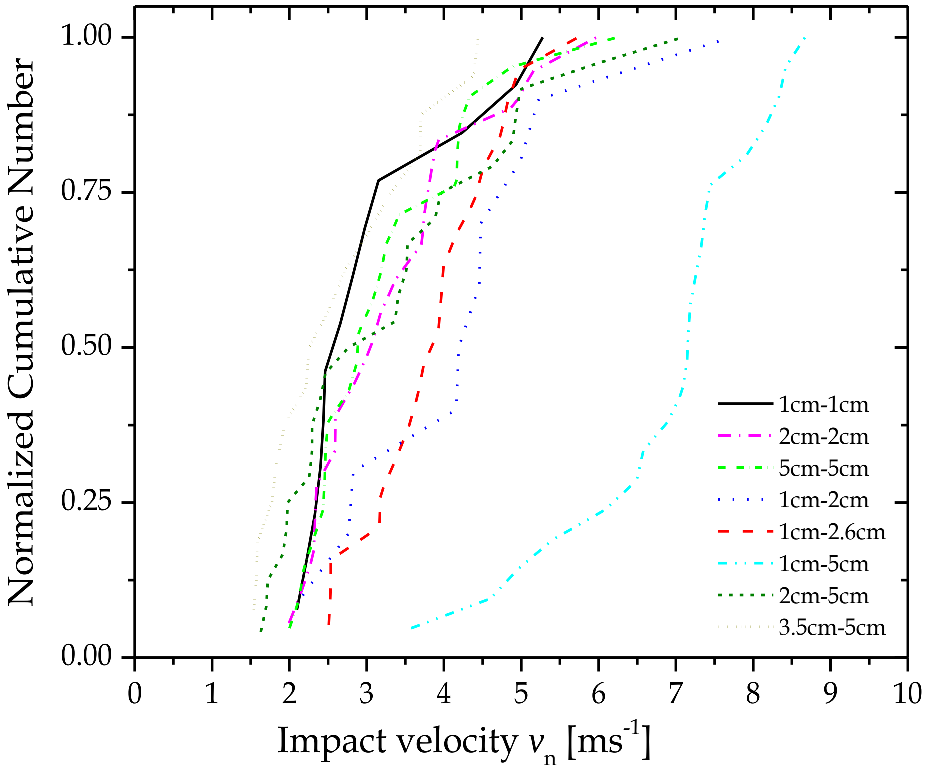

Figure 4.2. The normalised cumulative velocity distribution for all 8 series, it has mean impact velocity $\bar{v}_n = 4.51$ ms^{-1} (BS 17).

4.2 Fragmentation strength μ

In each collision the fragmentation strength of the collision, represented by μ, has been determined. As previously introduced by Beitz et al. (2011) the μ can be defined as a mass ratio of the largest fragment m_l observed in the collision to the initial target-mass m_t, such that

$$\mu = \frac{m_l}{m_t} . \tag{4.2}$$

Every collision, in principle, can have three possible outcomes; (1) catastrophic fragmentation when $\mu < 1$, (2) bouncing $\mu = 1$ and (3) mass transfer $\mu > 1$. It is summarised as follow

$$\mu \begin{cases} <1 & \text{fragmentation} \\ =1 & \text{bouncing} \\ >1 & \text{mass transfer} \end{cases} \tag{4.3}$$

Here it should be mentioned that the bouncing event has never been observed in this study, only the events of catastrophic fragmentation and mass transfer have been observed and hence remain the focus of discussion.

Contrary to the previous studies where μ has been analysed as a function of impact velocity, here it has been analysed as a function of kinetic energy E_{cm} at the centre of mass-system, because the role of mass in determining the μ (details in Sec. 4.3.1) can be observed. Hence one can write

$$E_{\mathrm{cm}} = \frac{1}{2} m' v_{\mathrm{n}}^{2} \quad , \tag{4.4}$$

where v_{n} is the normalised velocity given in eqn. (4.1) and m' is the reduced mass of the projectile-target system that is

$$m' = \frac{m_p m_t}{m_p + m_t} . \tag{4.5}$$

Here m_p and m_t, are the masses of projectile and target respectively.

4.3 The model of fragmentation strength μ

In previous studies a power law has been used to analyse the fragmentation strength and to determine the catastrophic threshold energy $E_{0.5}$, the energy required to half the target (see , e.g. Ryan et al. (1991)). Here the Hill-function, given in eqn. (4.6) is used, which interprets well to the data presented in Figure 4.3. Contrary to previous studies, the reason of using a Hill function is the assumption that the data fitting well to the power law has been a local behaviour of a global trend, and the regime where our collisions parameters lie, may not be explained merely by the power law (details in Sec. 4.3.1). Therefore the fragmentation strength μ can be modelled by using the Hill function such as

$$\mu\left(E_{\mathrm{cm}}\right) = 1 - \frac{E_{\mathrm{cm}}^{n}}{E_{0.5}^{n} + E_{\mathrm{cm}}^{n}} \quad , \tag{4.6}$$

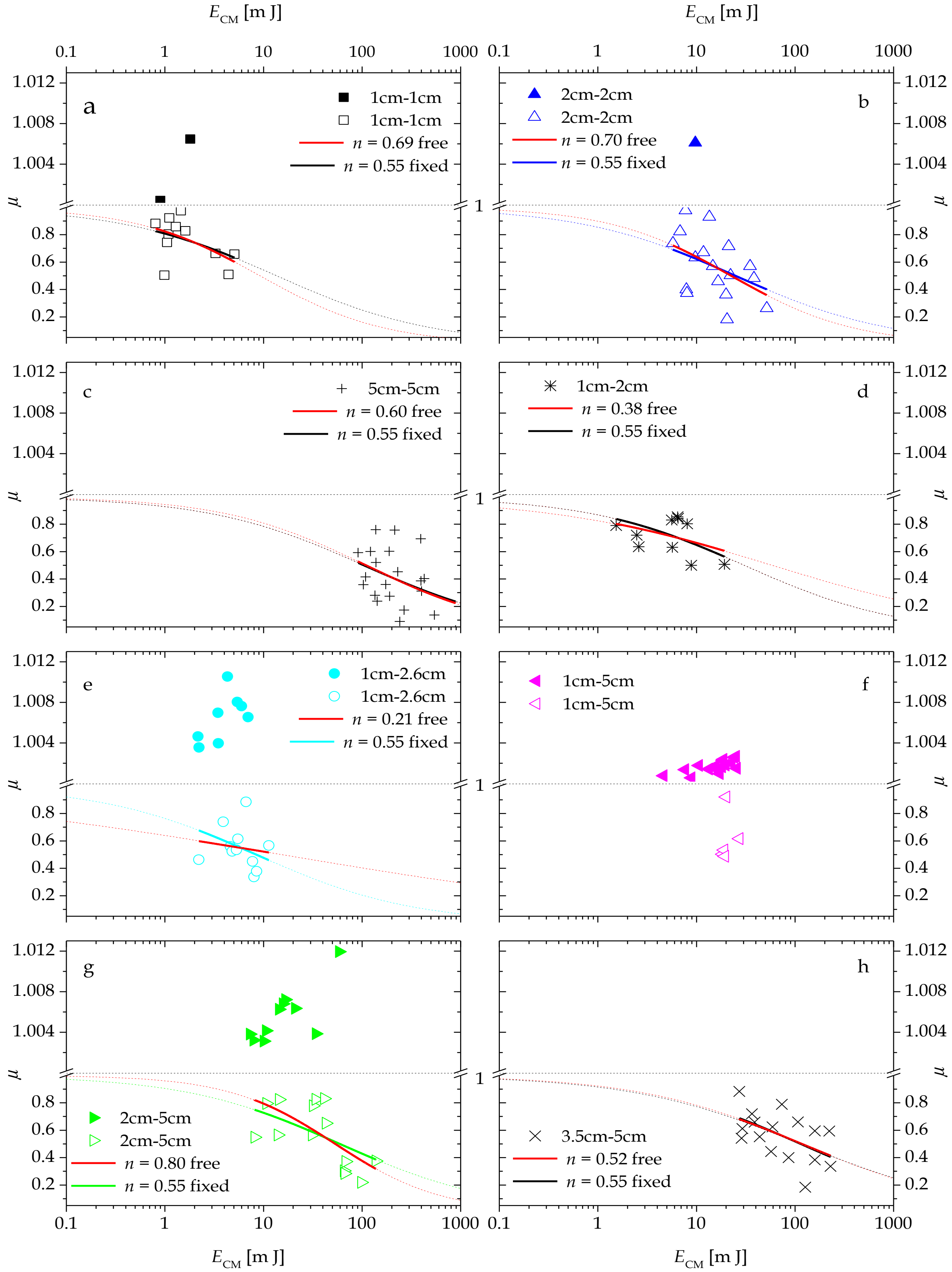

Figure 4.3. The Fragmentation strength μ as a function of centre of mass kinetic energy E_{CM}. Here the Hill function eqn. (4.6) has been fitted twice. First for n as a free parameter, shown in red-solid line. Second for the mean value $\bar{n}$ = 0.55 shown with the curve in the colour of the data points. The resulting values of $E_{0.5}$ in both cases are given in Table 4.2. Whereas the dotted lines are the extrapolation of the respective fit within the range of 0.1-1000 mJ. The y-axis has been split into two regions at μ = 1 and a black-dotted line stands for bouncing. It separates the region of mass transfer for μ > 1, shown with filled data points, from the region of fragmentation for μ < 1, shown with open data points. Due to the fewer data points in series 1 cm – 5 cm series, the Hill function could not be fitted. Hence the mean of the energies corresponding to μ = 0.5 has been taken, which has value $E_{0.5} \approx$ 19 mJ **(BS 17)**.

where n is the free parameter, which describes the dependency of fragmentation strength μ on collision energy. In Figure 4.3, the function has been elaborated by the two dotted curves, which extrapolates the Hill-function within the range 0.1 mJ to 1000 mJ. One can see as collision energy decreases, both curves asymptotically approaches to $\mu = 1$, to its natural limit. This asymptote, is assumed to lead to the bouncing regime where $\mu = 1$, shown in black-dotted grid line in Figure 4.3. In other words the dotted lines are predicting the collision energies where the given aggregates should bounce. As the collision energy increases, now depending on the size ratio, the curve would follow either positive slope (growth case $\mu > 1$) above the bouncing line or the negative slope (fragmentation $\mu < 1$) below the bouncing line. However at infinitely high collision energy the Hill curve flattens as well i.e. $\mu \rightarrow 0$, but the velocities tested here do not reach to such extant. On the basis of eqn. (4.6) a smooth transition is expected, whether it is from bouncing to growth or bouncing to fragmentation. Here the Hill-function is thought to be the closest approach for a function which can account simultaneously the events of fragmentation, bouncing and growth. In addition to the successful interpretation of the data it also has the advantage of yielding the catastrophic threshold energy $E_{0.5}$ directly, which plays a crucial role in determining the relative collision strength Q^* (see Sec. 4.4)

In Figure 4.3 the Hill function has been used in two steps. In first step the exponent n, has been treated as a free parameter, shown in red-solid curve. The value of n varies between $n \sim 0.2$ to $n \sim 0.8$, as shown in Table 4.2. In second step the mean value $\bar{n} = 0.55 \pm 0.11$ has been used and eqn. (4.6) is re-fitted for n fixed to its mean value for all the series (except 1 cm – 5 cm), the fit is shown with the solid-curve in the colour of data points. The corresponding new energy values $E_{0.5}$ ($\bar{n} = 0.55$) are shown as well in Table 4.2.

Table 4.2. The Hill-function has been fitted twice, first for n as a free parameter and second time for $n = 0.55$. The resulting correlation between fragmentation strength and collision energies, in both cases are shown in Figure 4.3. Due to fewer data point in the series 1 cm – 5cm, the value of $E_{0.5}$ is an estimation. Q^* is the relative collision strength which is proportional to $E_{0.5}$ (details in Sec. 4.4) and it inherits the error of $E_{0.5}$ such that $\Delta Q^* = (\Delta E_{0.5} \cdot Q^*)/E_{0.5}$

No.	Series	$E_{0.5}$ [mJ]	n	$E_{0.5}$ ($\bar{n} = 0.55$)	Q^*[J /kg]
1	1.0 cm – 1.0 cm	9.20 ± 7.70	0.69 ± 0.36	13.58 ± 5.57	18.61 ± 7.63
2	2.0 cm – 2.0 cm	22.52 ± 7.84	0.70 ± 0.35	24.82 ± 9.10	4.28 ± 1.57
3	5.0 cm – 5.0 cm	109.43 ± 50.21	0.60 ± 0.34	104.10 ± 34.06	1.14 ± 0.37
4	1.0 cm – 2.0 cm	58.24 ± 109.63	0.38 ± 0.31	30.42 ± 11.08	5.24 ± 1.91
5	1.0 cm – 2.6 cm	15.27 ± 37.32	0.21 ± 0.47	8.43 ± 3.02	0.67 ± 0.24
6	1.0 cm – 5.0 cm	~ 19.0	-	~ 19.0	0.21
7	2.0 cm – 5.0 cm	53.42 ± 14.97	0.80 ± 0.30	59.40 ± 21.65	0.65 ± 0.29
8	3.5 cm – 5.0 cm	117.29 ± 43.88	0.52 ± 0.23	114.24 ± 33.20	1.26 ± 0.36

In the case of the series 1 cm – 5 cm, owing to fewer data points, the Hill function could not be applied and $E_{0.5}$ has been approximated to $E_{0.5} \approx 19$ mJ. However in other series the catastrophic fragmentation energy varies from $E_{0.5} \sim 10$ mJ to $E_{0.5} \sim 117$ mJ.

First the three series of equal size aggregates 1 cm – 1 cm, 2 cm – 2 cm and 5 cm – 5 cm, with size ratio $f = 1$, were analysed and shown in Figure 4.3 (a), (b) and (c) respectively. In next step the series of unequal size aggregates, where $f > 1$, such as 1 cm – 2 cm, 1 cm – 2.6 cm, 1 cm – 5 cm, 2 cm – 5 cm and 3.5 cm – 5 cm have been analysed, as shown in Figure 4.3 (d), (e), (f), (g) and (h) respectively. Figure 4.3 shows that, the series where the size ratio $f > 2$, such as 1 cm – 2.6 cm, 2 cm – 5 cm and 1 cm – 5 cm, the probability that the target will survive the collision is higher, which mean the growth has been observed. However in the series where $f = 1$, the survival probability for the target becomes very low. As a result, only one event of growth in series 2 cm – 2cm and two events in 1 cm – 1 cm have been observed. Another interesting feature revealed by Figure 4.3 is the occurrence of growth and fragmentation at same value of E_{cm} (overlapping of growth and fragmentation events), which implies that in practical, the outcome of a collision is of probabilistic nature. The in-depth details on the probabilistic nature of growth have been provided in Sec. 4.5

4.3.1 The onset-velocity v_1 for fragmentation

The lowest velocity at which an aggregate fragments can be defined as the onset-velocity for fragmentation v_1. For this an alternative analysis of fragmentation strength μ has been performed. Here the assumption made in previous studies has been invoked that μ has power law dependence on collision velocity v_{n} and the length of the projectile P and target T. The relation can be defined as

$$\log \mu = C_\mu + \iota \log\left(\frac{v_1}{1\ \mathrm{m\ s^{-1}}}\right) + \omega \log\left(\frac{P}{1\ \mathrm{cm}}\right) + \Omega \log\left(\frac{T}{1\ \mathrm{cm}}\right). \tag{4.7}$$

To calculate the onset-velocity for fragmentation, only those events have been considered in which target is fragmented, it counts 105 experiments. The collision parameters are fitted to eqn. (4.7) and by minimising the reduced chi-square one obtains the following values:

$C_\mu = 0.18 \pm 0.07$ $\qquad \iota = -0.66 \pm 0.12$

$\omega = -0.58 \pm 0.10$ $\qquad \Omega = 0.13 \pm 0.11$

To check the goodness of the fitted values, the calculated exponents have been applied to the collision parameters and the correlation has been shown in Figure 4.4. Here one can see, as the velocity of collision decreases, the data points asymptotically approaches to $\mu = 1$. Therefore the dependence of μ on velocity and on aggregate size can not be adequately described merely by the power law as assumed in eqn. (4.7). In addition to this, the linear fit (to log scale), shown in blue line in Figure 4.4, points to another inability of power law. The exponent of velocity obtained from eqn. (4.7), $\iota = -0.66$ is significantly less than the velocity exponent $2n = -1.1$ calculated from the Hill-function in eqn. (4.6). The sharp slope in data points at higher velocities can not be explained with the exponent $\iota = -0.66$ derived from the power law. Thus it can be said that as compared to power law, the Hill-function more adequately describes the observed dependence of fragmentation strength μ and the centre of mass kinetic energy E_{cm}. By using $\log \mu = 0$ in eqn. (4.7), a general relation for the onset-velocity v_1 can be defined as

$$v_1 = \left(10^{C_\mu} \cdot P^{\omega} \cdot T^{\Omega}\right)^{-1/\iota}, \tag{4.8}$$

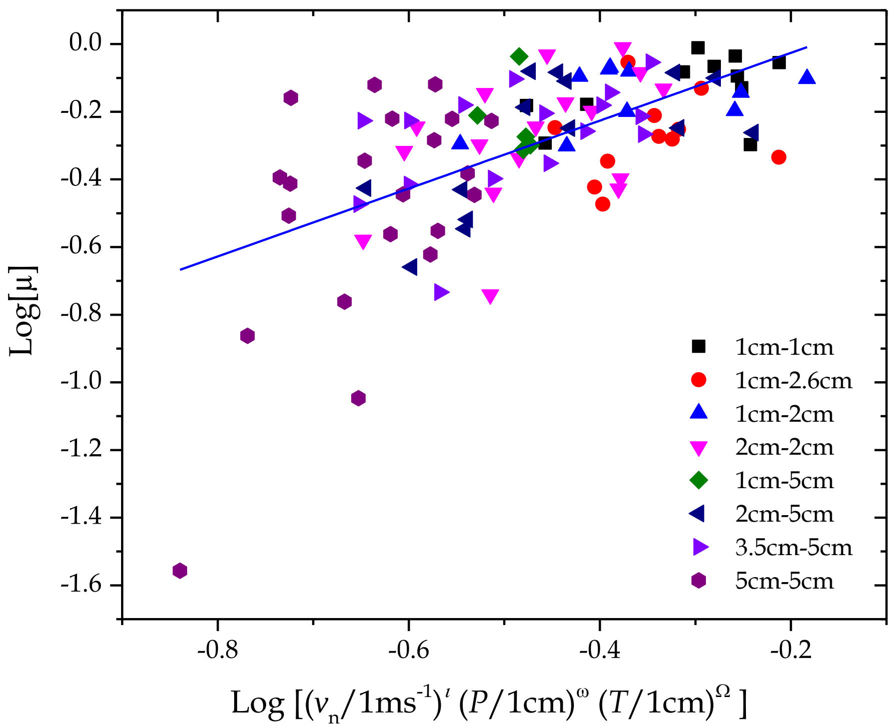

Figure 4.4. Fragmentation strength as a function of collision velocity, projecttile and target, with coefficient $ι = -0.66$ $ω = -0.58$, $Ω = 0.13$ and respectively. The blue solid line is the linear fit to the data with slope 1 (BS 17).

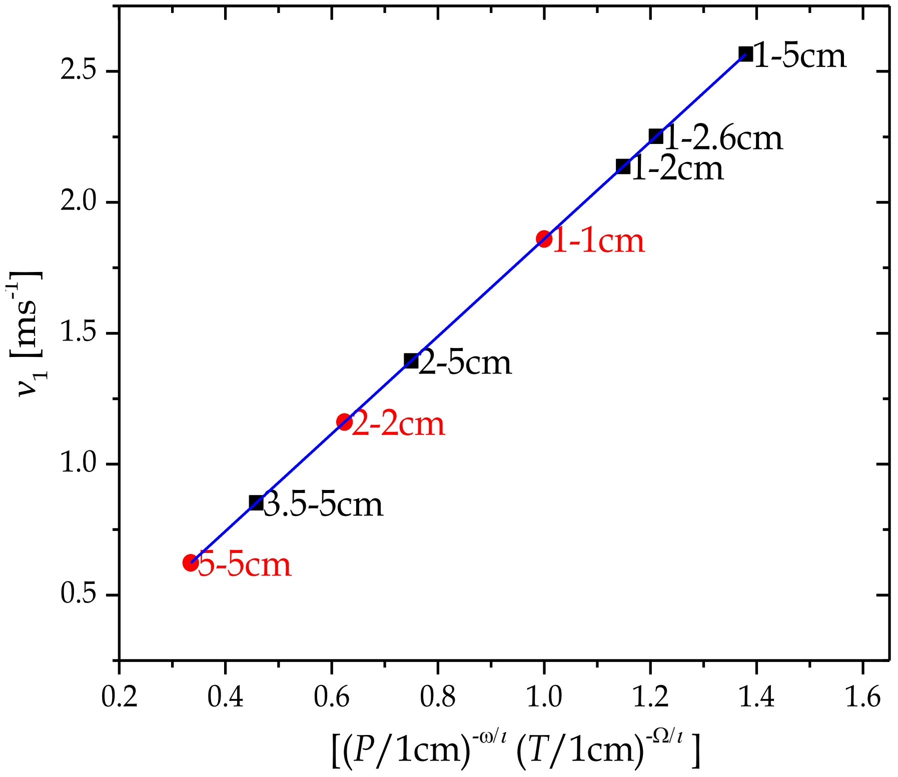

Figure 4.5. The onset-velocity of fragmentation as function of P and T. In the case of different size of aggregates, the onset-velocity of fragmentation is directly related to the target size and inversely to the projectile size. In the case where $P = T$ (shown in red spheres) the onset velocity inversely depends on the absolute size (or mass) of the aggregates, as defined by the relation defined in eqn. (4.11). The blue line is the linear fit and has slope 1.86.

$$\Rightarrow \qquad v_1 = 1.86 \cdot \left(\frac{P}{1\ \mathrm{cm}}\right)^{-0.88} \cdot \left(\frac{T}{1\ \mathrm{cm}}\right)^{0.20} . \qquad (4.9)$$

As expected the onset-velocity depends on the size ratio of the aggregates. A larger T has more mass, it can efficiently dissipate the collision energy, hence requires higher onset-velocity. On the other hand as the size of projectile decreases the onset-velocity for the given target increases. This is the reason that the series 1 cm – 5 cm has higher velocities, as shown in cyan-dashed-dotted curve in Figure 4.2 (more details in Sec. 4.4.2)

Corollary: If $P = T = A$ (A for aggregate) one obtains

$$v_1 \propto A^{-0.68} \ , \qquad (4.10)$$

or

$$v_1 \propto m_A^{-0.23} . \qquad (4.11)$$

In the case of same size aggregates, v_1 has dependence on mass with exponent -0.23. However in Figure 4.11 it will be shown that v_1 has some degree of dependence on surface to value ratio as well. In Figure 4.5 the blue line is fitted to eqn. (4.9), which fits well to all the 8 series. It should be noticed that the order of the same size aggregates (shown in red spheres) follow eqn. (4.11). Beitz et al. (2011) reported onset-velocity 0.2 m$\,$s^{-1} for same size aggregates of 2 cm, which is significantly less than 1.16 m$\,$s^{-1} estimated in this study. One possible reason of their lower onset-velocity could be their higher filling factor $\phi = 0.5$, comparing to $\phi = 0.35$ used in this study. As Meru et al. (2013) showed that at higher filling factors (≥ 37%), the compressive strength rapidly increases, making the body inefficient for dissipating the collision energy, hence vulnerable to fragmentation. The same can be said to the finding of Deckers & Teiser (2013), who reported onset-velocity 0.162 m$\,$s^{-1} for 12 cm aggregates with $\phi = 0.43$.

In the presence of above mentioned studies and Figure 4.5 it becomes clear that the fragmentation threshold velocity is well below 1 m$\,$s^{-1}, as previously assumed 1 m$\,$s^{-1} in Güttler et al. (2010). The reason why the larger aggregates fragment at lower velocities has been discussed in Sec. 4.4.1

4.4 The relative collision strength Q^*

Here the relative collision strength Q^* will be used to analyse the destruction efficiency of a given projectile. The relative collision strength can be defined as the energy $E_{0.5}$ required to halve the target per unit target mass m_t. Thanks to the Hill-function which has readily provided the catastrophic threshold energy $E_{0.5}$, so Q^* can be defined as

$$Q^* = \frac{E_{0.5}}{m_t} . \qquad (4.12)$$

Contrary to previous studies by Stewart & Leinhardt (2009) and Beitz et al. (2011) where total mass of the system has been used, here only the target mass has been considered. The reason for doing this is that in their studies mass ratios between target and projectile were not so extreme, but here it varies by more than two orders of magnitude. Therefore only mass of the target is relevant, thus catastrophic threshold energy $E_{0.5}$ is normalised to the mass of target. Another advantage of using m_t is the comparison with different projectile sizes with the same size of target, which helps to compare the destruction efficiency of one projectile to another. The higher is the Q^* value, the lower is the destruction efficiency of the given projectile in breaking the target into half.

In the following an in-depth analysis[5] of relative collision strength Q^* has been shown. In the first case, shown in Figure 4.6, Q^* has been analysed as a function of projectile size P for a fixed target size T = 5 cm. In the latter case shown in Figure 4.7, it has been investigated that how does the collision strength vary when the size of target T varies and the projectile size is kept constant at P = 1 cm. In both cases the projectile and the target have been varied in size by factor 5. It turns out, that the relative collision strength Q^* increases with the size of projectile with the exponent $\kappa = 1.12 \pm 0.25$ as shown in Figure 4.6. It implies that by increasing the projectile size more energy can be deposited into the system. However it reduces the efficiency of the projectile. On the other hand, Figure 4.7 shows that the relative collision strength Q^* decreases with the size of target with exponent $\lambda = -2.92 \pm 0.57$. However surprisingly the inverse relation of Q^* with the target goes roughly to the cube of the target size, implying that the system rapidly loses energy. In other words, when the size of projectile varies by factor 5, the resulting increase in Q^* is by factor ~ 7. Whereas the variation of same order in the size of target reduces the Q^* by factor more than 100. It suggests that collisions are significantly sensitive to the size of target and the efficiency of the given projectile can be increased considerably by increasing the size of target, i.e. the size ratio f.
For the cross check the collision strength Q^* has been analysed as a function of projectile and target size simultaneously, as shown in Figure 4.8. Here the series 2 cm – 2 cm which has been excluded in previous analyses is now also included. By learning the dependence of Q^* on P and T in Figure 4.6 and Figure 4.7 respectively, the following ansatz has been used

$$\log\left(\frac{Q^*(P,T)}{1\ \mathrm{J\ Kg^{-1}}}\right) = C_Q + \kappa \log\left(\frac{P}{1\ \mathrm{cm}}\right) + \lambda \log\left(\frac{T}{1\ \mathrm{cm}}\right). \tag{4.13}$$

The two dimensional least-square fit has yields the following values

$$\chi^2_{red} = 0.04614 \qquad C_Q = 1.24 \pm 0.16$$
$$\kappa = 1.12 \pm 0.35 \qquad \lambda = -2.68 \pm 0.37$$

In combined analysis the exponent for target $\lambda = -2.68$ is slightly less when fitted separately but still within standard errors, whereas the exponent of projectile $\kappa = 1.12$ is in fully agreement. It should be noticed that the inclusion of the missing series 2 cm – 2 cm did not change the values noticeably, which justifies its exclusion in previous analysis. The eqn. (4.13) can be written in standard form as

$$\left(\frac{Q^*(P,T)}{1\ \mathrm{J\ Kg^{-1}}}\right) = 17.38\left(\frac{P}{1\ \mathrm{cm}}\right)^{\kappa} \cdot \left(\frac{T}{1\ \mathrm{cm}}\right)^{\lambda}. \tag{4.14}$$

In Figure 4.8 the goodness of the fit values has been tested by using the exponents given above.

---

[5] Due to the symmetry reason, here the series 2cm-2cm is not shown but in second step it is included.

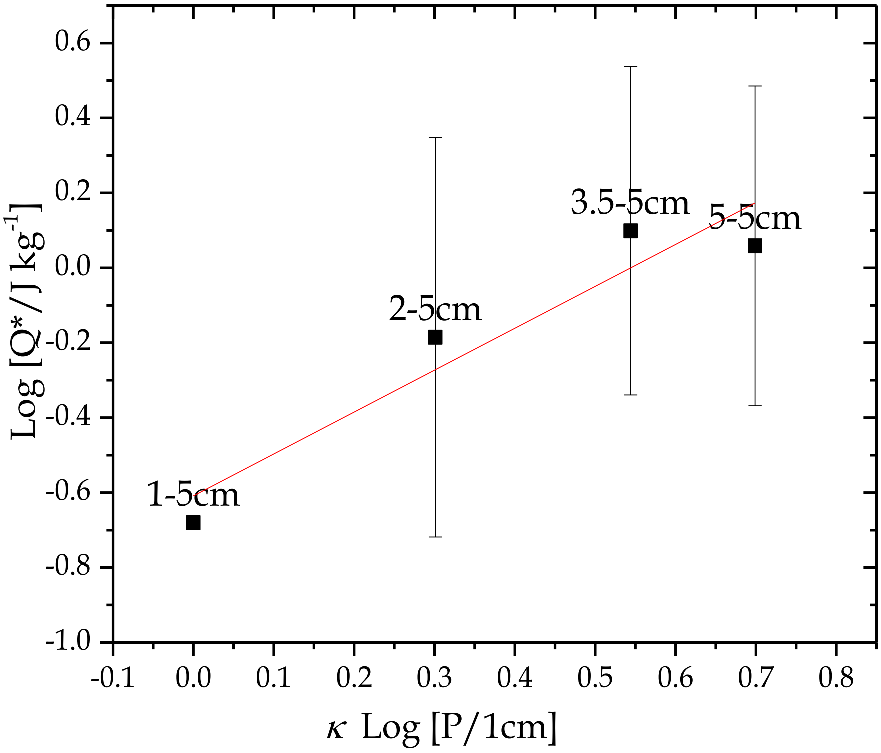

Figure 4.6. The relative fragmentation strength *Q** as a function of projectile size *P*, where the size of the target has been fixed to 5cm. *Q** increases almost linearly with *P* at slope $\kappa = 1.12$ which is derived by fitting the linear shown in red curve (BS 17).

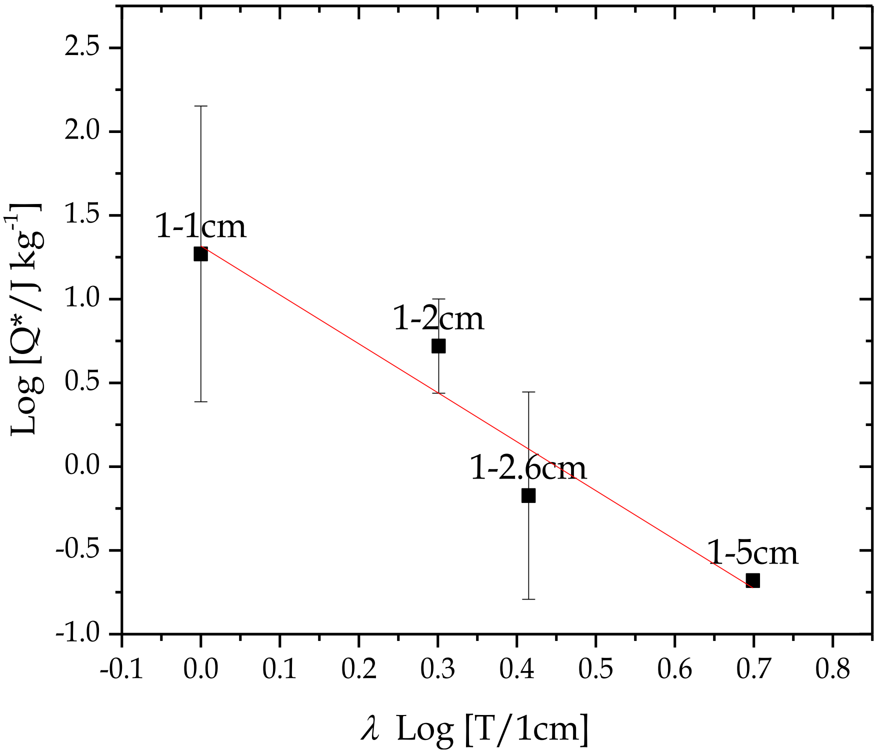

Figure 4.7. In second case the projectile is fixed at 1 cm and the size of target has been varied from 1 cm to 5 cm. Here λ = -2.92 is the slope of the linear fit shown in red. It shows that the relative fragment strength *Q** is very sensitive to *T*, its value declines with almost cube to the size of target *T* **(BS 17).**

As expected it gives almost a linear relation with slope ~ 1. Here it should also be noticed that the series of similar size ratio *f*, have similar Q^* value. It becomes evident, particularly in the case of the series 1 cm – 2.6 cm and 2 cm – 5 cm.

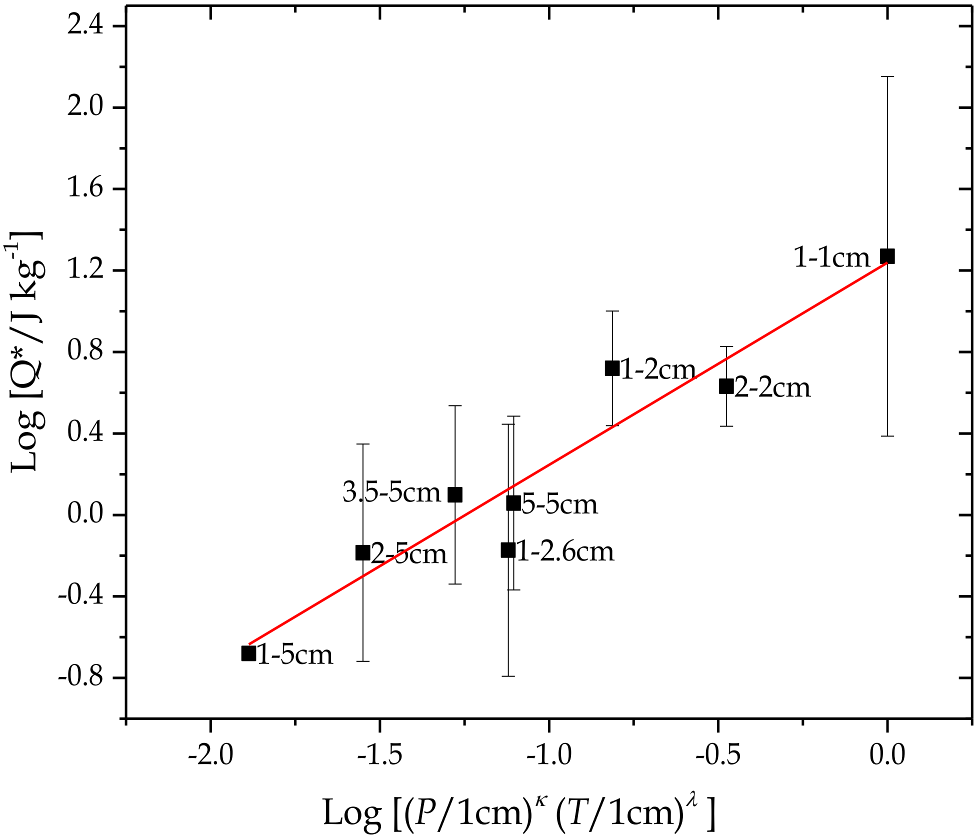

Figure 4.8. A linear dependency of Q^* on projectile and target arises when the size of projectile and target have been considered in the proportion defined by their exponents $\kappa = 1.12$ and $\lambda = -2.68$ respectively. The red line is the linear fit which has slope 1 (BS 17).

However this argument is not valid for the series where $f = 1$. It suggests that Q^* depends on something which is more fundamental and it should explain any size ratio. One possibility is surface to volume ratio (discussed in Sec. 4.4.1). The smaller aggregates have higher surface to volume ratio, more energy per unit area, they are more tightly bound, hence required higher velocity for fragmentation (see Figure 4.11), therefore show relatively a higher collision strength with the decreasing aggregate size.

Corollary: If $P = T = A$, eqn. (4.14) can be written as

$$\left(\frac{Q^*(A)}{1\ \text{J Kg}^{-1}}\right) = 17.38 \cdot \left(\frac{A}{1\ \text{cm}}\right)^{\kappa+\lambda} = 17.38 \cdot \left(\frac{A}{1\ \text{cm}}\right)^{-1.56} . \qquad (4.15)$$

Here the slope of the aggregate -1.56 is slightly steeper than the slope -0.95±0.38 estimated by Beitz et al. (2011). It is probably associated to higher filling-factor $\phi = 0.50$ used in their study. However in Figure 4.6 and Figure 4.7 it has been clearly shown that Q^* independently depends on both the target and the projectile. To the extent of present knowledge of the author, the dependence of Q^* on size ratio has not been described before and not included in collision evolution models.

4.4.1 Surface to volume ratio *h*

The reason of the strong dependence of Q^* on the size ratio, could be explained by the fact that Q^* is strongly correlated to the surface to volume ratio of cylinders h. One can define h_p and h_t as surface to volume ratio of the projectile and the target respectively and the same approach as in eqn. (4.13) can be applied. The difference is that here instead of the individual sizes of the projectile and target, their surface to volume ratio h_p and h_t have been considered such that

$$\log\left(\frac{Q^*(h_p,h_t)}{1\ \mathrm{J\ Kg}^{-1}}\right) = C_h + \kappa^\circ \log\left(\frac{h_p}{\mathrm{cm}^2/\mathrm{cm}^3}\right) + \lambda^\circ \log\left(\frac{h_t}{\mathrm{cm}^2/\mathrm{cm}^3}\right). \tag{4.16}$$

The same method of least-square fit has been used to determine following values

χ^2_{red} = 0.04614 $\qquad$ C_h = 0.024 ± 0.18

κ° = -1.12 ± 0.35 $\qquad$ λ° = 2.68 ± 0.37

Figure 4.9(a) reveals that the dependence of Q^* on surface to volume ratio is exactly the same as on the sizes of projectile and target. The only difference is the signs of the exponents of projectile and target have been reversed. One can compare eqn. (4.13) and (4.16) in standard form, with their respective fitted values, which reads the flowing

$$17.38 \cdot P^{1.12} \cdot T^{-2.68} = 51.29 \cdot h_p^{-1.12} \cdot h_t^{2.68}. \tag{4.17}$$

It gives rise to a perfect linear relation as shown in Figure 4.9(b). In other words the collision strength Q^* can be equally expressed in terms of surface to volume ratio of target h_t and projectile h_p. It helps to understand the sequence of the series along the fit-line.

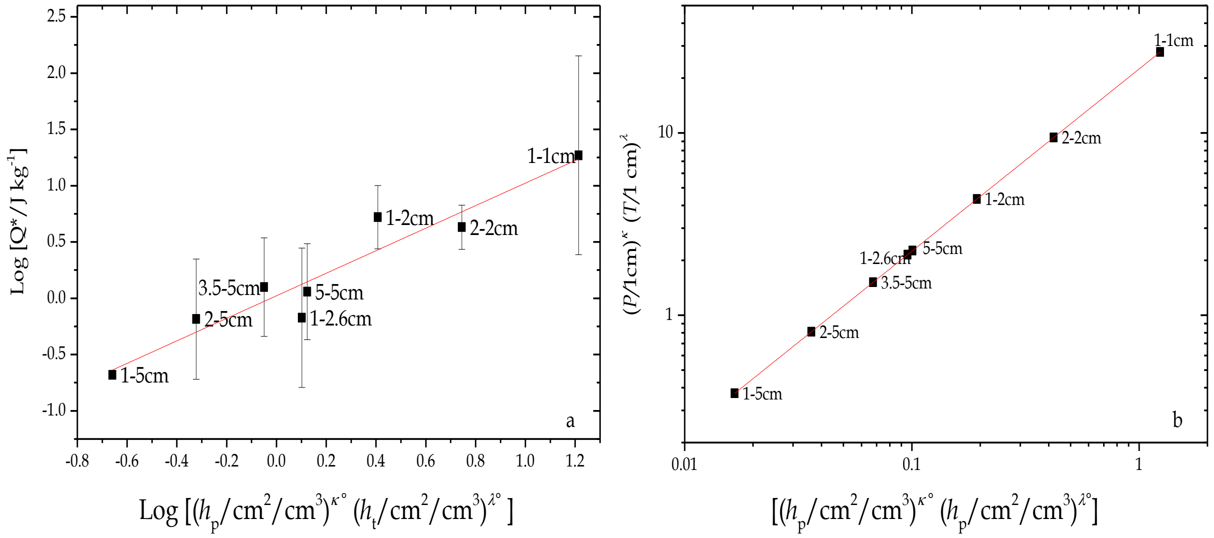

Figure 4.9. **(a)** The relative collision strength Q^* linearly increases with the surface to volume ratio of projectile and target with exponents κ°= -1.12 and λ° = 2.68 respectively. It successfully explains the order of same size aggregates as well as of different size aggregates. The red line is the linear to the data with slope 1. In **(b)** eqn. (4.17) has been expressed, where the linear fit in red with slope 1, shows one-to-one correlation between the size ratio and surface to volume ratio between projectile and target.

The difference between the two approaches is that in Figure 4.8 the positions of same size aggregates $f = 1$ can not be explained. However in the latter case the positions can be explained by the fact that the smaller the aggregate is, the higher is its surface to volume ratio, more tightly it is bounded, so harder it is to break apart, hence the higher Q^* value and vice versa. This explains why the larger targets are intrinsically weak. As a result in Figure 4.8 and Figure 4.9 (a) the series 1 cm – 1 cm and 1 cm – 5 cm are poles apart, while other series are simply ordered in-between.

4.4.2 Catastrophic threshold velocity $v_{0.5}$

The velocity at which the target fragments into the half of its original size is the catastrophic threshold velocity $v_{0.5}$, analogous to $E_{0.5}$. The formal expression can be derived by using eqn. (4.12) such as

$$v_{0.5} = \sqrt{2Q^*\left(1+\frac{m_t}{m_p}\right)} = \sqrt{2Q^*\left(1+\frac{T^3}{P^3}\right)} \quad . \tag{4.18}$$

By plugging eqn. (4.14) one obtains

$$v_{0.5} = 5.89\cdot\sqrt{\left(\frac{P}{1\ \mathrm{cm}}\right)^{1.12}\cdot\left(\frac{T}{1\ \mathrm{cm}}\right)^{-2.68}+\left(\frac{P}{1\ \mathrm{cm}}\right)^{-1.88}\cdot\left(\frac{T}{1\ \mathrm{cm}}\right)^{0.32}} \tag{4.19}$$

One can see both equations (4.9) and (4.19) point to the same fact that onset-velocity of fragmentation v_1 and catastrophic threshold velocity $v_{0.5}$ both depend on target to projectile size ratio.

Corollary: In the case $T = P = A$ one gets

$$v_{0.5} = 8.34\cdot A^{-0.78} \propto m_A^{-0.26}\ , \tag{4.20}$$

which is in same range as in eqn. (4.11).

Interestingly the values of exponents of the mass -0.23 in eqn. (4.11) and -0.26 in eqn. (4.20) match well with the predicated values -0.2 to -0.3 by Meru et al. (2013).
Once again it comes to notice that for 2 cm same sized aggregates the value of threshold velocity $v_{0.5} = 4.85\ \mathrm{m\,s^{-1}}$ is much higher than the value $v_{0.5} = 0.64\ \mathrm{m\,s^{-1}}$ reported by Beitz et al. (2011). According to Love et al. (1993) $Q^* \propto \phi^{-3.6}$, therefore this wide gap between the two studies could be explain by the higher filling-factor $\phi = 0.50$ used by Beitz et al. (2011). Moreover Meru et al. (2013) showed that the fragmentation threshold velocity exponentially declines above $\phi \geq 0.36$.

By using eqn. (4.11) and (4.20), the onset-velocity can be correlated with the catastrophic threshold velocity. It can be written as

$$\log\left(\frac{v_{0.5}}{\mathrm{m\ s^{-1}}}\right) = C_v + o\log\left(\frac{v_1}{\mathrm{m\ s^{-1}}}\right), \tag{4.21}$$

and by reducing the residuals one gets the coefficient $C_v = 0.55 \pm 0.05$ and exponent $o = 0.93 \pm 0.18$ with $\chi^2_{red} = 0.0063$. However the reduced chi-square slightly decreases to $\chi^2_{red} = 0.0054$. If in eqn. (4.22) the coefficient has been fixed to o = 1, one gets new values for C_v = 0.53 ± 0.027 as shown in Figure 4.10(a). Equation (4.21) can be independently used as a shortcut to determine the catastrophic threshold velocity, without involving the colliding bodies.

Alternative to this, the dependence of the catastrophic threshold velocity on reduced mass m' has been tested as well. Being guided by eqn. (4.20) one can assume $v_{0.5}$ has power law dependence, which can be expressed as

$$v_{0.5} = am'^{b} \tag{4.23}$$

Here the coefficient a = 1.0 ± 0.15, the exponent b = -0.27 ± 0.02 and to χ^2_{red} = 0.094.The slope value is in good agreement with the slope of mass given in eqn. (4.20), regardless to the fact here other series where $T \neq P$ are also included. Figure 4.10(b) reflects exactly the relation defined in eqn. (4.20). Therefore eqn. (4.23) is valid for the aggregates of equal as well as for unequal mass, hence it provides an alternative way to eqn. (4.19)

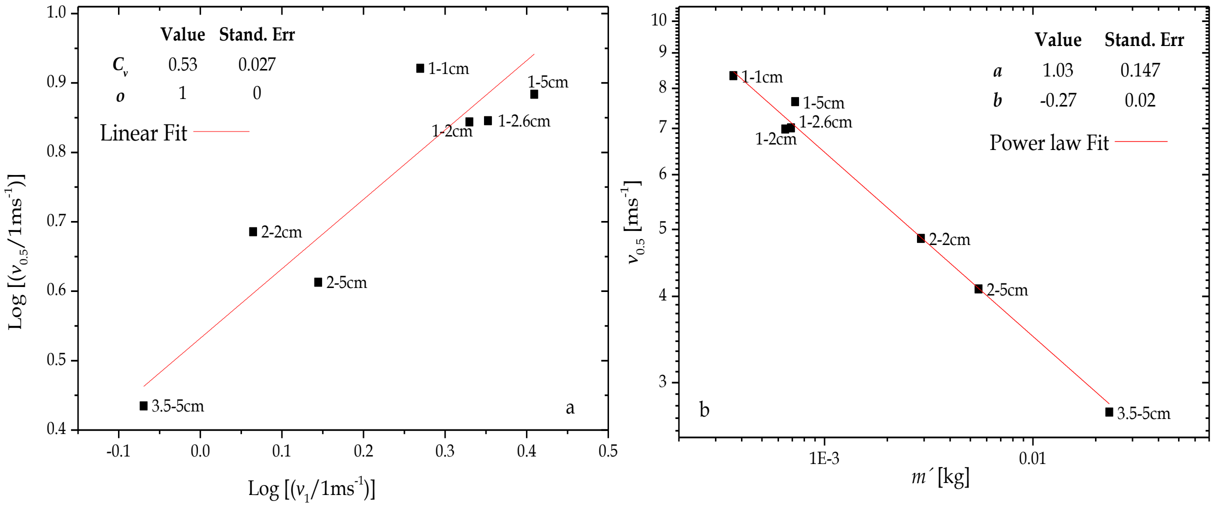

Figure 4.10 (a) The catastrophic threshold velocity shows fairly a linear trend with onset-velocity with slope o = 1 and off-set C_v = 0.54, after eqn. (4.21). Whereas in (b) the threshold velocity shows power law dependence on reduced mass, with exponent b = -0.27. Regardless to the fact the colliding aggregates are of same size or not, the trend is fully in accordance with eqn. (4.20).

size as well as for the unequal size. The reason, why the onset-velocity and the threshold velocity are inversely related to the reduced mass of the aggregate, could be explained by the argument of surface-to-volume ratio. Smaller aggregates being tightly bounded require higher onset-velocity as well as threshold velocity to fragment. In Figure 4.11 the catastrophic threshold velocity $v_{0.5}$ and the onset-velocity of fragmentation v_1 show a power law dependence on the sum of the surface to volume ratio of target h_t and projectile h_p. The values of the coefficient and exponent of power law fit to $v_{0.5}$ and v_1 are given in red and cyan blue inset respectively in the inset of Figure 4.11. The absolute values of v_1 and $v_{0.5}$ are given in Table 4.3.

Another fact to be noticed is, the test series 1 cm – 2.6 cm has the value of threshold velocity very close to the series 2 cm – 5 cm, which supports the assumption that the aggregates of same size ratio should behave in the same manner. However the same can not be said for the onset-velocity v_1.

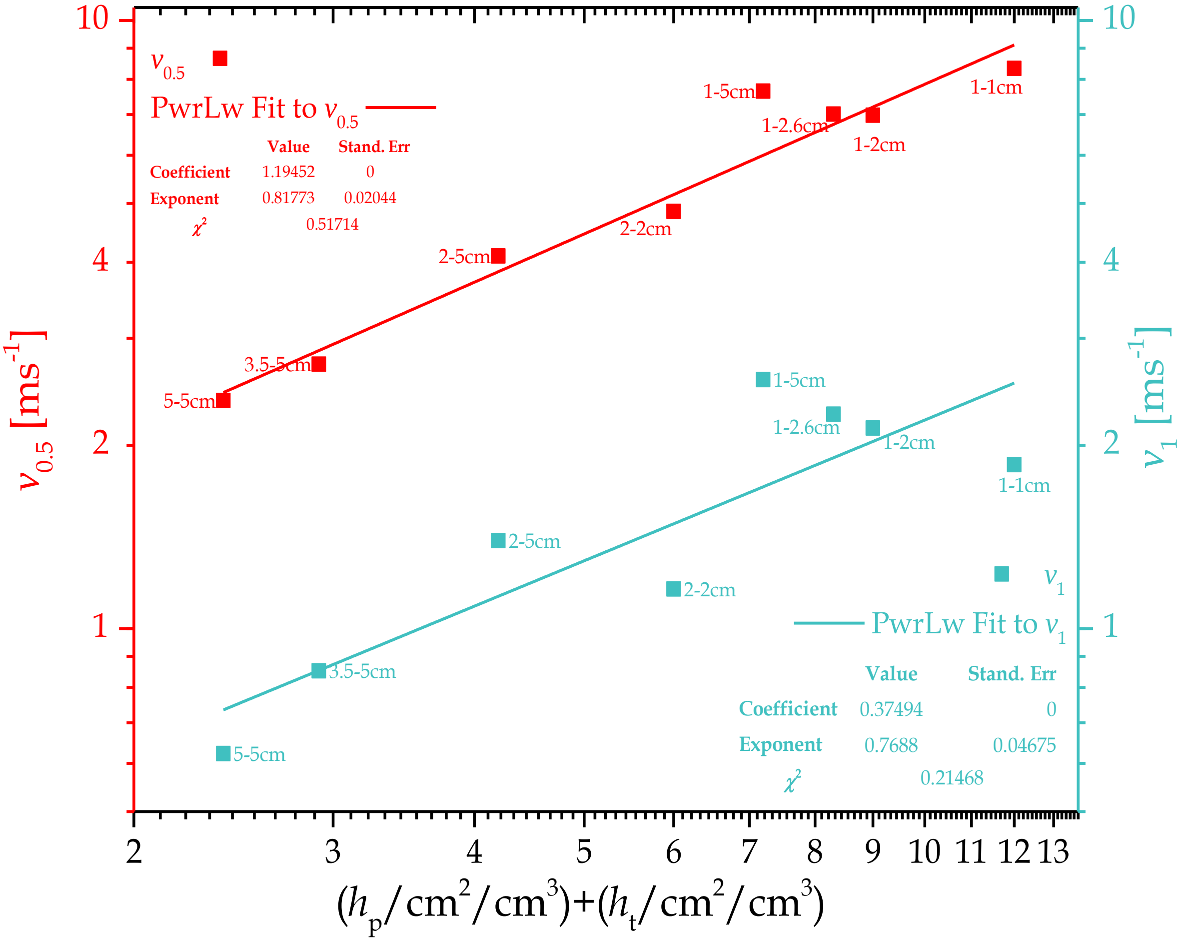

Figure 4.11. As the sum of the surface to volume ratio of projectile h_p and target h_t increases, the catastrophic threshold velocity and onset-velocity increases with the power law. The red spheres correspond to $v_{0.5}$ along left y-axis, which has exponent value ~ 0.83 and the coefficient ~1.20. Whereas v_1 shown in cyan blue squares along right y-axis has values of exponent ~ 0.77 and the coefficient ~ 0.37.

4.5 The probability function of mass transfer

As shown in Figure 4.1 there are two possible states the target can be in after the collision. In the first possibility, the target aggregate does not survive the collision and goes in state CF (catastrophic fragmentation). The second possibility is that it does survive the collision and goes in state MT (mass transfer), which leads to growth.

Here a complication arises when in some cases at approximately same collision energy E_{CM} the target aggregate showed both behaviours i.e. catastrophic fragmentation and mass transfer, as shown in Figure 4.3. Therefore by using the statistics of 142 experiments the probability P_{MT} of being in state MT can be determined. This is accomplished in two steps:

- First the survival velocity v_{sur} has to be defined. It is the maximum velocity at which the target aggregate after collision has been observed to be in state MT.

- Now the P_{MT} can be defined as a ratio between the numbers of events in which target is found to be in state MT to the total number of events up to the survival velocity v_{sur}, which can be written as

$$P_{MT} = \frac{\text{number of events target in state MT}}{\text{total number of events (MT and CF) up to } v_{sur}} . \tag{4.24}$$

The calculated values of the probability of mass transfer and the corresponding survival velocities are given in Table 4.3. In Figure 4.12 the probability P_{MT} of being in state MT has been plotted as a function of size ratio *f*. It turns out that P_{MT} increases as target to projectile ratio increases, i.e. $f > 1$ and reaches to unity at $f \geq 5.83$ as shown in eqn. (4.25). The series 1 cm – 5 cm of highest size ratio, where $f = 5$, enjoys the highest probability i.e. $P_{MT} = 0.8$ of being in state MT after the collision.

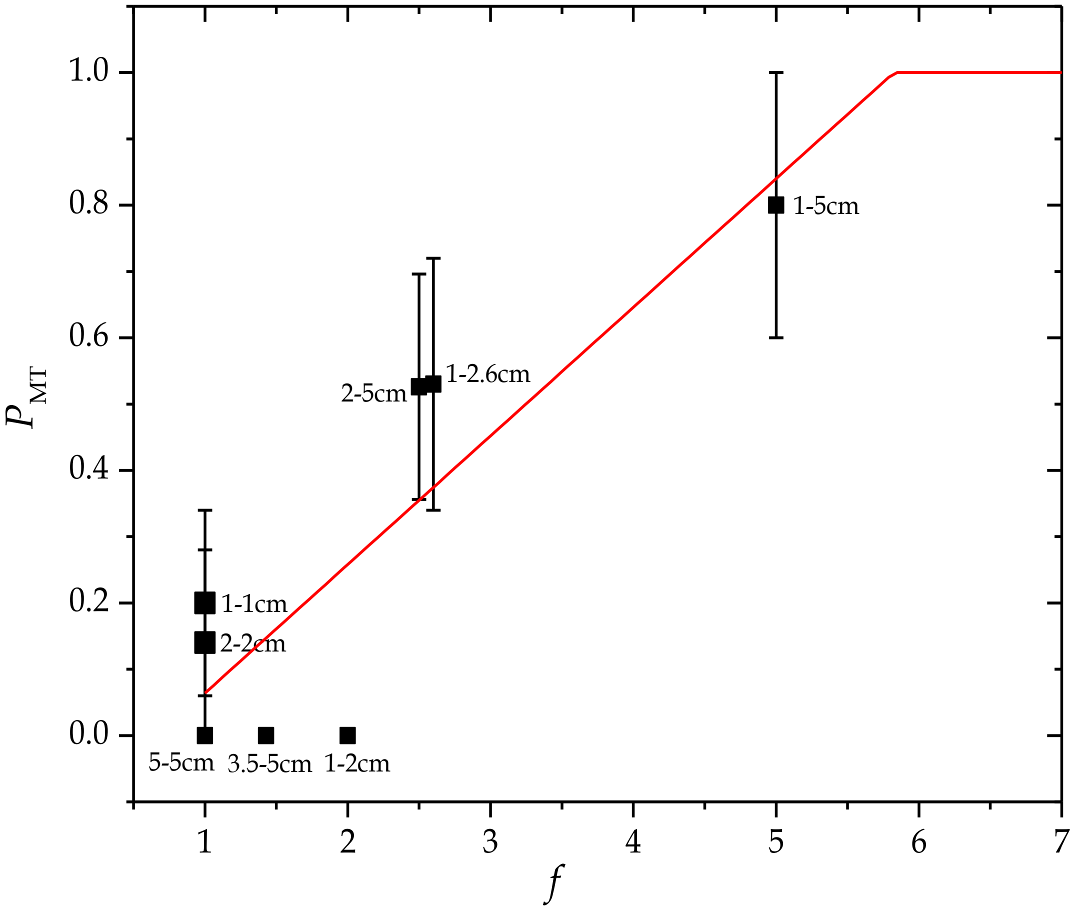

Figure 4.12. The probability of mass transfer as a function of size ratio *f*. The P_{MT} steadily increases with target to projectile size ratio and reaches to unity at $f \geq 5.83$. The red line is the fit to eqn. (4.24). The series of similar size ratio tend to have similar probability, for example see the series 1 cm – 2.6 cm and 2 cm – 5 cm **(BS 17).**

Therefore this series also has the highest survival velocity $v_{sur} = 8.4$ ms^{-1}. However the lowest probability of survival is $P_{MT} = 0.14$ which is observed in series 2 cm – 2cm, where $f = 1$.

In Figure 4.13 the survival velocity v_{sur} (red spheres) and catastrophic threshold velocity $v_{0.5}$ (cyan blue squares) have been plotted as a function of the size ratio *f*. One can see, as the size ratio increases the target aggregate can sustain higher velocities, consequently the catastrophic velocity and survival velocity increase accordingly. In the case where $f = 1$, the absolute size plays a role (or surface to volume ratio). As the absolute size of the aggregates decreases from the series 5 cm – 5 cm, 2 cm – 2 cm to 1 cm – 1 cm, their surface to volume ratio increases, so one

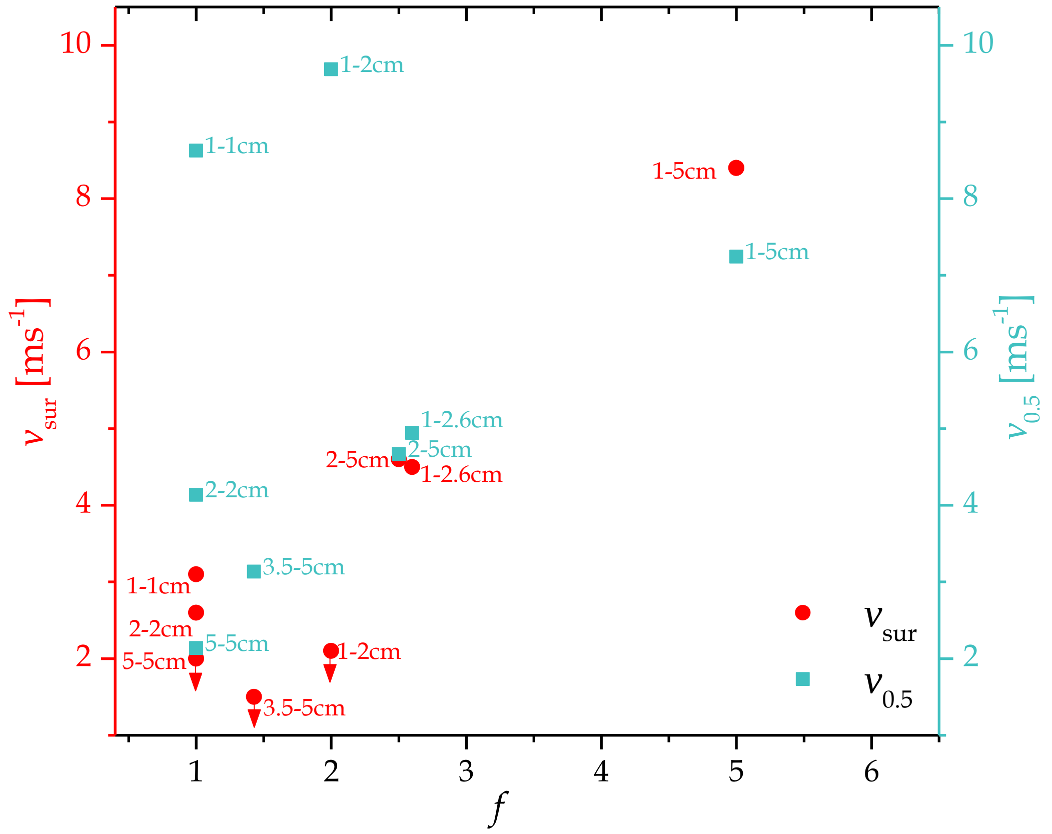

Figure 4.13. The survival velocity v_{sur} shown in red spheres along the left y-axis and the catastrophic threshold velocity $v_{0.5}$ in cyan blue squares along right y-axis, reflect a proportional relation with size ratio f. The down arrowheads tell that the survival velocity in the given series is below the range of collision velocities investigated here (BS 17).

Table 4.3. The relative collision strength Q^* and the resulting order of the collision series, can be expressed in terms of size ratio f and surface to volume ratio of target h_t and projectile h_p. These quantities have direct impact on catastrophic threshold velocity $v_{0.5}$, and the probability of mass transfer P_{MT}.

No.	Series	h_p [cm^{-1}]	h_t [cm^{-1}]	v_1 [ms^{-1}]	$v_{0.5}$ [ms^{-1}]	v_{sur} [ms^{-1}]	P_{MT}
1	1.0 cm – 1.0 cm	6.0	6.0	1.86	8.34	3.1	0.2 ± 0.14
2	2.0 cm – 2.0 cm	3.0	3.0	1.16	4.85	2.6	0.14 ± 0.14
3	5.0 cm – 5.0 cm	1.20	1.20	0.62	2.37	< 2	0
4	1.0 cm – 2.0 cm	6.0	2.0	2.14	6.98	< 2.1	0
5	1.0 cm – 2.6 cm	6.0	2.31	2.25	7.01	4.5	0.53 ± 0.19
6	1.0 cm – 5.0 cm	6.0	7.20	2.57	7.65	8.4	0.80 ± 0.20
7	2.0 cm – 5.0 cm	3.0	1.20	1.39	4.10	4.6	0.52 ± 0.17
8	3.5 cm – 5.0 cm	1.71	1.20	0.85	2.72	< 1.5	0

can see a steady increase in the survival velocity $v_{\text{sur}} = 2$ ms^{-1}, $v_{\text{sur}} = 2.6$ ms^{-1} and $v_{\text{sur}} = 3.1$ ms^{-1} respectively, which consequently leads to a degree of higher probability of mass transfer from $P_{\text{MT}} = 0$ to $P_{\text{MT}} = 0.14$ and $P_{\text{MT}} = 0.2$ respectively (see Table 4.3).

Figure 4.12 and Figure 4.13 once again lead our attention to the fact that the test series of similar size ratios 1 cm – 2.6 cm and 2 cm – 5 cm, have similar: 1) probability of mass transfer, as well as 2) the survival velocity and 3) the catastrophic threshold velocity. Therefore it can be concluded that in the case $f > 1$, only the relative size (or mass) of the colliding aggregates is relevant, not their absolute sizes. However the absolute size play role when $f = 1$. The general relation between the probability of mass transfer P_{MT} and size ratio f can be written as

$$P_{\text{MT}} = \begin{cases} 0.194\,f - 0.13 & \text{for} \quad 1 \le f \le 5.83 \\ 1 & \text{for} \quad f > 5.83 \end{cases}. \tag{4.25}$$

If $\quad 1 \le f \ge 5.83 \quad$ collision outcome is CF and MT
or $\quad f > 5.83 \quad$ collision outcome is only MT

The probability of catastrophic fragmentation P_{CF} is given by

$$P_{\text{CF}} = 1 - P_{\text{MT}} \tag{4.26}$$

In this study the more focuses is on the probability of mass transfer, whereas the probability of catastrophic fragmentation has not been analysed.

4.5.1 The mass-transfer efficiency

The mass-transfer efficiency can be defined as the fraction of projectile mass transferred to target per unit projectile mass $\Delta m/m_{\text{p}}$. In the modelling of the formation of planetesimals, the mass-transfer efficiency plays a critical role, as the variation can have a significant impact on the resulting planetesimal. Therefore it has been a centre of attention in recent studies, e.g. for varying size ratio see Fig. 6 in Wurm et al. (2005b), Fig. 5 in Kothe et al. (2010), Fig.8 in Deckers & Teiser (2014) and for the collision of same size aggregates Fig. 8 in Beitz et al. (2011)

In this study, in total 37 events of mass transfer have been recorded, which spans over the 5 series of different size combinations. Here it has been observed that the mass-transfer efficiency increases with size ratio f. For example; the minimum mass-transfer $\Delta m/m_{\text{p}} \approx 4\times10^{-4}$ has been observed in the series 1 cm – 1cm, where $f = 1$ and this value reaches to maximum $\Delta m/m_{\text{p}} \approx 0.35$ in the series 1 cm – 5 cm, where $f > 1$, see Figure 4.14 (a). These values are comparable with the studies mentioned above.

In this study the data is relatively diverse which gives one advantage over the previous studies in a way that here the mass-transfer efficiency can be analysed as a function of collision parameters, as the relation has been defined in eqn. (4.27). Here it is assumed that the accreted mass has power law dependence velocity v_{n}, projectile P and target T, which can be written as

$$\log\left(\frac{\Delta m}{m_p}\right) = C_{mt} + \sigma \log\left(\frac{v_n}{1\ \text{ms}^{-1}}\right) + \zeta \log\left(\frac{P}{1\ \text{cm}}\right) + \Gamma \log\left(\frac{T}{1\ \text{cm}}\right). \tag{4.27}$$

By minimising the reduced chi-square χ^2_{red}, the coefficient C_{mt}, and the exponents σ, ζ and Γ for velocity, projectile and target respectively have been determined in three runs. In first run all 37 events where $f \geq 1$ have been fitted to eqn. (4.27) and the resulting fit values are given in the first row of Table 4.4 and the correlation is shown in Figure 4.14 (a). One finds strong dependence on target and then projectile and to some extent on velocity. In second run, 3 events from the series where $f = 1$, have been taken out and only 34 events from the series where $f > 1$ have been fitted, the fit values are given in second row of Table 4.4. The elimination of just 3 events where $f = 1$ leads to drastic changes. For example, the dependence on T has almost vanished (which was previously dominant), suggesting no role of the target in the case of $f > 1$, whereas the dependence on velocity becomes significant. Moreover the value of χ^2_{red} decreases by a factor ~ 5. However the error in the value of ζ, the exponent of P is almost twice as large as the value itself, which suggests no dependence on projectile. Therefore in the third run, the coefficients of projectile and target in eqn. (4.27) have been set to zero, i.e. $\zeta = 0$ and $\Gamma = 0$, which leads to

$$\log\left(\frac{\Delta m}{m_p}\right) = C_{mt} + \sigma \log\left(\frac{v_n}{1\ \mathrm{m\,s^{-1}}}\right) . \tag{4.28}$$

One can see that the resulting fit value of σ, the exponent of velocity has been further refined and χ^2_{red} has reduced slightly (see third row Table 4.4). Figure 4.14 (b) shows the dependence of mass-transfer efficiency for the size ratio $f > 1$ as a function of velocity.

The results shown in Table 4.4 and Figure 4.14 enforce the distinction between two types of collisions i.e. collisions where $f = 1$ and the collision where $f > 1$, hence should be treated separately. Based upon the χ^2_{red} analysis, a complimentary relation between two types of collisions can be observed. If all the 37 events for $f \geq 1$ are considered then the sizes of individual aggregates play primary and the velocity has the secondary role in determining the rate of mass-transfer (first row Table 4.4). However, if the aggregates are intrinsically different in size $f > 1$, then the dependence of mass-transfer on the size of individual aggregates becomes negligible and only impact velocity v_n is the primary factor on which mass-transfer depends (second row Table 4.4).

Table 4.4. The dependence of mass-transfer on velocity v_n, projectile P and target T has been studied in 3 runs by reducing the chi square χ^2_{red}. In first run all the 37 events from the series where $f \geq 1$ have been fitted to eqn. (4.27). In second run, 34 events where $f > 1$ have been fitted, which strengthens the dependence of mass-transfer on velocity but reduces on sizes. In third run the exponents ζ and Γ have been neglected and the data of 34 events has been fitted to eqn. (4.28) and the resulting values are given in third row. The separation of the data on the base of size ratio f, reduces the χ^2_{red} by a factor 5, which indicates that the collisions with $f = 1$ are different than those where $f > 1$.

Run No.	Data points	C_{mt}	σ (v_n)	ζ (P)	Γ (T)	χ^2_{red}
1	37	-2.30 ± 0.24	0.52 ± 0.44	-0.72 ± 0.69	1.82 ± 0.40	0.111
2	34	-1.37 ± 0.14	0.81 ± 0.23	-0.22 ± 0.39	-0.05 ± 0.32	0.022
3	34	-1.42 ± 0.07	0.91 ± 0.11	0	0	0.021

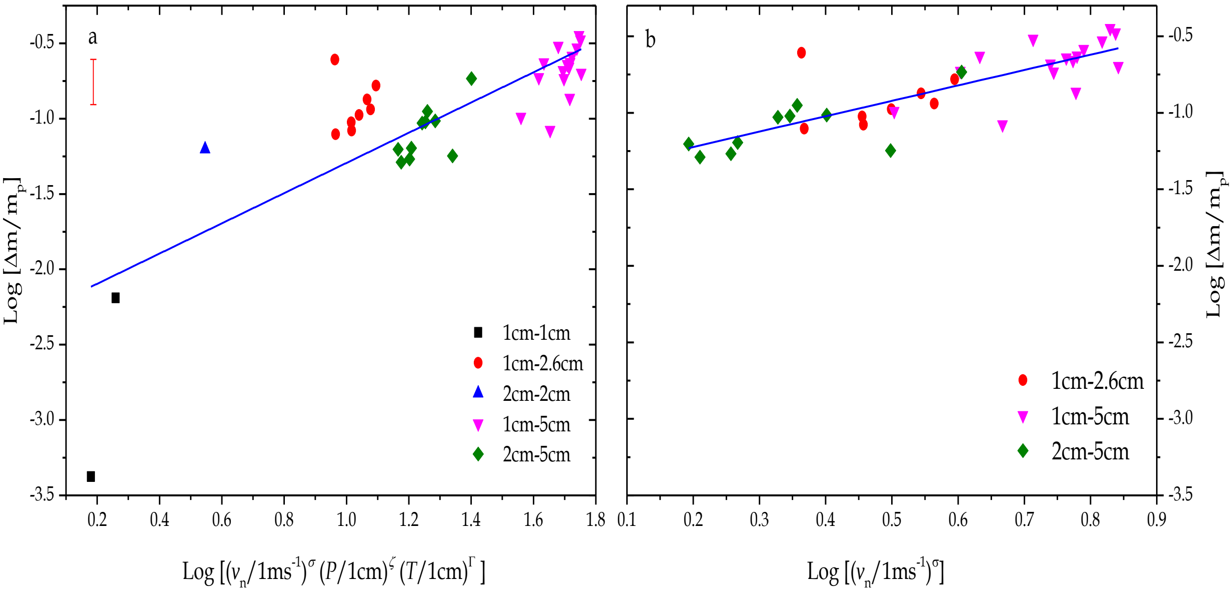

Figure 4.14. (a) The mas-transfer efficiency as a function of $v_{n,}$ P and T has been analysed in the case of all 37 events from the series where $f \geq 1$ and the fit values of the exponents correspond to first row in Table 4.4. **(b)** Mass-transfer efficiency, for 34 data points where $f > 1$, shows dependence only on velocity. As 3 data points from the series where $f = 1$ have been neglected, see fit values in Table 4.4, the dependence on P and T vanishes and the χ^2_{red} declines significantly. The blue lines in (a) and (b) are the linear fit to the respective data points and both curves have slope 1. Since the mass gain has been determined by counting the pixels of the cone (as encircled in Figure 4.1 (d), the mean error has been estimated by factor 2 in all 37 events, which is shown with the red vertical bar at top left in (a) **(BS 17)**.

Corollary: The sweep-up velocity

The sweep-up velocity v_{sp} is defined as the velocity at which a complete projectile will stick to the target. Using $\Delta m/m_{\mathrm{p}} = 1$ in eqn. (4.28), the sweep-up velocity can be written as

$$\left(\frac{v_{\mathrm{sp}}}{\mathrm{m\ s^{-1}}}\right) = 10^{C_{mt}/\sigma} \approx 36.34\ \mathrm{m\ s^{-1}}. \tag{4.29}$$

After observing the outcome of 142 experiments, it can easily be ruled out that the 5 cm sized target will survive such a high impact velocity. However the highest reported mass-transfer efficiency is 70% which is observed by Wurm et al. (2005b) at 13 ms^{-1} for $f \sim 10$ (mm-sized projectile and cm-sized target). Later Teiser & Wurm (2009a) experimentally showed that growth with the said aggregate sizes is possible even at 60 ms^{-1}. In the case of extremely high size ratio i.e. $f >> 10$, then cratering becomes important.

4.6 Area-frequency distribution

In proto-planetary disc a prolonged presence of small grains suggests, that the disc had been replenished with fragments to assist the growth. The width of the size distribution is one of the factors, which determines the porosity and the structure of a planetesimal. From the fragment size distribution one can know how the collision energy is dissipated. Therefore in this study a special attention has been paid to model the size and mass frequency distribution.

The fragment size distribution has already been observed in the previous studies by Blum & Münch (1993) and more recently by Deckers & Teiser (2014). In both studies the size distribution has been observed to be in two regimes, first the continuous regime of very small fragments, following the power law and second the discrete regime of fewer counts of the large fragments. The same pattern has been observed in this study.

This phenomenon could be explained by the energy dissipation rate of sound waves produced at the moment of the first contact between the two dust aggregates. Initially the energy dissipation rate is maximum (more energy per unit length is available), hence more bonds are broken, which gives rise to the higher count of small fragments. This part of the distribution can be well explained by the power law distribution. As the sound waves propagate inside the material the energy dissipation rate decreases exponentially. Less energy can break only weak bonds (bonds which are already under strains maybe due to inhomogeneity). Therefore the fragment-size goes larger and the count fewer. Technically the largest fragment in such collisions is actually the remnant of the original aggregate where the impact of the sound waves has been minimum.

4.6.1 The method of fragments count

In previous experiments, owing to technical limitations, the factors influencing the fragment size distribution have been obscure. But thanks to the high frame rate 7500 frames per second (i.e. temporal resolution ~ 133 μs) of the high speed cameras one could trace back the trajectories of the distinguishable fragments and analyse the time evolution of the fragmentation process. In order to count the fragments, an algorithm of a time series was generated with the following conditions:

1- In principle the fragment size distribution is completed immediately after the collision energy is consumed and the last bond is broken. The size of the smallest and the largest fragment has been determined and fixed.
2- If the first assumption is true then the slope of area-frequency distribution should be same at any instant after the collision, given that the influence of secondary collisions is negligible.
3- After collision, the smaller the fragment are separated earlier from the parent body than the larger fragments. Therefore the small fragments are also faster, so they leave the field of view before the larger fragments become optically thin.
4- This fact requires the selection of the later frames when the cloud of fragments becomes optically thin and the largest fragment is accessible.

5- However the very late frames can not be selected as well because then the secondary collisions start to dominate (among fragments and between fragments and wall of the drop tower).

The implementation of these criteria left a small window of time for the analysis of size distribution, usually about ~ 50 ms after the collision.

Thanks to the free software Image-J (Fiji) which made image processing (flat fielding and background subtraction) very easy. After processing the selected frames, all the distinguishable trajectories of the fragments were traced and counted by the provided tool “Particle Analyser”. The cross-sectional area of each fragment (1 pixel = 0.174 mm^2) was recorded up to the size of the largest fragments (which has been already separated out and used in eqn. (4.2)). Hereafter the fragments have been analysed in terms of their cross-sectional area, which has been later translated into mass distribution. Any single fragment can be counted more than once and maximum it can be counted equal to the number of frames selected.

4.6.1.1 Invariant slope (α) of area frequency distribution

In order to test these assumptions whether the statistical analysis of about ~ 50 ms is a realistic approximation of the actual distribution, the variation in the slope α (see eqn. (4.30)) of area-frequency distribution has been analysed at different time intervals.

For this, randomly an experiment, named 3Jun-6 from the series 3.5 cm – 5 cm (the complete series is in Figure 4.16), has been presented. From the images of this experiment, a new time series was generated and then segmented in 6 equal intervals, each of 50 frames, covering total time 40 ms after collision. In each time interval T, the variation in α has been traced. Since the power law relation between the fragment of area x and cumulative count $N_{\text{cum}}(x)$ has been shown in previous studies (Blum & Münch 1993) (Deckers & Teiser 2014), therefore the same is followed here, such as

$$N_{\text{cum}}(x) = \sum_{x=x_{\max}}^{x} N(x) = C_N x^{-\alpha} . \tag{4.30}$$

Here, C_N is the total fragment-frequency count, which gives the sum of the frequencies of all fragments (more details in Sec. 4.7.3). The summation starts from the largest fragment area $x_{\max}$ to any fragment of area x, with bin width Δx = 1 pixel. The $x_{\max}$ is not necessarily the largest fragment of the actual distribution, corresponding to μ. Therefore to reduce the impact of the few large fragments on the slope α, eqn. (4.30) has been applied to the area range depicted in the rectangular box in Figure 4.15(a). Here the curve of black squares T1 and the curve of green left triangle T6 represent the first and the last time interval respectively. For reference the complete data of 3Jun-6 experiment is also plotted, here represented by red vertical dash. As the time after the collision elapses, the count of each fragment bin $N(x)$ increases which shifts the subsequent curve upward. At the same time the larger fragments get separated from its environment and become countable, so the curve shifts rightwards to larger cross-section. As a result slope does not change so much as depicted in Figure 4.15 (b). In the same figure one can see the mean value of the slope $\bar{\alpha}$ = 0.897±0.0086 remains within the narrow interval.

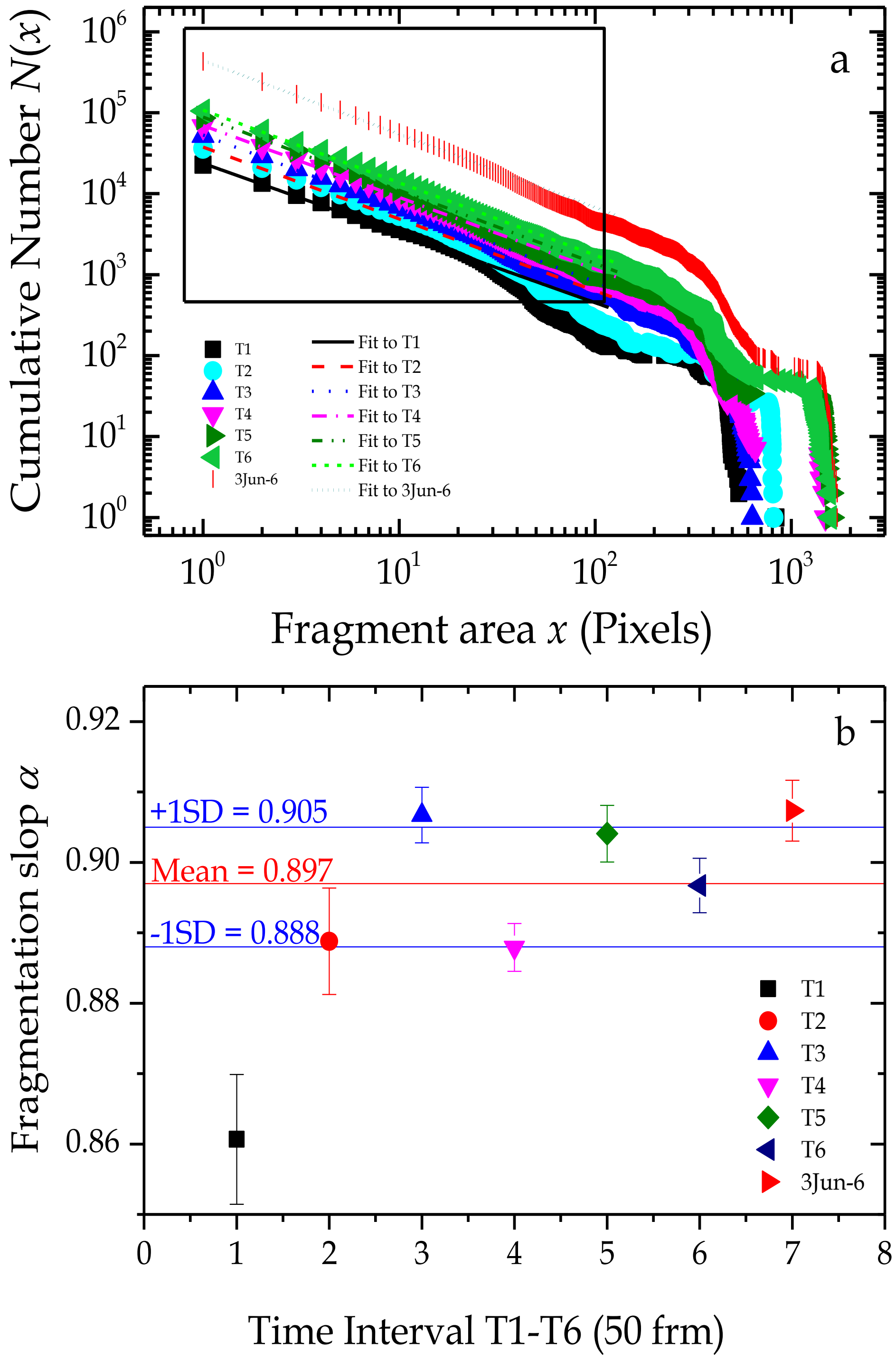

Figure 4.15. (a) The time series of the single fragmentation curve 3Jun-6 (red bars) is analysed in 6 equal time intervals from T1 to T6, each of 50 frames. In **(b)** the slope of each time interval remains same with mean value 0.897 and SD ~ 0.009 represented by red and blue grid lines respectively **(BS 17)**.

It is in good match with the reference slope $\alpha = 0.907$ of the 3Jun-6 for the full time interval, in red right-triangle. Here it should be mentioned the mean $\bar{\alpha}$ is taken from T2 to T6. The first interval T1 is not included due to the fact, all the fragments were not optically thin and the distribution was not mature. T1 corresponds to 6.67 ms after the collision, when the collision site was almost opaque. However few smaller fragments, owing to their higher velocity managed to escape the collision site, were detected and gave rise to an immature size distribution.

Hence it can be concluded, the slop of fragmentation, observed at any instance after the collision, remains almost same and the method fragment count and the statistical analysis of about ~ 50 ms is a good representation of the actual distribution.

4.7 A complete area- frequency distribution

In previous studies, only the continuous regime of size distribution, which follows the power law (eqn. (4.30)) has been analysed and the larger fragments were not included in the distribution. However in this study the larger fragments have been included as well, due to the fact they possesses a large fraction of mass and have to play a role in dust evolution. Therefore their inclusion into the distribution becomes crucial, in particular when $\mu \geq 0.5$.

In order to include the larger fragments, the power law in eqn. (4.30) has been modified and a cut-off term has been introduced. The complete size distribution can be expressed as

$$N_{\text{cum}}(x) = \sum_{x=x_{\max}}^{x} N(x) = C_N x^{-\alpha} e^{-\left(\frac{x}{x_i}\right)^{\upsilon}} . \tag{4.31}$$

As the size of the fragments increases, $N(x)$ declines with a slope $-\alpha$, up to the critical fragment size x_i, the knee of the distribution. It indicates the end of the continuous regime of power law. Above this the $N(x)$ exponentially drops with an exponent $-(x/x_i)^{\upsilon}$.

For the representation of the data analysis, here the collision series 3.5 cm – 5 cm has been presented in Figure 4.16. The analysis of all 142 experiments from eight collision series has been provided in Appendix A. The eqn. (4.31) has been fitted to the experimental data and the four parameters C_N, x_i, α and υ have been determined. Here $\upsilon = 2$ has been fixed to all the data sets. The fitting values for α varies from 0.2 to 2 as shown in Figure 4.17 and the critical fragment size x_i varied from 50 pixels to 10,000 pixels. The curves are arranged with respect to collision energy (mJ). The inner curves, e.g. cyan green bar and green star, tend to have steeper slope and smaller critical fragments size, whereas the outer curves possess shallower slope and larger critical fragment size, see curve of black square and blue up-triangles.

The reason for the steeper slope could be associated with the low energy dissipation rate, which means at the beginning more energy per bond is available. More small fragments are produced. As the sound waves proceed deeper into the volume, the energy dissipation rate decreases and so the size of the fragments increases. As the fragment size reaches to its critical value x_i, not enough energy is available to produce smaller fragments, so one can see large chunks appearing, which are actually the remnants of the original aggregate, and responsible for the exponential decline in the count. The inset in Figure 4.16 zooms into the details of this region and makes the trend prominent. The vertical features in the curves indeed represent the *largest observable fragment* in the distribution (here the largest fragment observed is *not necessarily* the actual largest fragment m_l of the distribution).

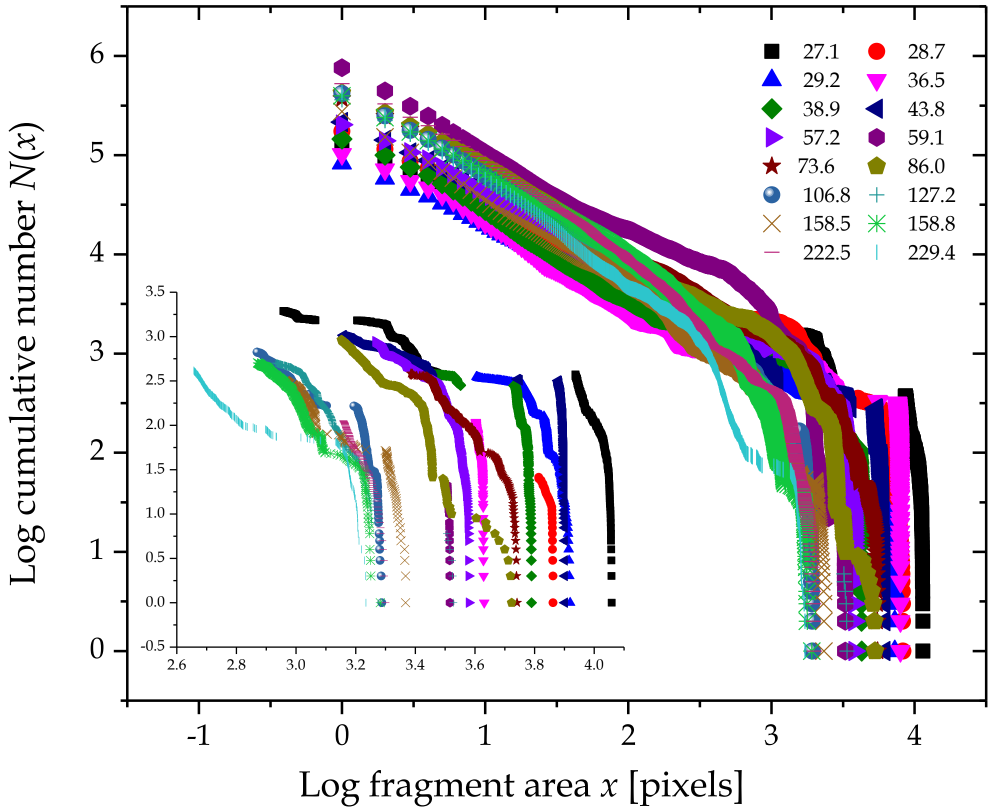

Figure 4.16. A typical cumulative area distribution of the representative series 3.5 cm – 5 cm. The inset is the zoom into the region of larger fragments which are responsible for the vertical features. The curves are sorted with respect to collision energy (mJ) as shown in the legend **(BS 17)**.

As the fragment moves its size projected onto the camera slightly varies (~ few 100 pixels), hence it is perceived few 100 times more often as a new particle. This is what giving rise to the vertical features. The gaps with smooth bending to the left can be associated with the second and the third largest fragments respectively. Here it should be mentioned that in any case due to resolution limit of the camera 1 pixel = 0.174 mm^2, the fragments smaller than this could not be detected. However the y-intercept extrapolation suggests that the size of the smallest possible fragment could be by factor 10 smaller (~ 0.0174 mm^2).

4.7.1 Variation in slope α of area- frequency distribution

In Sec. 4.6.1.1 it has been shown that within a collision the fragmentation slope α remains almost same. However a variation in the slope has been observed (see Figure 4.16) as the collision energy varied. For a quantitative analyses of the fragmentation slope, the dependency of α on velocity v_n, projectile P and target T has been checked. The assumption of a power law continues, such as

$$\alpha = C_\alpha + \delta \log\left(\frac{v_n}{1\ \mathrm{m s^{-1}}}\right) + \varepsilon \log\left(\frac{P}{1\ \mathrm{cm}}\right) + \psi \log\left(\frac{T}{1\ \mathrm{cm}}\right). \tag{4.32}$$

Here one follows the same approach as in Sec. 4.5.1, the model equation will be fitted and the unknown parameters will be determined. If any parameters is found to have either very high error or very low value, it will be set to zero in the model and the given equation will be refitted. From onward the same approached will be applied in rest of the analysis. Here eqn. (4.32) has been fitted to fragmentation slope α of all 141 (one data point being outlier is not included in the fit)[6] experiments. The minimising of the residuals gives the following fit parameters

Table 4.5. The fit parameters of α are derived by fitting eqn. (4.32) and eqn. (4.33)

Run No.	C_α	$\delta\,(v_n)$	$\varepsilon\,(P)$	$\psi\,(T)$	χ^2_{red}
1	0.15 ± 0.09	1.01 ± 0.14	-0.02 ± 0.11	0.36 ± 0.12	0.066
2	0.14 ± 0.08	1.02 ± 0.11	0	0.34 ± 0.09	0.065

The first run of fitting shows that the projectile has error higher than its values $\varepsilon = -0.02 \pm 0.11$, therefore it becomes obvious that dependence of α on projectile is negligible. The variation in P by factor 5 returns maximum deviation in $\alpha \sim 0.01$, which is significantly less than the range of α shown in Figure 4.17.

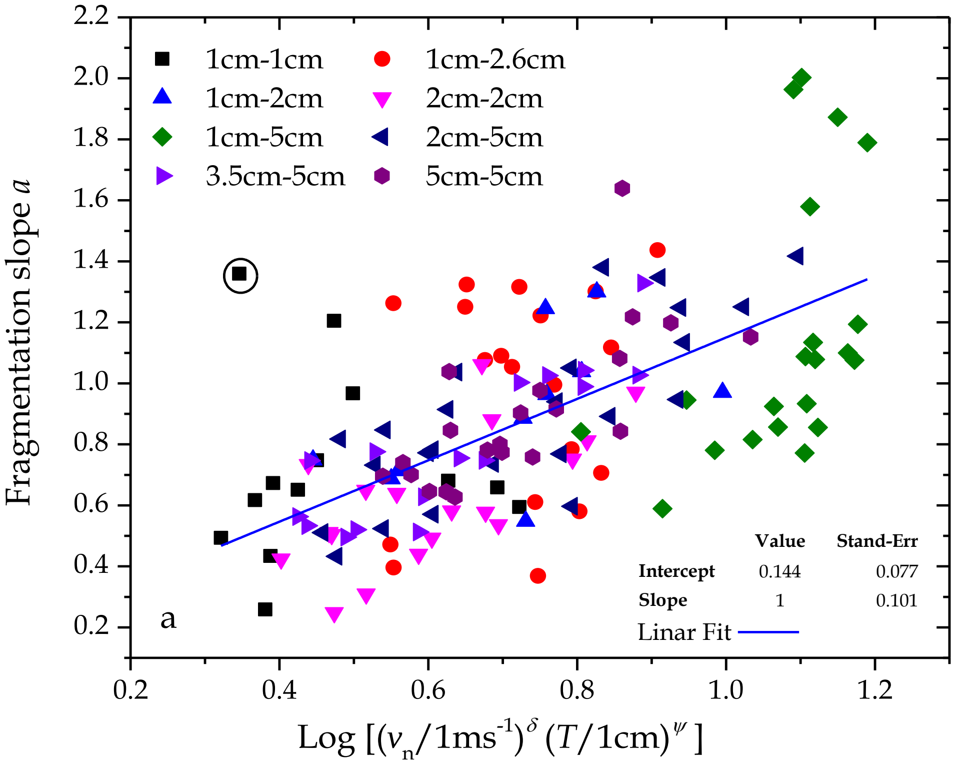

Figure 4.17. The slope α for 141 experiments as a function of v_n and T. The slope increase with velocity and the size of target with exponent $\delta = 1.02$ and $\psi = 0.34$ respectively. The circled data point is treated as an outlier, hence not included in fitting. The blue line is the linear fit with slope 1, to the data for the parameters given in second row of Table 4.5 **(BS 17)**.

---

[6] The reason of exclusion is the poor fit to the data of experiment 7Okt-1, see Figure A 1 in appendix A

Therefore in eqn. (4.32) $\varepsilon = 0$ has been set and one gets the following form

$$\alpha = C_\alpha + \delta \log\left(\frac{v_n}{1\ \mathrm{m s^{-1}}}\right) + \psi \log\left(\frac{T}{1\ \mathrm{cm}}\right). \tag{4.33}$$

The above equation is refitted and the values are given in the second row of Table 4.5. One can see that the new values are slightly refined and hence have been used in Figure 4.17 to show the dependence of α on velocity and target. The figure shows that the quantities, which have profound impact on the fragmentation slope α, are the impact velocity and the size of the target.

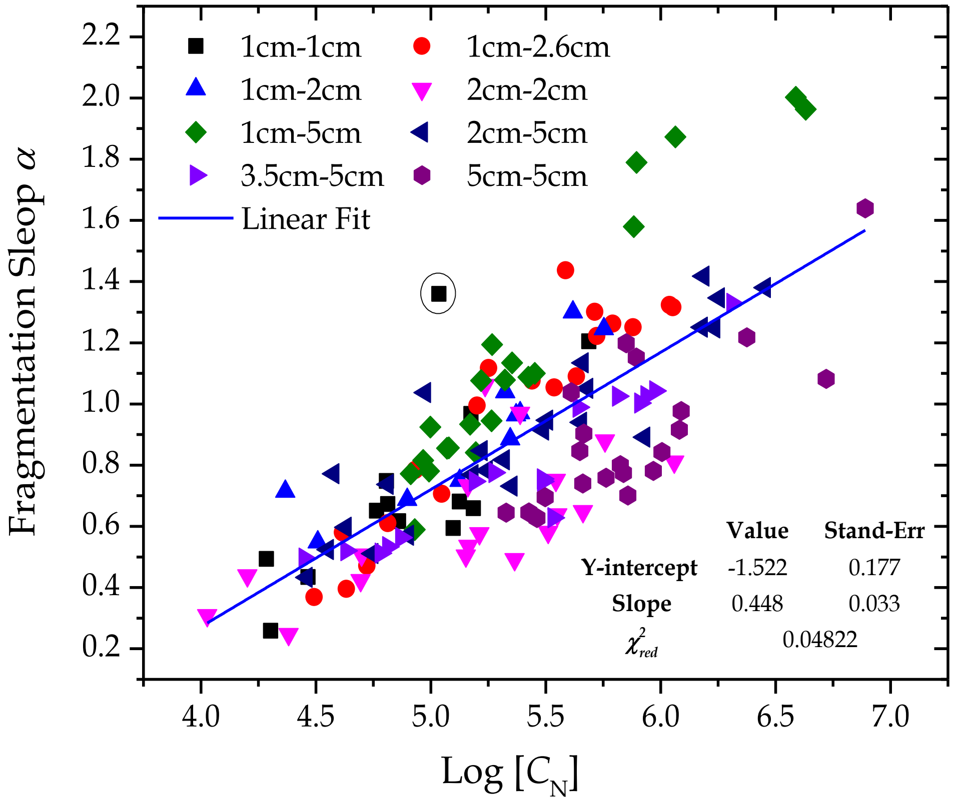

Figure 4.18. Fragmentation slope α as a function of fragment-frequency count C_N. The blue line is the linear fit to $\alpha = i + j \log(C_N)$ where $i = -1.52 \pm 0.18$ is the y-intercept and $j = 0.45 \pm 0.03$ is the slope of the curve. The encircled data point has been neglected for the reason given in foot note ii.

The dependency of α on collision velocity and the size of target could be explained by the fact that α is proportional to fragment-frequency count C_N, as shown in Figure 4.18 and in turn C_N is direct function of collision energy (see Figure 4.21 and details in Sec. 4.7.3). Hence the slope α indirectly depends on collision energy, as a result one sees the dependence of α on velocity as well as size of the target.

Corollary: Here the catastrophic slope of fragmentation $\alpha_{0.5}$ can be defined as a slope when the aggregates of same size i.e. $P = T = A$ collide at catastrophic fragment velocity $v_{0.5}$. By plugging eqn. (4.20) in eqn. (4.33) and one gets the following

$$\alpha_{0.5} = 1.08 - 0.46 \log\left(\frac{A}{1\ \mathrm{cm}}\right) \tag{4.34}$$

An intense fragmentation is expected when $\alpha \geq \alpha_{0.5}$.

4.7.2 The critical fragment area x_i

In area-frequency distribution, given eqn. (4.31), the critical fragment size x_i plays an important role. It defines the boundary between the continuous size distribution and the discrete size distribution. In other words it defines the upper size limit by which the distribution follows the power law. Therefore one should be interested to see its dependence on collision parameters, i.e. velocity, projectile and target. By using the assumption that x_i has power law dependence one can define

$$\log x_i = C_x + \theta \log\left(\frac{v_n}{1\ \mathrm{m\,s^{-1}}}\right) + \eta \log\left(\frac{P}{1\ \mathrm{cm}}\right) + \tau \log\left(\frac{T}{1\ \mathrm{cm}}\right) . \tag{4.35}$$

The preliminary analyses suggested that the events of catastrophic fragmentation (105 events in which projectile and target both fragmented) should be separated from the events of mass transfer (37 cases in which target remained intact and accreted the mass). Because in the case of mass transfer, projectile is the one which fragments and the critical fragment size x_i exclusively belongs to the projectile, hence raises the dependence on projectile significantly, as shown in the first row of Table 4.6 with all 142 values of x_i. Therefore to avoid any predisposition, only 105 events of catastrophic fragmentations have been selected, where projectile and target both are fragmented. The eqn. (4.35) has been refitted for 105 events and the new fit vales are given in second row of Table 4.6

Table 4.6. The fit parameters of critical fragment size x_i are obtained by fitting eqn. (4.35)

Run No.	C_x	θ (v_n)	η (P)	τ (T)	χ^2_{red}
1 (142 events)	2.92 ± 0.10	- 0.57 ± 0.16	1.87 ± 0.14	- 0.47 ± 0.14	0.095
2 (105 events)	3.01 ± 0.12	- 0.82 ± 0.19	1.44 ± 0.17	- 0.04 ± 0.17	0.087
3 (105 events)	3.01 ± 0.11	-0.84 ± 0.18	1.41 ± 0.11	0	0.086

In the second run of the fit, the projectile with exponent η = 1.44 ± 0.17 is still the dominant parameter in determining the size of x_i. However the dependence on target has almost vanished and the error in the value of τ = - 0.04 ± 0.17 is higher than the value itself, hence it should be neglected. Therefore eqn. (4.35) is refitted for the third time for τ = 0 and new fit parameters have been determined which are given in the third row of Table 4.6.

In the values of the third run, one can see the exponent of collision velocity θ = -0.84 ± 0.18 has gradually gained the prominence. Here negative sign of the velocity exponent is quite intuitive, i.e. higher is the velocity, smaller will be the fragments. However one still finds a strong dependence on the size of projectile; larger projectile in, larger debris out.

One possible explanation is $v_{0.5} \propto P^{-0.94}$ (see eqn. (4.19)), as the projectile size was increased the target started to halve at lower velocities. The decrease in velocity gave rise to larger debris. In other words, the increase in the size of projectile required to decrease the velocity and the decrease in velocity led to larger x_i. In addition a slightly lower χ^2_{red} = 0.086 favours the outcaste of target. The possible explanation for the dominating role of projectile is discussed in next section.

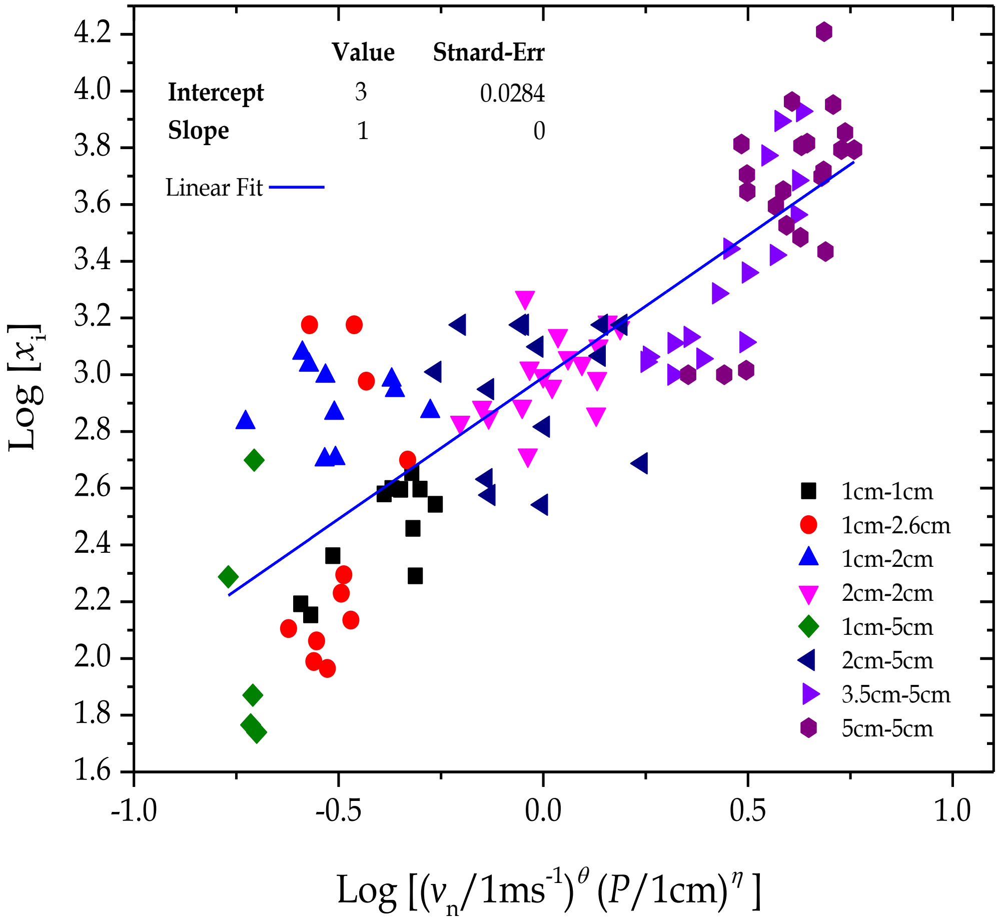

Figure 4.19. The critical fragment size x_i for 105 events of catastrophic fragmentation. According to the parameters given in third row of Table 4.6, the x_i has clear dependence on velocity with exponent θ = -0.84, whereas the dependence on the projectile is significantly higher η = 1.41. However the dependence of target has been neglected i.e. τ = 0. The blue line is linear fit with slope 1 **(BS 17)**.

4.7.3 The total fragment-frequency count C_N

As discussed in Sec. 4.6.1.1 that each fragment has been counted multiple times (maximum for number of selected frames), therefore the absolute frequency of a given fragment size is not so reliable. However in the following, the aim is to demonstrate that the total fragment-frequency C_N is not which matters, but its relation to other quantities in its environment, such as collision parameters, slope of fragmentation α and the critical fragment size x_i. With this argument C_N can be expressed such as

$$\log C_N = C_{N*} + \theta * \log\left(\frac{v_n}{1\ \text{ms}^{-1}}\right) + \eta * \log\left(\frac{P}{1\ \text{cm}}\right) + \tau * \log\left(\frac{T}{1\ \text{cm}}\right). \tag{4.36}$$

Here the same approach has been followed; in the first run the negligible parameter will be searched. If there exists any, it will be set to zero and eqn. (4.36) will be refitted for the final parameters. The fit values are given in following table

Table 4.7. The fit parameters of fragment-frequency C_N are derived by fitting eqn. (4.36)

Run No.	C_{N^*}	θ^* (v_n)	η^* (P)	τ^* (T)	χ^2_{red}
1	4.06 ± 0.14	1.78 ± 0.23	1.21 ± 0.19	0.05 ± 0.20	0.190
2	4.06 ± 0.14	1.81 ± 0.21	1.23 ± 0.15	0	0.188

The first run of fit shows that the fragment-frequency count C_N strongly depends on the collision velocity, with exponent $\theta^* = 1.78$, which is again an intuitive outcome; whereas the dependence on the size of projectile is still significant. Here projectile is acting in parallel with velocity and contributes to C_N. However, once again a vanishing role of the target can be seen. Therefore a second run of eqn. (4.36) is required where the exponent of target $\tau^* = 0$ has been used. The fit values are given in second row of Table 4.7. A slightly lower value of reduced chi-square, $\chi^2_{red} = 0.188$ justifies the drop of the target and confirms the expected trend.

Figure 4.20 has been drawn to show the dependence of C_N on impact velocity and projectile. Here one finds that the dependence of C_N on velocity and projectile has been slightly enhanced and the values are relatively refined as comparted to when target was included. On the basis of this analysis, it can be concluded that in any collision the impact velocity and the size of projectile play the key role in defining x_i, the boundary between the continuous and discrete regimes of size distribution, and the absolute fragment count C_N.

In Figure 4.19 and in Figure 4.20, the prominent role of the projectile and the diminished role of target could be explained by the selection of centre of mass system, where primarily the mass of the smaller body determines the energy of the system. The contribution of the target is only by its velocity and marginally by mass. Therefore the quantities such as x_i and C_N show strong dependence on projectile and negligible (or no) dependence on target. From Figure 4.6 one learns $Q^* \propto P^{1.12}$, as the projectile size increases, more energy per unit mass has been delivered into the system to halve the same target. This higher energy must be dissipated and the most efficient channel is by increasing the frequency of smaller fragments, which leads to a higher C_N. As the collision energy increases, more copies of smaller fragments are produced as shown in Figure 4.21, which in turn increases the fragmentation slope α (see Figure 4.18).

Corollary: For the cross check, the combined impact of the critical fragment size x_i and the fragment-frequency count C_N has been analysed in terms of collision parameters. For this eqn. (4.36) can be modified and to make differentiation in parameters (°) as a superscript has been used as shown in the following

$$\log\ [x_i \cdot C_N] = C_{xN} + \theta^\circ \log\left(\frac{v_n}{1\ \mathrm{ms}^{-1}}\right) + \eta^\circ \log\left(\frac{P}{1\ \mathrm{cm}}\right) + \tau^\circ \log\left(\frac{T}{1\ \mathrm{cm}}\right). \tag{4.37}$$

The reducing of the residuals leads to values given in Table 4.8

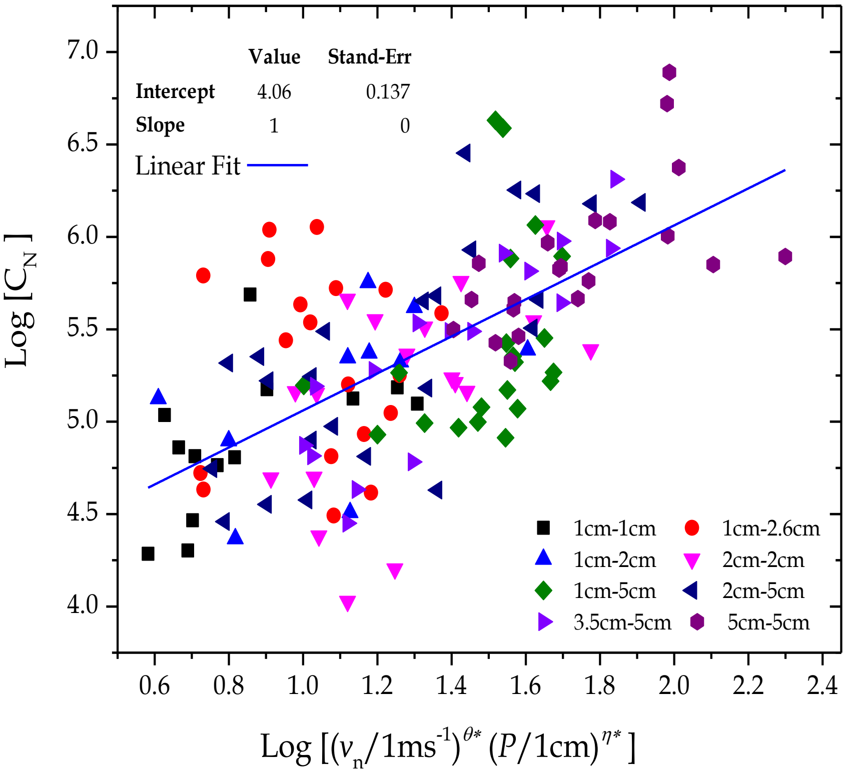

Figure 4.20. The fragment-frequency count C_N has strong dependence on velocity and projectile. Here the fit parameters for velocity is $\theta^* = 1.81$ and for projectile $\eta^* = 1.24$ have been used, as given in Table 4.7. The blue line is the linear fit to the data, which has slope = 1.

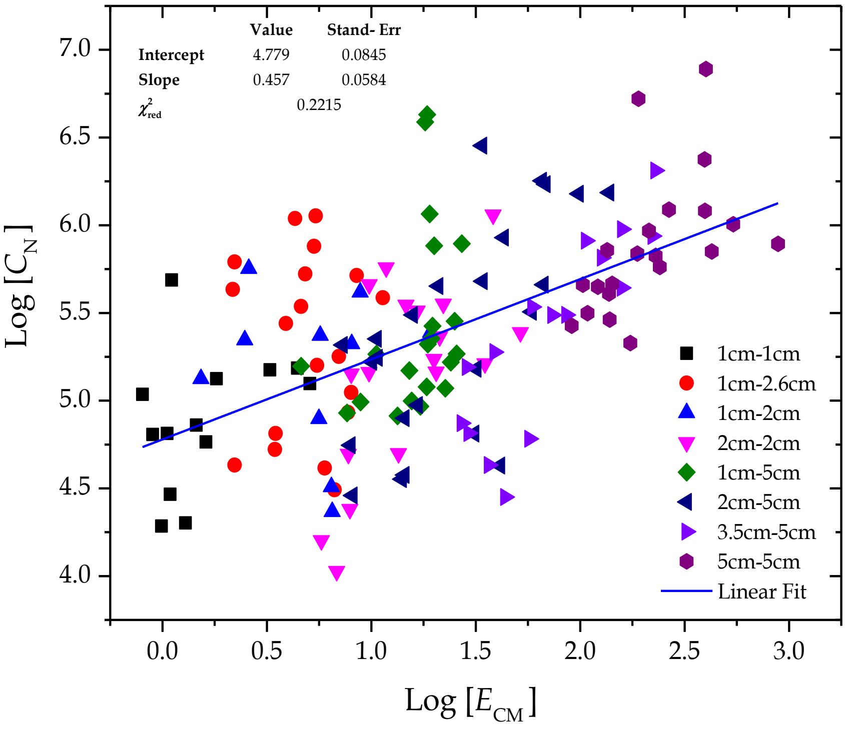

Figure 4.21. The fragment-frequency count shows a proportional relation with collision energy at centre of mass system. The blue line is the linear fit with slope 0.46 ± 0.06.

Table 4.8. The fit parameters derived by fitting eqn. (4.37)

Run No.	C_{xN}	$\theta°$ (v_n)	$\eta°$ (P)	$\tau°$(T)	χ^2_{red}
1	7.00 ± 0.21	1.00 ± 0.33	2.45 ± 0.29	0.28 ± 0.31	0.2694
2	7.02 ± 0.20	1.11 ± 0.31	2.66 ± 0.20	0	0.2690

As expected the dependence on target is negligible owing to high error. Therefore in the second run the exponent of the target was neglected by setting $\tau° = 0$.

The above given values reveal that the two important quantities of eqn. (4.31), namely the critical fragment size x_i and the fragment-frequency count C_N both are the function of impact velocity and projectile size but not the function of target. Now the final exponents can be compared by dividing eqn. (4.37) with eqn. (4.36) such that

$$\frac{x_i C_N \propto v^{1.1} P^{2.66}}{C_N \propto v^{1.81} P^{1.24}},$$

$$\Rightarrow \qquad x_i \propto v^{-0.71} P^{1.42} \tag{4.38}$$

If these values of the exponents are compared with the second row in Table 4.6 (θ with $\theta°$ and η with $\eta°$), one can see that the velocity exponent is slightly off the value but still within standard error, whereas the exponent of the projectile is in good agreement. Figure 4.22 shows that a linear correlation between $x_i C_N$ and collision velocity and projectile can be established by using the fit parameters given in second row of Table 4.8

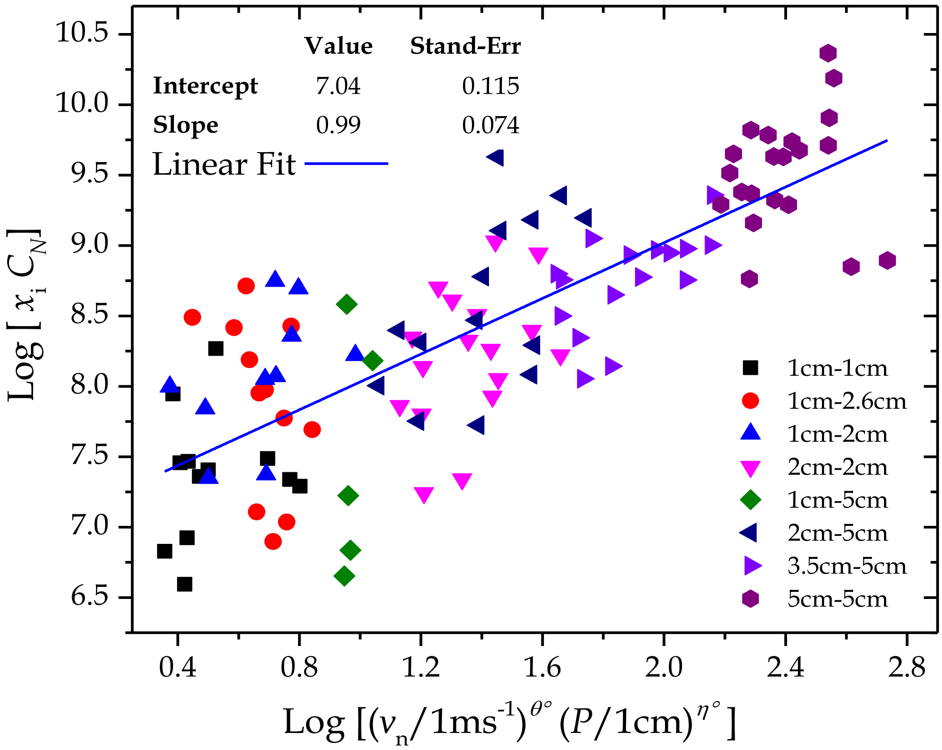

Figure 4.22. The x_i and C_N both have been simultaneously analysed as function of collision parameters. The fit parameters used here are follow the second run in Table 4.8. The blue line is the linear fit to the data 0.99 ± 0.07.

4.8 Mass-frequency distribution

In the next step the mass-frequency distribution of the fragments has been analysed, shown in Figure 4.23. Contrary to the absolute size distribution, here our interest is driven by the normalised distribution, required for the modelling. By using the pixel cross-sectional area x = 0.00174 cm^2 of each fragment, the corresponding fragment mass $m_f = \phi.\rho.x^{3/2}$ has been calculated in the units of grams, assuming each fragment as a sphere. Here $\rho = 2.65$ g cm^{-3} is the material density of SiO$_2$ and $\phi = 0.35$ is the volume filling-factor. Afterward, each fragment mass is normalised to the target mass m_t, such that $\mu_f = m_f/m_t$. By using eqn. (4.30) for the area-frequency distribution, the cumulative mass-frequency distribution $M_{cum}(\mu_f)$ can be derived such as

$$M_{cum}(\mu_f) = \begin{cases} M_{tot}\left(1-\left(\dfrac{\mu_f}{\mu_i}\right)^{\beta}\right) & \text{for} \quad \beta > 0 \\ M_{tot}\left(\dfrac{\mu_i}{\mu_0}\right)^{\beta}\left(\left(\dfrac{\mu_f}{\mu_i}\right)^{\beta}-1\right) & \text{for} \quad \beta < 0 \end{cases}, \tag{4.39}$$

where

$$\beta = 1 - \frac{2\alpha}{3} \tag{4.40}$$

is slope of the mass-frequency distribution, which is derived by using the value of α. In most of the cases $\alpha < 3/2$, so β is positive and one gets $M_{cum}(\mu_f) = M_{tot}$ as $\mu_f \rightarrow 0$.

In the case of high velocity collisions where $\alpha > 3/2$ and $\beta < 0$, there one gets $M_{cum}(\mu_f) = \infty$ as μ_f approaches to zero. In order to avoid infinity, μ_f must be greater than zero. For this it is required to use the relative minimum mass $\mu_0 = m_0/m_t$, where m_0 is minimum unit mass or alternatively the monomer mass could be used as well. Hence in the case where $\beta < 0$ eqn. (4.39) is valid as long as $\mu_0 < \mu_f < 1$. Whereas $\mu_i = m_i/m_t$ is the critical relative fragment mass analogous to x_i (details in Sec. 4.8.1). Figure 4.23 shows cumulative mass-frequency distribution of a single experiment, called 1 June-2, taken from the representative series 3.5 cm – 5cm. Equation (4.39) has been applied with β fixed to 0.4967 and the free parameters M_{tot} and μ_i were determined. The analysis of all 142 experiments from the eight collision series has been provided in Appendix B. It is important to mention that owing to the multiple fragment count M_{tot} is not conserved. Since β is related to α, it is good to check its dependence on collision parameters as well. Analogous to fragmentation slope in Sec. 4.7.1, the relation can be defined as

$$\beta = C_{\beta} + \delta * \log\left(\frac{v_n}{1\ \text{ms}^{-1}}\right) + \varepsilon * \log\left(\frac{P}{1\ \text{cm}}\right) + \psi * \log\left(\frac{T}{1\ \text{cm}}\right). \tag{4.41}$$

The above mentioned equation has been fitted and the values are given in the following.

Table 4.9. The fit parameters derived by fitting eqn. (4.41)

Run No.	C_β	δ^* (v_n)	ε^* (P)	ψ^* (T)	χ^2_{red}
1	0.85 ± 0.06	-0.62 ± 0.10	0.03 ± 0.08	-0.21 ± 0.08	0.0323
2	0.86 ± 0.05	-0.65 ± 0.08	0	-0.19 ± 0.07	0.0321

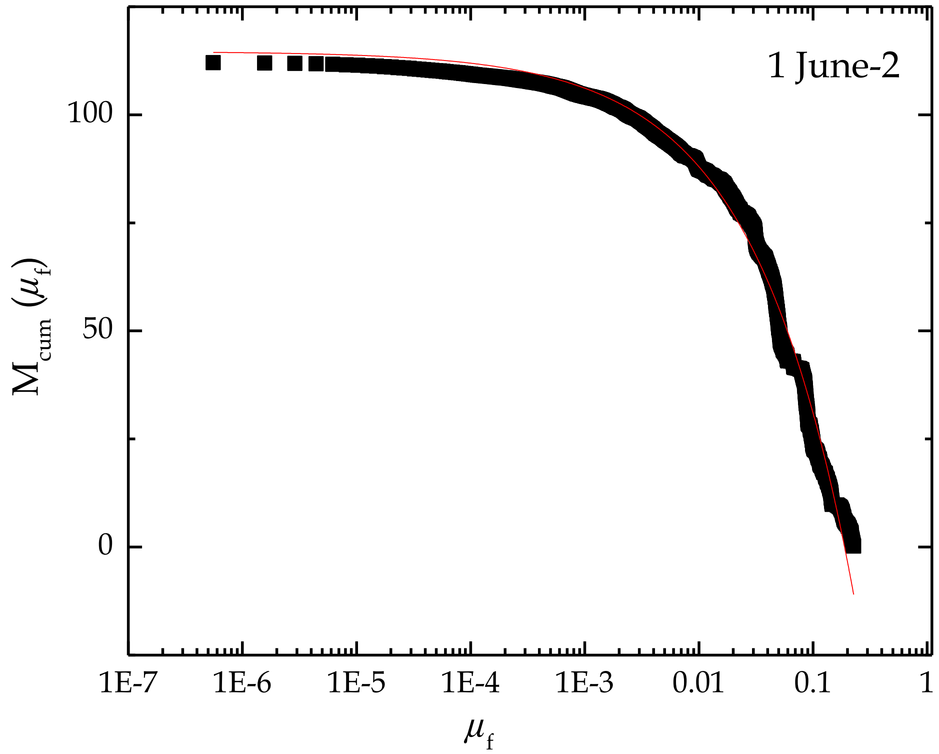

Figure 4.23. The cumulative mass-frequency distribution, starting from largest to smallest fragment. The data is one of the experiment called 1 June-2, which is taken from the collision series 3.5 cm – 5cm. Here eqn. (4.39) has been fitted with β = 0.4967. The reason of using y-axis as linear, is to show the lower end of the distribution where the slope is almost constant (see Figure 4.25) **(BS 17)**.

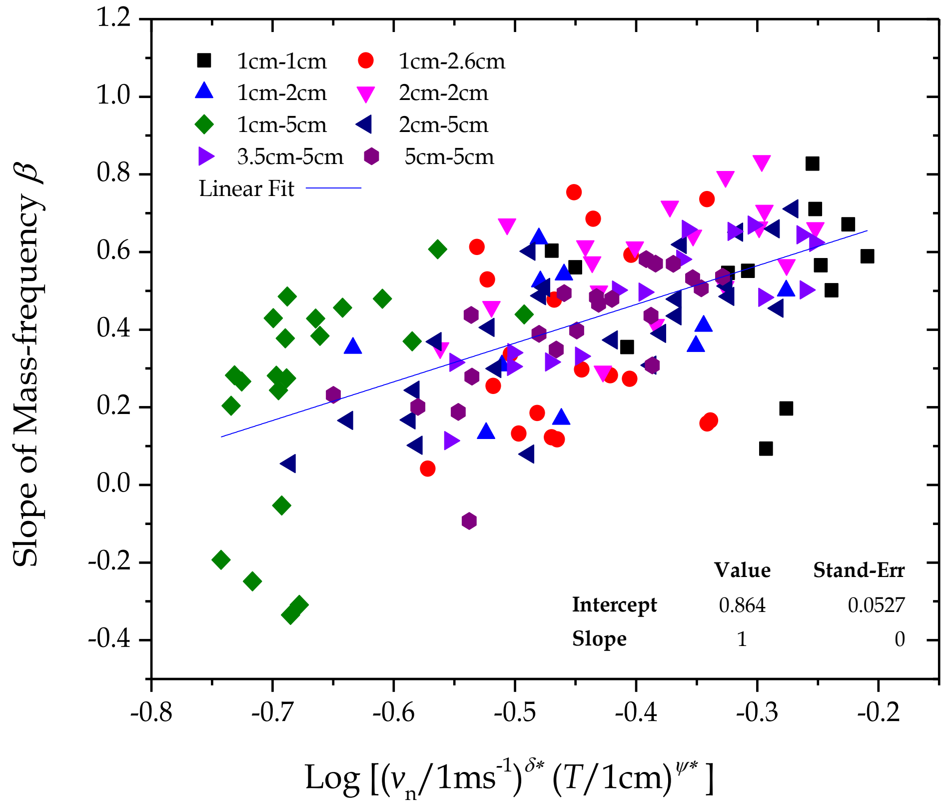

Figure 4.24. The slope of the mass-frequency distribution, in contrast to the slope of area-frequency, is negatively related to v_n with δ^* = -0.65 and T with ψ^* = -0.19 The blue line is the linear fit to new parameters and has slope 0.99.

In the first run of the fit, one finds that the exponent of projectile has higher error $\varepsilon^{*} = 0.03 \pm 0.08$, hence neglected in the second run. The fit values of the second run show that, the slope of mass-frequency β has dependence only collision velocity and the size of the target as shown in Figure 4.24, which is same as in the case of α (see Table 4.5). However in contrast to α here the dependence is inversely related to collision velocity and target.

Contrary to the results of area-frequency distribution where power law is valid over a long range of size distribution, as shown in Figure 4.15. However here in the case of mass-frequency distribution the data starts to deviate from power law little earlier, i.e. after first few fragments. In order to elaborate this fact, Figure 4.25 has been shown, where mass-frequency distribution starts from the smallest to the largest fragment. The data shown in the box covers first 10 fragment masses, on which the power law has been fitted. One can see, outside the box the data curve (black squares) starts to deviate from power law curve in red.

To make sure whether the trend is same in all experiments and series, the first 10 data points has been tested in all 142 experiments. In Figure 4.26 the slope of the said range in all experiments has been shown as a function of collision velocity. One can see that the slope remains almost constant, with a mean value 0.71 which has standard deviation 0.13.

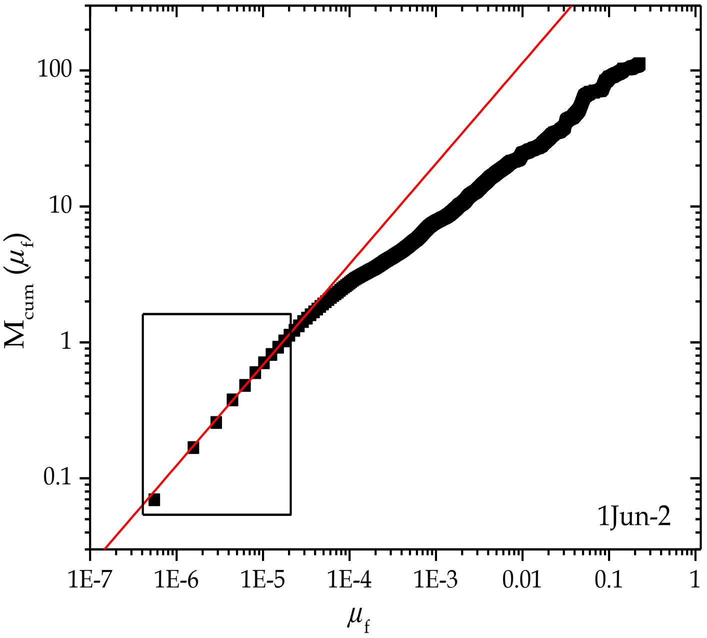

Figure 4.25. The cumulative mass-frequency distribution, starting from the smallest to the largest fragment. The red solid line is the power law fit to first 10 data points shown in box. The extrapolation of the curve shows that after a certain fragment mass, the distribution starts to deviate from power law. Here the same experimental data 1June-2 has been used **(BS 17)**.

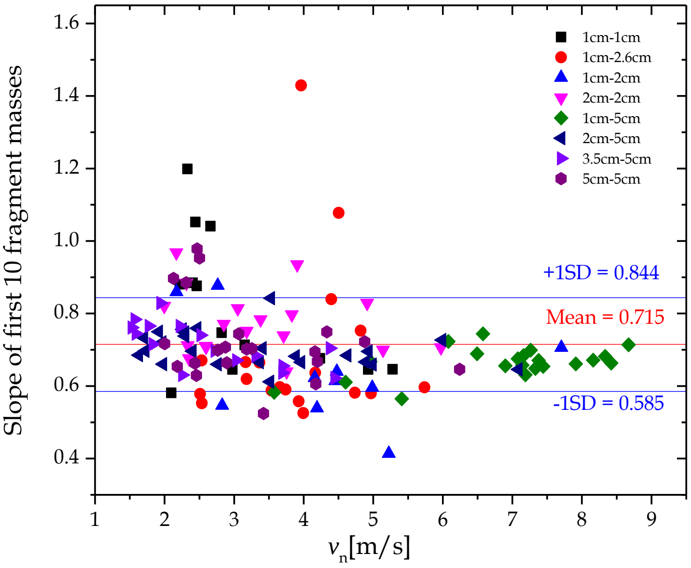

Figure 4.26. The slope of power law fit to first 10 data points has been shown as a function of impact velocity. Here the test has been applied to all 142 experiments from 8 series. The blue and the red horizontal lines show the standard deviation and mean values respectively (BS 17).

4.8.1 The correlation between critical fragment area x_i and mass μ_i

Since the mass of the fragments has been derived from the cross-sectional area of the fragments, therefore it is intuitive to expect a correlation between the critical fragment area x_i (introduced in eqn. (4.31)) and the critical fragment mass $\mu_i = m_i / m_t$ used in eqn. (4.39). To test whether there is a correlation, the critical fragment size x_i has been normalised to its respective target size x_t, so both sides are unit less. The relation can be written as

$$\log\left(\frac{m_i}{m_t}\right) = C_m + 1.5\ \log\left(\frac{x_i}{x_t}\right), \tag{4.42}$$

or

$$\mu_i = \frac{m_i}{m_t} = 10^{C_m} \cdot \left(\frac{x_i}{x_t}\right)^{1.5}, \tag{4.43}$$

where $C_m = 0.32 \pm 0.02$ has been obtained by the linear fit to the data shown in Figure 4.27. One can see there exists a linear correlation between x_i and μ_i which confirms the consistency between the model of area-frequency distribution given in eqn. (4.31) and the model of mass-frequency distribution given in eqn. (4.39).

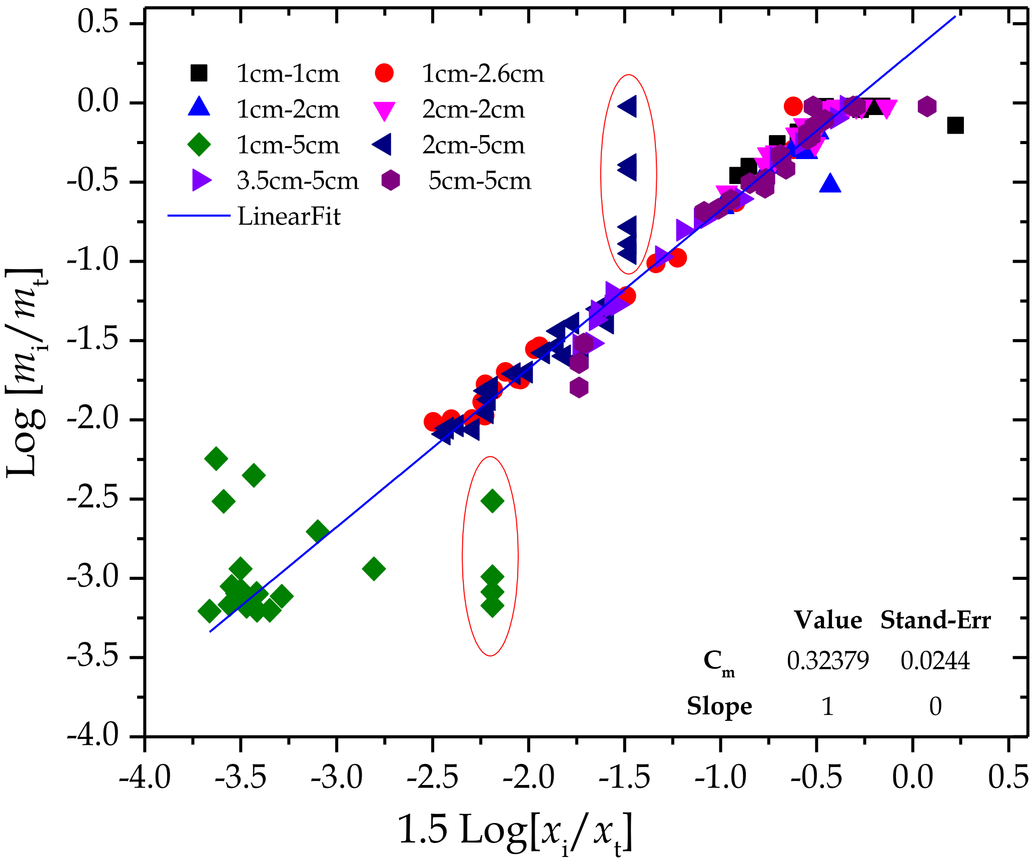

Figure 4.27. A linear correlation between the size and mass of the critical fragment, normalised to respective target, is observable. The blue line is the linear fit to the fit values of x_i and m_i which were derived from eqn. (4.31) and eqn. (4.39) respectively. The data points shown in ellipse are the few events in which x_i was enforced to be within a specific range, value less than x_t **(BS 17).**

4.8.2 The correlation between the μ_i and actual largest relative fragment μ

In this section the emphasis is on the fact that the critical relative fragment mass $\mu_i = m_i/m_t$, observed in the continuous mass-frequency distribution eqn. (4.39), is different than the actual largest relative fragment mass $\mu = m_l/m_t$ used in eqn. (4.2).

In Figure 4.28, one can see there exists no correlation between μ and μ_i. In addition, the first point to be noticed is $\mu_i \leq \mu$ or $m_i \leq m_l$ and the absence of the correlation between the two implies that the fragments subsequent to the largest fragment are independent from the upper limit of the largest fragment. In other words the size of the second or third the largest fragment does not depend on the first largest fragment. Hence it justifies the earlier separation of the largest fragment and the independent treatment, as discussed in Sec. 4.2.

However one possible explanation that why there is no correlation between the first largest fragment and the subsequent fragments, could be their increasing dependency on velocity. For example; from eqn. (4.6) (for n = 0.55) it is $m_l \propto v_n^{-1.1}$, whereas eqn. (4.35) gives $m_i \propto x_i^{3/2} \propto v_n^{-1.26}$. As the fragment gets smaller, its dependence on impact velocity increases.

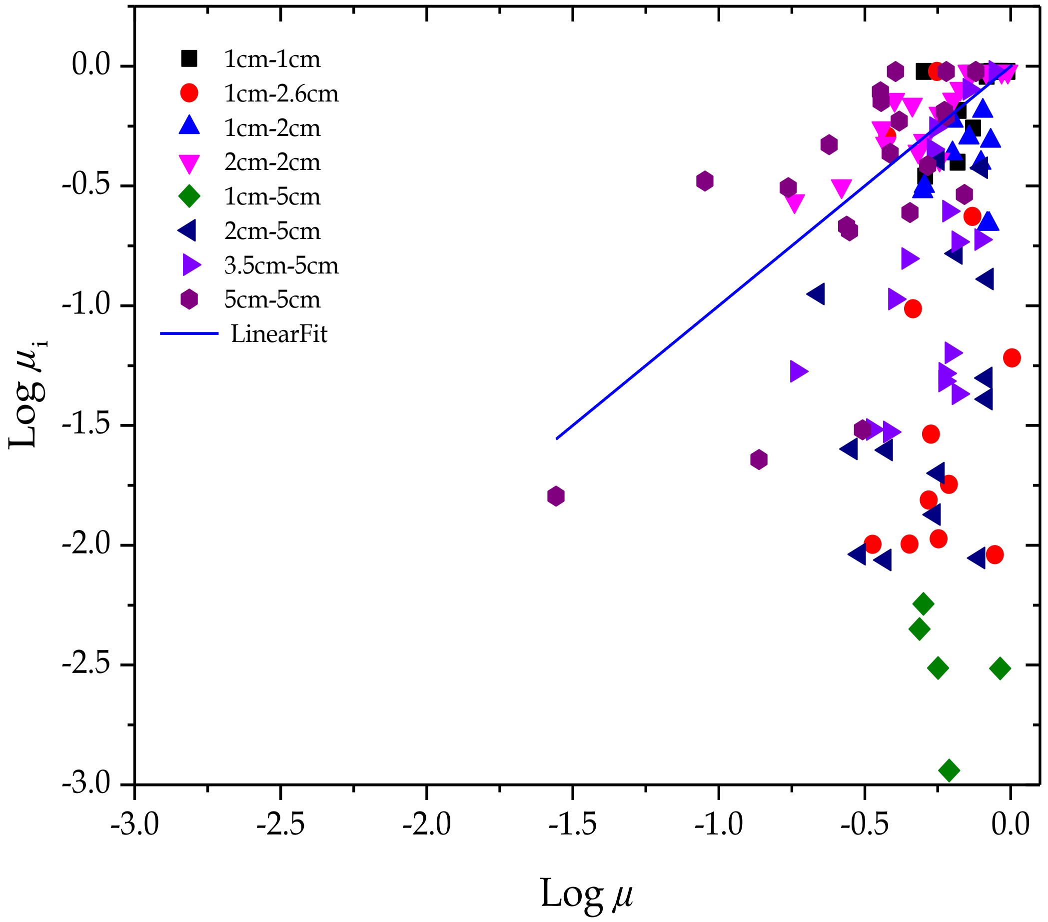

Figure 4.28. There exists no correlation between the critical fragment mass μ_i and the fragmentation strength μ. It supports the idea that the size of the second or third largest fragment does not depend on the size of the first largest fragment μ. The blue line is the linear fit to the data (BS 17).

4.9 The model of fragment velocity distribution

Although in this study the secondary collisions have been neglected, however in the context of protoplanetary disc (in particular the inner region where relative velocities are higher) the secondary collisions, which often lead to cascade fragmentation, play an important role and can significantly change the fragment size distribution. Therefore in this section the analysis of the fragment velocity distribution is presented.

4.9.1 The method of velocity measurements

Here the method of image selection and processing is the same as discussed in Sec. 4.6.1. However the difference is the use of an eclipsing disc, which acts as a coronagraph. The disc is placed at time $t = 0$, the moment of first contact between the two aggregates as depicted in Figure 4.29a. The x and y coordinates of the contact point have been taken and used as the centre of the disc, as shown in Figure 4.29b. The radius s of the disc has been varied between 15 cm – 20 cm, from one experiment to another, depending on the optical depth, the size of the dust cloud and available field of view. The purpose of this exercise is to give the dust cloud an ample time to expand and become optically thin. It is assumed that now fragments will not have any collision and they will scatter on a stable and traceable trajectory.

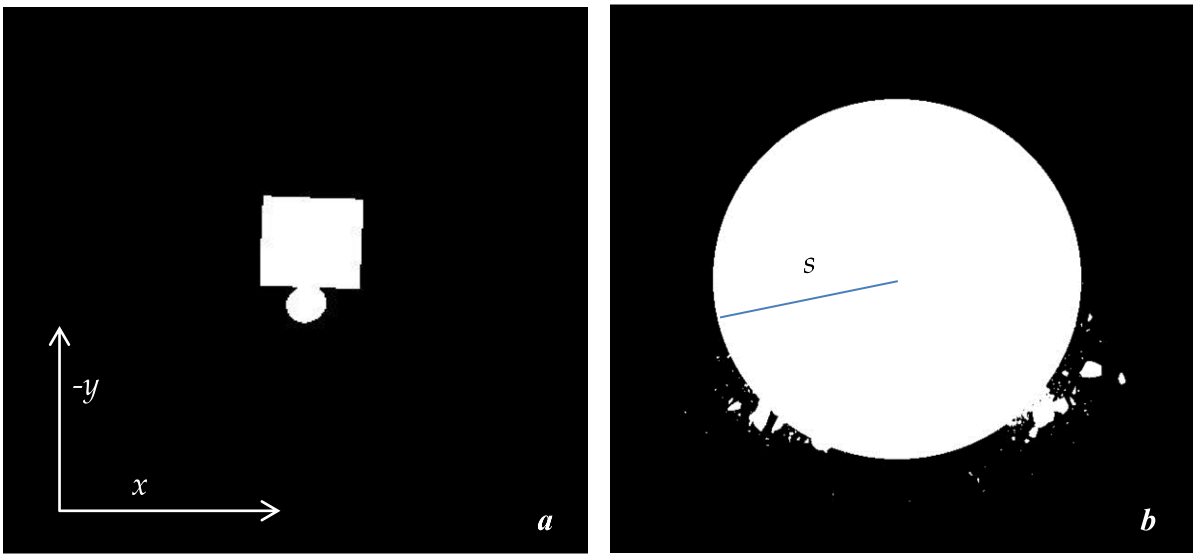

Figure 4.29. (a) The moment of first contact at $t = 0$ between 1 cm and 2.6 cm aggregates. At the coordinates of the contact point the centre of the disc has been placed, which eclipse the collision site. **(b)**. As the time elapses the fragments starts to appear outside the disc, their time (Frame No.) and position are recorded. Here 1pixel = 0.4167mm as unit for distance and 1 Frame = 133 μs as unit for time have been used. However to determine the velocity in laboratory frame, the radius s of the disc has been used rather the position of the fragment where it appeared.

As the fragments appear outside the disc, as shown in Figure 4.29(b), their time t' in terms of frame number and the coordinates are recorded and the distance covered with respect to the centre of the disc has been calculated. On the basis of first-appear-first-recorded principle, the double count of any single fragment has been avoided. However this criterion gave privilege to the fragments which were broken off from the surface of the aggregates, which could not be avoided. Another cause of error which was encountered in some cases was the thin trail of the fine dust (observable in Figure 4.1(a)) in the region outside the disc, which was left by the aggregates on their course prior to collision. Regardless to the vacuum up to ~ 10^{-3} mbar inside the drop tower, the fine dust remained suspended until it mixed up with dust and fragments produced after the collision. However their intensity has been reduced by the threshold selection during the image binarisation.

4.9.2 The result of velocity distribution

In first step the x-y components of the velocity as v_x and v_y in laboratory frame have been calculated. In second step the y-component of the velocities has been corrected for the gravitational component of the velocity v_g and the velocity of the centre of mass v_{CM}, because both components are directed along – y-axis.

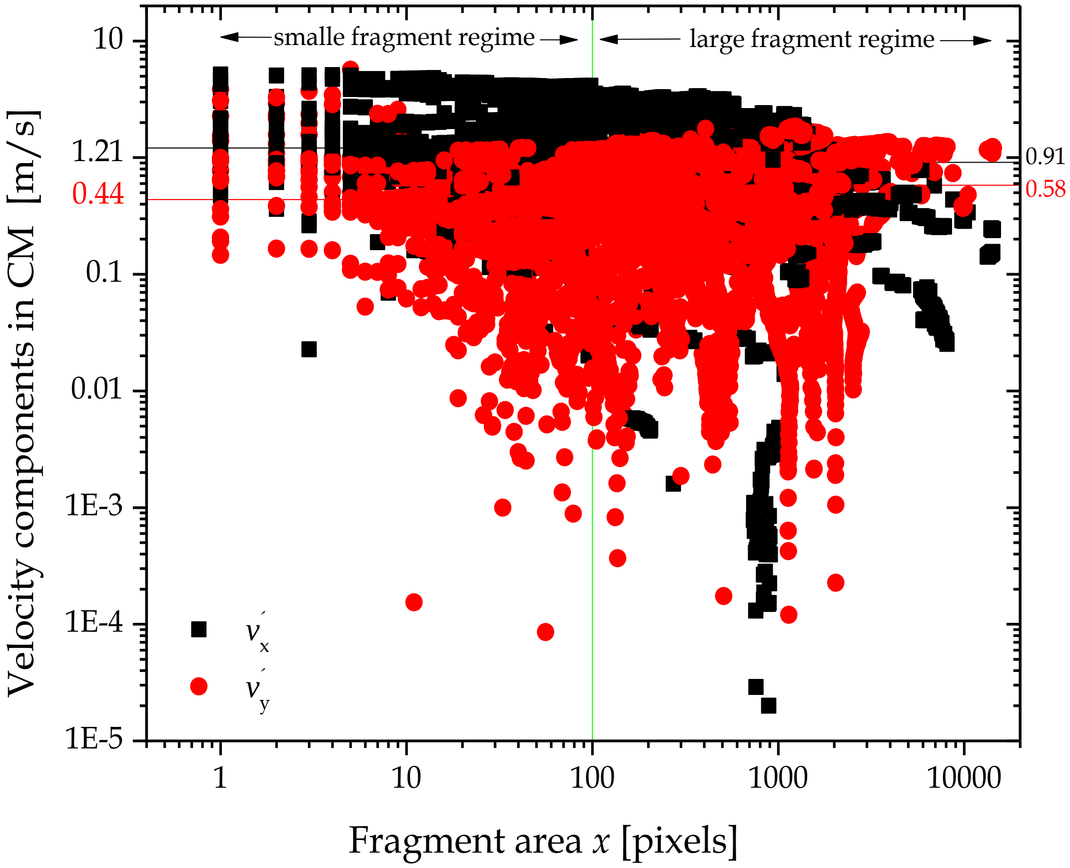

Figure 4.30. The v'_x in black squares and v'_y in red circles are the velocity components of the fragments in the centre of mass frame, which are given as a function of the fragment area x. The vertical green line at x = 100 pixels splits the data into small fragment regime, i.e. 1 – 100 pixels and into large fragment regime, 100 – 15000 pixels. The black and the red horizontal lines show the mean values of v'_x and v'_y respectively in the two regimes. In small fragment regime, on average $v'_x \sim 2.8\, v'_y$ and in large fragment regime, v'_x is only factor 1.56 higher than v'_y. However v'_x decreases with the size of fragments, whereas v'_y increases as the size of the fragment increases. The data is taken from the representative series 3.5 cm – 5 cm.

If x' - y' are the coordinates in centre of mass frame then v'_x and v'_y are the respective velocities, which can be expressed as follows

$$v'_x = v_x\,, \tag{4.44}$$

$$v'_y = v_y - \left(v_g = g\,.\,dt\right) - v_{\mathrm{CM}}\,, \tag{4.45}$$

where g = 9.8 ms^{-2} is the gravitational acceleration and dt is the time interval between first frame at t = 0 and t' the frame where the fragment was first recorded.

In Figure 4.30 the v'_x in black squares and v'_y in red circle being the components of the velocity in the centre of mass frame, have been shown as a function of fragment area. In order to analyse better the data has been split into two regimes, the small fragment regime which is from 1 pixel to 100 pixels and the regime of large fragments spans from 100 pixels to 15000 pixesl. One can see, the smaller fragments on average have velocity higher than that of larger fragments. As a result the small fragments escape the site of collision before the larger the fragments make their way out of optically thick dense cloud. This justifies the assumption made in Sec. 4.6.1.

Another aspect which is revealed in Figure 4.30 is that in the case of smaller fragments i.e. 1 – 100 pixels, v'_x is factor 2.8 higher than v'_y. It implies that the collision energy released perpendicular to the line of head-on collision is roughly 7 times higher than along the line of collision. The possible explanation in hand could be the geometry of the collision. As discussed in Sec. 4.1 that the geometry of the collision has been set in such a way that neither of the symmetry axis point in the velocity direction. So the collision can be approximated for two spheres. The contact point between two aggregates can be thought of as a site of a spherical explosion, where the collision energy radially disperses into the aggregate bodies through the contact point, as shown in Figure 4.31. The equal numbers of bonds should be broken in all directions. However the escape route from the body is not the same. One can see in the figure on right that the y-axis, the axis of the collision is shielded by the mass of the aggregates, the fragments can not escape from this axis. Whereas the x-axis and z-axis are completely free, therefore the fragments closer to x-z-plane easily escape from the aggregate body; while fragments along y-axis can not escape but can transfer the momentum to the next neighbour. The momentum by reaching the end of the body is significantly dissipated. As a result the velocity of the fragments along y-axis v'_y is accordingly reduced. Since the z-axis owing to the experimental design is inaccessible, therefore it has been neglected and only the x-axis remains a part of discussion. However the z-axis, by the symmetry of the collision, can be considered as synonymous to the x-axis in terms of velocity distribution.

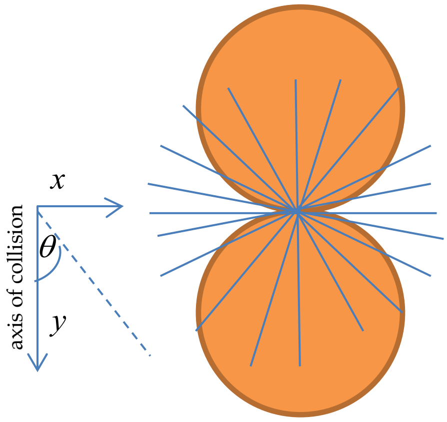

Figure 4.31. The geometry of the collision. The cylindrical aggregates rotated by 90° have same contact area as between the two spheres. As the fragment closer to x-axis is, higher will be its velocity. The fragments along y-axis are shielded by the mass of the aggregates, therefore have lower velocity.

If the assumption; as the fragments closer to x-axis are, higher is their velocity is correct, then the condition of conservation of energy requires that most of the fragments should scatter close to x-axis. For this the scattering angle θ between v'_x and v'_y has to be defined as

$$\theta = \arctan\left(\frac{v'_x / v_{\mathrm{cm}}}{v'_y / v_{\mathrm{cm}}}\right). \tag{4.46}$$

Here both components of the velocity, i.e. v'_x and v'_y have been normalised to the velocity of the centre of mass v_{CM}. By using eqn. (4.46), first the scattering angle of each fragment has been calculated in all 16 experiments. Then the count of every angle is determined by counting how often a single angel appears within bin size 4.5°, which corresponds to number of fragments in that bin. Figure 4.32 shows the number of fragments on left y-axis and their cumulative frequency on right y-axis of the angles as function of scattering angle. One can see about 65% fragments have trajectories above 45°, which implies that a large fraction of fragments scatter close to x-axis (the axis normal to the line of collision). As it has been shown earlier that the larger fragments have lower velocities and fewer counts, therefore it is intuitive to think that larger fragment tend to have scattering angle less than 45°, i.e. they scatter more close to y-axis.

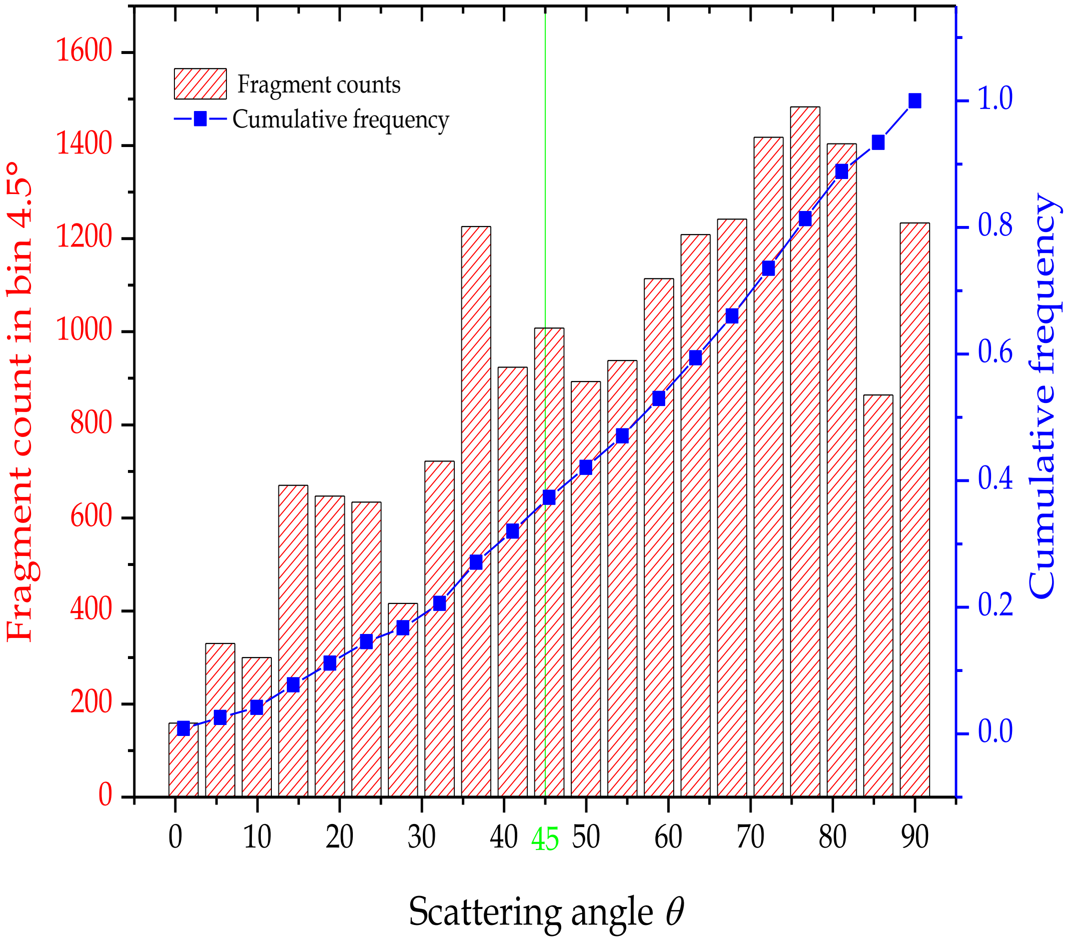

Figure 4.32. Number of fragments in bars associated to left y-axis are given as a function of scattering angle with bin size 4.5°. The fragment number corresponds to how often a given angle is repeated in 16 experiments. The blue-connected points associated to right y-axis show the cumulative frequency of the angle. The vertical green line at 45° emphasizes that about 65% fragments scatter close to x-axis. Here the data of the collision series 3.5 cm – 5cm has be used.

4.9.3 The velocity distribution in centre of mass (CM) and laboratory frame

The resultant velocity of fragments in centre of mass frame v_{cmf} is given as

$$v_{\mathrm{cmf}} = \sqrt{\left(v'_x\right)^2 + \left(v'_y\right)^2} = \sqrt{\left(v_x\right)^2 + \left(v_y - v_g - v_{\mathrm{CM}}\right)^2} \; . \tag{4.47}$$

In Figure 4.33 (a) the resultant velocity v_{cmf} of the fragments in the centre of mass frame has been shown as a function of fragment size. It should be mentioned that the data in Figure 4.33 (a)(b) is a single experiment called 1 June-2 from the series 3.5 cm – 5 cm, taken as a representative case. However owing to higher degree of noise in the data, the correlation could not be defined qualitatively. Therefore the velocity of fragments in the laboratory frame v_{Lab} has been analysed as well.

In the laboratory frame, for distance rather than using the coordinates of the fragments, the radius of the disc *s*, as shown in Figure 4.29(b), has been considered for the distance *ds*. In this way those fragments which were randomly scattered in the field of view, prior to collision, now have been assumed to lie at the disc radius. Moreover they will be not counted until the actual fragments appeared outside the disc. The velocity of fragments in laboratory frame is given by

$$v_{\mathrm{Lab}} = \frac{ds}{dt} \, , \tag{4.48}$$

where *dt* is the time to traverse the disc of radius *ds*. Figure 4.33(b) shows the fragment-velocity in laboratory frame v_{Lab} as a function of fragment area *x*. Since the position of every fragment was approximated to disc radius, in this way the weightage of the undesired fragments in the field of view has been reduced. As a result one finds the correlation, between the fragment-velocity and fragment-size, is better in the laboratory frame than that of in centre of mass frame, see Figure 4.33 (a). In addition, the values of the reduced chi-square, for the function given in eqn. (4.49), have been compared between the two reference frames. It turned out; in most of the experiments the reduced chi-square value for the data associated to laboratory frame has been lower. For example; in the given experiment 1 Jun-2, the reduced chi-square in Figure 4.33(b), is about ~ 4% less than in the centre of mass frame shown in Figure 4.33(a).

From the optic view of Figure 4.33(b) one finds the break of slope within small fragment regime, for example, see the encircled region in same figure. Therefore to define the shape of the curve in Figure 4.33(b), the argument used in Sec. 4.7 has been repeated in the following way: The reason of the initially very shallow slope (or almost flat within small fragment regime) could be associated to the fact that at the beginning more energy per bond was available, so more small fragments were produced and they fly away with higher velocity and it is almost same till the critical fragment size, this is what flattens the curve. As the sound waves proceed deeper into the volume, the energy dissipation rate decreases, less and less energy is available, so the larger chunks were produced and also less energy available for them to escape with. Therefore, the larger a fragment is, fewer is the count and the lower is its velocity and vice versa. The relation between the velocity of fragments (in both reference frames) and the size of the fragments is assumed to follow some form of power law or a truncated power law, which should reflect the shallower part of the curve (for smaller fragments) and the steeper part (for larger fragments) followed by the critical fragment size. Therefore an empirical function has been used introduced in the following form

$$v_{\text{Lab}} = v_{\max}\left(1+\frac{x}{x_j}\right)^{-\beta^*} . \tag{4.49}$$

Here $v_{\max}$ is the maximum velocity of the fragments which decreases beyond the critical fragment size x_j with slope $-\beta^*$. Since the data has high noise in the large fragment regime, i.e. above 100 pixels (see Appendix C) and x_j could not be determined in many cases, therefore during the fit-process x_j has been forced to look the value within 1 – 100 pixels.

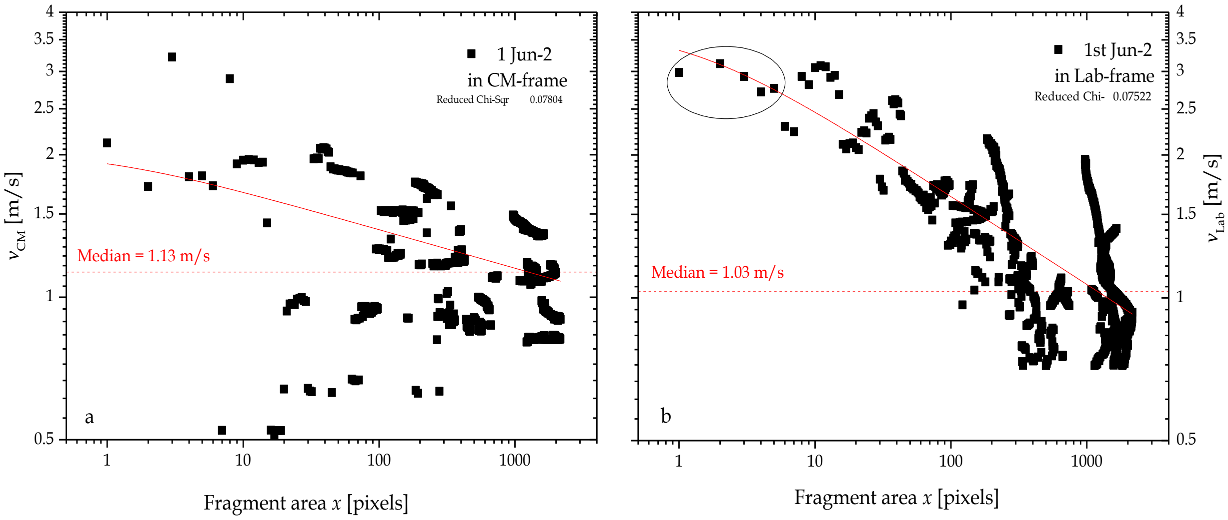

Figure 4.33. (a) The velocity of fragments in centre of mass frame and **(b)** in laboratory frame respectively, has been given as a function of fragment area x. The eqn. (4.49) has been fitted, shown in red-solid lines to the fragment velocity in both reference frames, the value of chi-square has turned up to be lower in laboratory frame. The dashed lines in both cases represent the median velocity of the fragments. Here a single experiment 1 June-2 from the collision series 3.5 cm – 5cm is presented.

The analysis of all 141 experiments[7] from eight collision series has been provided in Appendix C. However to know how realistic the fit-function given in eqn. (4.49) is, the slope of the curve β^* and the maximum fragment velocity $v_{\max}$ have been investigated as a function of initial collision parameters, i.e. collision velocity v_n, and the size of projectile P and target T. First the slope β^* has been analysed and for this the assumption of a power law dependence has been used in the following form

$$\beta^* = C_{\beta^*} + \vartheta \log\left(\frac{v_n}{1\ \text{ms}^{-1}}\right) + \gamma \log\left(\frac{P}{1\ \text{cm}}\right) + \varsigma \log\left(\frac{T}{1\ \text{cm}}\right) . \tag{4.50}$$

The minimising of the residuals yields the fit parameters given in Table 4.10. One can see a slight dependence on velocity and on target. However, the exponent of projectile $\gamma = 0.007 \pm 0.056$ has high error value and hence can be neglected. The same argument applies on the coefficient C_{β^*}. Therefore, eqn. (4.50) has been refitted for $\gamma = 0$ and $C_{\beta^*} = 0$ and the new fit-parameters are given

---

[7] One experiment 7Okt-4 from series 1 cm – 1cm is not included, because the conditions mentioned in Figure 4.29 could not be maintained. Hence the analysis of β^* and $v_{\max}$ based on 141 experiments.

in the second row of Table 4.10. The value of the reduced chi-square remains unchanged therefore, in addition to this, the other two fit parameters were tested for $\varsigma = 0$ and $\vartheta = 0$ one by one. The value of χ^2_{red} increased from 0.0167 to 0.0186 respectively. At least this confirms that the β* has dependence primarily on the collision velocity and then on the size of the target, as shown in Figure 4.34.

Table 4.10. The fit parameters for β^* derived by fitting eqn. (4.50)

Run No.	C_{β^*}	$\vartheta\,(v_n)$	$\gamma\,(P)$	$\varsigma\,(T)$	χ^2_{red}
1	0.0485 ± 0.043	0.314 ± 0.068	0.007 ± 0.056	0.137 ± 0.058	0.0162
2	0	0.363 ± 0.039	0	0.175 ± 0.040	0.0162

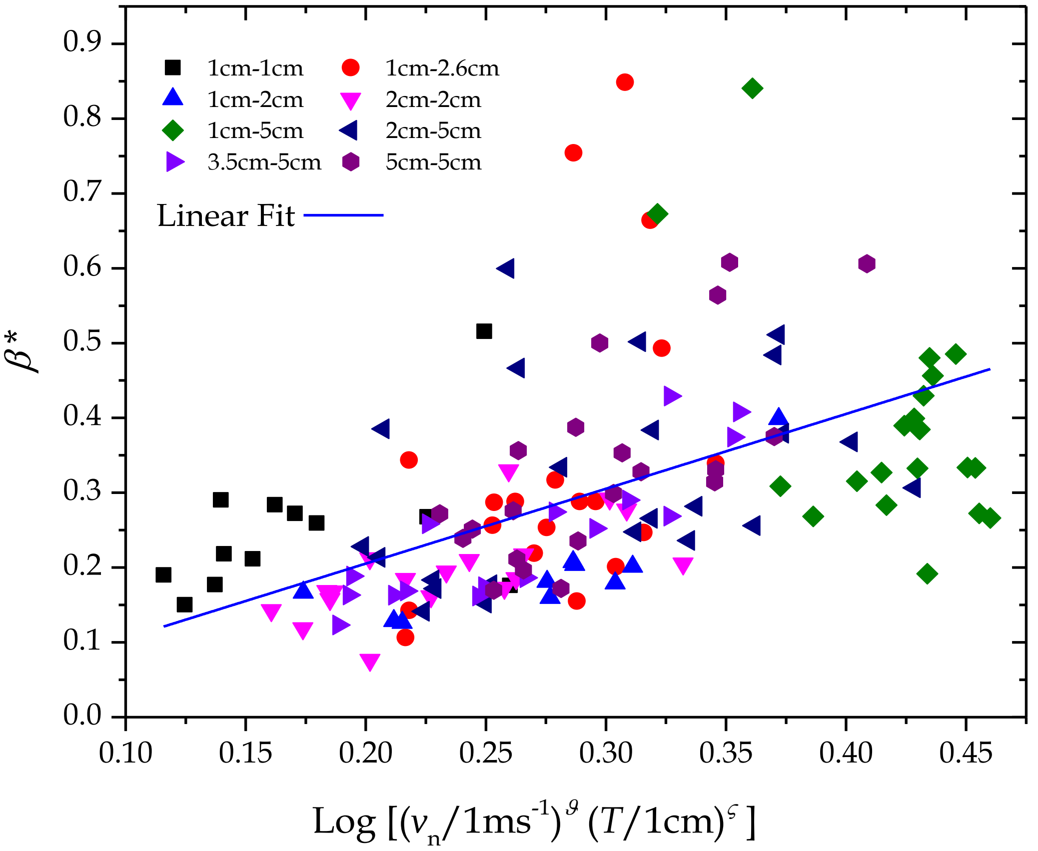

Figure 4.34. The least square fit analysis shows a non-trivial dependence of β* on collision velocity and the size of the projectile size with $\vartheta = 0.36$ and $\varsigma = 0.17$ respectively. The blue line shows a linear correlation which has slope = 1.

In the next step, the $v_{\max}$ has been analysed, with the assumption it has power law dependence on v_n, P and T, which can be expressed as

$$\log\left(\frac{v_{\max}}{1\ \text{ms}^{-1}}\right) = C_{\text{Lab}} + A\log\left(\frac{v_n}{1\ \text{ms}^{-1}}\right) + B\log\left(\frac{P}{1\ \text{cm}}\right) + X\log\left(\frac{T}{1\ \text{cm}}\right). \tag{4.51}$$

The above equation has been fitted and the fit-values are given in the Table 4.11. The first run of the fit shows that $v_{\max}$ depends primarily on the collision velocity and the dependence on projectile is secondary. However in the case of target, the value of the exponent $X = 0.084 \pm 0.062$ is very low and the value of error is of comparable magnitude, therefore eqn. (4.51) has been refitted for $X = 0$ and the new fit values are given in the second row of Table 4.11. By using these fit-parameters Figure 4.35 has been drawn to show the correlation between $v_{\max}$ and the collision parameters. The dependence of the maximum fragment velocity $v_{\max}$ on collision velocity is intuitive, high velocities in, high velocities out. However the dependence on projectile can be explained by the same argument (used in Sec. 4.7.3) of relative collision strength, $Q^* \propto P^{\kappa}$ such that the size of projectile is proportional to the energy delivered into the system. This extra energy is consumed in two ways, first by raising the value of C_N and then in the velocity of the fragments.

Table 4.11. The fit parameters of $v_{\max}$ derived by fitting eqn. (4.51)

Run No.	C_{Lab}	*A* (v_n)	*B* (*P*)	*X* (*T*)	χ^2_{red}
1	0.120 ± 0.046	0.675 ± 0.073	0.292 ± 0.060	0.084 ± 0.062	0.0186
2	0.13 1± 0.045	0.712 ± 0.045	0.341 ± 0.049	0	0.0187

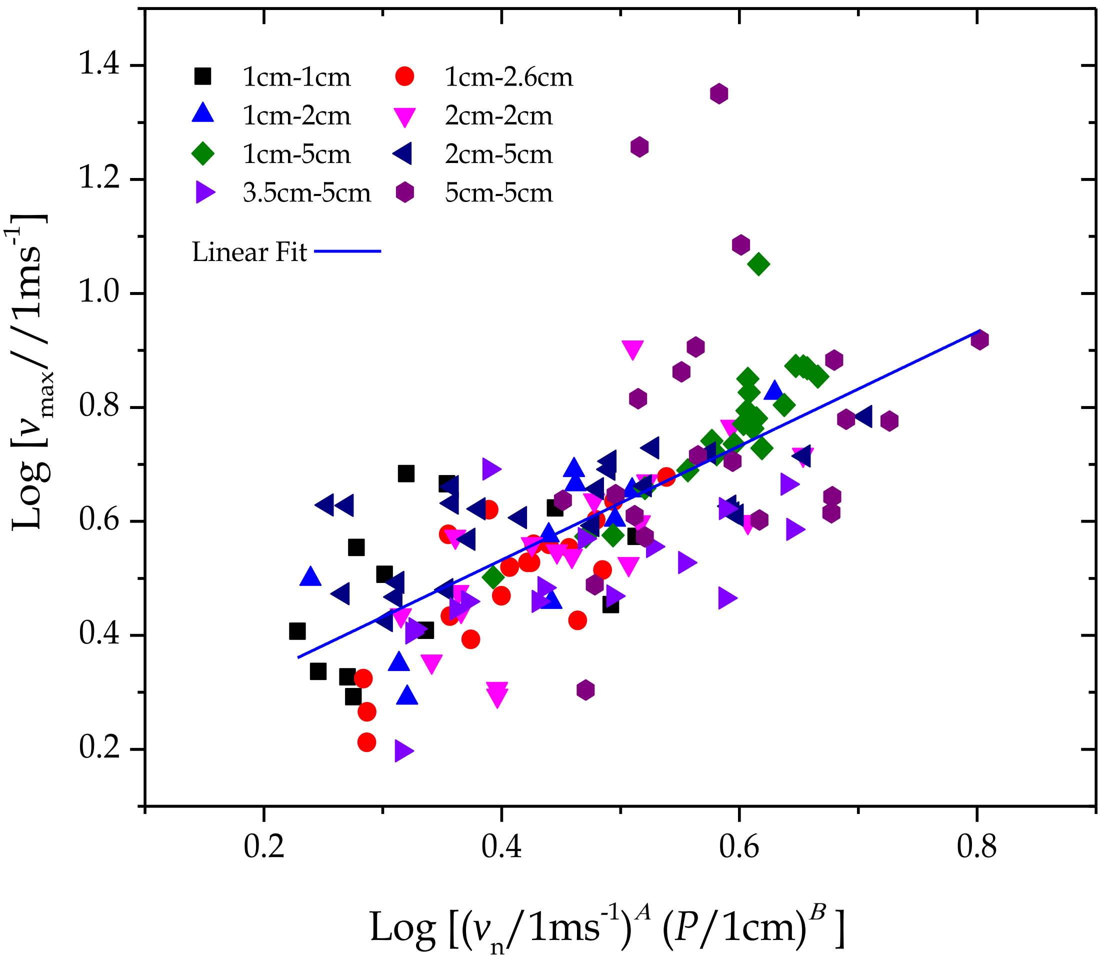

Figure 4.35. The maximum fragment velocity $v_{\max}$ increases with impact velocity with exponent $A = 0.71$ as well as with the size of projectile with exponent $B = 0.34$ respectively, however it shows no dependence on target. The blue line is the linear fit to the data which has slope = 1.

4.10 The grand pebble fragmentation model

After the in-depth analysis of 142 experiments, a grand pebble fragmentation model can be proposed, which consists of three main models of the experimental study. First is the model of fragmentation strength μ, second is the probability function of mass transfer P_{MT} and the third model is the complete description of the fragments size-distribution $N_{\mathrm{cum}}(\mathrm{x})$, which is also translated for the mass-frequency distribution $M_{\mathrm{cum}}(\mu_{\mathrm{f}})$. The collision between the pebbles and the outcome can be described by the above mentioned quantities.

The model can be implemented to a scenario in which a cloud of pebbles owing to self-gravity undergoes gravitational collapse. During the collapse how the pebbles will interact, it has been explained in the following steps.

1- Determine the fragmentation strength

First determine the fragmentation strength μ given in eqn. (4.2), because it tells the nature of the collision.

i) If $\mu = 1$, it implies pebbles are bouncing, very little energy dissipation. This can be further confirmed by making sure $v_{\mathrm{n}} < v_{1,}$ given in eqn. (4.1) and (4.9).

ii) If $\mu < 1$, it makes sure $v_{\mathrm{n}} > v_1$, one will see fragmentation and $\mu \leq 0.5$ implies catastrophic fragmentation.

iii) In the case $\mu > 1$ growth is the outcome, which still involves fragmentation. Since both events (ii) and (iii) dissipate energy, which can accelerate collapse.

As the cloud collapses, one should see the following sequence of events:

2- Growth and fragmentation simultaneously

Before every collision, the size ratio f of the colliding binaries is determined. Depending on the f value, the eqn. (4.25) would determine the collision outcome; such that

i) If $f \geq 5.83$ then collision outcome is necessarily the mass transfer with probability $P_{\mathrm{MT}} = 1$, which leads to the growth of target aggregate, given that $v_{\mathrm{n}} < v_{\mathrm{sur}}$

ii) If $f < 5.83$ then the probability of mass transfer is $0 < P_{\mathrm{MT}} < 1$ and the probability of catastrophic fragmentation is $P_{\mathrm{CF}} = 1 - P_{\mathrm{MT}}$.

iii) As the impact velocity is $v_{\mathrm{n}} \rightarrow v_{0.5}$, the probability of catastrophic fragmentation $P_{\mathrm{CF}} \rightarrow 1$.

3- Determine the mass of the largest fragment and the amount of mass transfer

i) In the case of catastrophic fragmentation, by using eqn. (4.2) determine the mass of the largest fragment i.e. $m_{\mathrm{l}} = m_{\mathrm{t}}\, \mu$.

ii) In the case of mass transfer, by using eqn. (4.28) determine the mass gained $\Delta m/m_{\mathrm{p}}$ by the surviving aggregate.

4- Determine the catastrophic threshold velocity $v_{0.5}$

The catastrophic threshold velocity $\boldsymbol{v}_{0.5}$ is composed of two important quantities; the catastrophic threshold energy $E_{0.5}$ and the collision strength Q^*, therefore it is a good indicator to predict the outcome of collision and the state of the collapse. It is determined in the following steps

i) First by exploiting the relation of fragmentation strength μ given in eqn. (4.6), the catastrophic threshold energy $E_{0.5}$ is determined.
ii) This can be used in eqn. (4.12) and the collision strength Q^* can be determined.
iii) As Q^* has been calculated, it is used in eqn. (4.18) and finally the value of the catastrophic threshold velocity $v_{0.5}$ is determined.

5- Define the fragment size distribution

Whether the outcome of a collision is catastrophic fragmentation or fragmentation with mass transfer, fragments of a wide size distribution are produced.

i) By using eqn. (4.31) the complete size distribution can be defined. The model can be implemented by selecting any value of α given in Figure 4.18 which covers a wide range, i.e. 0.2 – 2.
ii) As α is known, it can be used in eqn. (4.40) and the slope of mass-distribution β can be determined.
iii) Once β has been determined, it can be used in eqn. (4.39) and the total mass M_{tot} can be estimated by normalising eqn. (4.39) to the total mass in the distribution, which is $m_{\mathrm{t}} + m_{\mathrm{p}} - m_{l}$.

The optional step

6- Using α as a dynamic variable

The slope α of the fragment size distribution can be used to know whether the cloud is depleted from small grains or replenished. For the evolution of dust growth, the replenishment of small grains is crucial, as they dissipate collision energy more efficiently and participate in growth.

i) Determine the mean collision velocity and the mean pebbles size at any instant during the collapse.
ii) If the above two values are known then by using eqn. (4.33) the value of α can be constantly updated and can be fed into eqn. (4.31).

4.10.1 Implementation of the pebble fragmentation model

With the help of our colleagues at Lund Observatory, the above described model of pebble growth and fragmentation has been implemented in the gravitation collapse of a pebble cloud, which has been described in details in Sec 2.4.2. The pebble have fixed size, which is 1 cm and fixed filling-factor $\phi = 0.35$.

The collapse has been analysed for four different models, two real fragmentation models and two hypothetical models. Each model shows a different way to reach a planetesimal of radius R_{solid}. It should be reminded that here the radius R_{solid} has been defined as the radius of the cloud when it has reached the filling-factor from 0.35 to 1, in other words it has the density of solid $\rho_{\mathrm{SiO2}} = 2.5\ \mathrm{g\,cm^{-3}}$. The details of each models are given in Table 4.12.

Table 4.13. The four different models of a collapse of a pebble cloud

The real fragmentation models		
1	Frag. $\alpha = 0.5$:	The eqn. (4.25) is used to determine the collision outcome. If $f < 5.83$ then $P_{\mathrm{MT}} < 1$. The resulting distribution of fragments follows eqn. (4.30) in which the slope is fixed to $\alpha = 0.5$. In the case of mass transfer, the model follows eqn. (4.28) and assumes that the mass transfer from projectile to target is $\Delta m / m_{\mathrm{p}} \approx 30\%$.
2	Frag. $\alpha = 0.9$:	This is another case of real fragmentation model but the difference is that here fragmentation slope is $\alpha = 0.9$.
The hypothetical models		
3	Bimod-Frag	This model does not follow the prescribed fragmentation model. In this case, the fragmentation is bimodal, which consists of one large remnant and many fragments of monomer size (1 μm). The model was first time used in WJJ 2014.
4	100% MT- $\alpha = 0.9$	This is a hybrid model which is the mixture of real fragmentation model and hypothetical model. Here again eqn. (4.25) has been used, however in case of mass transfer $\Delta m / m_{\mathrm{p}} \approx 100\%$ has been assumed, which is the hypothetical part of the model. In the case of fragment-ation the second model where slope $\alpha = 0.9$ will be followed, which is the real part of the model.

The real fragmentation models $\alpha = 0.5$ and $\alpha = 0.9$ will be used as reference model for the purpose of comparison, because they truly based on the fragmentation model.

The results presented in the following have been produced by using the unpublished data provided by the courtesy of WJ 2016.

4.10.2 The two size (mass) dependent regimes of planetesimals

The pebble fragmentation model is valid over a wide size distribution of planetesimals.
In Figure 4.36 the mass weighted mean pebble size has been shown as a function of the size of planetesimal. Here two planetesimal size regimes have been introduced. The planetesimals of radius between 10 km to 100 km, shown in dense-crossed region can be considered the regime of small size planetesimals and the sparse-crossed region spans from 100 km to 1200 km has been associated with the regime of large size planetesimals. The hashed region will be discussed shortly.

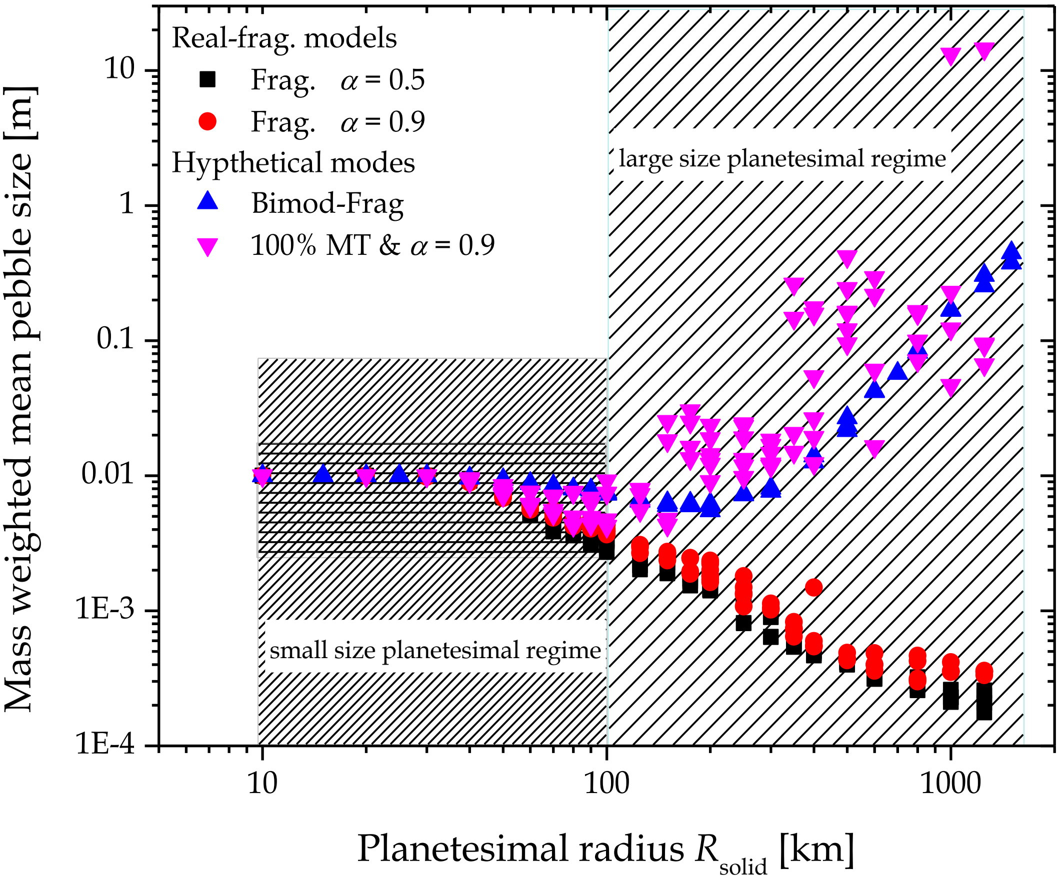

Figure 4.36. The mass weighted mean pebble size has been shown as a function of planetesimal radius. The dense-crossed region between 10 – 100 km reflects the small size planetesimal regime, whereas the sparse-crossed region between 100 – 1200 km show the large size planetesimal regime. In the first regime owing to very few fragmenting collisions the mean pebble size merely varies and the resulting planetesimal are predominantly pebble pile. And all the models behave almost in same fashion. However in large size planetesimal regime the fragmenting collisions are frequent and above 80 km one finds a split between the real fragmentation models and the hypnotical models. In real fragmentation model mean pebble size steadily decease with the size of planetesimal and vice versa in the case of hypothetical model. The hashed region reflects the hybrid nature of 100% Mt with $\alpha = 0.9$ model. In this range the size ratio remains $f < 5.83$ which leads to $P_{\text{MT}} < 1$ and the model behaves same as the real model with $\alpha = 0.9$. This figure has been published in WJ 2016

However in the subsequent discussion the introduction of the two regimes will be justified by showing the distinction between the real fragmentation models, namely Frag. $\alpha = 0.5$ and Frag. $\alpha = 0.9$, and the hypothetical models, namely Bimod-Frag and 100% MT- $\alpha = 0.9$.

All the models show that in the small size planetesimal regime, almost all the primordial pebbles do survive the collapse and lead to a planetesimal which is predominantly a pebble pile. The reason can be traced in virial velocity and in turn the relative velocity, given in eqn. (2.62) and eqn. (2.63) respectively, which are proportional to the mass of the cloud. In the regime of small size clouds the relative collision velocity (~ 0.1 $\mathrm{m\,s^{-1}}$ see Figure 1 in WJ 2017) remains well below the onset-velocity of fragmentation (~ 1 $\mathrm{m\,s^{-1}}$), i.e. $v_n < v_1$, (see eqn. (4.1) and (4.9)). With these collision parameters, i.e. cm-sized pebbles at ~ $\mathrm{cm\,s^{-1}}$, one would find $\mu = 1$ in eqn. (4.2), which implies that collision result in bouncing. However not in this study but the bouncing collision with aforementioned parameters have been experimentally observed by Beitz et al. (2011). In this size regime, the clouds dissipate energy very slowly which increases their collapse time as shown in Figure 4.37. The collisions resulting in fragmentation do happen, although they happened lately but they bring two benefits as well. First, these collisions reduce the mean collision velocity down to a few $\mathrm{mm\,s^{-1}}$ and second increase the size ratio f. As a result pebbles "hit and stick" and start to pile up.

However in the regime of large size planetesimals, a distinction between the real models and the hypothetical models starts to appear. In the case of real fragmentation models the mass weighted mean pebble size starts to decline for $\alpha = 0.5$ and $\alpha = 0.9$ shown in black squares and red spheres respectively. It can be explained by the fact that in massive clouds the collision velocity are higher i.e. above 1 $\mathrm{m\,s^{-1}}$, which trigger fragmentation earlier. As a result the mass weighted mean pebble size starts to decline as shown in Figure 4.36. The cloud dissipates the energy rapidly and contracts on the order of free-fall time scale $t_{\mathrm{ff}} \approx 25.1$ yrs (see eqn. (2.68)), as shown in Figure 4.37. Whereas the hypothetical models behave in contrast. The mass weighted mean pebble size starts to increase in the bimodal fragmentation model and 100% MT-$\alpha = 0.9$ model, shown in blue-up triangles and magenta-down triangles in Figure 4.36. Here one finds as the size of planetesimal increases, the increasing collision velocities contribute to the growth of the pebbles. One possible explanation is that the size ratio increases as a result of fragmentation and the increasing value of f absorbs the increasing velocity such that the large pebbles can accrete fine dust and grow in size.

In Figure 4.36 the hashed region between 10 km and 100 km leads to the fact that in this range the hypothetical model 100% MT-$\alpha = 0.9$ has been behaving virtually identical to the real fragmentation models, in particular with Frag. $\alpha = 0.9$. The overlapping of the two models becomes prominent in the planetesimals which have radii between 60 km and 100 km and can be traced back to initial size. This is possible, because the model 100% MT with $\alpha = 0.9$ is of hybrid nature and has a real component in the form of fragmentation slope with $\alpha = 0.9$.
This can be explained by the fact that in this models the hypothetical part is the condition of 100% mass transfer i.e. $\Delta m/m_{\mathrm{p}} = 1$. But this condition requires $P_{\mathrm{MT}} > 0$, which is more probable when $f > 1$. However as discussed above that in the small size clouds the bouncing collisions are the most frequent collisions and in such collisions $P_{\mathrm{MT}} = 0$. Therefore the condition of 100% mass transfer remains ineffective and model behaves exactly same as real Frag. model $\alpha = 0.9$. This explains the overlapping of the two models in the hashed region.
However in the regime of massive clouds, the increasing value of f (thanks to fragmentation) raises the probability of mass transfer such that $0 < P_{\mathrm{MT}} < 1$. In this way the hypothetical part of

the model, i.e. $\Delta m/m_p = 1$ becomes effective and the overlapping is lifted and the distinction between the two models starts to appear above 100 km.

4.10.3 The collapse time and the limitation of the pebble fragmentation model

Here it is important to mention that the pebble fragmentation model requires a minimum planetesimal mass, which is 10 km. The planetesimal smaller than 10 km will not have fragmentation at all, so the real fragmentation models, Frag. $\alpha = 0.5$ and Frag. $\alpha = 0.9$ will not function and the resulting planetesimals will be merely the pebble pile.

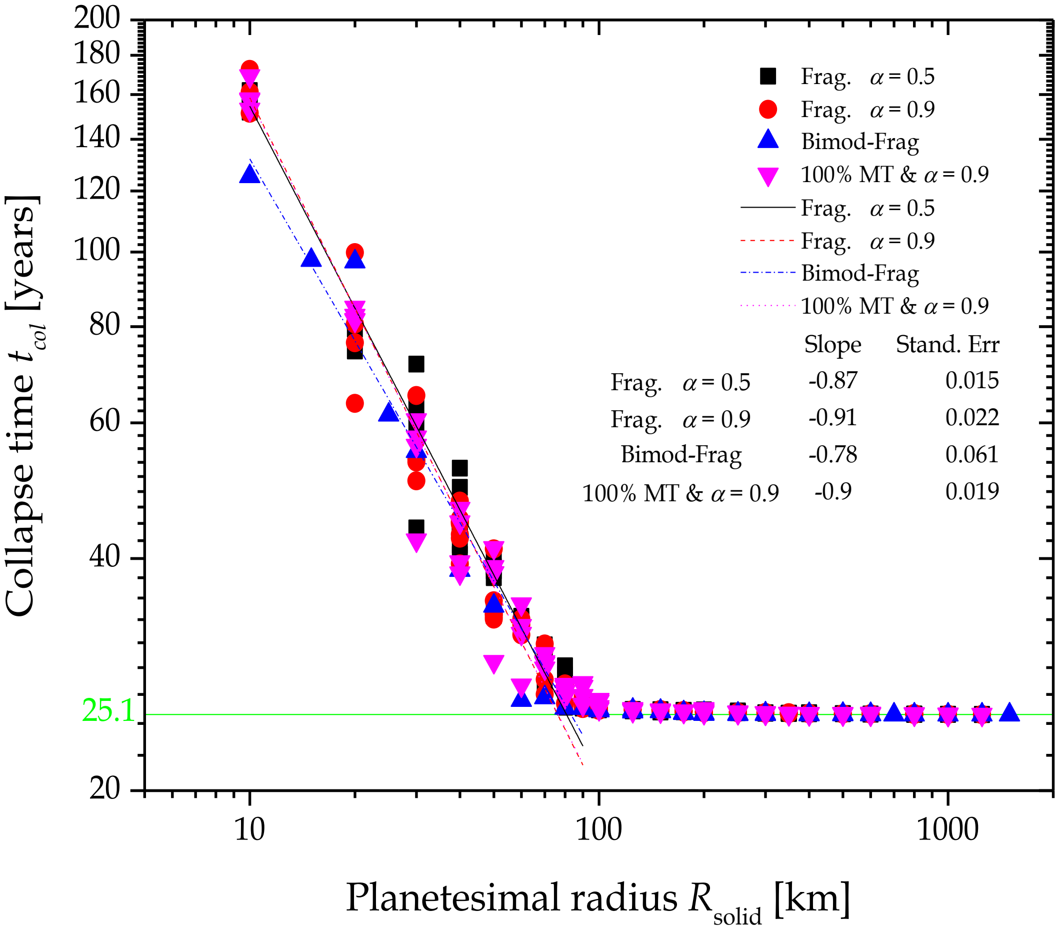

Figure 4.37. The collapse time t_{col} of a pebble cloud has been given as a function of the radius of the planetesimal R_{solid}. One can see that in small size planetesimal regime, the collapse time follows $t_{col} \sim R_{solid}^{-1}$ and reaches to its free-fall limit of 25.1 yrs, shown in green-solid line. Above 100 km, the relation does not hold and the collapse time in all models remains on the order of free-fall time. The power law has been fitted to the planetesimal radius between 10 km to 100 km. It should be noticed that the slope of Frag. $\alpha = 0.90$ model, shown in red-dashed fit, has slope = -0.91, which is very close to the slope = -0.90 of the 100% MT-$\alpha = 0.90$ model shown in magenta-dotted fit line. It supports the argument that 100% MT-$\alpha = 0.90$ is of hybrid nature and in small size planetesimal regime behaves identical to the real models. Whereas the slope of Frag. $\alpha = 0.5$ is -0.87 which is quite in the range of the aforementioned models. However the Bimod-Frag. model shown in blue-dashed-dotted has slope = -0.78, which is slightly less than the all other models.

However, in addition to this, the minimum planetesimal mass also imposes a temporal limit on the collapsing time. In the clouds smaller than 10 km, throughout the collapse, the collision velocity would be well below the onset-velocity of fragmentation and size ratio will remain f = 1. As discussed before, these collision parameters result in bouncing i.e. $\mu = 1$, it can significantly slow down the process of energy dissipation, hence a cloud would require a longer time to reach R_{solid}. In eqn. (2.60) it has been shown that the collapse time of a pebble cloud is inversely related to the solid radius of the planetesimal, i.e. $t_{\text{col}} \sim R^{-1}_{\text{solid}}$. However in the following it will be shown that this relation is also size dependent and valid only within the small size planetesimal regime.

Figure 4.37 shows that within the fragmentation model, the slowest possible collapsing time is $t_{\text{col}} \approx 170$ yrs. The real models would be not valid if the collapse prolongs longer than 170 years, which can be defined as the upper time limit. However the lower limit of the collapse time is also limited by the free-fall time limit which is $t_{\text{ff}} \approx 25.1$ yrs at 40 AU, here shown in green-grid line in the same figure.

As shown in Figure 4.37 the collapse time rapidly declines in the small size planetesimal regime, therefore it is required to determine the value of the slopes for all the models in the range between 10 km to 100 km. WJJ 2014 used the power law to determine the slope, therefore the same is followed here.

In the inset of Figure 4.37, one can see that the Frag. $\alpha = 0.9$-mdoel, shown in red-dashed fit-line and the 100% MT-$\alpha = 0.9$ model shown in magenta-dotted fit-line, have almost same values of the slopes, 0.91 ± 0.02 and 0.90 ± 0.02 respectively. The results encourage the idea that in small size planetesimal regime both models are identical. The Frag. $\alpha = 0.5$-model, shown in black-solid fit-line, has slope = -0.87, which is well within the errors of the aforementioned models. However the Bimod-Frag-model, shown in blue-dashed-dotted fit-line, turns out to be the real hypothetical model, as this model has slope = -0.78 ± 0.06, which is slightly less than the slopes of the rest of the models.

It must be mentioned that the Bimod-Frag-model originates from WJJ 2014 and the value of slope estimated in their study is -1.05 (see their Figure 3), which is relatively higher than the value of slope -0.78 found in this study. It is difficult to say what are the reasons of this difference, however one could think of the resolution of simulation, here 250 representative particles have been used against their 1000 particles used in WJJ 2014. And moreover they measured the slope for the planetesimal of radii between 1 km to 100 km, whereas in this study it is from 10 km to 100 km.

4.10.4 The internal structure of the large size planetesimal

In this section a large size pebble cloud of radius $R_{\text{solid}} = 500$ km has been taken and the process of its collapse and the internal structure has been analysed and discussed. The reason of selecting this size is that the large size clouds are more interesting objects in terms of collision activities. Here one finds, bouncing, fragmentation and mass transfer, all the three types of collisions can be explained by eqn. (4.6). And moreover in this size range the real fragmentation models and the hypothetical models behave distinctively different, hence provide an opportunity to learn better the role of real fragmentation models.

The cloud has same initial conditions as explained in Sec 2.4.2, but has only a larger initial Hill radius R_0 = 5058.84 R_{solid}. The cloud undergoes a gravitation collapse with the velocity of collapse on the order of free-fall velocity (see eqn. (2.67)) and meets the solid density at radius R_{solid}, in time on the order of free-fall time $t_{\mathrm{ff}} \approx 25.1$ years.

4.10.4.1 The real fragmentation models $\alpha = 0.5$ and $\alpha = 0.9$

In general, when a massive cloud contracts, its gravitational potential energy is converted into the kinetic energy of the pebbles, collision frequency increases and so the kinetic energy of the

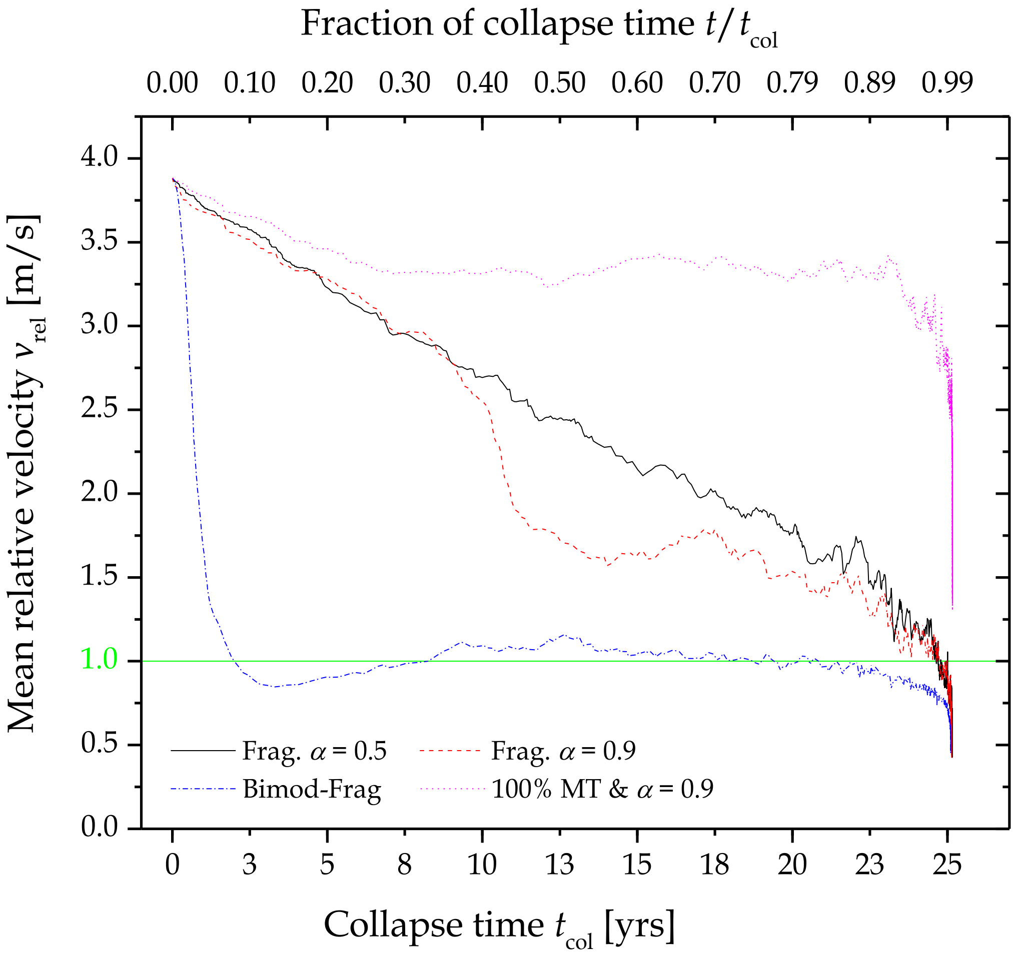

Figure 4.38. The mean relative velocities (after eqn. (2.66)) as a function of collapse time. The onset velocity of fragmentation $v_n = 1$ m s^{-1} is shown by the green-solid grid line. The pebble clouds represented by $\alpha = 0.5$ and $\alpha = 0.9$, shown in black-solid and red-dashed curve respectively, about 99% of collapse time maintain the collision velocity higher than 1 m s^{-1}, which inevitably result in fragmenting collisions. In Bimod-Frag model shown in blue-dashed-dotted curve, the relative velocity exponentially declines and within 3 years falls below 1 m s^{-1}, indicating the higher energy dissipation due to the production of monomers. Whereas in the case of 100%MT model, the magenta-dotted curve, the collision velocity in contrast to other models remains relatively higher for a prolonged duration. In this model energy dissipation is minimum, because of fewer collisions. However at the end of the collapse the collision velocity exponentially declines due to the fragmenting collisions.

pebbles is dissipated mainly in the process of fragmentation, consequently the relative collision[8] velocity decreases, as shown in Figure 4.38. For example; in real fragmentation models $\alpha = 0.5$ and $\alpha = 0.9$ shown in the black-solid and red-dashed curves respectively, the mean collision velocity of the pebbles steadily decreases. However the important point is that for about 99% of the collapse time the collision velocity remains above 1 $\mathrm{m\,s^{-1}}$, which inevitably results in $\mu < 1$ and the probability of catastrophic fragmentation as given in eqn. (4.25) leads to $P_{\mathrm{CF}} \to 1$.

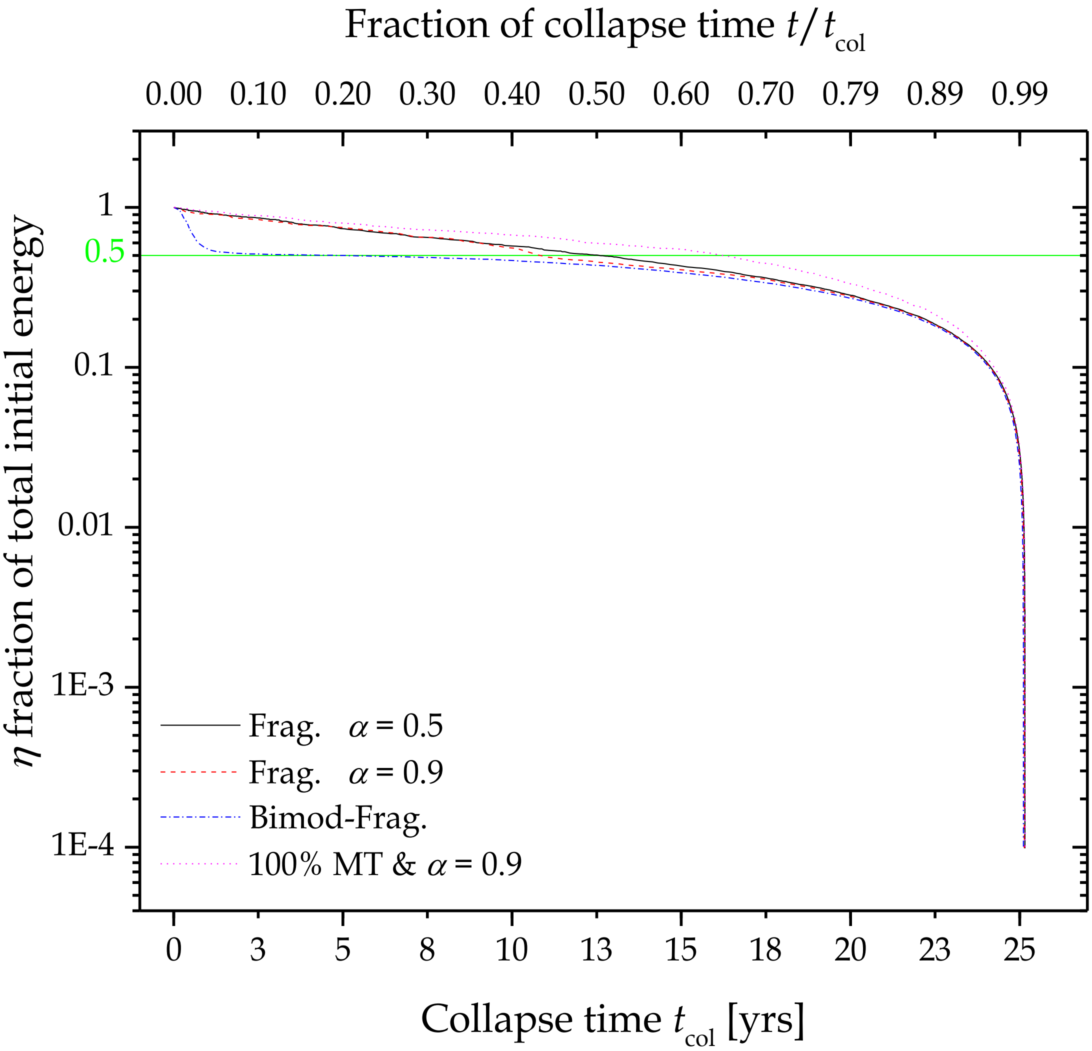

Figure 4.39. The cloud contraction parameter η as a function of collapse time. As the collapse evolves, its total internal energy decreases and becomes more negative, indicating it is becoming more tightly bound. The green-solid grid line at $\eta = 0.5$ implies that now $E(t)$ of the cloud is twice of the E_0 and cloud is twice as bounded as it was at the start. The black-solid curve for $\alpha = 0.5$ and the red-dashed curve for $\alpha = 0.9$ dissipate energy at similar rate and require almost same time ~ 12 years to reach $\eta = 0.5$. However the blue-dashed-dotted curve of Bimod-Frag reaches to η = 0.5 just within 3 years. This rapid decline is due to the formation of monomers, which dissipate energy very efficiently. The slowest energy dissipation rate, owing to in inelastic restructuring of the aggregates, is in 100% MT model shown in magenta-dotted curve. Here cloud needs ~ 16 years to reach $\eta = 0.5$. In the last few weeks all the models dissipate internal enteral energy on the order of 10^3 times.

---

[8] From eqn. (4.1) one can approximate the collision velocity to relative velocity, i.e. $v_n \sim v_{\mathrm{rel.}}$

Figure 4.38 once again reminds that the two real fragmentation models behave very different than the hypothetical models.

In Figure 4.39 the cloud contraction parameter $\eta = E_0/E(t)$ (see eqn. (2.64)) has been shown as a function of collapse time t_{col}. Here the negative sign of $E(t)$ should be remembered which implies that the cloud is losing internal energy. As more energy a cloud dissipates, more tightly it is bounded. In other words, to reach the solid density, the cloud has to dissipate its internal energy on the order of ~ 10^4 times of E_0. One can see both models $\alpha = 0.5$ and $\alpha = 0.9$ require almost the same time (~ 12) years to reach $\eta = 0.5$, the value marked by the greed gird line in Figure 4.39. However the interesting point is; in both models, in about 25 years the clouds dissipate only 1/10 of their initial energy and in the last few weeks the cloud will dissipate 1/1000 of its initial energy E_0. It implies that collapse becomes rapid in the last phase.

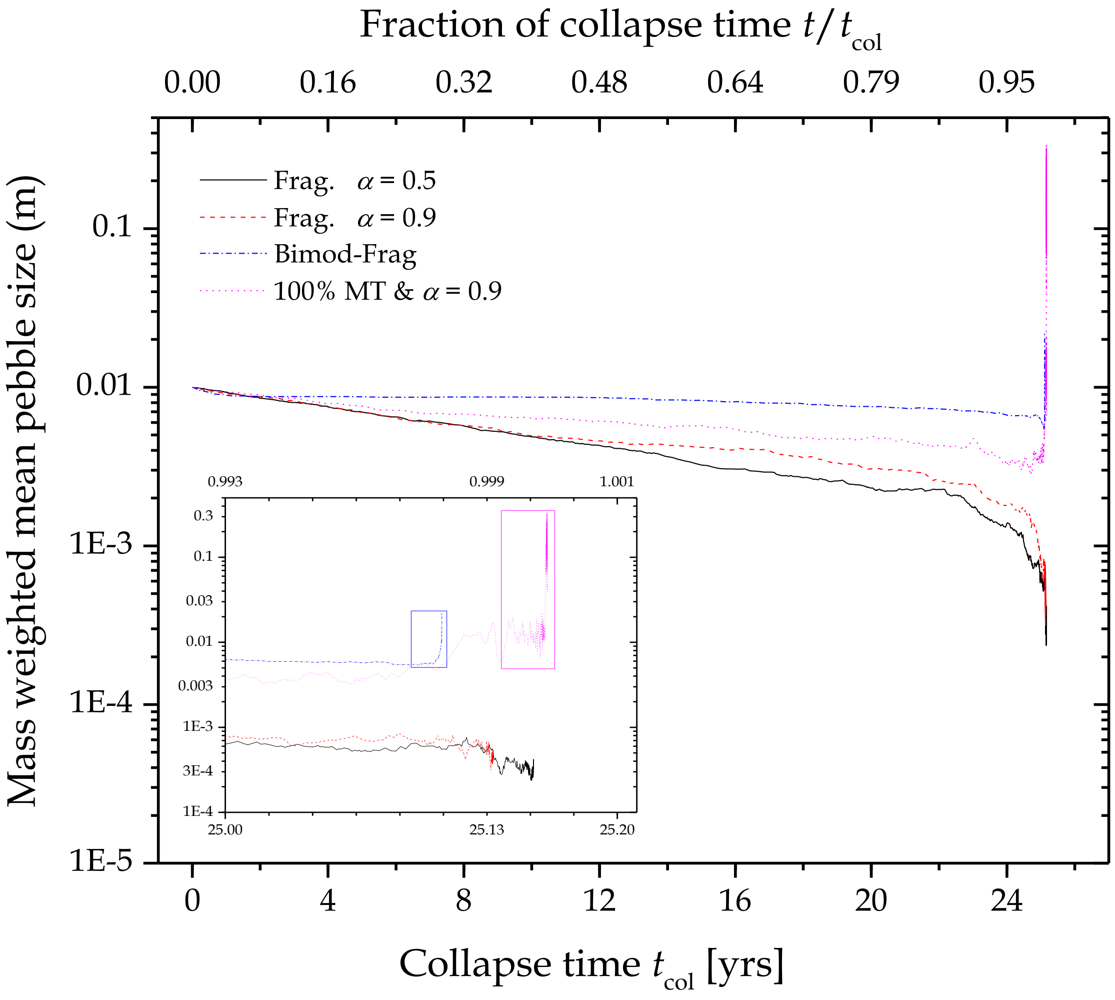

Figure 4.40. As the collapse evolves the increasing collision frequency leads to fragmenting collisions and consequently the mass weighted mean pebble size decreases. It has the most impact on $\alpha = 0.5$ and $\alpha = 0.9$, black-solid and red-dashed curve respectively. Whereas the least impact is on blue-dashed-dotted curve for bimodal fragmentation. The inset zooms into the last 8.5 weeks of the collapse. The blue box representing Bimod-Frag. shows the last 5.5 days of the collapse, when mean pebbles starts to increase and goes up to 2cm. Similar pattern is observed in the 100% MT-model shown in magenta-dotted curve. First mean pebble size decreases, but this decline does not live long. The magenta box in the inset shows the last 8.4 days when mean pebble size starts to increases rapidly and reaches up to ~ 30 cm by the end of collapse.

It means the collision frequency will increase proportionally in the last days. This process is reflected in Figure 4.40, where the mass weighted mean pebble size has been shown as a function of collapse time. One finds the mass weighted mean pebble size declines by factor ~ 8 in 25 years and by the same amount it would decline in the next few weeks before the collapse ends. Figure 4.41 shows the final mass fraction as a function of the actual mean pebble size. Here one can see that the black-solid and red-dashed curves lie completely on the left side of vertical green-solid line at 1 cm, which means all the primordial pebbles have been processed. And a large fraction is concentrated in 0.1 – 1 mm-sized particles, which contribute 40%– 45% mass of the planetesimal respectively. As the collapse reaches to its end, the collision frequency and energy dissipation rapidly increase, fragmentation becomes intense and pebbles get grinded to a few tens of microns.

It should be mentioned that here the events resulting in mass transfer do occur with mass transfer rate ~ 30%. But these aggregates which have gained mass do not live long and fragment, so the net particles size decreases. Once a primordial pebble is fragmented, it remains unable to reclaim its initial size.

Another interesting fact comes to light is that according to the experimental results shown in Figure 4.18, the fragmentation model $\alpha = 0.9$ is expected to have fragment-frequency C_N about 8 times higher than that of $\alpha = 0.5$. Intense fragmentation means, a rapid decline in the mean collision velocity. However neither the Figure 4.38 nor any other simulation in this study show such a correlation, which is quite counter intuitive. This is because the step 6 (the optional step) defined in Sec. 4.10 has not been implemented and the fragmentation slope α remains a fixed value in eqn. (4.31). If it were modelled according to eqn. (4.33), then the distinction between the two models could have appeared.

4.10.4.2 The bimodal fragmentation model

This is a hypothetical model and the uniqueness of this model is, here the collision between the pebbles yields a bimodal size distribution, which of course does not happen in reality. It means a large fraction of mass is in a remnant and the rest of the mass is in monomers. The immediate impact is that the cloud dissipates the energy very rapidly, just within 3 years, it reaches $\eta = 0.5$, see the blue-dashed-dotted curve in Figure 4.39. As discussed in Sec. 4.4.1, the smaller the particle is, the more tightly it is bounded, hence it requires more energy to break apart. Therefore the release of gravitational potential energy is immediately consumed in the production of monomers. As a result the mean pebble velocity declines very rapidly, which is reflected in blue-dashed-dotted curve in Figure 4.38. In this scenario the most frequent interaction would be between monomers and remnants (owing to larger cross section and velocity), which results in mass accretion. In the process of accretion, energy dissipates in inelastic restructuring, which is not an effective way to dissipate the gravitational energy. As a result a shallow slope of the blue-dashed-dotted curve in Figure 4.39 after ~ 3 years can be seen. However the remnant-remnant interaction would still produce monomers and continue to dissipate collision energy.

As the relative velocities decline to $\leq 1\ \mathrm{m\,s^{-1}}$, whether now the interaction is between monomers or between monomers and remnants the growth is the most likely outcome. By the end of collapse the mean pebble size starts to increase, see blue-dashed-dotted curve in Figure 4.40.

The inset in Figure 4.40 zooms into the last 8.5 weeks of the collapse. Here the region in blue box, shows the last 5.5 days before the cloud reach to R_{solid},. One can see that the mass weighted pebble size increases up to ~ 3 cm, by factor ~ 3 of its initial size. In Figure 4.41, the region of the blue-dashed-dotted curve which lie on the right side of the green-solid line, suggests that the remnants have grown up to 3 cm – 6 cm and claim ~ 45% mass of the planetesimal.

The second large concentration of mass (~ 28%) is in 0.1 mm, which could be associated to remnants or to the accretion of monomers by the remnants. Perhaps this is why no monomers are found in the final planetesimal.

4.10.4.3 The 100% Mass transfer model with $\alpha = 0.9$

However in this model, pebbles do not lose much kinetic energy and enjoy higher relative velocities, i.e. on average ~ 3.5 m s^{-1} for about 99% of the collapse time, see magenta-dotted curve in Figure 4.38. But whenever the pebbles interact with $v_n >> v_1$ and $f \sim 1$, then the very probable out-come is catastrophic fragmentation. According to eqn. (4.25) the probability of mass transfer is very low i.e. $P_{\mathrm{MT}} << 1$. It means the frequency of the collisions resulting in fragmentation with slope $\alpha = 0.9$ is as high as in the model Frag. $\alpha = 0.9$. This is why in Figure 4.40 the mass weighted mean pebbles size, for the 100%MT-α = 0.9 model and the real Frag. α = 0.9 model, decreases with time. However the slope of magenta-dotted curve is relatively shallower than that of the red-dashed curve. This is thanks to the 100% mass transfer efficiency. The primordial pebbles and other larger remnants will accrete everything which comes on their way. Although these collisions resulting in mass transfer are less frequent in the beginning but their frequency rapidly increase in the last days of the collapse.

The growth of pebbles which have size ratio $f \sim 1$ could be explain by the lower filling-factor. The primordial pebbles had the filling-factor $\phi = 0.35$ which is in the regime where the higher compressive strength acts to stabilise the aggregate when the tensile and the shear strengths tend to destabilise the aggregate (see Meru et al. (2013)). Therefore the aggregate could easily sustain the collision at the given velocities and keep contributing to growth.

However after ~ 25 years, the radius of the cloud shrinks exponentially and so the mean free path of the pebbles. The collision frequency increases and pebbles dissipate energy, as a result the relative velocity takes nosedive, see magenta-dotted curve in Figure 4.38. Because of low velocities, whether it is the primordial pebble or the remnant, they hit and stick together, as a result the mass-weighted mean pebble size tremendously increases in the last days of the collapse. The region of the magenta-dotted curve selected in the box in the inset of Figure 4.40 shows that the mass weighted mean pebble size in last 8.4 days increases by factor ~ 57 and reaches from ~ 0.6 cm up to ~ 34 cm. The same is reflected in Figure 4.41, here one can see that the actual mean pebble size, shown in magenta-dotted curve, has reached to that of a boulder of a few meters in size. However they comprise merely ~ 3% mass of the planetesimals, whereas the 22% of the mass is still in primordial pebbles, which either did not participate in collision and simply enjoyed the free-fall or are the fragments which have reclaimed their initial size by accreting the monomer mass.

The resulting planetesimal is expected to have a core consisting of grains of 0.1 – 1 mm.

Since most of the growth takes place in the last phase of the collapse, when mean pebble size reaches up to decimetres, therefore the outer shells are expected to be less compact.

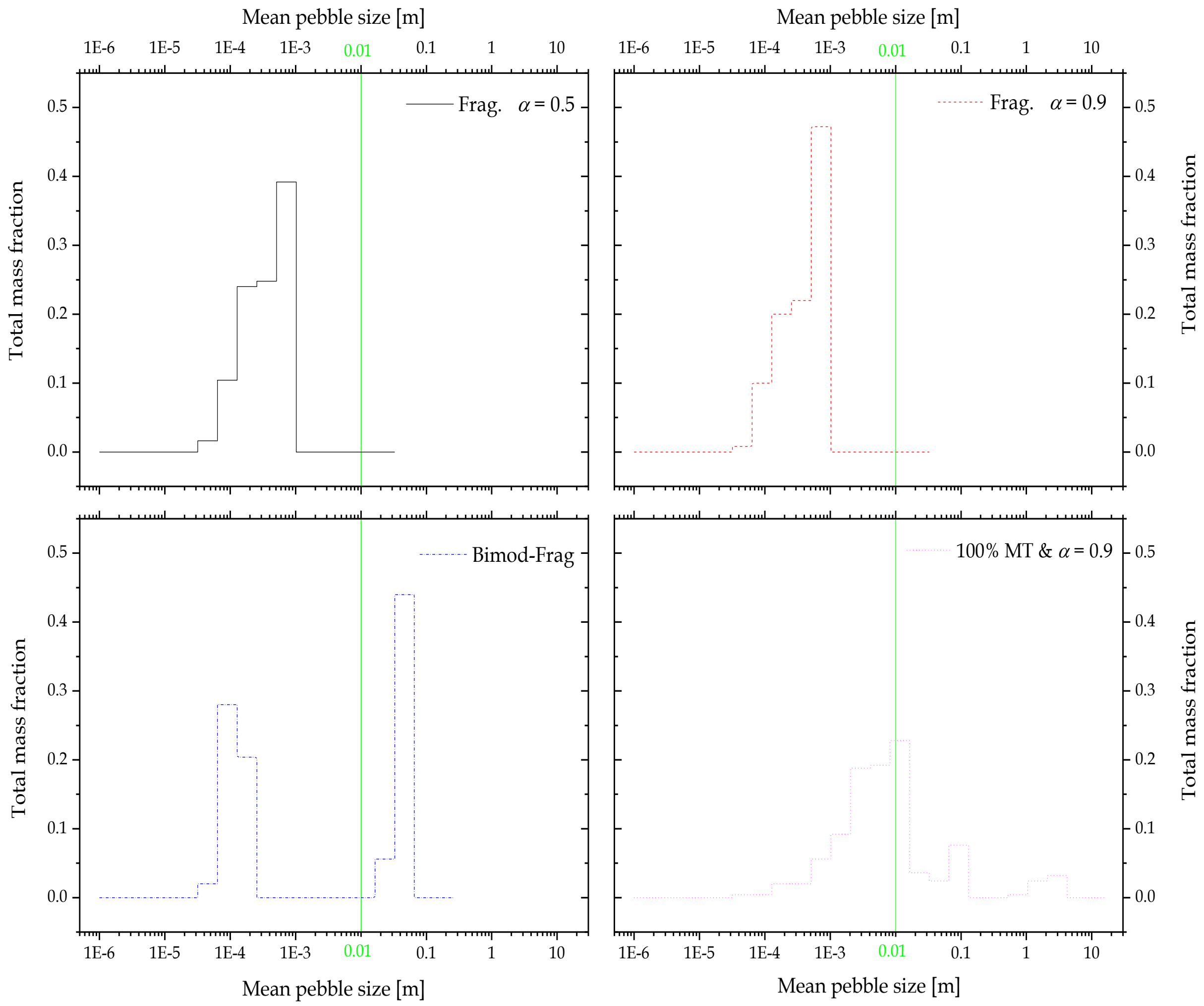

Figure 4.41. Here the fraction of total mass inside the planetesimal of $R_{\mathrm{solid}} = 500$ km has been shown as a function of mean pebble size distribution. The green-solid vertical line at 1 cm indicates the position of the primordial pebbles or the pebbles which have reclaimed their initial size. The left side of the line represents the region of fragmentation, whereas the region on the right side of the line represents the growth of the primordial pebbles. As the cloud approaches to R_{solid}, the pebbles get processed but with different rates. For example: in continuous fragmentation model for $\alpha = 0.5$ and $\alpha = 0.9$, shown in black-solid and red-dashed curves respectively, the fragmentation starts early and most of the primordial pebbles fragment into mm-sized pebbles, which contribute a large fraction 40%– 45% mass of the planetesimal. However owing to intense fragmentation in the last phase pebbles have been turned into fine dust of few tens of microns. In the case of the blue-dashed-dotted curve representing bimodal fragmentation, a large fraction ~ 44% of the planetesimal mass is in the pebbles of size 3 cm – 6 cm, which indicates the growth of the remnants. The second concentration of mass is in ~ 0.1 mm-sized pebbles which contributes ~ 28% mass of the planetesimal. The 100%MT model, shown in magenta-dotted, exhibits the widest pebble size distribution, from grains of a few tens of microns to boulders of a few meters. However the largest concentration ~ 23% of mass is in 1 cm size pebbles. It is very likely that these are the primordial pebbles, however there is a reasonable probability of regrowth of a mm-sized pebble into a cm-sized pebble. The boulders which are larger than 1 m can be associated to the growth of primordial pebbles, however they weigh merely 2%–3% of the planetesimal mass.

Chapter 5: Discussion and conclusion

5.1 What was the original goal of this study?
5.2 What do we learn from experiments?
5.3 What do we learn from numerical models?
5.4 Relevance to 67P/Churyumov-Gerasimenko
5.5 The limitation of this study and the future prospects
5.6 Conclusion

5.1 What was the original goal of this study?

This study began with the following two goals:

1. Developing a grand pebble fragmentation model within the collision parameters predicted by the recent studies on streaming instabilities by Youdin & Johansen (2007), Johansen & Youdin (2007) and Johansen et al. (2009), (2012) etc. This model will define the rules for collision outcomes, depending on the size and the velocity of pebbles.
2. Developing a numerical model which would execute the pebble fragmentation model and would explain the formation process of a planetesimals.

In order to reach the first goal, an experimental setup was built. In the new setup the collision scenario of cm-sized pebbles, which are expected to take place during the early phase of planet formation, were experimentally simulated. The prominent observations and features of the experimental study are discussed in the next section.

5.2 What do we learn from experiments?

In this study the filling-factor has been fixed to $\phi = 0.35$. The principle guide-line though out the study has been the fine tuning of collision parameters, namely the collision velocities v_n, the size of projectile P and the target T. What should be the value of these parameters which lead to our favourite collision outcome, i.e. the fragmentation with mass transfer? For this 142 experiments were conducted and on the basis of these experiments a pebble fragmentation model has been developed, which can be summarised as follows.

Two collision outcomes

The collision parameters which are tested in this work, show two specific collision outcomes: 1) catastrophic fragmentation (CF), and 2) mass transfer (MT). On the basis of these results several models have been assembled together to develop the grand pebble fragmentation model. The three main constituent models are the following.

1. The fragmentation strength model

In Sec. 4.3 and eqn. (4.6), a model has been proposed which can explain the observed outcomes of the collisions, i.e. fragmentation and mass transfer. In addition to this, the model is equally valid for the collisions resulting in bouncing, although it is not observed in this study. It also helped to determine the values of important quantities which explain the material properties, such as catastrophic threshold energy $E_{0.5}$ in Sec. 4.3, the relative collision strength Q^* in Sec. 4.4 and even the probability of mass transfer P_{MT} (as a function of v_{sur}) in Sec. 4.5.

2. The probability function for mass transfer

The collision parameters investigated in this study suggest that this is the size ratio f, which determines whether the target will survive or fragment. For example; in experiments show that on average the 5 cm target survived 52 times more often when it was hit by a projectile of 2 cm. The chances of survival went up to 80% when the same target was hit by a 1 cm projectile (see Table 4.3 Sec. 4.5). If f is known, then by using eqn. (4.24), the probability of the collision outcome can be determined. The survival probability of the target is expected to reach 100% when $f \geq 5.83$.

The reason of the two above mentioned collision outcomes is the two types of size ratios. All the colliding binaries with a size ratio of $f > 1$, tend to have the same collision outcome and all those which have $f = 1$ tend to have the same collision outcome. For example; the series 1 cm – 2.6 cm and 2 cm – 5 cm have similar size ratio, hence they have similar collision outcomes, e.g. the similar values of Q^*, P_{MT}, v_{sur} and $v_{0.5}$. However in the case of $f = 1$, the aforementioned quantities show a dependence on surface-to-mass ratio of the individual aggregate or the absolute size.

It is expected that toward the inner radii (within snowline) of the protoplanetary disc, the collision of high size ratio should be prominent, as they can absorb the increasing collision velocities.

The findings of this study regarding to mass transfer are quite consistent and comparable with the studies undertaken by Wurm et al. (2005b), Teiser & Wurm (2009) and Deckers & Teiser (2014). And moreover the numerical simulation of Meru et al. (2013) showed the same trend. Therefore on the basis of new results, a model of mass transfer efficiency in eqn. (4.27) has been presented.

Another fact, which is consistent with the studies mentioned above, is that in the case of growth it has always been the projectile which fragments and causes the growth onto the target. This phenomenon could be explained by the fact that the collision energy is stored in the elastic loading of both aggregates. The target being the massive one can easily dissipate collision energy in the oscillations of phonon and hence maintains its form. On the other hand, the collision energy which goes into the share of projectile is high enough; this can be released only by the plastic deformation of the projectile, which finally appears as a kinetic energy of its fragments. According to Schräpler et al. (2012) this is inelastic rolling and sliding of the monomers which are the most important dissipative channels. The target aggregate being larger in size can effectively dissipates the collision energy. The same line of arguments has been used by Meru et al. (2013) for the explanation of high threshold velocities for larger targets.

3. A complete model for area-frequency distribution and the fragmentation slope α

In eqn. (4.30) a complete model for the fragment size distribution has been introduced, which does not explains only the continuous part of the distribution but the discrete part as well.

The earliest experimental studies on the slope of area-frequency α distribution can be traced back to Blum & Münch (1993), where the collision between mm-sized aggregates of $ZrSiO_4$ with filling-factor of 0.36 at velocities between 0.15 – 4 $m s^{-1}$ were studied. In their analytical model, the slope of the fragment distribution curve was found to be constant at -5/3 and -2, for area-distribution, as well as for mass-distribution respectively. However in this study, the slope of area-frequency distribution α, see eqn. (4.32) and Figure. 4.17, show a significant variation (by factor ~ 10) with collision velocity and the size of the target aggregate. And same is true for β, the slope of mass-frequency distribution given in eqn. (4.39) and Figure. 4.24. This we interpret as dependence on the collision energy (see Figure 4.18 and Figure 4.21). One possible explanation for constant α in Blum & Münch (1993) could be the lower collision energies used in their studies.

In more recent numerical simulation by Geretshauser et al. (2011) the power-law index (for cumulative mass distribution, corresponding to β in this study) is found to be inversely proportional to the impact velocity and the same is observed in experiments (see second row Table 4.9). They think, this is because the higher collision velocities result in a large number of smaller fragments, which is consistent with the findings shown in Figure 4.20. However the experimental data, in addition to velocity, does find dependence on target as well, which is not mentioned (or observed) in their study. In addition to this, it was also not clear to Geretshauser et al. (2011) whether the deviation from the power-law distribution, at smaller fragments, is a physical phenomenon or is a result of a low number of SPH particles (≤ 100) per fragment. However with the help of new results shown in Figure 4.25, this study can confirm this is a physical phenomenon, possibly associated to how the collision energy is dissipated per unit length inside the material, discussed in Sec. 4.6.2.

5.3 What do we learn from numerical models?

The second goal of this study was the numerical modelling, which has been accomplished with the help of our colleagues at Lund Observatory. Some of the unpublished results have been presented and discussed in Sec. 4.9.

These numerical simulations showed that by using the laboratory results (under the conditions discussed in Sec. 2.4.2) one can explain the formation of planetesimals of a wide size distribution i.e. 10 – 1200 km. However it turns out that the pebble fragmentation model is more effective for the planetesimal of radius above 100 km.

In the numerical simulations, two real fragmentation models and two hypothetical models of a pebble cloud have been analysed. Results have shown that the real models are intrinsically different than their hypothetical counterpart. The important features of the numerical study can be summarised as follows.

1. The two regimes of planetesimal sizes

In Figure 4.36, Sec. 4.9.2 one can see the two distinct regimes of planetesimal size. The small size planetesimal regime starts from radius 10 km to 100 km, whereas the regime of large planetesimal is from 100 km to 1200 km. The reason of these regimes lie in their masses. In low mass clouds the collision velocity remains well below the onset-velocity of fragmentation, i.e. $v_\mathrm{n} << v_{1,}$ (followed by eqn. (4.1) and eqn (4.9)), which leads to bouncing collisions and hence a prolonged collapse time, as shown in Figure 4.37. In low mass clouds all the four models behave very similar and follow the relation $t_{col} \sim R_\mathrm{solid}^{-0.91}$. The planetesimal in this regime are the pebble pile. The regime of the large size planetesimal is interesting because of two reasons. First, owing the higher mass collision velocity goes beyond the onset-velocity of fragmentation, i.e. $v_\mathrm{n} >> v_{1.}$ Here all the three types of collision out-come, namely bouncing, fragmentation and mass transfer do occur. Second, in this regime the real fragmentation models Frag. $\alpha = 0.5$ and Frag. $\alpha = 0.9$ manifest clear distinction from the hypothetical models Bimod-frag and 100MT-$\alpha = 0.9$ model. These clouds can collapse on the order of free-fall time $t_{col} \sim t_\mathrm{ff} \approx 25.1$ years.

2. The minimum planetesimal mass and collapse time

As discussed in Sec. 4.9.3 and shown in Figure 4.37 that the cloud smaller than 10 km will be purely pebble pile. There will be neither fragmentation nor mass transfer, hence the proposed fragmentation model will be not valid. The minimum mass limit brings the upper limit to collapse time, which is $t_{col} \approx 170$ years for a planetesimal of radius $R_\mathrm{solid} = 10$ km.

3. The real fragmentation models

Results have shown that the real fragmentation models, Frag. $\alpha = 0.5$ and Frag. $\alpha = 0.9$, behave very similar regardless to what the size of a planetesimal is. As presented in Sec. 4.9.4, both paths of the collapse are very similar and therefore result in a planetesimal of very similar internal structure. In both models, regardless of some events of mass transfer, the mean pebble size remained smaller than that of primordial pebbles. Because in 99% of the collapse time (i) the relative velocities were higher than the onset-velocity of fragmentation, $v_\mathrm{n} > v_1$, (ii) the largest fragment remained less than 1, i.e. $\mu < 1$ (see eqn. (4.2)) and as a result almost in every collision (iii) the probability of mass transfer remained also less than 1, i.e. $P_\mathrm{MT} << 1$ (see eqn. (4.24)). In both models 40%– 45% mass of the planetesimal is accumulated in pebbles of size 0.1 mm, see black-solid and red-dashed curves in Figure 4.41. Since the width of the mean pebble size distribution is relatively narrower than the other models, therefore the planetesimals are expected to be relatively porous with lower internal strength. If the planetesimal is cut into half, one would find larger to smaller pebbles from inner to outer radius.

4. **Bimodal fragmentation model**

This hypothetical model has showed that a large fraction (~ 44%) of the planetesimal mass is the result of growth of the primordial pebbles, which did grow up to ~ 6 cm, by accreting the monomers. And the second large concentration of mass (~ 28%) is in the pebbles of size ~ 0.1 mm (see blue-dashed-dotted curve in Figure 4.41). These accumulation of mass in two size-bins could be the reflection of the bimodal nature of fragmentation. In such a planetesimal the inner region is expected to consist of small grains ≤ 0.1 mm and the large pebbles of few centimetres would be deposited in outer shells.

5. **The 100% MT – $\alpha = 0.9$ planetesimal**

This model owing to its hybrid nature leads to a planetesimal a different characteristics. First distinction is its wide width of final mean pebble size distribution, which spans from few 10s of microns to few metres, see magenta-dotted curve in Figure 4.41. Here during the collapse phase the growth process has been 100% efficient, which explains the presence of boulders of few metres in size. Another interesting feature is that here a significant fraction (~ 22%) of the primordial pebbles which had initial size of 1 cm did survive the collapse, which is not observed in other models. The planetesimal in this model is expected to be less porous, which means higher internal strength. Here the small grains between 0.01 – 1 mm, which were produced in early phase of the collapse, are expected to compose the inner region of the planetesimal and larger pebbles and boulder (few cm to few m), which are formed in the last few days of the collapse, are assumed to form the outer shells of the planetesimal. This planetesimal will have internal structure in contrast to the real fragmentation models, where the larger pebble were inside and smaller in outer shells.

5.4 Relevance to 67P/ Churyumov-Gerasimenko

One can find two prominent similarities between the observation of 67P and the above discussed models. For example; the GIADA (Grain Impact Analyser and Dust Accumulator, the on board instrument of Roseta mission) has detected the fluffy grains of size 0.2 mm to 2.5 mm within the coma of 67P (e.g., see Fulle et al. (2015) and Della Corte et al. (2016)). These grains are assumed to be released from the core of the comet. In this case it is consistent with the hybrid model 100% MT-$\alpha = 0.9$.

According to Mottola et al. (2015), the high resolution images of 67P taken by ROLIS (Rosetta Landing Image System) from the Agilkia site during its descent onto the comet, show the presence of pebbles of few centimetres to the boulders of a few metres. These boulders are expected to be outcrop from the underlying bedrock. Moreover, they assume that these bumpy features of few cm in size are "possibly a remnant of the comet's formation mechanism".

In addition to this, Pajola et al. (2016) analysed the images of OSIRIS (Optical, Spectroscopic, and Infrared Remote Imaging System the main imaging system of the Rosetta mission) and have reported several 100 boulders larger than 7 m on the surface of 67P.

The observed pebbles and boulders on the surface of 67P could be associated to the late phase of the collapse, as explained in the hybrid model 100% MT-$\alpha = 0.9$.

However the inconsistency between observation and the presented models is the density. In the models of this study, the density of the planetesimal is equal to monomer density $\rho_{\mathrm{SiO2}} = 2.5\ \mathrm{g\,cm^{-3}}$, which is indeed a compact body. However the observations of 67P suggest that comets are porous bodies (70 – 75% porous depending on dust to ice ratio) (Wahlberg Jansson et al. 2016) which has bulk density $\rho_{\mathrm{67P}} \sim 0.5\ \mathrm{g\,cm^{-3}}$ (El-Maarry et al. 2015). This difference could be explained by the initial mass (or size) of the cloud. According to the models presented in this study the 67P is assumed to have formed by a low mass cloud, probably $R_{\mathrm{solid}} < 10$ km. For example, Wahlberg Jansson & Johansen (2014) in their Fig. 5 showed that in low mass clouds ($R_{\mathrm{solid}} = 5$ km) the collision velocity remains lower than the onset-velocity of fragmentation, i.e. $v_{\mathrm{n}} < v_1$ and pebbles simply pile up over each other. This is what makes a body very porous. However in this study, the cloud which is has been analysed internally has planetesimal radius $R_{\mathrm{solid}} = 500$ km, which is relatively a massive cloud. In such a cloud, from the collision velocities are well above the fragmentation threshold i.e. $1\ \mathrm{m\,s^{-1}}$, which leads to fragmentation and hence a denser planetesimal.

5.5 The limitation of this study and the future prospects

In this study only SiO_2 has been used to produce pebbles, however a real planetesimal is composed of dust and ice. In order to develop a more realistic fragmentation model it would be useful to use materials which are more relevant to the composition of a real planetesimal. For this, the already existing cryogenic experimental setup could be modified to facilitate the collisions between dust-ice-aggregates.

The model of fragment velocity distribution presented in Sec. 4.8.3 can be improved by using three dimensional imaging. It will provide the information along z-axis which has been inaccessible within the current experimental setup.

In the case of the numerical simulation, the major simplification is the neglect of the gas drag, which can have impact on the relative velocities and hence the structure of the planetesimal.

The second simplification has been the use of 1 cm sized monodisperse primordial pebbles. If a realistic cloud is desired then the primordial pebbles should have a certain initial size distribution. Another simplification is the neglect of the net angular momentum of the cloud, which is important for the explanation of the binary planetesimals.

In addition to this, in next generation of numerical models the step 6 (a dynamic α) defined in Sec. 4.10 can be implemented. It would provide more accuracy about the process of energy dissipation during the collapse of a pebble cloud and the final pebble mass fraction.

5.6 Conclusion

This is the first experimental study of its kind which has used the numerical simulation as an input and feeds back to the numerical simulation as an output.

With the help of experiments it has been shown that the collision parameters investigated in this study lead to two types of collision: i) catastrophic fragmentation and ii) mass transfer, but do not lead to bouncing. The absence of the bouncing collisions is important, because in such collisions the energy dissipation is slow and it can prolong the collapse of a pebble cloud. With this argument, the smallest possible planetesimal whose formation can be explained by the pebble fragmentation model, has radius R_{solid} = 10 km. The model will be not valid for the clouds in which neither fragmentation nor mass transfer occur.

Hence it can be concluded that the collisions parameters which have been predicted by the studies of streaming instability are more relevant for the pebble cloud above 100 km radius. Since the pebble fragmentation model is based on these parameters, therefore it is also more effective for the planetesimals above 100 km. In the context of SI, another important thing to confirm is the prediction of a shorter time scale required for the formation of a planetesimal. In Figure 4.37 it has been shown that planetesimal up to 1200 km can be formed in about 25 years and in the slowest case 170 years for a 10 km size body, which is still a fraction of the orbital period of the Pluto. The process is significantly efficient than the classical approach of forming planetesimals, which requires about a million years.

The pebble fragmentation model, which is the outcome of laboratory work, has foundation on material properties, therefore the proposed model of fragmentation strength (Hill function in eqn.(4.6)) is expected to be valid outside the range of collision parameters tested in 142 experiments, given that the filling-factor remains same. Since the hybrid model 100MT-α = 0.9 has turned up to be more relevant to the observation of 67P, it implies that the mass transfer rate higher than 30% should be possible within the given collision parameters. However the future experiments will determine the robustness of the model.

The outcome of the whole exercise is to visualise a gravitational collapse of a pebble cloud, which helps to understand the process of formation of a planetesimal.

If it is asked, whether we really know for sure that what happens when nature turns the pebbles of the size of a sugar cube into a body of the size of a city. It is difficult to say what actually does happen, but in this thesis one of the simple scenario has been contemplated, which is allowed by the laws of physics.

Appendices

Appendix A: Area-frequency distribution after eqn. (4.30)

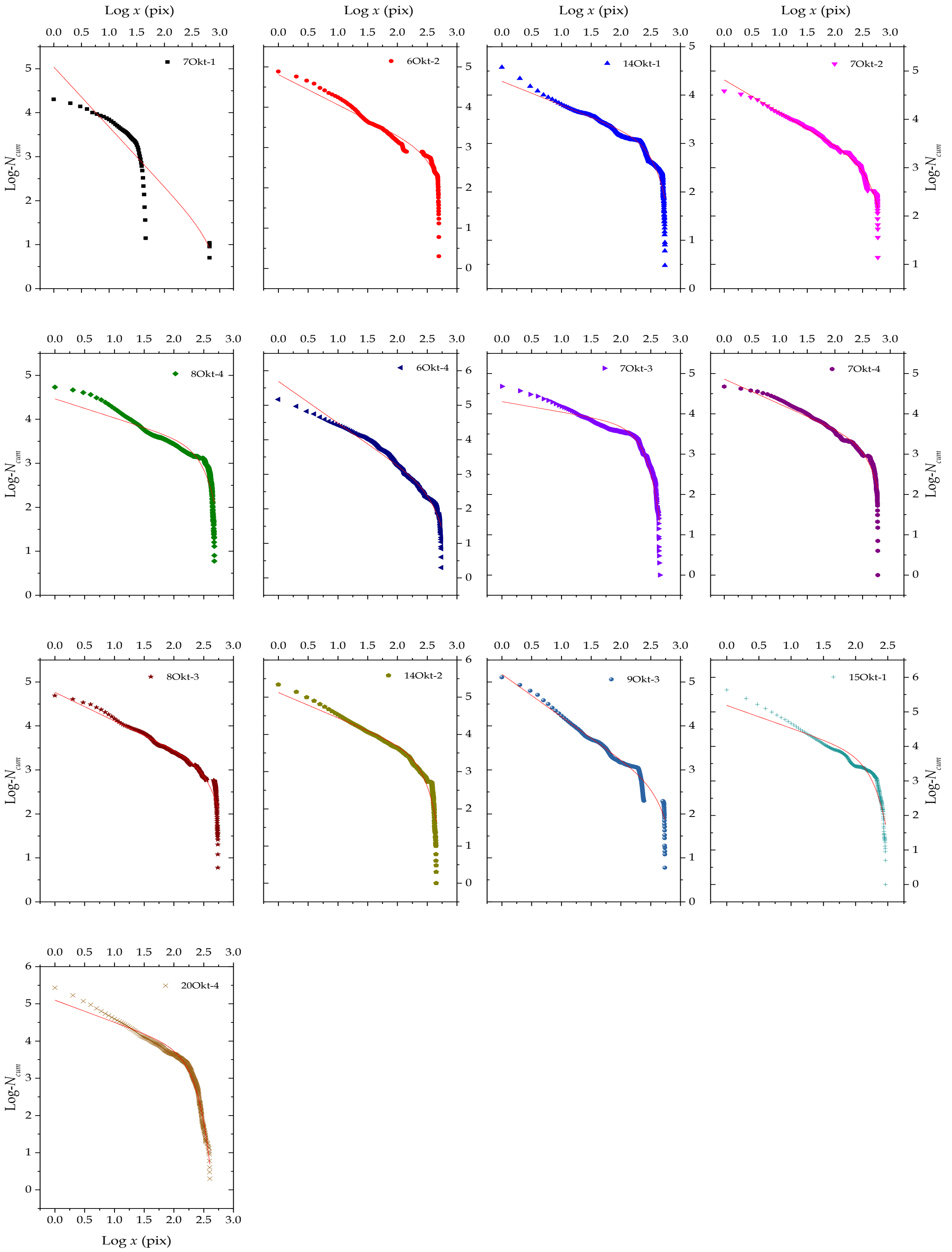

Figure A 1. Area-frequency distribution of individual experiments in the 1 cm - 1 cm series.

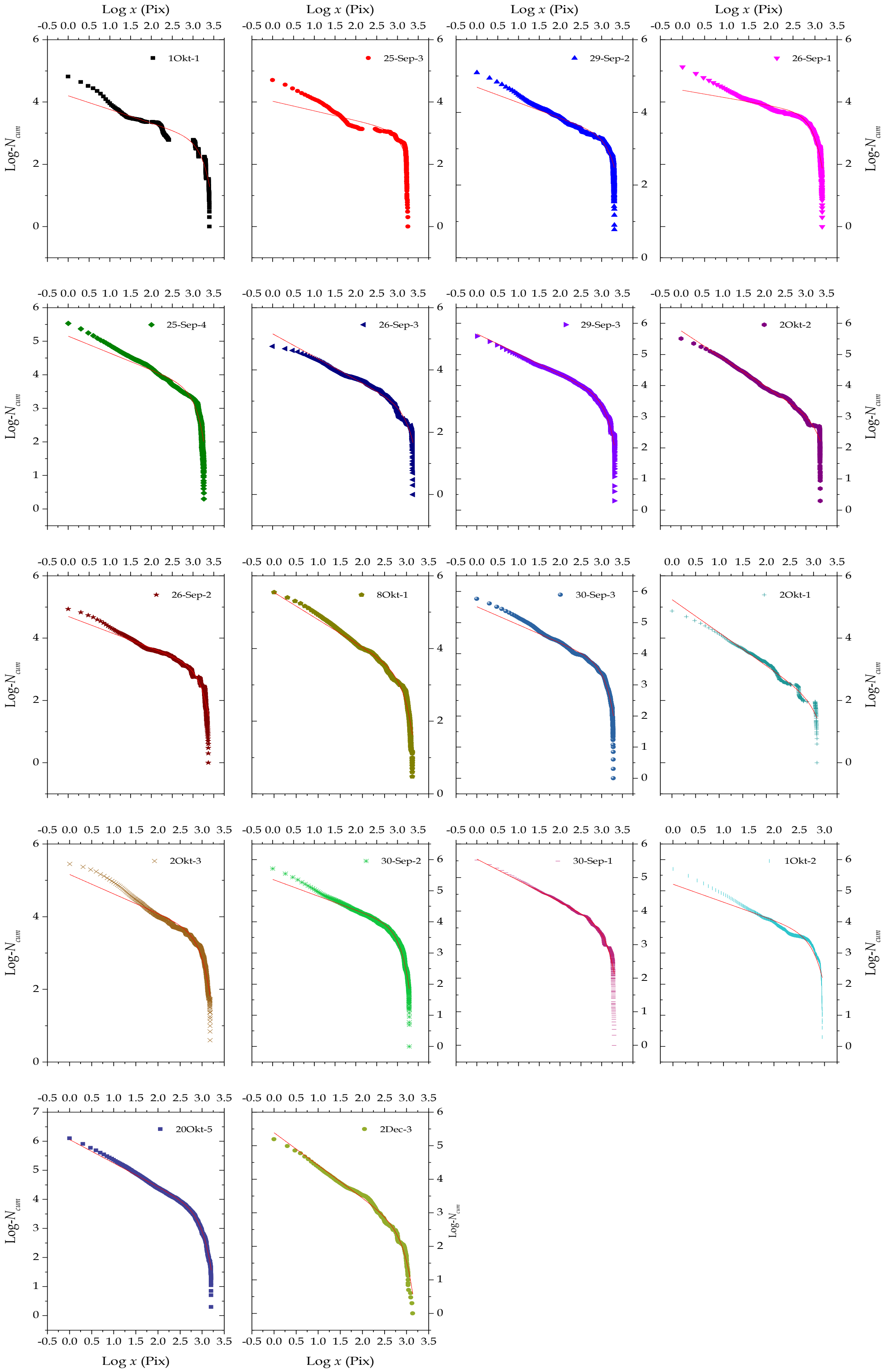

Figure A 2. Area-frequency distribution of individual experiments in the 2 cm - 2 cm series.

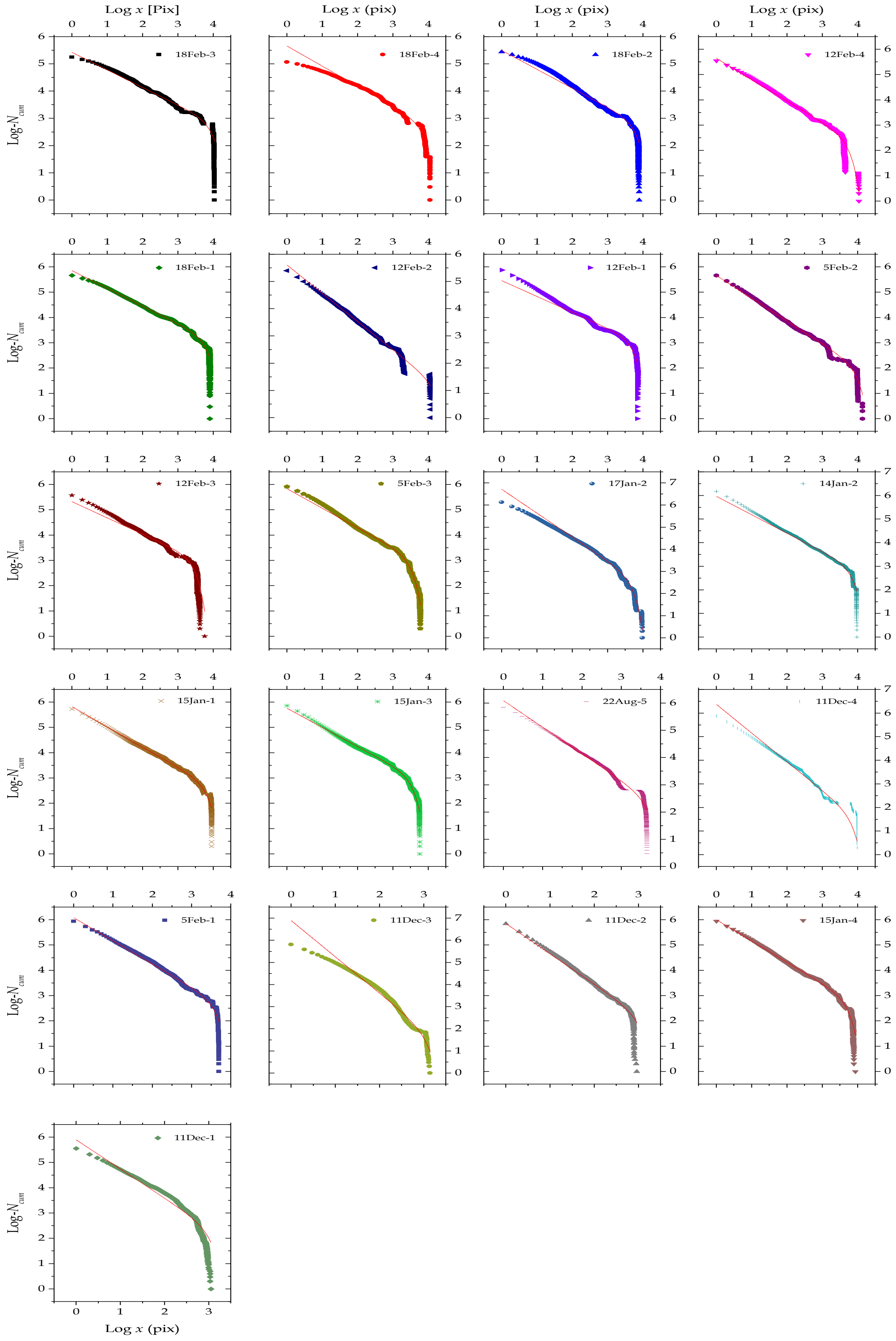

Figure A 3. Area-frequency distribution of individual experiments in the 5 cm - 5 cm series.

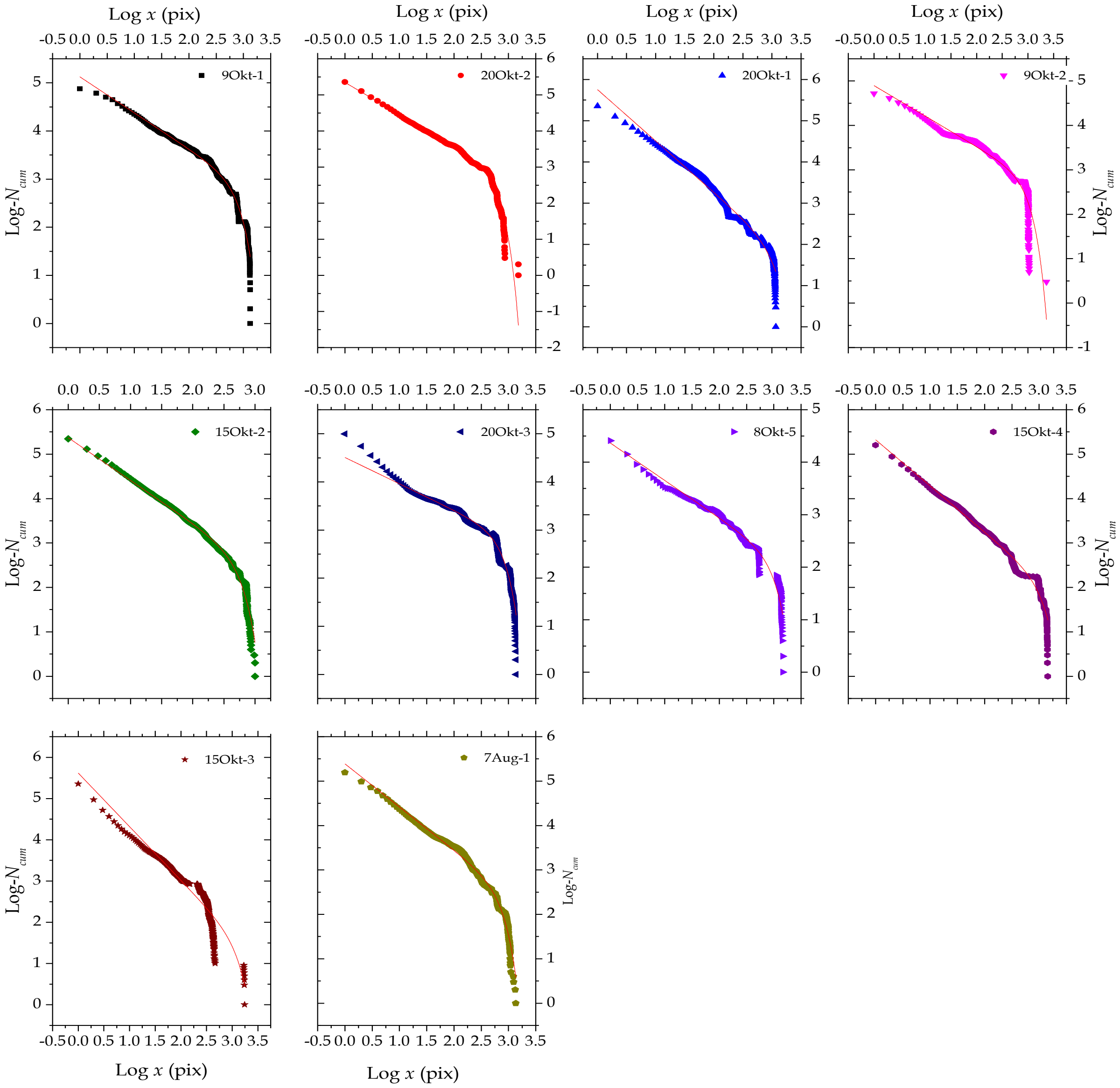

Figure A 4. Area-frequency distribution of individual experiments in the 1 cm - 2 cm series.

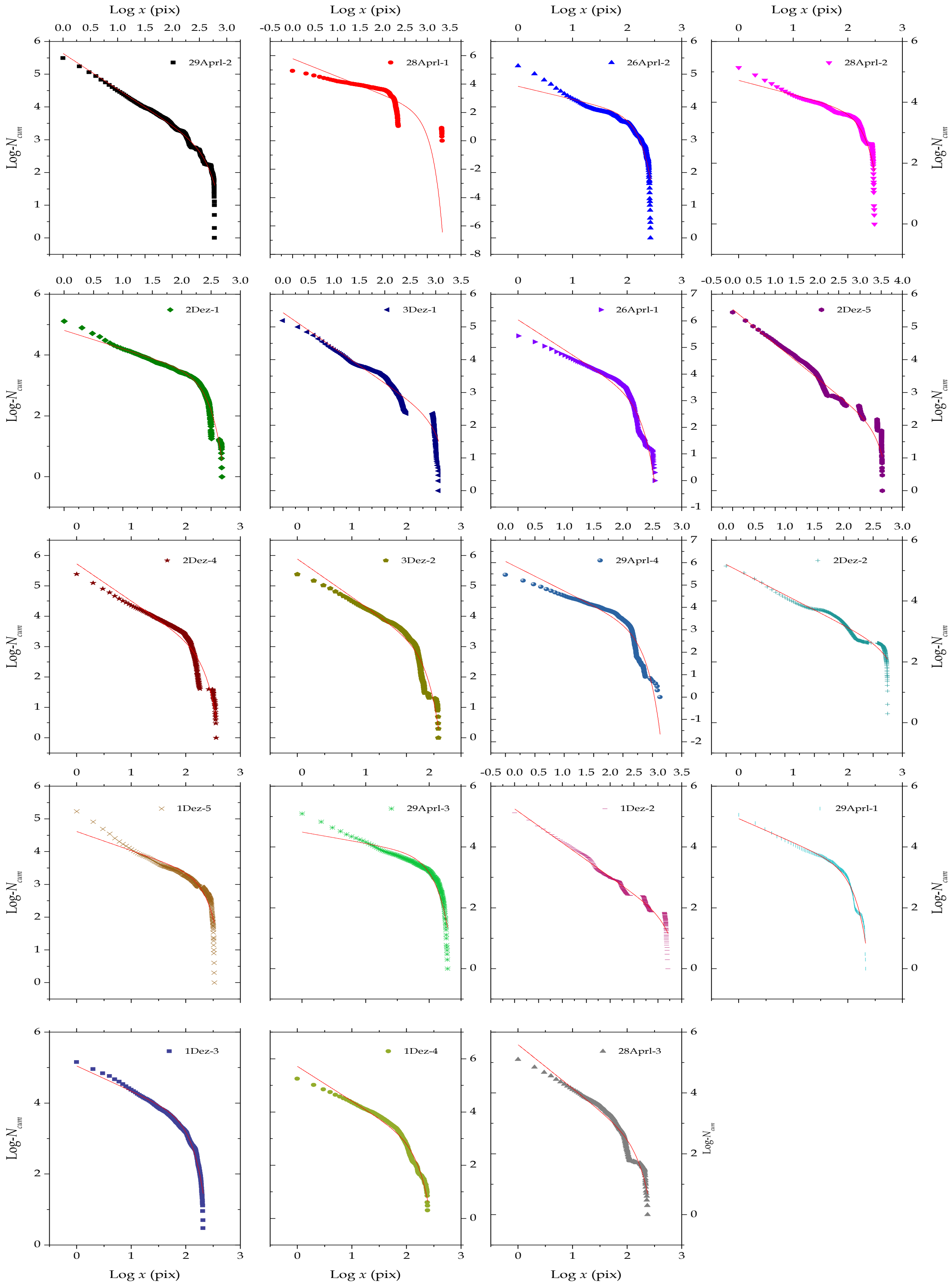

Figure A 5. Area-frequency distribution of individual experiments in the 1 cm – 2.6 cm series.

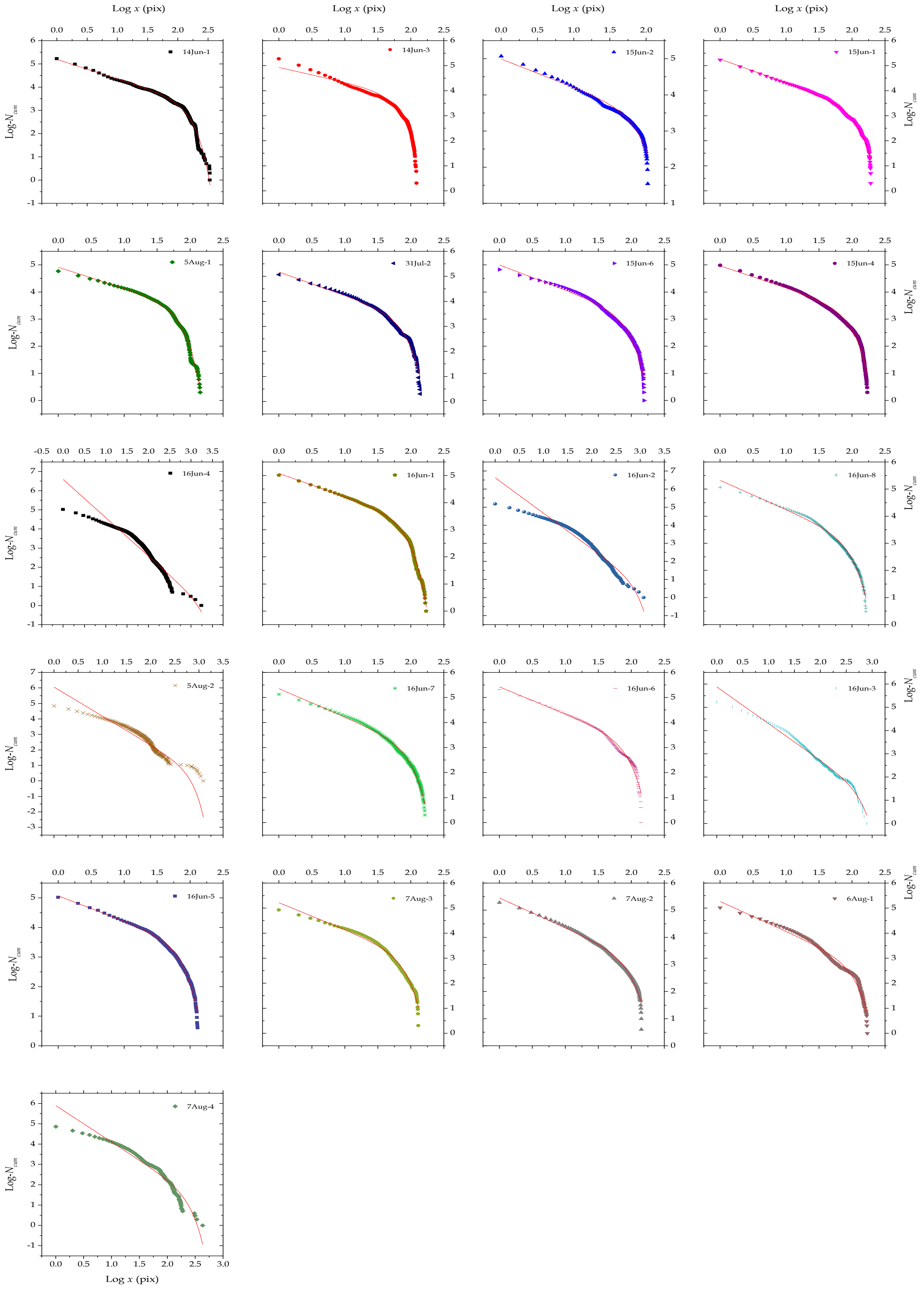

Figure A 6. Area-frequency distribution of individual experiments in the 1 cm – 5 cm series.

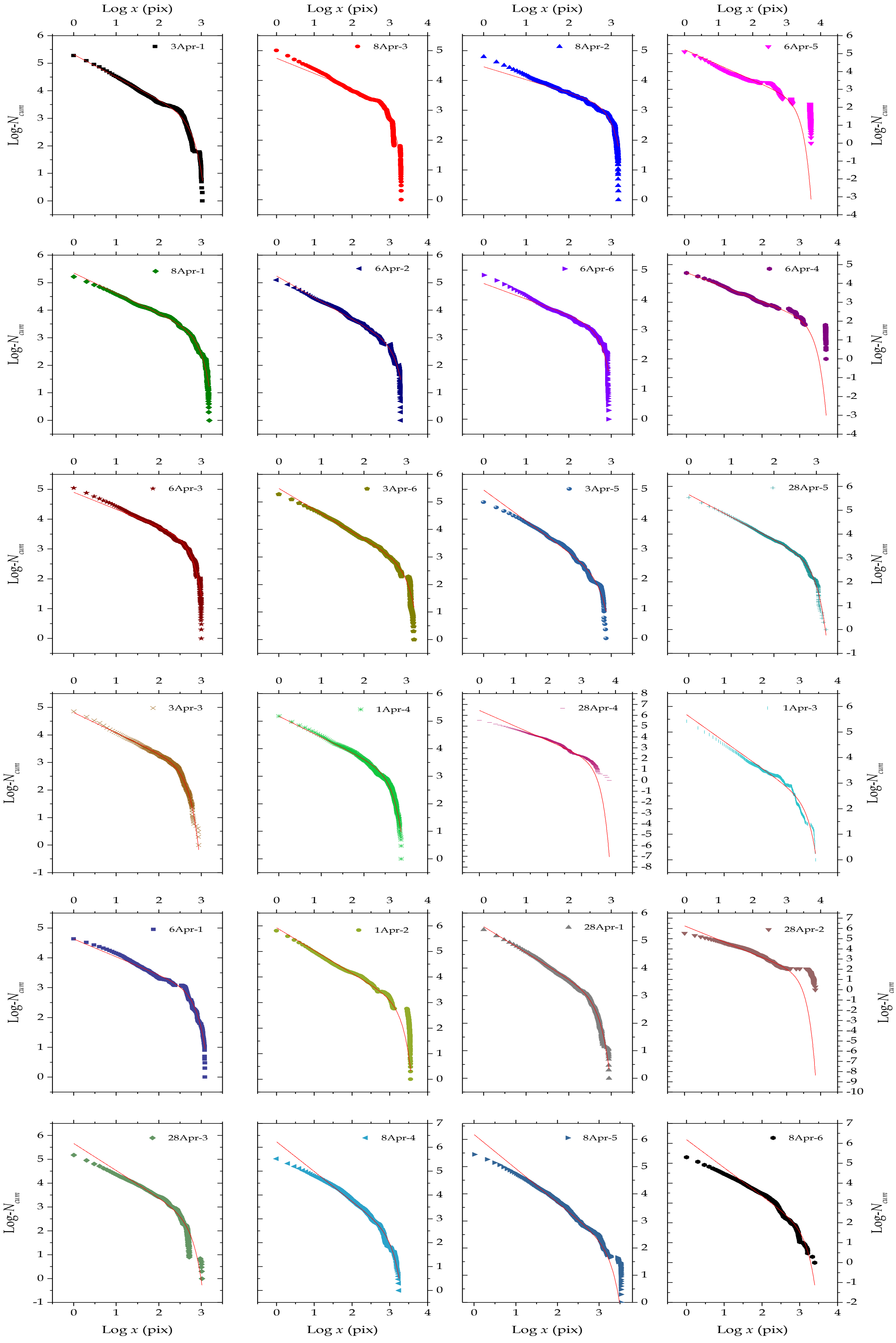

Figure A 7. Area-frequency distribution of individual experiments in the 2 cm – 5 cm series.

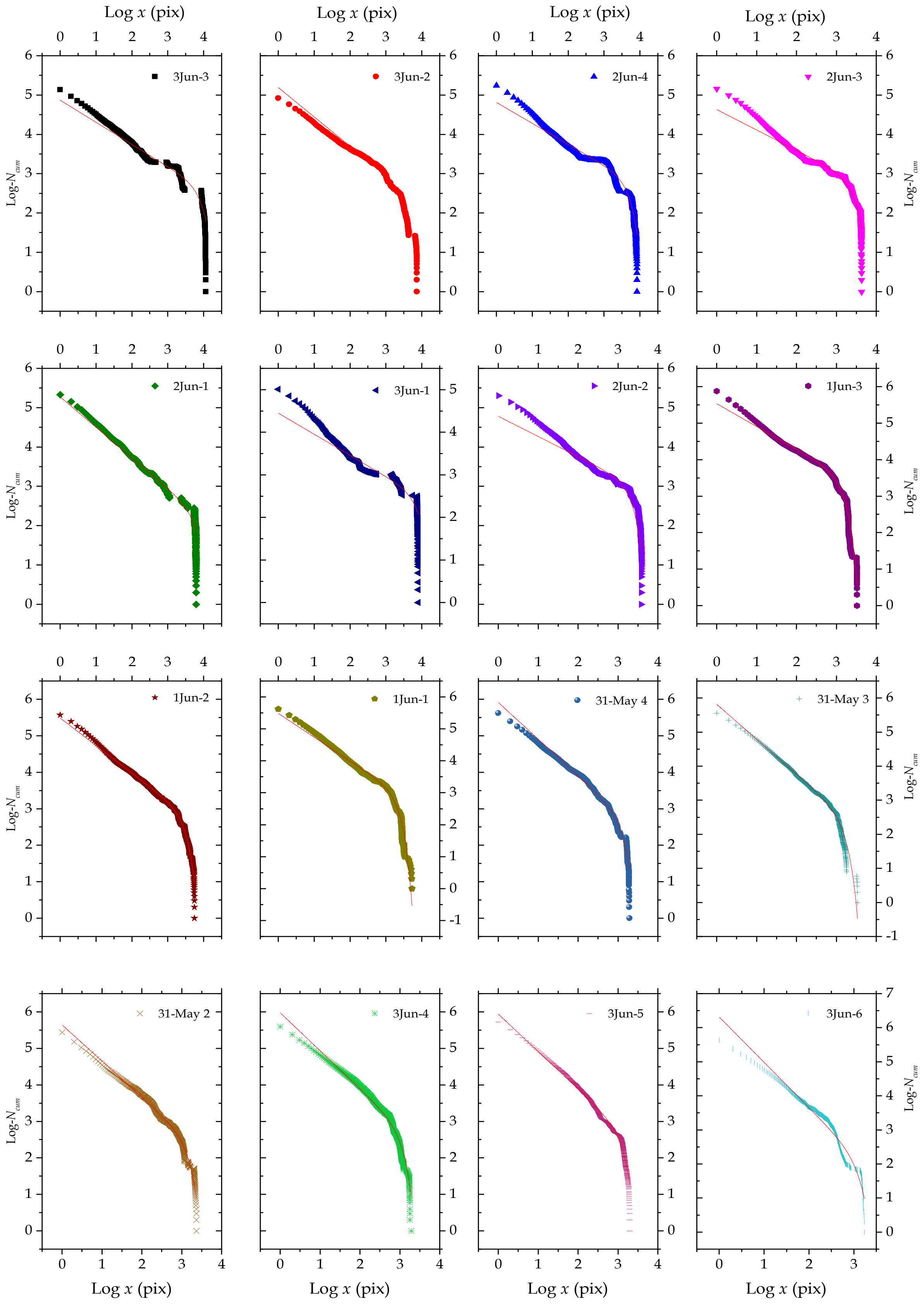

Figure A 8. Area-frequency distribution of individual experiments in the 3.5 cm – 5 cm series.

Appendix B : Mass-frequency distribution after eqn. (4.38)

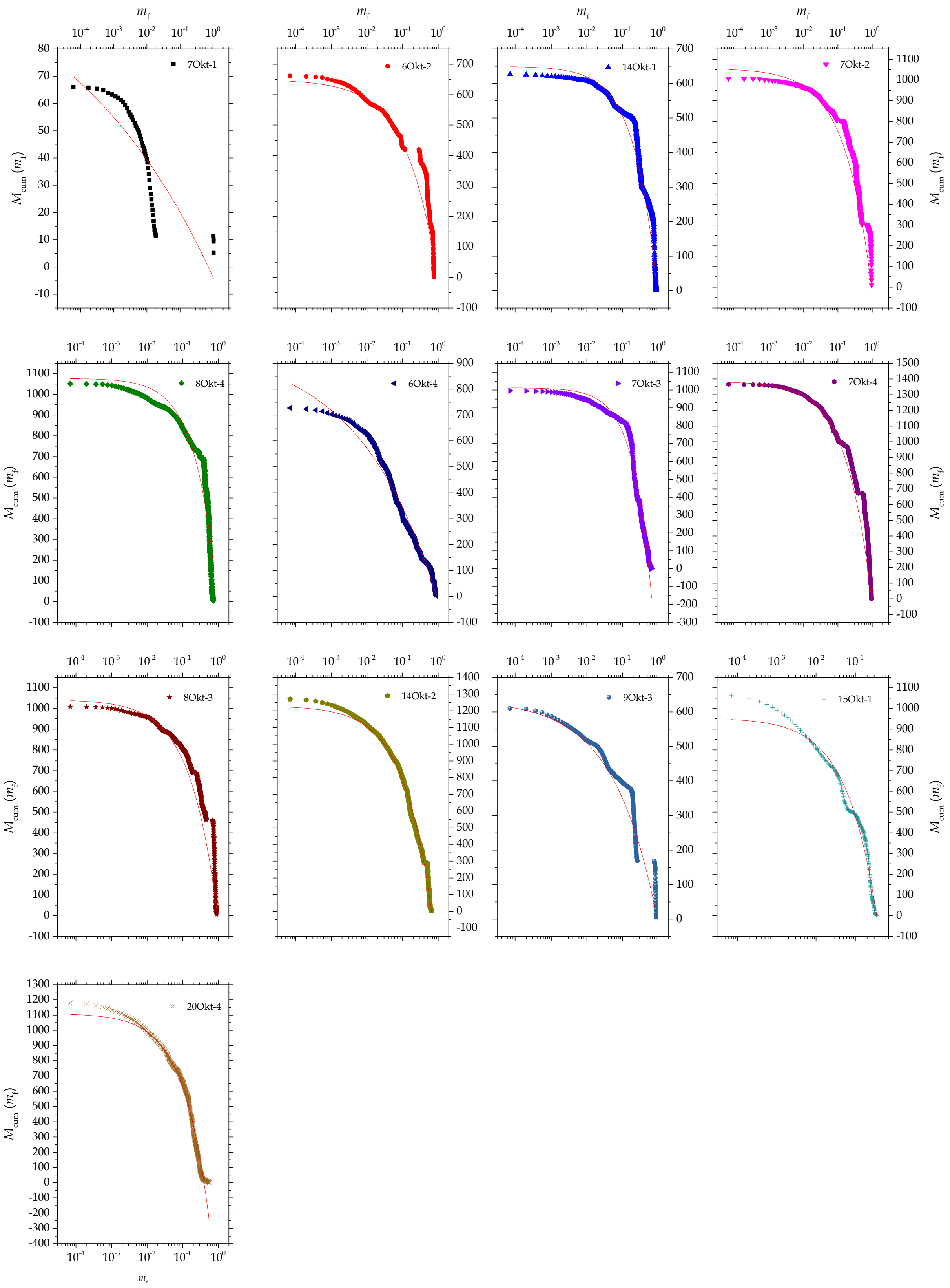

Figure B 1. Mass-frequency distribution of individual experiments in the 1 cm - 1 cm series.

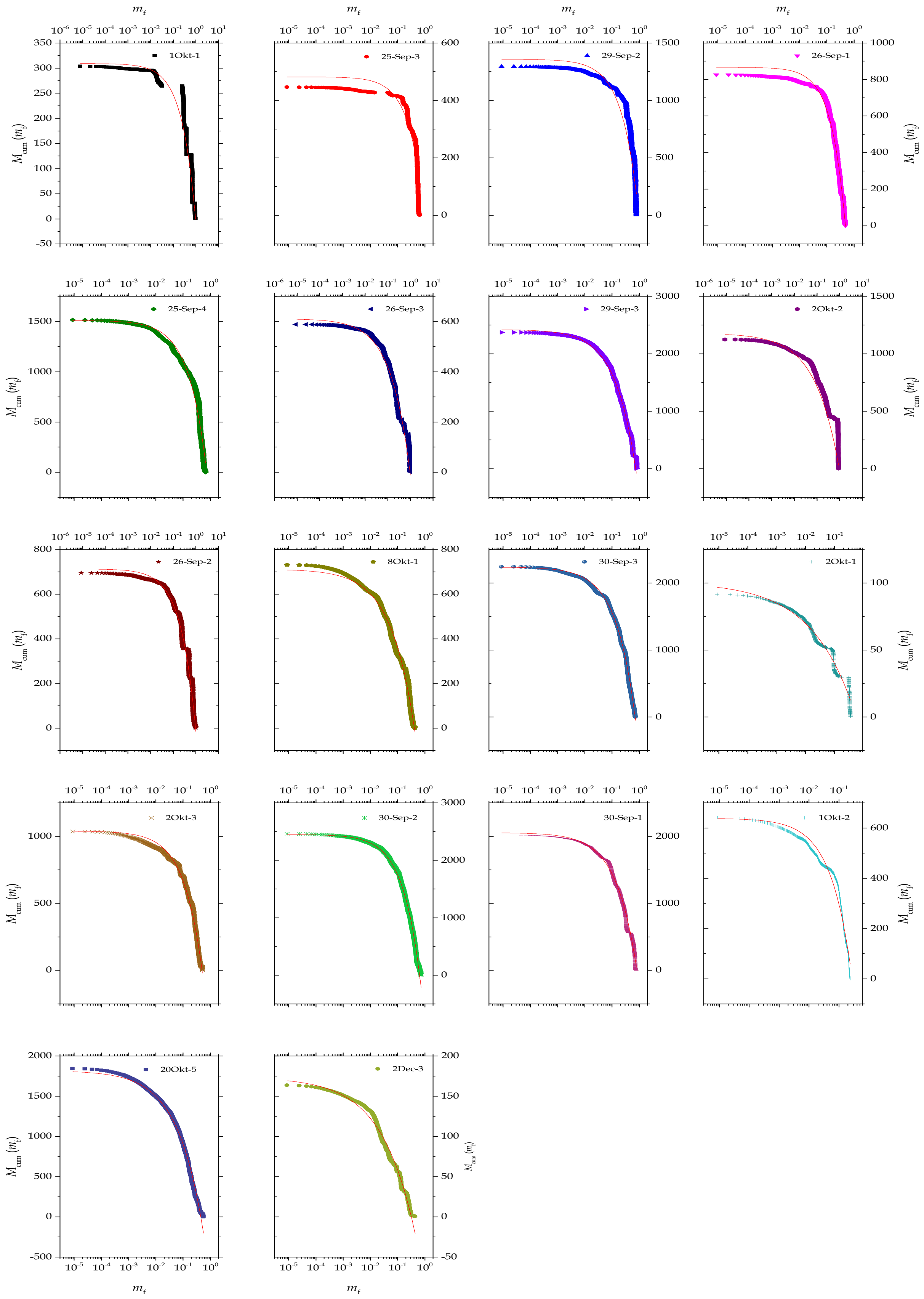

Figure B 2. Mass-frequency distribution of individual experiments in the 2 cm - 2 cm series.

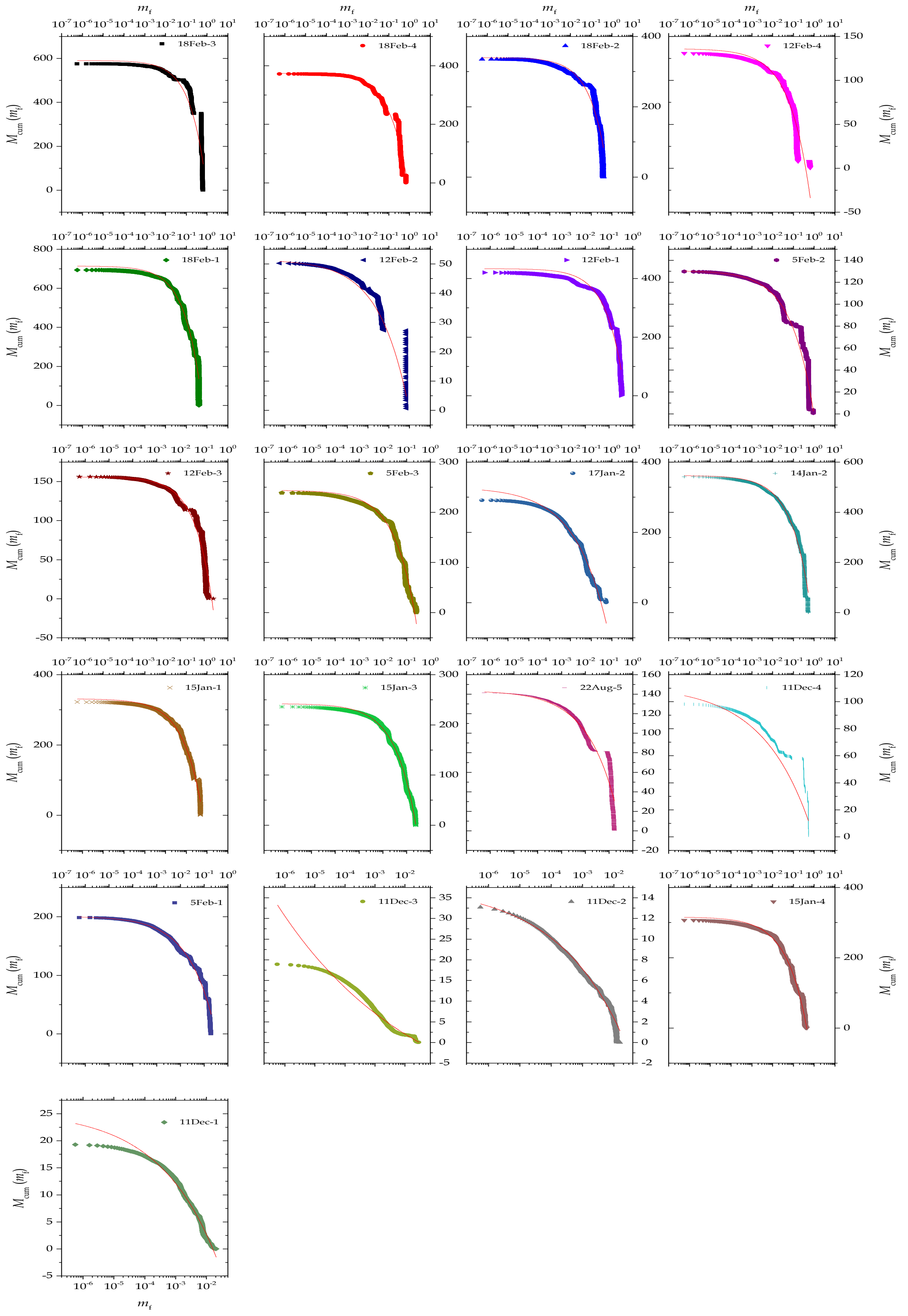

Figure B 3. Mass-frequency distribution of individual experiments in the 5 cm - 5 cm series.

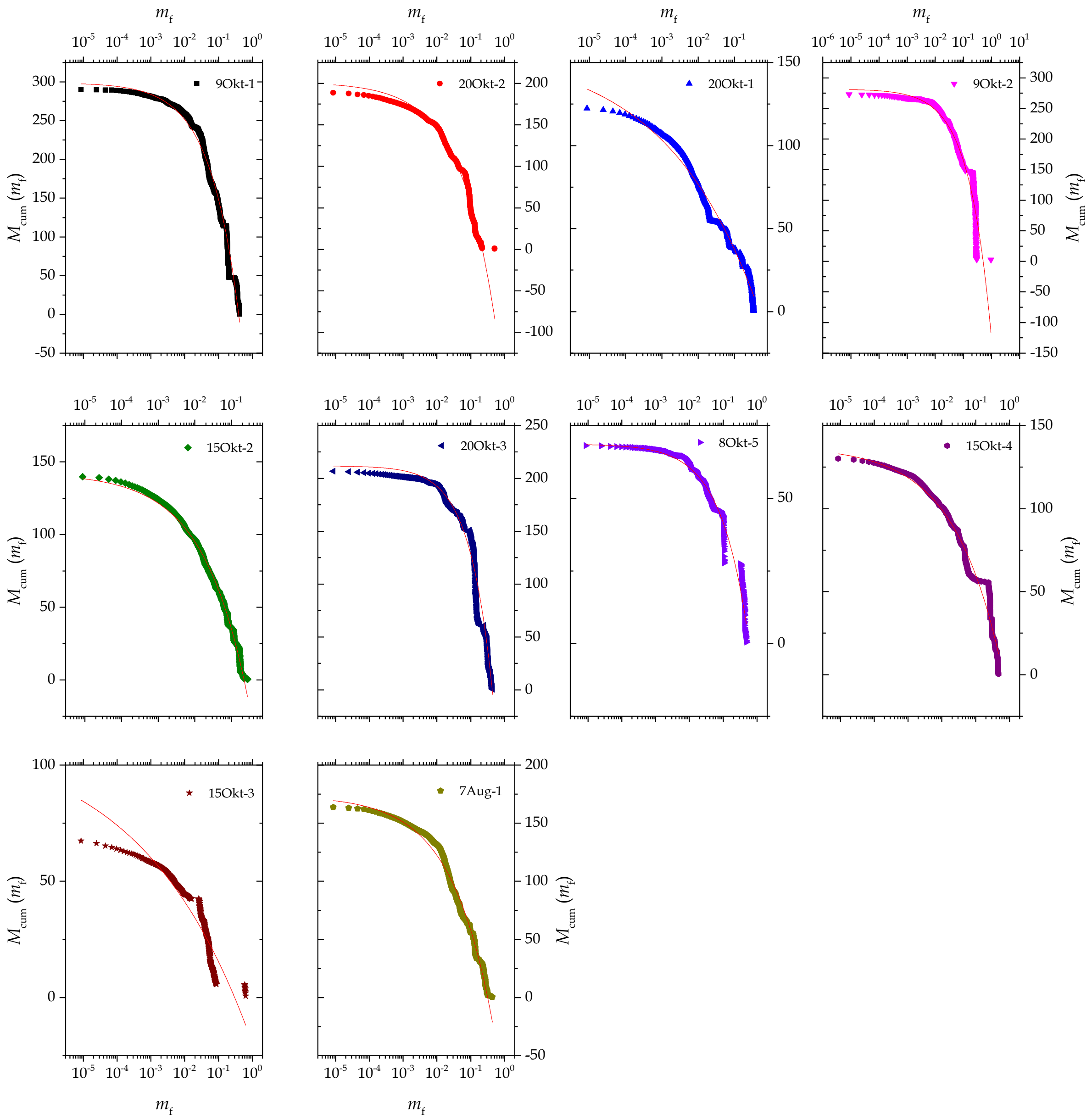

Figure B 4. Mass-frequency distribution of individual experiments in the 1 cm - 2 cm series.

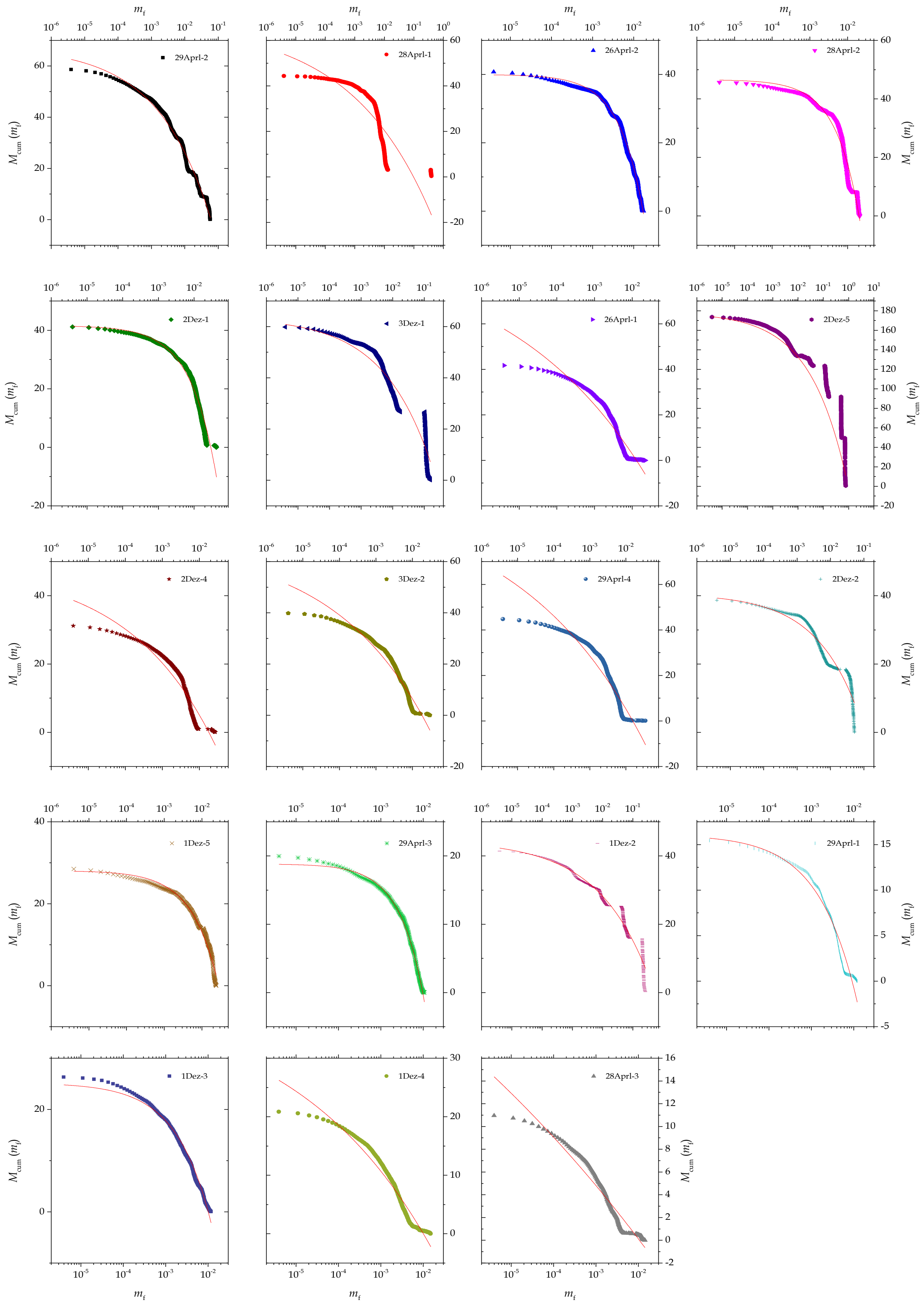

Figure B 5. Mass-frequency distribution of individual experiments in the 1 cm – 2.6 cm series.

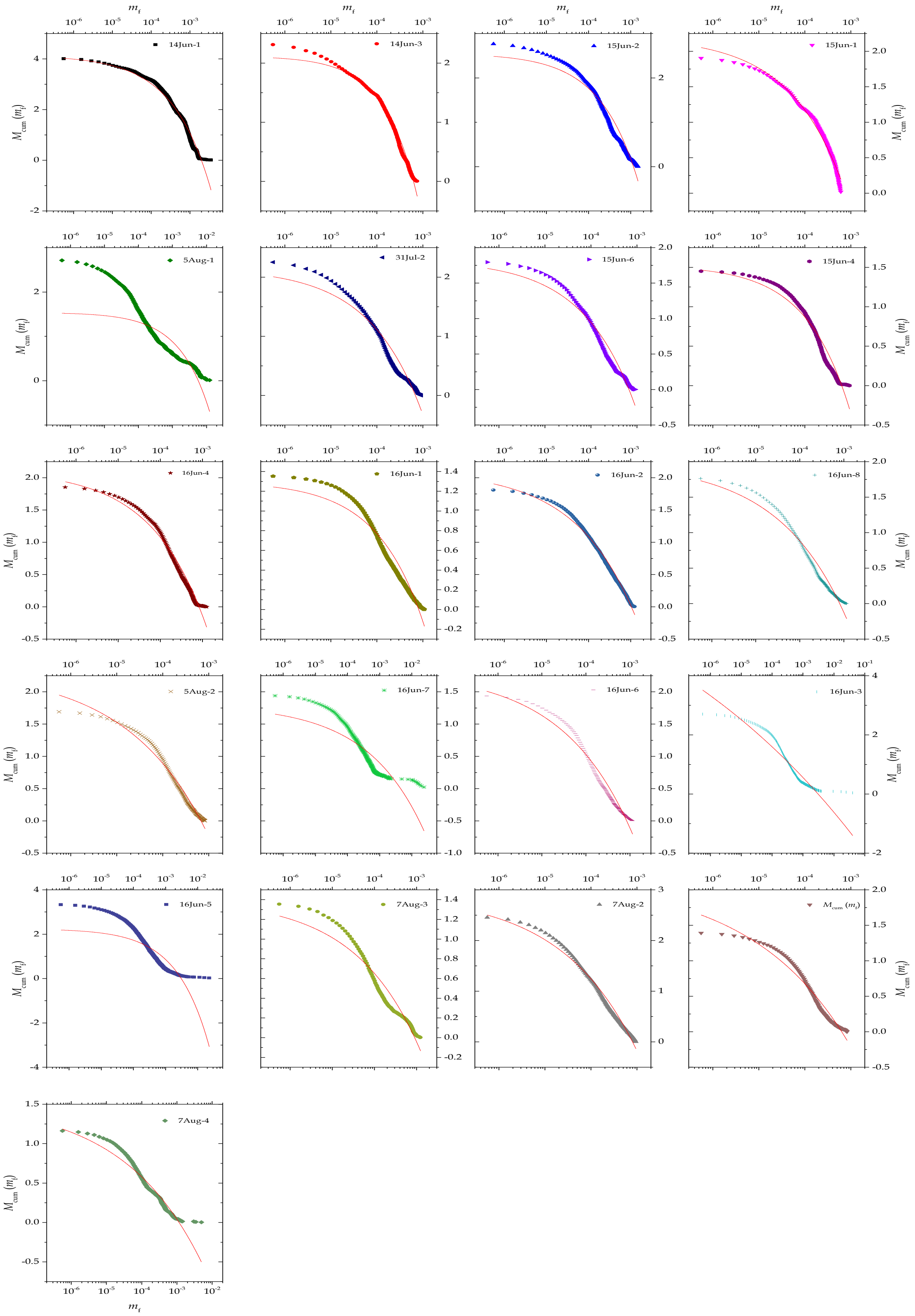

Figure B 6. Mass-frequency distribution of individual experiments in the 1 cm – 5 cm series.

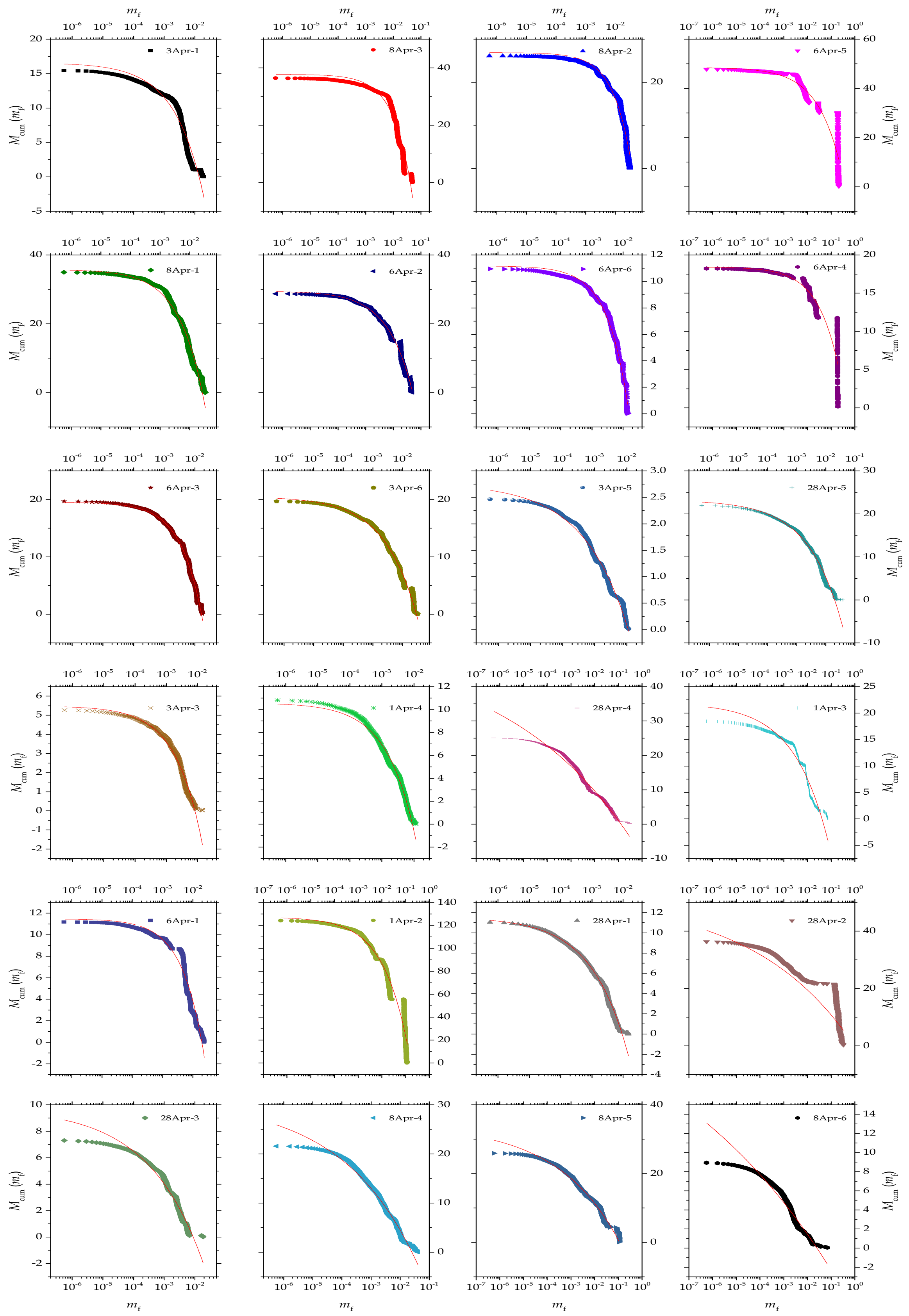

Figure B 7. Mass-frequency distribution of individual experiments in the 2 cm – 5 cm series.

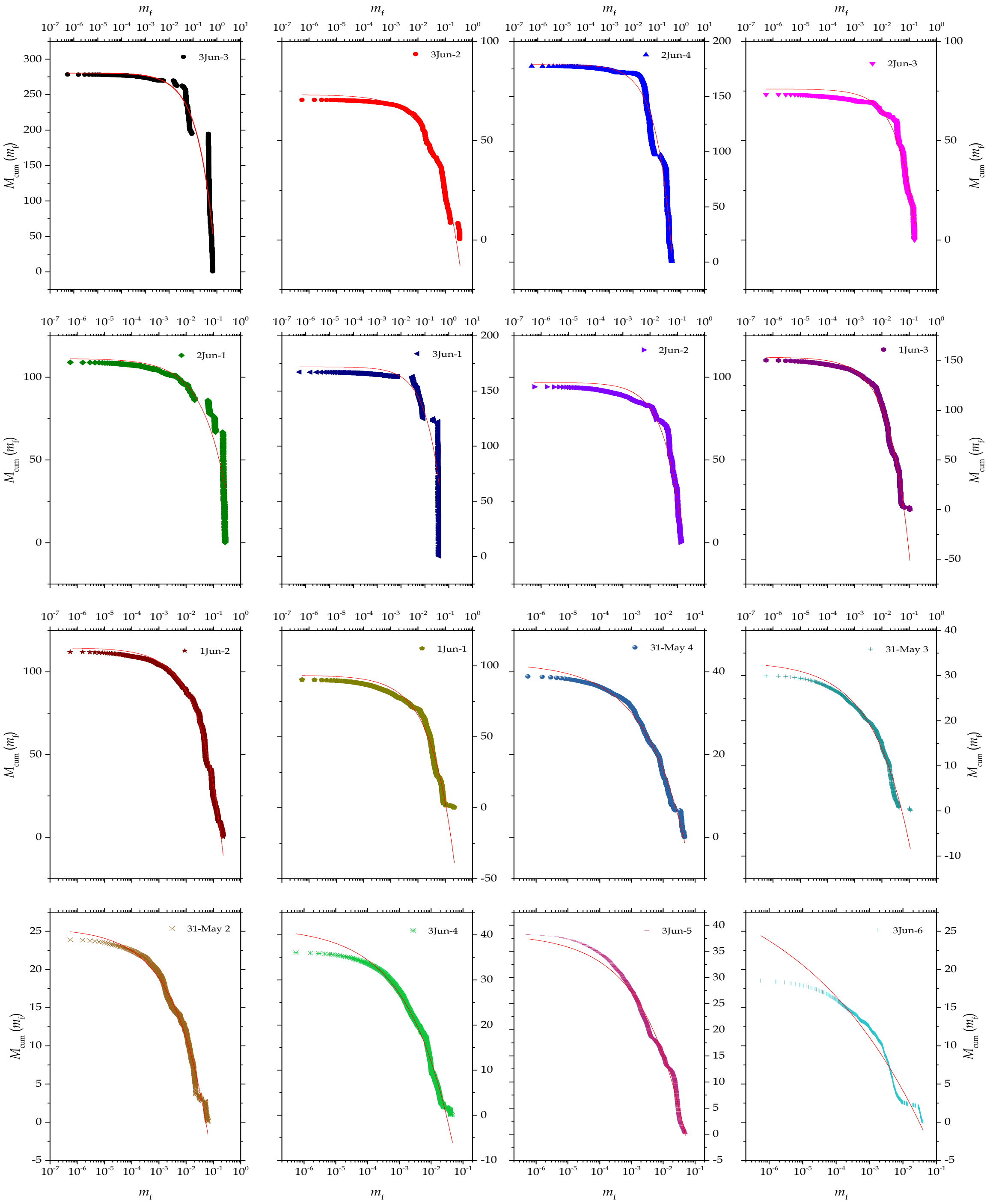

Figure B 8. Mass-frequency distribution of individual experiments in the 3.5 cm – 5 cm series.

Appendix C[1] : Fragment velocity distribution[2] after eqn. (4.48)

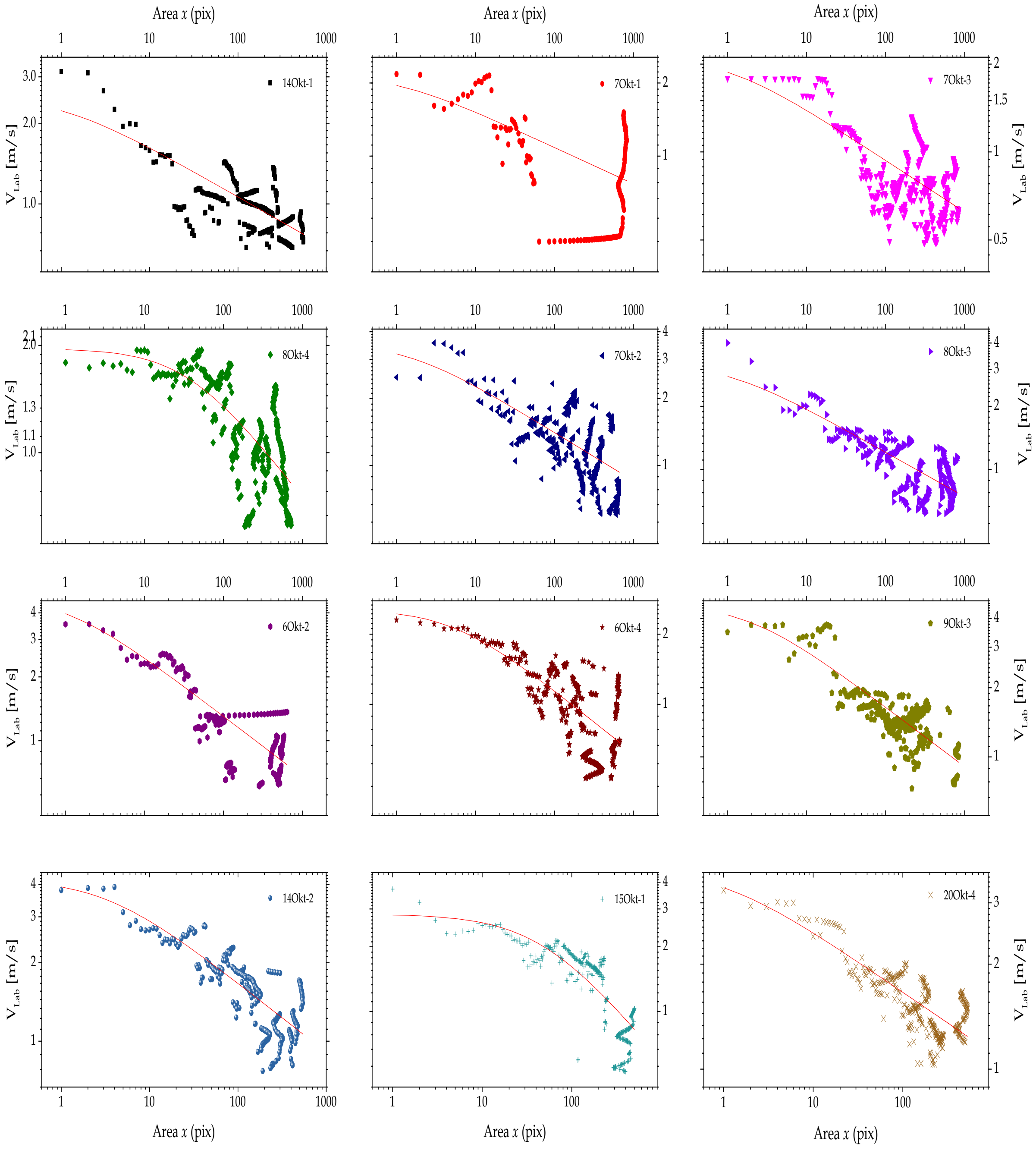

Figure C 1. Fragment velocity distribution of individual experiments in the 1 cm – 1 cm series.

---

[1] The experiments in Appendix C are sorted with respect to collision energy.

[2] One experiment 7Okt-4 in 1cm-1cm series could not be analysed, hence not included here.

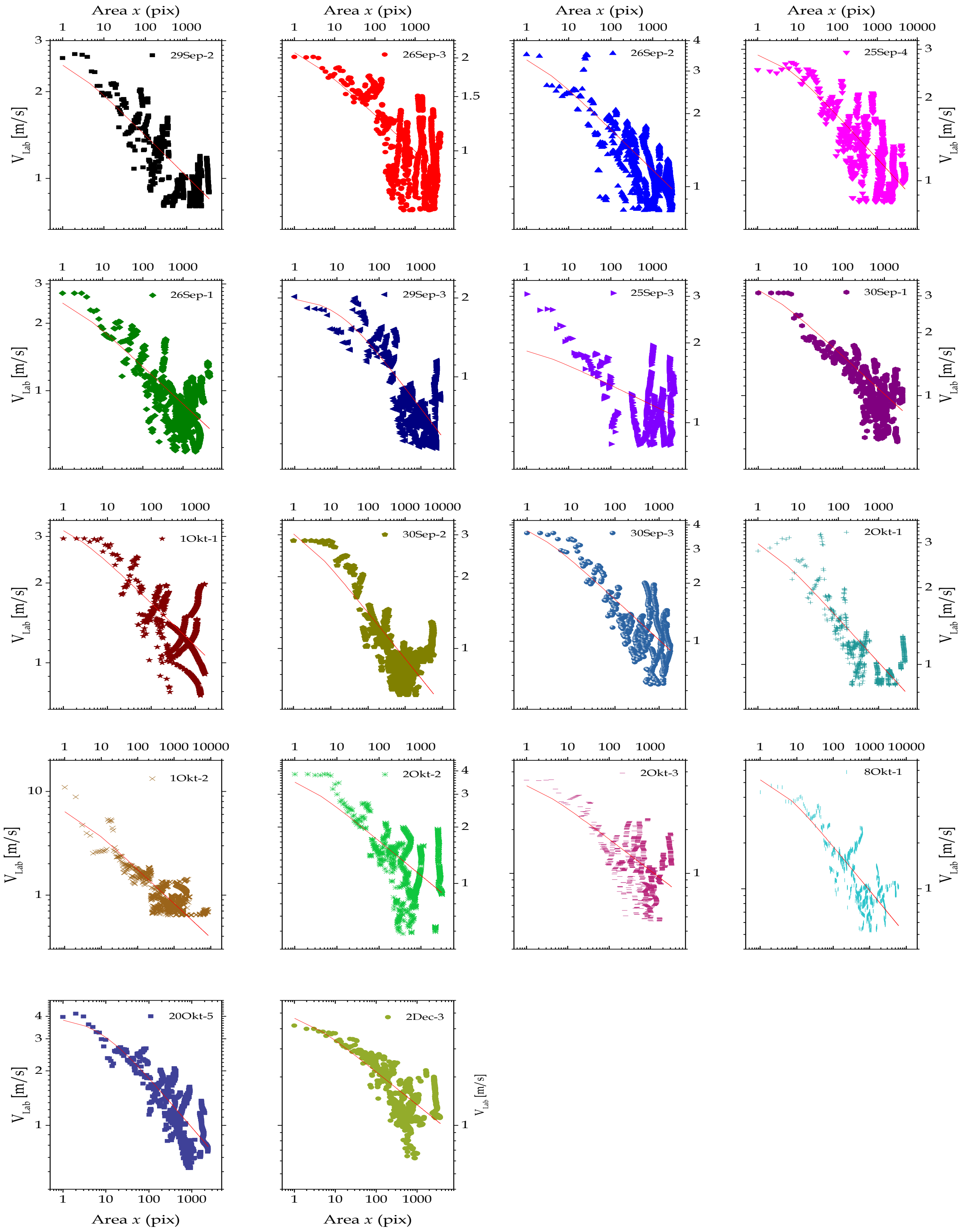

Figure C 2. Fragment velocity distribution of individual experiments in the 2 cm – 2 cm series.

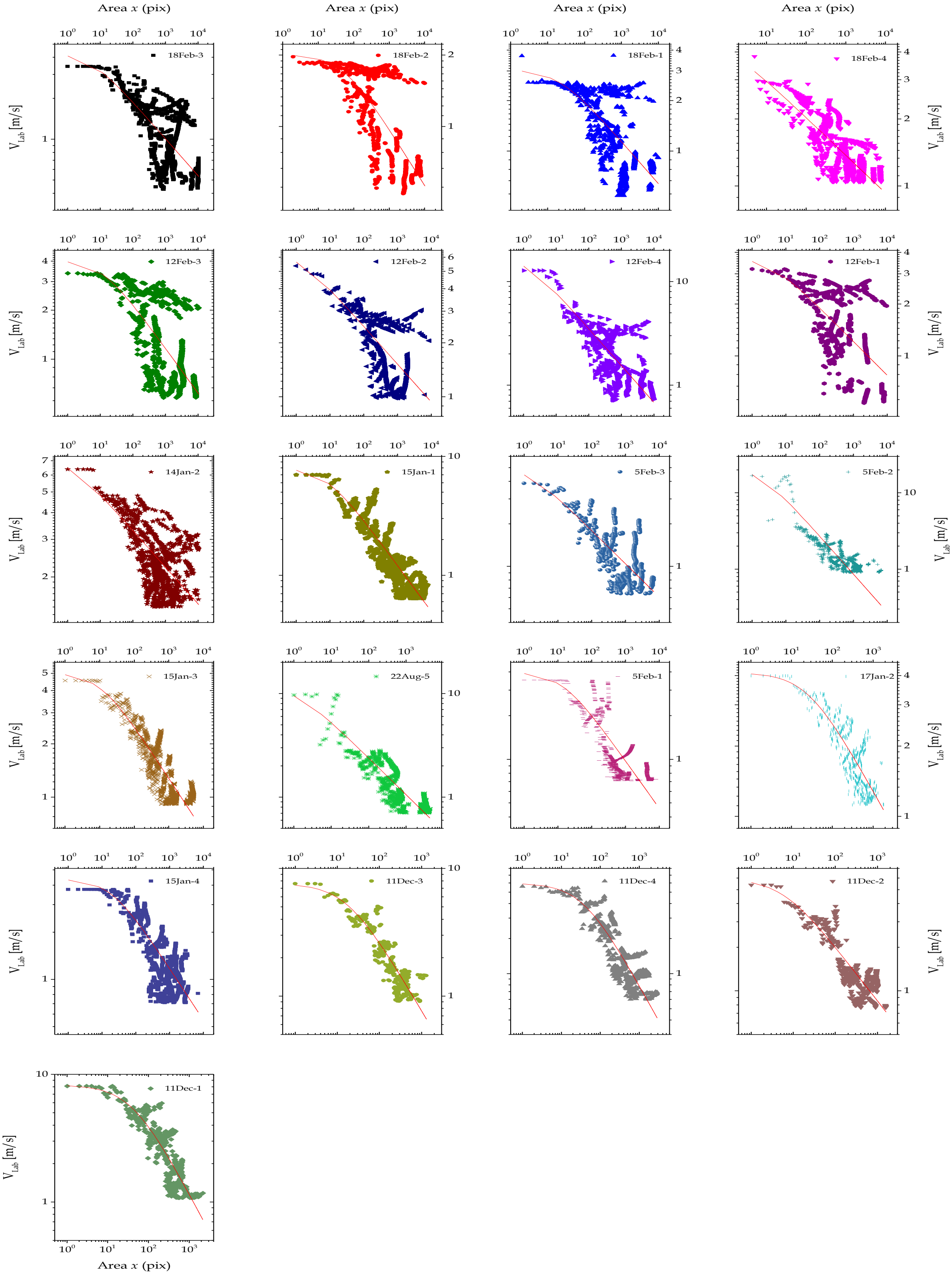

Figure C 3.. Fragment velocity distribution of individual experiments in the 5 cm – 5 cm series.

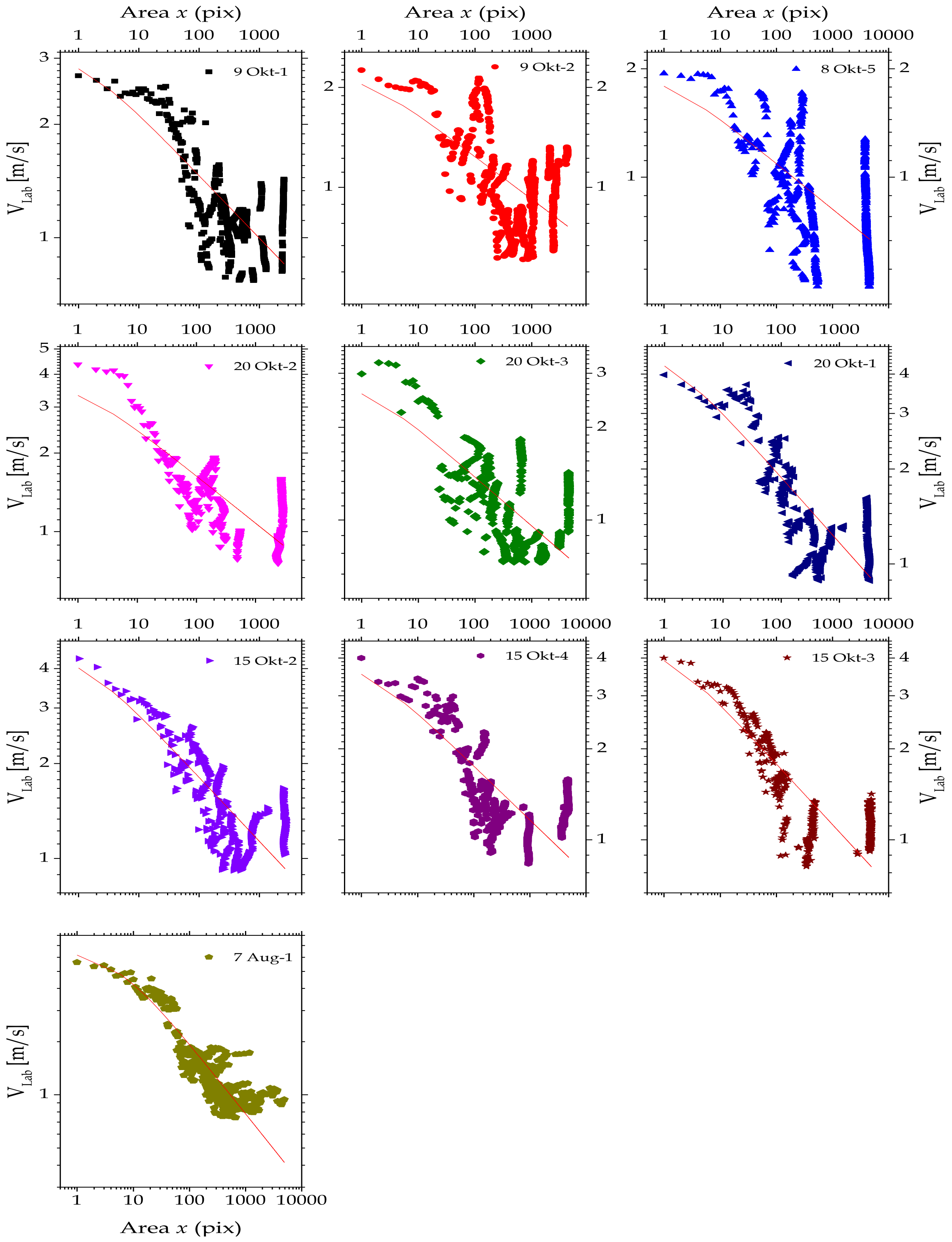

Figure C 4.. Fragment velocity distribution of individual experiments in the 1 cm – 2 cm series.

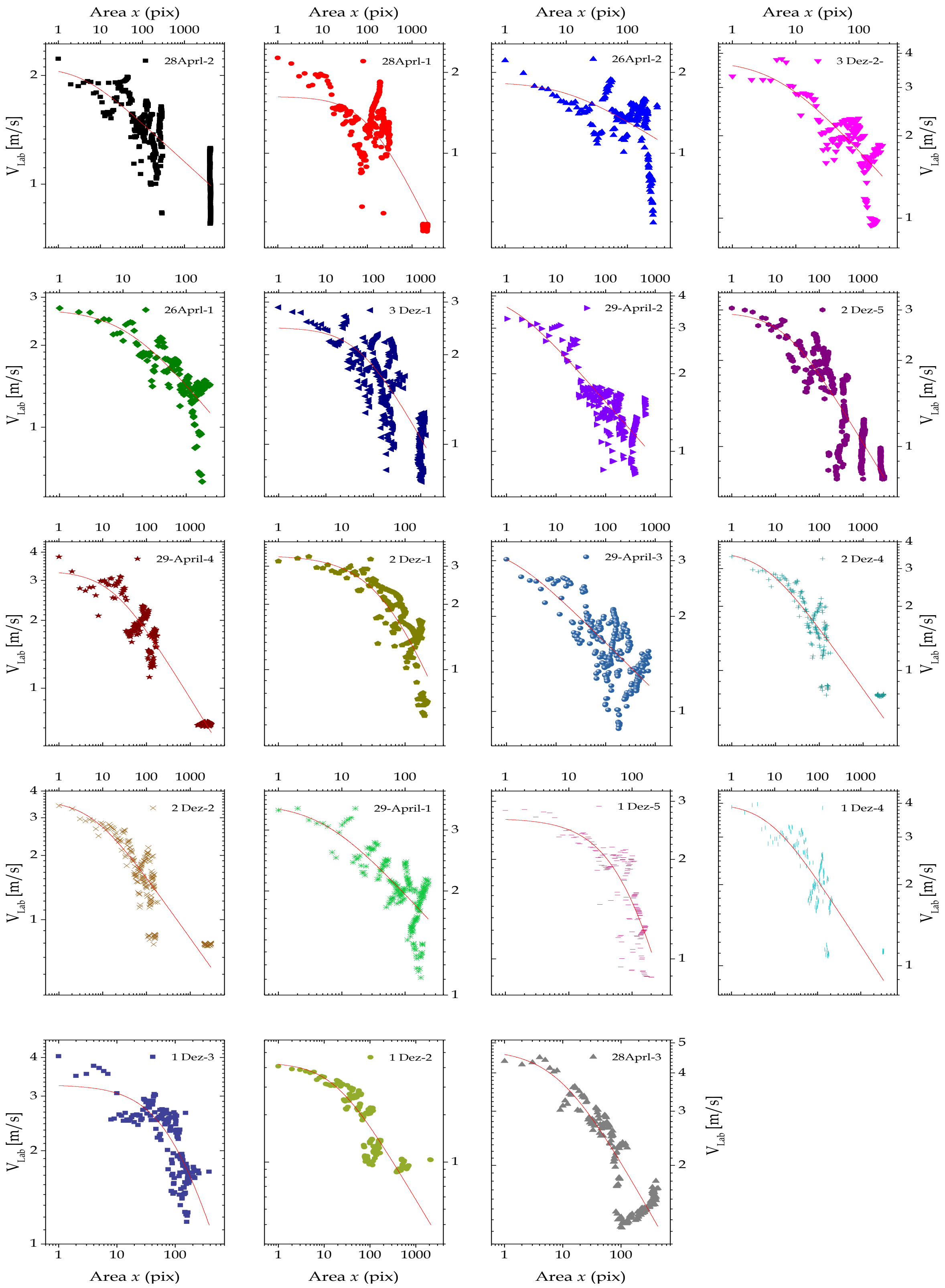

Figure C 5.. Fragment velocity distribution of individual experiments in the 1 cm – 2.6 cm series.

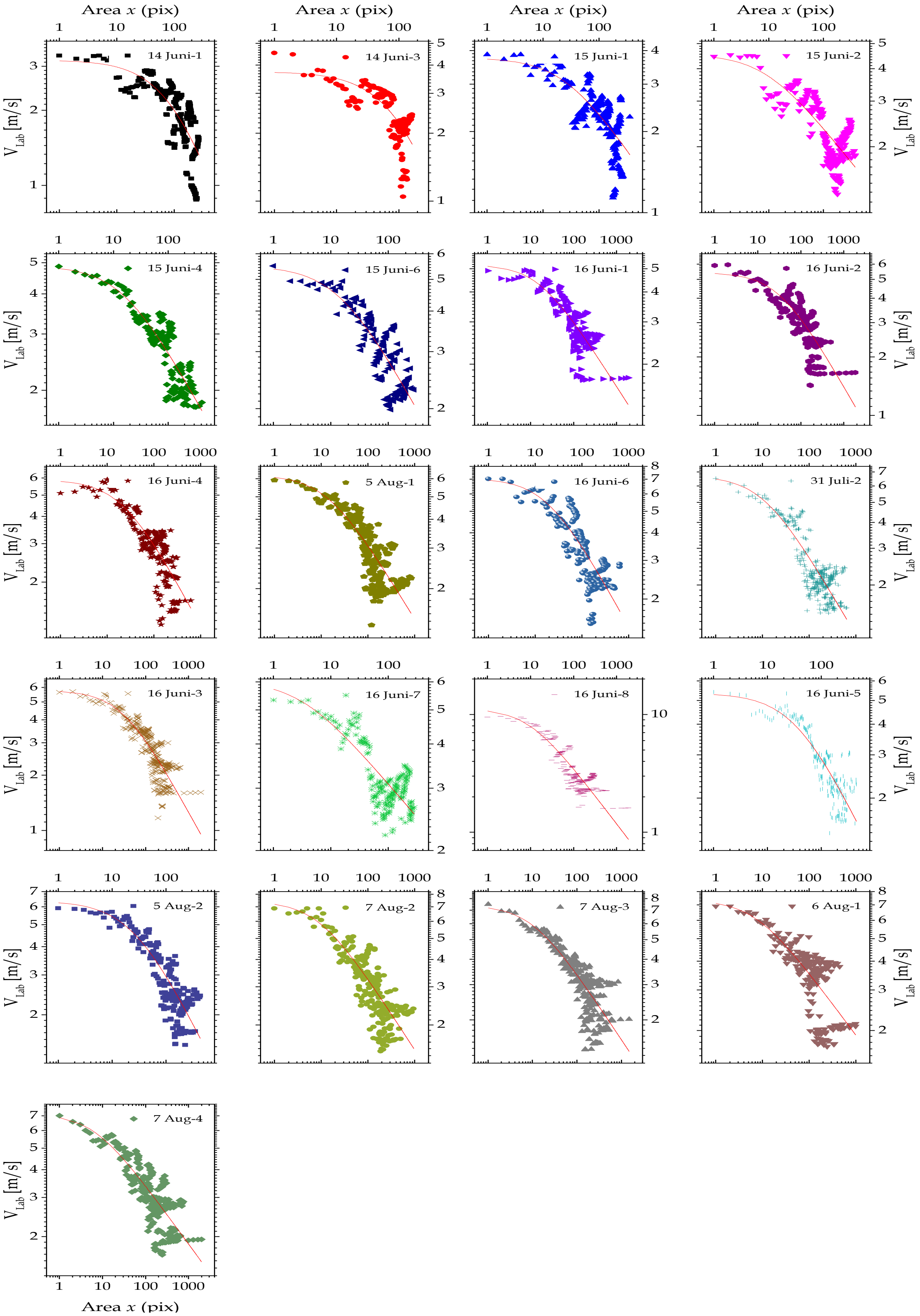

Figure C 6.. Fragment velocity distribution of individual experiments in the 1 cm – 5 cm series.

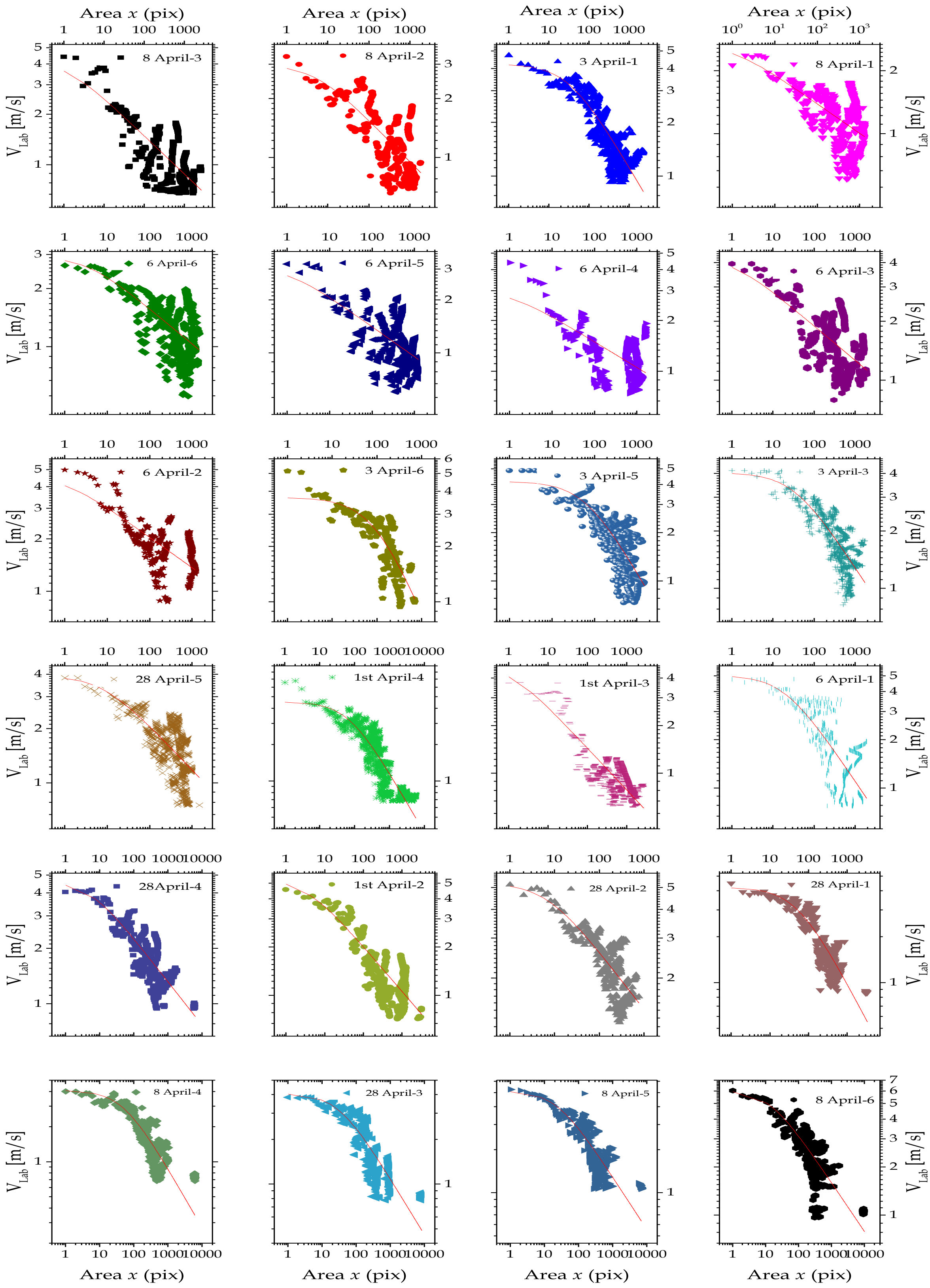

Figure C 7.. Fragment velocity distribution of individual experiments in the 2 cm – 5 cm series.

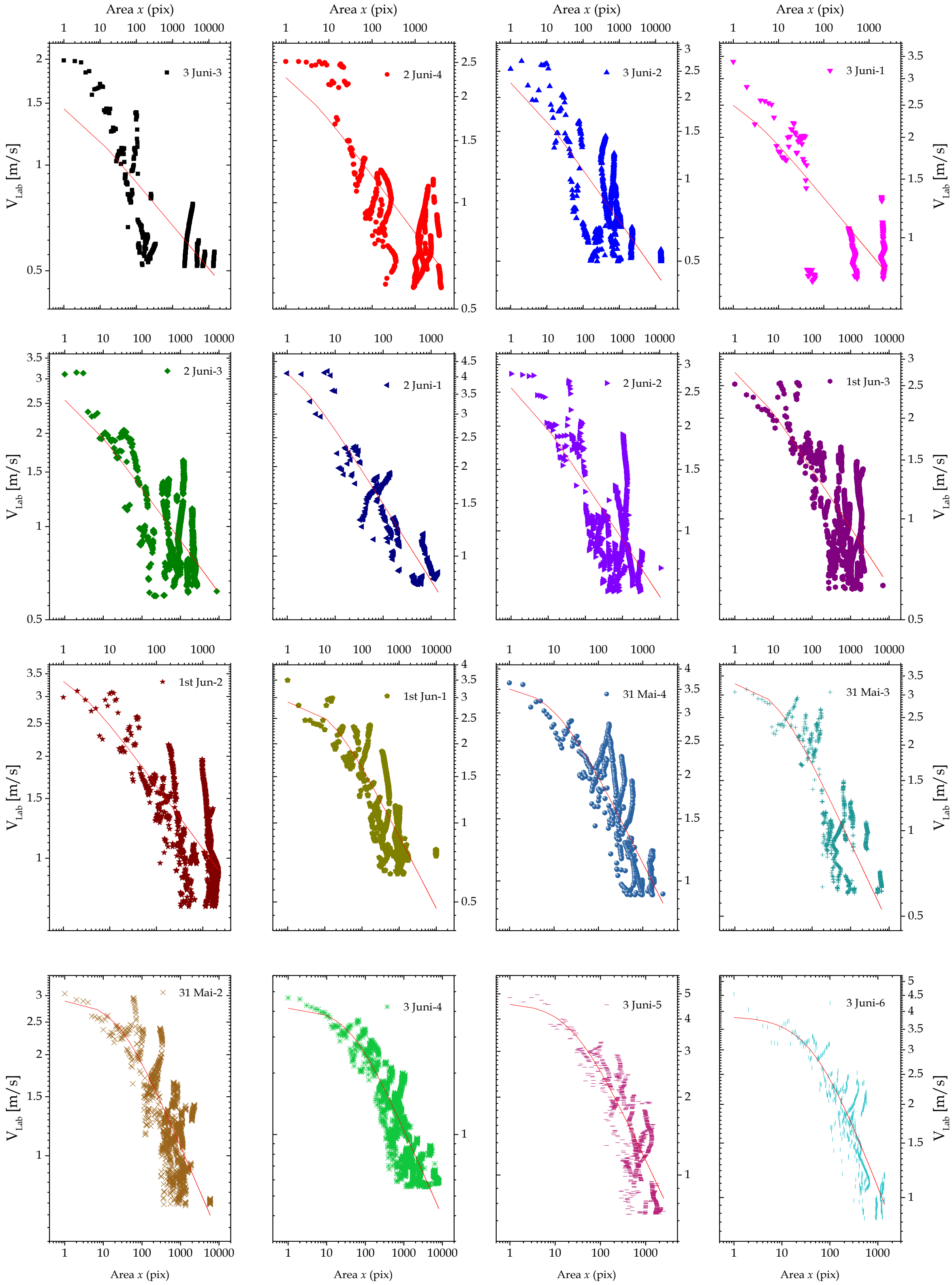

Figure C 9. Fragment velocity distribution of individual experiments in the 3.5 cm – 5 cm series

Appendix D : Supplementary images of experimental setup

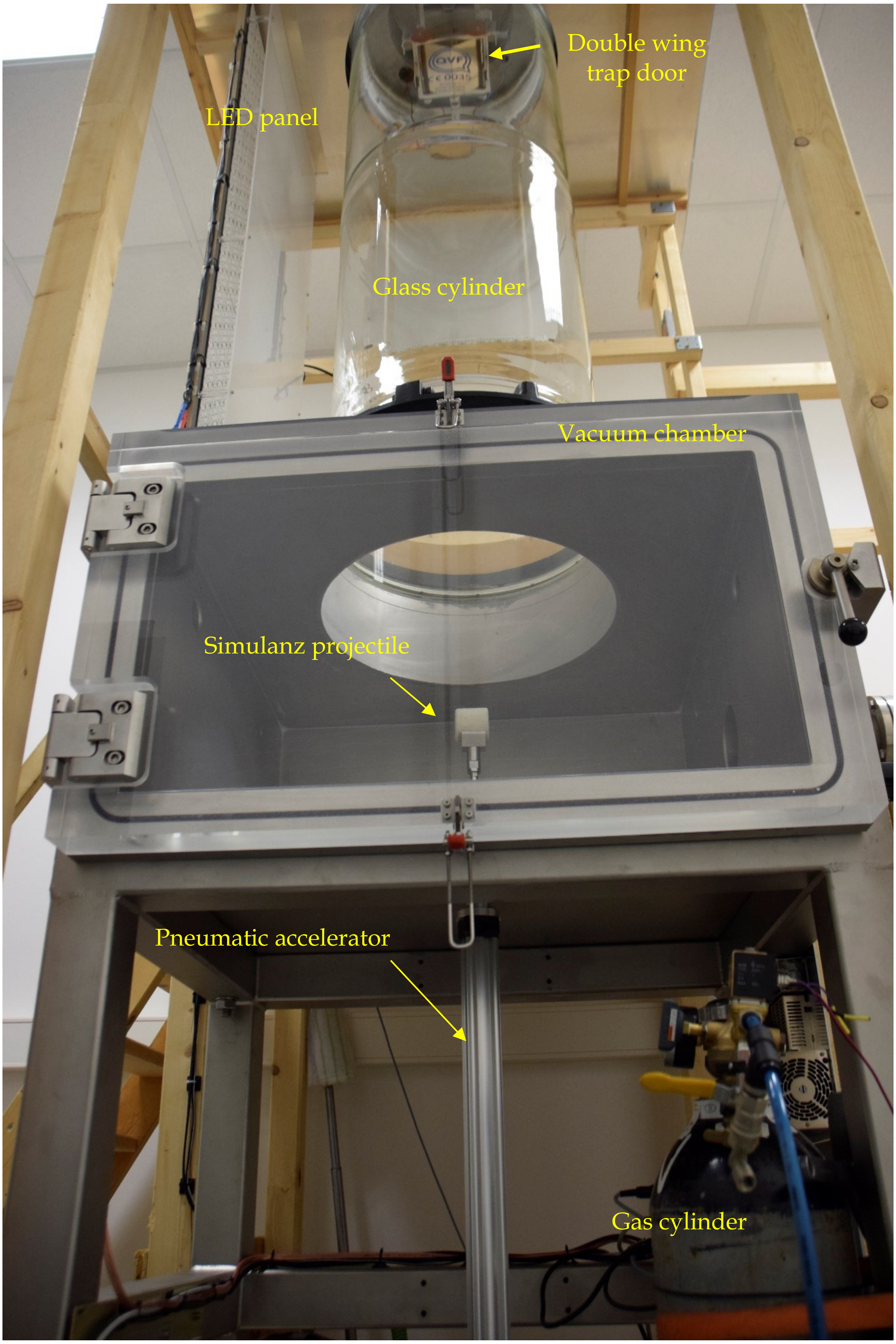

Figure D 1. Front view the of drop tower

Figure D 2. The side view of the drop tower and it is the direction from where the collisions are observed by the cameras.

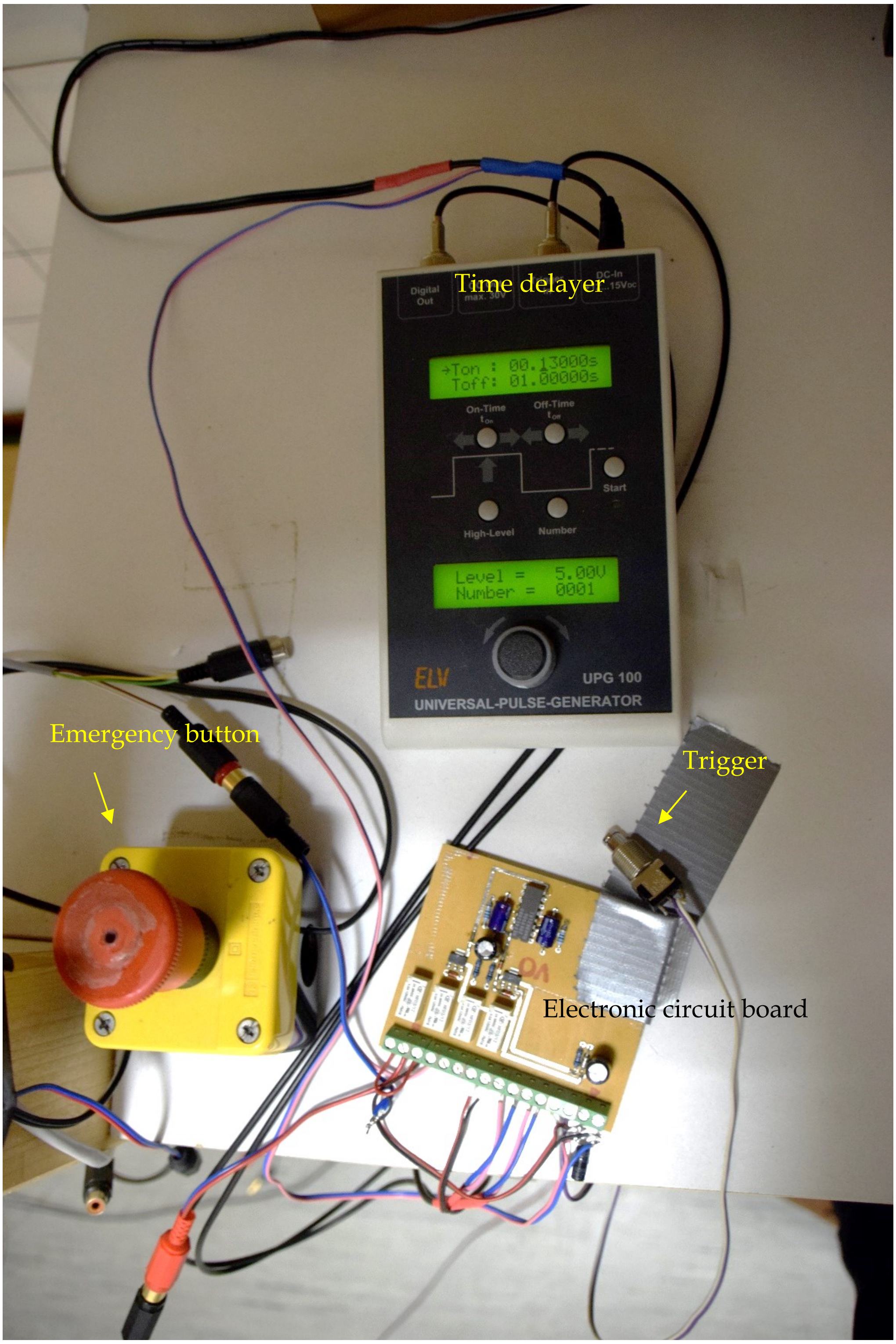

Figure D 3. The high speed cameras and the pneumatic accelerator are connected to the electronics circuit board which are sequenced by the time delayer. As the trigger is pressed experiment is accomplish.

Figure D 4. A simulant aggregate is being accelerated for calibration.

Figure D 5. In order to avoid the contamination of laboratory-air with dust, an industrial vacuum cleaner has been used to main low pressure in the drop tower, when experimenter cleans the setup.

Bibliography

Andrews, S. M., Wilner, D., Hughes, A., Qi, C., & Dullemond, C. 2009, The Astrophysical Journal, 700, 1502
Armitage, P. J. 2007, in arXiv preprint astro-ph/0701485
Bai, X.-N., & Stone, J. M. 2010, The Astrophysical Journal, 722, 1437
Beitz, E., Güttler, C., Blum, J., Meisner, T., Teiser, J., & Wurm, G. 2011, The Astrophysical Journal, 736, 34
Beitz, E., Güttler, C., Nakamura, A., Tsuchiyama, A., & Blum, J. 2013, Icarus, 225, 558
Bernasconi, R. 2002, Philosophers on race: critical essays, 145
Beuther, H., Klessen, R. S., Dullemond, C. P., & Henning, T. K. 2014, Protostars and Planets VI (University of Arizona Press)
Birnstiel, T. 2011, arXiv preprint arXiv:11073466
Birnstiel, T., Dullemond, C., & Brauer, F. 2010, Astronomy & Astrophysics, 513, A79
Blum, J. 2010, Research in Astronomy and Astrophysics, 10, 1199
Blum, J., et al. 2014, Journal of visualized experiments: JoVE
Blum, J., Bodenschatz, E., Wagner, C., & Xu, H. 2011, in (TU Braunschweig, University of Goettingen: DFG/SFB 963), 24
Blum, J., Gundlach, B., Mühle, S., & Trigo-Rodriguez, J. M. 2014, Icarus, 235, 156
Blum, J., & Münch, M. 1993, Icarus, 106, 151
Blum, J., & Wurm, G. 2000, Icarus, 143, 138
---. 2008, Annu Rev Astron Astrophys, 46, 21
Blum, J., Wurm, G., Kempf, S., & Henning, T. 1996, Icarus, 124, 441
Blum, J., et al. 2000, Physical Review Letters, 85, 2426
Blum, J., Wurm, G., Poppe, T., & Heim, L.-O. 1999, in Laboratory astrophysics and space research (Springer), 399
Booth, R. A., & Clarke, C. J. 2016, Monthly Notices of the Royal Astronomical Society, stw488
Brauer, F., Dullemond, C., & Henning, T. 2008, Astronomy & Astrophysics, 480, 859
Brauer, F., Dullemond, C., Johansen, A., Henning, T., Klahr, H., & Natta, A. 2007, Astronomy & Astrophysics, 469, 1169
Bukhari Syed, M. A., & Blum, J. 2013. in Protostars and Planets VI, The outcome of dust-aggregate collisions in streaming and gravitational instabilities (Heidelberg)
---. 2014a. in The Formation of the Solar System I, The outcome of dust-aggregate collisions in streaming and gravitational instabilities (Bonn)
---. 2014b. in Planet Formation and Evolution, Transition between growth and fragmentation in dust-agglomerate collisions (Kiel)
---. 2015. in The Formation of the Solar System I I, The outcome of dust-aggregate collisions in streaming and gravitational instabilities (Berlin)
---. 2016. in Planet Formation and Evolution II, The outcomes of dust-aggregate collisions during the gravitational collapse in planetesimal formation (Duisburg)
Bukhari Syed, M. A., Blum, J., Wahlberg Jansson, K., & Johansen, A. 2017, The Astronomical Journal, 834
Carpenter, J. M., Mamajek, E. E., Hillenbrand, L. A., & Meyer, M. R. 2006, The Astrophysical Journal Letters, 651, L49
Carrera, D., Johansen, A., & Davies, M. B. 2015, arXiv preprint arXiv:150105314
Chiang, E., & Youdin, A. 2009, arXiv preprint arXiv:09092652
Cuzzi, J. N., Dobrovolskis, A. R., & Champney, J. M. 1993, Icarus, 106, 102
Cuzzi, J. N., Hogan, R. C., Paque, J. M., & Dobrovolskis, A. R. 2001, The Astrophysical Journal, 546, 496
Deckers, J., & Teiser, J. 2013, The Astrophysical Journal, 769, 151
---. 2014, The Astrophysical Journal, 796, 99
Della Corte, V., et al. 2016, Monthly Notices of the Royal Astronomical Society, stw2529
Desch, S. 2007, The Astrophysical Journal, 671, 878
Dominik, C., & Tielens, A. 1997, The Astrophysical Journal, 480, 647
Drążkowska, J., & Dullemond, C. P. 2014, Astronomy & Astrophysics, 572, A78
Drążkowska, J., Windmark, F., & Dullemond, C. 2013, Astronomy & Astrophysics, 556, A37
Dullemond, C. 2013, in, eds. C. f. A. Z. Heidelberg University, & I. f. T. A. (ITA), 15
Dullemond, C., & Dominik, C. 2005, Astronomy & Astrophysics, 434, 971
Dullemond, C., Hollenbach, D., Kamp, I., & d'Alessio, P. 2006, arXiv preprint astro-ph/0602619
El-Maarry, M., et al. 2015, Astronomy & Astrophysics, 583, A26
Fulle, M., et al. 2015, The Astrophysical Journal Letters, 802, L12
Garaud, P., Meru, F., Galvagni, M., & Olczak, C. 2013, The Astrophysical Journal, 764, 146

Geretshauser, R. J., Meru, F., Speith, R., & Kley, W. 2011, Astronomy & Astrophysics, 531, A166
Goldreich, P., & Lynden-Bell, D. 1965, Monthly Notices of the Royal Astronomical Society, 130, 97
Goldreich, P., & Ward, W. R. 1973, The Astrophysical Journal, 183, 1051
Güttler, C., Blum, J., Zsom, A., Ormel, C. W., & Dullemond, C. P. 2010, Astronomy & Astrophysics, 513, A56
Haisch Jr, K. E., Lada, E. A., & Lada, C. J. 2001, The Astrophysical Journal Letters, 553, L153
Heim, L.-O., Blum, J., Preuss, M., & Butt, H.-J. 1999, Physical Review Letters, 83, 3328
Heißelmann, D., Fraser, H. J., & Blum, J. 2007, in 58th International Astronautical Congress 2007 (Hyderabad, India)
---. 2011, arXiv preprint arXiv:11064760
Hill, A. V. 1910, J Physiol (Lond), 40, 4
Ida, S., & Lin, D. 2008, The Astrophysical Journal, 685, 584
Imara, N., & Blitz, L. 2011, The Astrophysical Journal, 732, 78
Jansson, K. W., & Johansen, A. 2014, Astronomy & Astrophysics, 570, A47
Johansen, A., Blum, J., Tanaka, H., Ormel, C., Bizzarro, M., & Rickman, H. 2014, arXiv preprint arXiv:14021344
Johansen, A., Brauer, F., Dullemond, C., Klahr, H., & Henning, T. 2008, Astronomy & Astrophysics, 486, 597
Johansen, A., Oishi, J. S., Mac Low, M. M., Klahr, H., Henning, T., & Youdin, A. 2007, Nature, 448, 1022
Johansen, A., & Youdin, A. 2007, The Astrophysical Journal, 662, 627
Johansen, A., Youdin, A., & Klahr, H. 2009, The Astrophysical Journal, 697, 1269
Johansen, A., Youdin, A., & Mac Low, M.-M. 2009, The Astrophysical Journal Letters, 704, L75
Johansen, A., Youdin, A. N., & Lithwick, Y. 2012, Astronomy & Astrophysics, 537, A125
Joy, A. H. 1945, The Astrophysical Journal, 102, 168
Kadono, T., Arakawa, M., & Mitani, N. K. 2005, Physical Review E, 72, 045106
---. 2005, Physical Review E, 72, 045106
---. 2005, Physical Review E, 72, 045106
Kempf, S., Pfalzner, S., & Henning, T. K. 1999, Icarus, 141, 388
Klahr, H., & Brandner, W. 2006, Planet formation: theory, observations, and experiments, Vol. 1 (Cambridge University Press)
Kleingeld, P. 2007, The Philosophical Quarterly, 57, 573
---. 2007, The Philosophical Quarterly, 57, 573
Kothe, S., Blum, J., Weidling, R., & Güttler, C. 2013, Icarus, 225, 75
Kothe, S., Güttler, C., & Blum, J. 2010, The Astrophysical Journal, 725, 1242
Krause, M., & Blum, J. 2004, Physical review letters, 93, 021103
Langkowski, D., Teiser, J., & Blum, J. 2008, The Astrophysical Journal, 675, 764
Lissauer, J. J. 1993, Annual review of astronomy and astrophysics, 31, 129
Love, S. G., Hörz, F., & Brownlee, D. E. 1993, Icarus, 105, 216
Lynden-Bell, D., & Pringle, J. 1974, Monthly Notices of the Royal Astronomical Society, 168, 603
Meru, F., Geretshauser, R. J., Schäfer, C., Speith, R., & Kley, W. 2013, Monthly Notices of the Royal Astronomical Society, stt1447
Mizuno, H. 1980, Progress of Theoretical Physics, 64, 544
Mottola, S., et al. 2015, Science, 349, aab0232
Nakagawa, Y., Nakazawa, K., & Hayashi, C. 1981, Icarus, 45, 517
Natta, A., Testi, L., Calvet, N., Henning, T., Waters, R., & Wilner, D. 2006, arXiv preprint astro-ph/0602041
Natta, A., Testi, L., Calvet, N., Henning, T., Waters, R., & Wilner, D. 2007, in (B. Reipurth, D. Jewitt, & K. Keil (Tucson, AZ: Univ. Arizona Press))
Okuzumi, S., Tanaka, H., Kobayashi, H., & Wada, K. 2012, The Astrophysical Journal, 752, 106
Ormel, C., & Cuzzi, J. 2007, Astronomy & Astrophysics, 466, 413
Ormel, C., Cuzzi, J., & Tielens, A. 2008, The Astrophysical Journal, 679, 1588
Pajola, M., et al. 2016,
Pérez, L. M., et al. 2012, The Astrophysical Journal Letters, 760, L17
Peters, N. 1999, Journal of Fluid mechanics, 384, 107
Pollack, J. B., Hubickyj, O., Bodenheimer, P., Lissauer, J. J., Podolak, M., & Greenzweig, Y. 1996, Icarus, 124, 62
Poppe, T., Blum, J., & Henning, T. 2000a, The Astrophysical Journal, 533, 454
---. 2000b, The Astrophysical Journal, 533, 472
Ricci, L., et al. 2011, Astronomy & Astrophysics, 525, A81
Rucinski, S. 1985, The Astronomical Journal, 90, 2321
Ryan, E. V., Hartmann, W. K., & Davis, D. R. 1991, Icarus, 94, 283
Safronov, V. 1960. in Annales d'Astrophysique, On the gravitational instability in flattened systems with axial symmetry and non-uniform rotation, 979
Schräpler, R., & Blum, J. 2011. in EPSC-DPS Joint Meeting 2011, Erosion of large aggregates in protoplanetary

disks as a source of micrometer-sized particles, 6
Schräpler, R., Blum, J., Seizinger, A., & Kley, W. 2012, The Astrophysical Journal, 758, 35
Schräpler, R., Blum, J., von Borstel, I., & Güttler, C. 2015, Icarus, 257, 33
---. 2015, Icarus, 257, 33
Sekiya, M. 1998, Icarus, 133, 298
Shakura, N., & Sunyaev, R. 1973, Web of Science® Times Cited, 4641
Shi, J.-M., & Chiang, E. 2013, The Astrophysical Journal, 764, 20
SIGMA-ALDRICH. 2012, in, ed. SIGMA-ALDRICH
Skorov, Y., & Blum, J. 2012, Icarus, 221, 1
Song, I., Zuckerman, B., Weinberger, A. J., & Becklin, E. 2005, Nature, 436, 363
Stepinski, T., & Valageas, P. 1996, Astronomy and Astrophysics, 309, 301
Stewart, S. T., & Leinhardt, Z. M. 2009, The Astrophysical Journal Letters, 691, L133
Takeuchi, T., & Lin, D. 2002, The Astrophysical Journal, 581, 1344
Takeuchi, T., Muto, T., Okuzumi, S., Ishitsu, N., & Ida, S. 2011, The Astrophysical Journal, 744, 101
Teiser, J., Engelhardt, I., & Wurm, G. 2011a, The Astrophysical Journal, 742, 5
Teiser, J., Küpper, M., & Wurm, G. 2011b, Icarus, 215, 596
Teiser, J., & Wurm, G. 2009b
Astronomy & Astrophysics, 505, 351
Testi, L., et al. 2014, Protostars and Planets VI, 1, 339
Tsiganis, K., Gomes, R., Morbidelli, A., & Levison, H. 2005, Nature, 435, 459
Ulrich, R. K. 1976, The Astrophysical Journal, 210, 377
van Boekel, R., et al. 2004, Nature, 432, 479
Völk, H., Jones, F., Morfill, G., & Röser, S. 1980, Astronomy and Astrophysics, 85, 316
Wahlberg Jansson, K., & Johansen, A. 2014, Astronomy & Astrophysics, 570, A47
Wahlberg Jansson, K., Johansen, A., Bukhari Syed, M., & Blum, J. 2017, Astronomy & Astrophysics, 570, A47
Weidenschilling, S. 1977, Monthly Notices of the Royal Astronomical Society, 180, 57
---. 1980, Icarus, 44, 172
---. 1997, icarus, 127, 290
Weidling, R., Güttler, C., & Blum, J. 2012, Icarus, 218, 688
Weidling, R., Güttler, C., Blum, J., & Brauer, F. 2009, The Astrophysical Journal, 696, 2036
Whipple, F. 1972, in (London: Wiley)
Whipple, F. L. 1972, In From Plasma to Planet (A. Elvis, ed.: Wiley, New York)
Williams, J. P., & Cieza, L. A. 2011, arXiv preprint arXiv:11030556
Wilner, D., D'Alessio, P., Calvet, N., Claussen, M., & Hartmann, L. 2005, The Astrophysical Journal Letters, 626, L109
Windmark, F., Birnstiel, T., Güttler, C., Blum, J., Dullemond, C. P., & Henning, T. 2012, Astronomy & Astrophysics, 540, A73
Windmark, F., Birnstiel, T., Ormel, C., & Dullemond, C. 2012a, Astronomy & Astrophysics, 548, C1
Windmark, F., Birnstiel, T., Ormel, C., & Dullemond, C. P. 2012, Astronomy & Astrophysics, 544, L16
Windmark, F., Birnstiel, T., Ormel, C. W., & Dullemond, C. P. 2013. in Protostars and Planets VI Posters, Planetesimal formation by sweep-up coagulation
Wurm, G., Paraskov, G., & Krauss, O. 2005, Physical Review E, 71, 021304
---. 2005b, Icarus, 178, 253
Wyatt, M. C. 2008, Annu Rev Astron Astrophys, 46, 339
Youdin, A., & Johansen, A. 2007, The Astrophysical Journal, 662, 613
Youdin, A. N., & Chiang, E. I. 2004, The Astrophysical Journal, 601, 1109
Youdin, A. N., & Goodman, J. 2005, The Astrophysical Journal, 620, 459
Youdin, A. N., & Kenyon, S. J. 2013, in Planets, Stars and Stellar Systems (Springer), 1
Youdin, A. N., & Shu, F. H. 2002, The Astrophysical Journal, 580, 494
Zsom, A., & Dullemond, C. 2008, Astronomy & Astrophysics, 489, 931
Zsom, A., Ormel, C., Güttler, C., Blum, J., & Dullemond, C. 2010, Astronomy & Astrophysics, 513, A57

Lebenslauf

Mohtashim Ahmad **Syed Bukhari**
geboren am 04.03.1982
in Multan, Pakistan
deutsche Staatsangehörigkeit

Geysostraße 2, 38106 Braunschweig
Telefon: +49 531 295 75227
Mobil: +49 176 3736 1315
m.bukhari@tu-braunschweig.de

Berufserfahrung

05.2012 – 12.2017

Wissenschaftlicher Mitarbeiter
Institut für Geophysik und Extraterrestrische Physik, TU Braunschweig

- Bildbearbeitung zur Datenerfassung, Datenmanipulation, Einzelpartikelverfolgung, Zeitreihenanalyse, Chi-Quadrat-Test, Bestimmung der statistischen Signifikanz der relativen Gewichte, Dimensional-Reduktion.
- Entwicklung eines Phasendiagrams und die mathematische Modellen um die Anzahl, Größenverteilung und Geschwindigkeitsverteilung der Teilchen zu beschreiben.
- Entwickelung eines Algorithmus als „Grand Fragmentation Model" das den innere Aufbau einer Sternschnuppe erklärt.
- Experiment Design und Aufbau eines Fallturms mit zwei Hochgeschwindigkeitskameras, optimierung der Mess und Verfahrenstechnik für die Staub-Kollision.
- Tagungen, Seminars und Veröffentlichungen der Arbeit.

03.2012 – 05.2012

Wissenschaftlicher Mitarbeiter
Fakultät für Physik und Geowissenschaften, Universität Leipzig

- Experiment Design und Aufbau der Plasmakammer, ZnO-Schichten mit PLD
- H^+ Dotierung an ZnO-Filme.
- Datenerfassung und Auswertung aus SQUID-Test um die magnetischen Eigenschaften von ZnO-Filme zu modellieren.

08.2009 – 07.2010

Wissenschaftliche Hilfskraft Student
Fraunhofer Institut, Center für Silizium-Photovoltaik, Halle

- Untersuchung von neuen Verfahrenstechnik zur Herstellung der Si-Filme durch Sputtern des Si-Targets. Optimierung des das Beschichtungsprozess.
- Untersuchung von den Absorption, Raman und Röntgen Spektren für die optische und strukturelle Charakterisierung den Si-Filme.
- Untersuchung der elektrische Eigenschaften (die Leitfähigkeit, den Leitungswiderstand und die Rekombinationszeit) mit vier-Punkt-Probe und Photolumineszenz.

10.2008 – 11.2008

Wissenschaftliche Hilfskraft, Student
Max-Planck-Institut für Extraterrestrische Physik, Garching

- Datenanalyse der Oberfläche des Spiegels vom Röntgenteleskop

03.2007 – 07.2007

Schriftsetzer
Da-TeX GmbH, Leipzig

Akademische Ausbildung

05.2012 – 12.2016	**Promotion, (Disputation am: 6. April 2017)** Institut für Geophysik und Extraterrestrische Physik, TU Braunschweig Thema der Dissertation: The role of pebble fragmentation in planetesimal formation during the gravitational collapse of a pebble cloud. Validitätstest der Planetenentstehung durch „streaming instability“ und „gravitational instability“
02.2011 – 01.2012	**Deutsch Sprachkurs mit dem C2 Zertifikat** Volkhochschule, Leipzig
10.2007 – 09.2010	**Diplomstudium Physik** Ludwig-Maximilians-Universität München
10.2003 – 09.2007	**Diplomstudium Physik (Vordiplom/B.Sc)** Universität Leipzig
09.1999 – 09. 2002	**Bachelor of Science**, Govt. College of Science, Multan
03.1986 – 09.1998	**Sekundar 1+2** Govt. College Civil Lines, Multan

Zusatzkenntnisse/ Praktika

04.2017 – 05.2017	**Relational Datenbanken mit MS-SQL** Alfatraining, Braunschweig,
12.2012 – 12.2012	**ESA Zero Gravity (Parabolic Flight) Campaign** Bordeaux, Frankreich
12.2008 – 12.2008	**Praktikum, Exo-planet Search** Universitäts- Sternwarte, München
11.2008 – 11.2008	**Praktikum, Beobachtung: Kugelsternhaufen** Universitäts- Sternwarte, Wendelstein
09.2008 – 11.2008	**Vorlesung/Prüfung, Astrokurs** Max Plank Institut für Astrophysik
WS 2008 – 2009	**Vorlesung/Prüfung, Plasma Physik** Fakultät für Physik, LMU, München
WS 2008 – 2009	**Vorlesung/Prüfung, Compac stars und Supernovae I-II** Fakultät für Physik, LMU, München

Sonstiges

Softwarekenntnisse	OriginLab 9.0	(für Big Data Auswertung & Modellierung)
	Relational Datenbanken mit MS-SQL	(für Big Data Verwaltung)
	Imag J,	(für Bildbearbeitung)
	MS Office, MS Frontpage, MS Publisher	
Sprachkenntnisse	Undu – Muttersprache	Hindi – verhandlungssicher
	Deutsch – verhandlungssicher	Englisch – verhandlungssicher

Soziales Engagement

STUBE, Sachsen
Studienbegleitprogramm für Studierende aus Afrika, Asien, Lateinamerika und Südosteuropa. Vorbereitung und Teilnahme an Veranstaltungen und Seminaren zu Sozio-politischen, Sozio-ökonomischen, Interkulturellen–Interreligiösen Themen

Solidarität International e.V.
Unterstützung von Opfern durch Krieg und Naturkatastrophen im Ausland

Haus der Kultur, Braunschweig
Vorbereitung und Teilnahme an lokalen kulturellen Veranstaltungen

Referenzen

Prof. Dr. Jürgen Blum, IGEP TU Braunscheig,
j.blum@tu-braunschweig.de
Barbara Irmer Coordinator STUBE Sachen,
stube@infozentrum-dresden.de
Prof. Dr. Dieter Freude, Universität Leipzig,
freude@uni-leipzig.de
Prof. Dr. Otmar Biebel, LMU, München,
otmar.biebel@physik.uni-muenchen.de

Braunschweig, 01.05.2017

Mohtashim Bukhari